3-D Transonic Flow Dynamics with Nonequilibrium Condensation

by
Kevin A. Goodheart

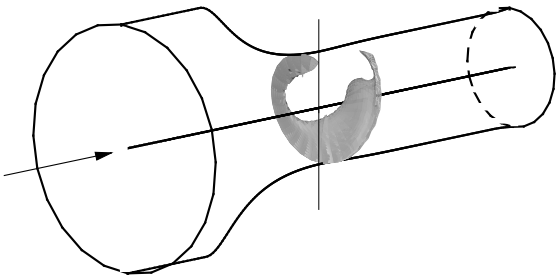

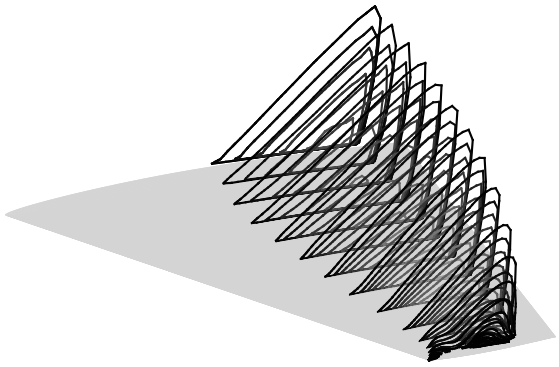

Munich 2004

Title Picture: Top: Snapshot of unsymmetric oscillation mode in the 3-D axisymmetric nozzle, [T_{01}=295 K, p_{01} = 1 bar, ϕ_0=95%, $f \approx$ 1350 Hz].

Bottom: Mach contour on the top surface of the F-16 Fighting Falcon wing, [T_∞ = 295 K, p_∞ = 1 bar, M_∞ = 0.9, $\alpha = 0°$, $N_{het,0} = 10^{12}\ m^{-3}$, R_p = 1x10^{-8} m, ϕ_∞ = 90%, MAC = 2.72 m, $Re_{\infty,MAC}$ = 54.8 10^6].

Technische Universität München

Lehrstuhl für Fluidmechanik

3-D Transonic Flow Dynamics with Nonequilibrium Condensation

Kevin A. Goodheart

Vollständiger Abdruck der von der Fakultät für Maschinenwesen der Technischen Universität München zur Erlangung des akademischen Grades eines

Doktor-Ingenieurs

genehmigten Dissertation.

Vorsitzender:	Univ.-Prof. Dr.-Ing. Dr.-Ing. habil. Rudolf Schilling
Prüfer der Dissertation:	
1.	Univ. Prof. Dr.-Ing. habil. Günter H. Schnerr
2.	Univ.-Prof. Dr.-Ing. Dr.-Ing. habil. Rainer Friedrich

Die Dissertation wurde am 22.10.2003 bei der Technischen Universität München eingereicht und durch die Fakultät für Maschinenwesen am 26.01.2004 angenommen.

Preface

The work in this thesis could not have been done without the understanding and patience of my wife. I thank her for making it through these times.

I must make a special thank you to Dr. Inz. Slawomir Dykas who took the time to teach me CFD in regards to compressible flow.

The final thesis was prepared at TU Munich but two years of the work was spent at the University of Karlsruhe (TH) in the Fachgebiet Strömungsmaschinen and my appreciation and regards go out to the group there.

The final year of the work was performed at TU Munich in the Lehrstuhl für Fluidmechanik under the direction of Prof. Dr.-Ing. habil. R. Schilling it is his group and ideas that made my stay here comfortable and fun, I will miss the Kaffeerunden and Sommerfest.

and to

Prof. Dr.-Ing. habil. G.H. Schnerr thank you for giving me the freedom to explore CFD, we made it through.

Muggensturm, in February 2004 Kevin A. Goodheart

Contents

Symbols

Latin Symbols:

c	Sound speed [m/s]
c_f	Frozen sound speed [m/s]
c	Chord length [m]
c_D	Drag coefficient
$c_{D,p}$	Pressure drag coefficient
c_f	Friction coefficient
c_L	Lift coefficient
c_p	Pressure coefficienct
c_p	Specific heat at constant pressure $[J/kg-K]$
c_v	Specific heat at constant volume $[J/kg-K]$
C^*	Concentration of a critical droplet $[1/m^3]$
C^*_μ	Variable in the EASM turbulent model
CFL	Courant-Friedrichs-Lewy number
D^*	Critical collision frequency for a vapor molecule $[1/s]$
e	Specific internal energy $[J/kg]$
E	Total internal energy $[J/kg]$
E_{ratio}	Eddy viscosity ratio [1-10]
$\mathbf{E}$	Vector for the convective fluxes in the ξ-direction
$\mathbf{E_v}$	Vector for the viscous fluxes in the ξ-direction
f	Frequency $[1/s]$
f	Favre mass-weighted operator
$f_\beta, f_\beta*$	Turbulent closure coefficients
F_1, F_2	Blending functions for SST model
$\mathbf{F}$	Vector for the convective fluxes in the η-direction
$\mathbf{F_v}$	Vector for the viscous fluxes in the η-direction
g	Condensate mass fraction
G	Gibbs free energy $[J]$
$\mathbf{G}$	Vector for the convective fluxes in the ζ-direction
$\mathbf{G_v}$	Vector for the viscous fluxes in the ζ-direction
h	Specific enthalpy $[J/kg]$
h^*	Throat height $[m]$
J	Nucleation rate $[m^{-3}s^{-1}]$

J	Determinate of the Jacobian $[m^3]$
k	Boltzmann's constant [1.380622 x $10^{-23} J/K$]
k	Heat conductivity $[W/m-K]$
k	Turbulent kinetic energy $[J/kg$ or $m^2/s^2]$
Kn	Knudsen number $Kn = \frac{\lambda}{2r}$
l	Characteristic length [m]
l_{tu}	Turbulence length scale
L	Latent heat (heat of vaporization) [J/kg]
m	Mass of a specific molecule [kg]
M	Mach number
M	Mass [kg]
n_{hom}	Number density of droplets [1/kg]
$N_{het,0}, n_{het}$	Number density of particulates [1/m^3]
NI, NJ, NK	Maximum grid points in x,y, and z direction
p	Pressure [Pa]
P	Turbulent production $[N/m^2 - s]$
Pr	Prandtl number
q	Heat flux $[W/m^2]$
$\mathbf{Q}$	Time vector
r	Droplet radius [m]
$\overline{r}$	Mean droplet radius [m]
r^*	Critical radius [m]
R	Specific gas constant [J/kg-K]
R_p	Particle radius [m]
R^*	Radius of nozzle wall curvature at the throat [mm]
Re	Reynolds number
Re_t	Turbulent Reynolds number
S	Entropy [J/kg-K]
S	Supersaturation: $S = p_v/p_{s,\infty}(T)$
$\mathbf{S}$	Source vector
S_{ij}	Strain tensor $[1/s]$
t	Time [s]
t	Thickness [%]
T	Temperature [K]
T''	Turbulent intensity [m/s]
u	Velocity compenent in x-direction $[m/s]$
v	Velocity compenent in y-direction $[m/s]$
V	Volume $[m^3]$
w	Velocity compenent in z-direction $[m/s]$
x	Absolute air humidity: $[x = \frac{g_{max}}{1 - g_{max}}]$
x, y, z	Cartesian coordinate [m]
y^*	Half the throat distance in a nozzle [mm]

y^+	Dimensionless wall distance
Z	Zeldovich factor

Greek Symobls:

α	Angle of attack
α	Mass accomodation coefficient
β_o, β^*	Turbulent closure coefficients
γ	specific heat capacity ratio
γ_1, γ_2	Turbulent closure coefficients
δ_{ij}	Operator $i = j, = 1, i \neq j, = 0$
Δ	Difference
κ	Constant [$\kappa = 0.41$]
λ	Free mean path [m]
μ	Dynamic viscosity [$kg/m - s$]
ν	Kinematic viscosity [m/s^2]
ξ, η, ζ	General coordinates for computational domain
$\xi_{x,y,z}, \eta_{x,y,z}, \zeta_{x,y,z}$	Metrics [m^2]
ρ	Density [kg/m^3]
$\overline{\rho u_i'' u_j''}$	Reynolds-Stress tensor [N/m^2]
$\overline{\rho u_j'' h''}$	Reynolds heat flux [W/m^2]
$\sigma, \sigma*$	Turbulent closure coefficients
σ	Surface tension [N/m]
τ	Shear stress [N/m^2]
ϕ	Relative humidity [%]
ϕ_0	Relative humidity at total conditions: $\phi_0 = p_{v,01}/p_{s,\infty}(T_{01})$
χ_ω, χ_k	Turbulent closure coefficients
ω	Specific dissipation rate [$1/s$]
Ω_{ij}	Rotation tensor [$1/s$]

Subscript Indices:

a	Air
exp	Experiment
f	Frozen, which relates to a diabatic situation
$F\text{-}S$	Model from Fuchs-Sutugin
Gy	Model from Gyarmathy
hom	Homogeneous condensation
het	Heterogeneous condensation
i, j, k	Variable index in the computational domain
$init$	Initial values before starting simulation
l	Liquid
L	Left extrapolated state

m	molecular
mac	Mean aerodynamic chord
max	Maximum value
n	Normal component
out	Outlet condition
p	Particle
R	Right extrapolated state
s	Saturation
t	Turbulent
v	Vapor
0	Total conditions (zero velocity)
01	Total conditions at inlet ahead of heat addition
∞	Infinite plane
∞	Free stream condition

Superscript Indices:

$*$	Condition at $M = 1$
$*$	Critical condition for droplet
$*$	dimensionless variable
$*$	Primitive variable before boundary condition correction
$-$	Mean value
$'$	Fluctuation in the Reynolds-Averaging
$''$	Fluctuation in the Favre-Averaging

All symbols that are not found in the list are defined in the text.

1. Introduction

1.1. Scope

With advancement of computer hardware and turbulence modeling the effects of condensation with turbulence and 3-D geometries are examined. Two areas of focus are nozzle flow with self-excited oscillations and external flow around wings in regards to boundary layer separation.

1.2. Literature Overview

The literature overview section gives insight into the major works in the fields of condensation and turbulence modeling. It will start with a short history of condensation modeling with an emphasis on water vapor / carrier gas mixtures followed by 3 sections that detail the different aspects of condensation modeling and their major conclusions. The final section is a short summary of the turbulence models used in this thesis but in no way a complete overview of turbulence modeling.

1. Homogeneous and heterogeneous condensation modeling
2. Thermal choking-internal flow
3. Oscillating flows with homogeneous condensation
4. Condensation on airfoils / wings
5. Turbulence modeling

Homogeneous and Heterogeneous Condensation Modelling
Short History
In the late 1800's work in condensation consisted of atmospheric physics, supersonic steam nozzle by de Laval, and the Wilson cloud chamber. It was Prandtl though who brought condensation to aerodynamics in 1935 at the Volta Congress, where he introduced a schlieren picture of two oblique shock like patterns near the throat in a nozzle. Wieselsberger remarked at the meeting that this structure was dependent on the initial humidity of the air. So what turned out to be a bug for experimentalist turned into a field of condensation modeling. The fix for the wind tunnel is to dry the air before entering the experimental chamber. Hermann in the period between 1934 and 1936 published results on these

disturbances, calling them "condensation shocks" and noting that close to the throat they are normal (high humidities) and further downstream take on the X-shape structure (low humidities). In 1942 Oswatitsch presented a general kinetic and thermodynamic treatment of condensation in supersonic nozzles. One of the major contributions was that the foreign nuclei present in the wind tunnel does not play a role in condensation because of the time scale (cooling rate). Oswatitsch had difficulties with his theory in predicting the onset of condensation because of the lack of knowledge in surface tension and other properties at such low temperatures for water. So now at this time it was known that the effect of condensation was dependent on nozzle geometry (throat and wall curvature), initial humidity, and time scale of expansion.
In parallel to the work seen in supersonic wind tunnels, Lord Kelvin showed that the vapor pressure of a drop is given by

$$p/p_\infty = \exp\left(\frac{2\sigma}{r}\frac{1}{\rho_l R_v T}\right) \quad . \tag{1.1}$$

where σ is the surface tension, r is the droplet radius. Equation 1.2 is sometimes referred to as the Gibbs-Thomson equation. Gibbs introduced the idea of a critical nucleus that is required to start the growth of a droplet. In 1926, Volmer and Weber first suggested the theory of homogeneous nucleation, which relates the rate of formation of these critical droplets in pure vapor. The theory is only applicable in the complete absence of foreign nuclei or if the cooling rate is high enough where the foreign nuclei do not play a role in the condensation process. The Nucleation rate from Volmer [96] is

$$J \sim e^{-\Delta G^*/kT} \quad . \tag{1.2}$$

The ΔG^* is the work required to produce one stable droplet of critical size and k is the Boltzmann constant. Using thermodynamics Gibbs [30] reasoned

$$\Delta G^* = \frac{16\pi\sigma^3\mu^2}{3R^2T^2\rho_l \ln^2(p_v/p_s)} \quad .$$

The kinetic factor ΔG^* in eq. 1.2 was argued by Becker and Döring in 1935 that it represents the work of a mean growth of a surface. Zeldovich [109] proposed a factor to account for the concentration gradient of the critical nuclei. Putting everything together the classical nucleation theory of Volmer[96], Frenkel [28], and Zeldovich [109] for formation of clusters of critical size in homogeneous condensation is

$$J = Z_{hom} D^*_{hom} C^*_{hom} \quad . \tag{1.3}$$

See chap. 2 sec. 2.4 for details of the terms in eq. 1.3. The above theory of nucleation also goes by the name of non-equilibrium condensation. The explanation of this is done best by paraphrasing Wegener and Mack [99]. If a drop accidentally absorbs just one molecule

the surrounding vapor will become supersaturated and the drop will grow, if on the other hand the drop loses one molecule the surrounding vapor will be superheated with respect to the drop, which will then evaporate completely. It is this meta-stable condition that leads to the collapse of "local" equilibrium with respect to small nuclei formed by eq. 1.3. A summary of droplet behavior follows from Schnerr [88]

$r < r^*$	cluster	unstable
r^*	nucleus	metastable
$r > r^*$	droplet	stable

With the ground work for a theoretical model it is time to go back to experiments to validate the theory and begin the task of empirical adjustments. From early experiments of steady shocks due to heat addition in supersonic nozzles, one must mention the name of Wegener. In a 1964 paper [100], Wegener and Pouring make a dividing line between sub- and supercritical heat addition. For any steady diabatic compressible flow there is a maximum amount of heat addition Q_{max} per unit mass of mixture. An expression is derived for $Q_{max} = f(\gamma M)$, which is valid for $Q < Q_{max}$ and is derived for a 1-D constant area flow. A graphical interpretation of the function is provided by fig.1.1.
For any given supersonic Mach number there are two solutions, one is a weak compression and the other is a shock. As $Q \rightarrow Q_{max}$ both solutions approach the Mach 1 line. For $Q > Q_{max}$ for a given supersonic Mach number the flow becomes unsteady. Going back to the dividing line definition of sub- and supercritical heat addition, for flows with $M > 1$ it is regarded as supercritical heat addition when a shock occurs due to heat addition, resulting in a pressure increase. Subcritical heat addition occurs as weak compression for flows with $M > 1$ and a weak expansion for flows with $M < 1$.

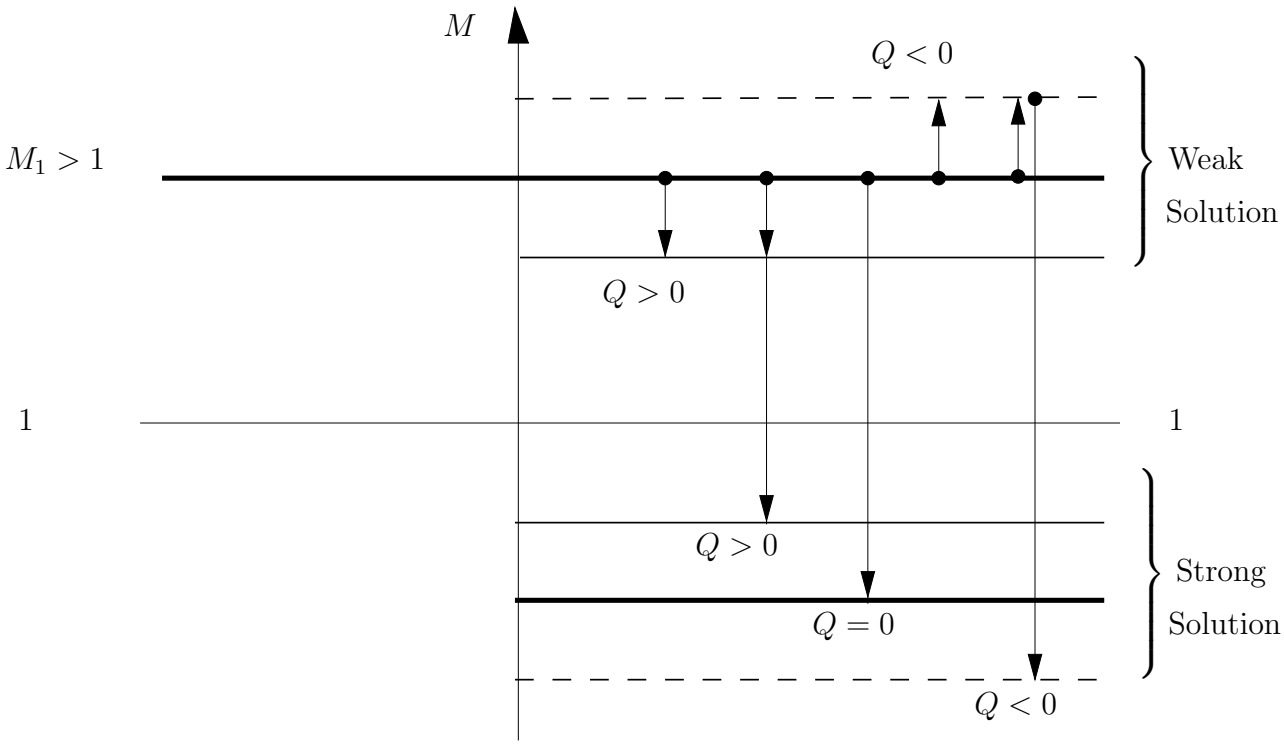

Figure 1.1.: Possible states involved in heat addition or cooling for supersonic flows, Schnerr [89].

Wegener then applies the equation of motion in 1-D, which results in 6 unknowns, p, A, u, ρ, T, and q, but using results from experiments the pressure and area are known, thus the continuity, momentum, energy, and q as a function of Mach number are solved. With q known the mass fraction can be then obtained. Thus using experimental data and fluid equations one can then compare results based on nucleation theory. One problem faced by Wegener was if the latent heat was between vapor-liquid or vapor-solid phase transition. The final statement of the paper in comparing the nucleation theory with experiment was that for a weak condensation zone the current theory was adequate with adjustment of the condensation coefficient α but for a higher humidity with a condensation shock the current theory needs to be re-analyzed or a fresh start made. From the current point of view, the problem faced by Wegener in 1963 was not entirely the nucleation theory but rather being able to properly resolve shocks.
Also during the time of Wegener, with more emphasis on numerics was the development of the Hill [40] equations for homogeneous condensation. Which consisted of solving a set of 4 transport equations based on the surface averaged droplet radius.
Going back into the direction of experiments the work of Schnerr [81] is fundamental to

the advancement of the physical models. The work includes quality Schlieren pictures of steady and unsteady condensation dynamics as well as the development of a similarity law for onset condensation Mach number which is a function of relative humidity and temperature gradient [81, 83]. More on Schnerr et al. findings is found in the following detailed sections of condensation.
The group of prof. Hoeijmakers in the Netherlands, Put[71] and van Noordenburg1[60] is involved with research in real gas effects and condensation in vortex flow using structured or unstructured grids. The group of prof. van Dongen in the Netherlands, Luijten[52, 53], Prast[69], Peeters[64, 66], and Lamanna [46] consists of experimental and numerical research in condensation dealing with the nucleation process in gas/vapor carrier mixtures and pure vapors.
So far the discussion has been limited to homogeneous condensation but for example, atmospheric flight or steam turbines, heterogeneous effects must be considered. A few of the main papers dealing with heterogeneous condensation that focus on a transitional model for droplet growth include Gyarmathy [35], Young [107, 108], and Kotake and Glass [45]. For these models they are trying to take into account the complete range of Knudsen numbers, from free molecule to continuum limit for vapor / carrier gas mixtures as well as pure vapor (steam). The Knudsen number is the ratio of the mean free path of the gas and the diameter of the droplet. Thus the assumption for vapor / carrier gas mixtures the $Kn \gg 1$. The different regimes can be classified as the free molecular level where droplet growth is dominated by a pressure difference between the surrounding vapor and the saturation pressure of the liquid droplet, corrections can be applied to go from a flat liquid-vapor interface to a spherical interface. Here the surface tension is the important variable. At the continuum regime the droplet growth is dominated by a temperature difference between the droplet and the surrounding vapor where conduction and diffusion coefficient play a role. Kotake and Glass go into detail of the droplet structure with two mechanism of direct impingement of a simple molecule and impingement by desorption of the already existing absorbed molecules. The nucleation equation then takes on an added factor that is a function of the radius of the solid particle, radius of the absorbed molecule and contact angle. The growth equation is similar to that developed by Gyarmathy. Chirikin [15] takes on a slightly different approach for heterogeneous condensation in the sense that an arbitrary size distribution of particles are used. The nucleation rate is the classical approach but the droplet growth law is from Oswatitsch, which is very similar to the Hertz-Knudsen law except for the addition of the latent heat. As a first approximation for vapor / carrier gas mixtures the Hertz-Knudsen model can be applied since the solid particle radius plus the condensate formed on the particle is still less than the mean free path of the vapor, see sec. 4.5.

Thermal choking-internal flow
In nozzle flows with or without the presence of foreign nuclei, condensation nuclei form in the vapor phase itself, if the characteristic timescale of the cooling is comparable to the time scale of the agglomeration of vapor molecules. In flows with fast expansion the development of the liquid phase is dominated by homogeneous condensation. If the con-

densation Mach number is in the transonic regime, the flow is near the maximum mass flux density and small changes due to heat addition can affect the flow, with excessive heat addition or higher humidities the flow can become thermally chocked producing condensation shocks in a nozzle with no back pressure compared to adiabatic shocks in nozzle with back pressure [22].
Schnerr [[81],[83]] has done experiments on 6 different types of supersonic nozzles. Two groups can be formed, 3 nozzles with a constant y^*/R^* ratio of 0.3 and 3 nozzles with a constant cooling rate or $1/\sqrt{y^* R^*}$ at $8.14 K/cm$ or $6000 mm^2$. From these experiments many outstanding Schlieren pictures of condensation phenomena, similarity law for the condensation onset Mach number, and a deeper understanding of the physics of condensation in nozzles has been discovered. Some of the main conclusions between the two nozzle groups are

1. For a constant time scale $-(dt/dx)^*$ the increase of relative humidity will cause a decrease in the condensation onset Mach number.

2. For a constant y^*/R^* ratio of 0.3 the nozzle with the higher cooling rate, $2y^* = 30$ compared to $2y^* = 120$, the condensation Mach number is higher and the disturbance is further downstream.

3. Decreasing the radius of wall curvature, while keeping $y^* R^*$ constant, the throat height increases and thus between the 3 nozzles the "X-Shock" is more pronounced for the larger throat at a constant ϕ_0.

Oscillating flows with homogeneous condensation
The occurrence of self-excited oscillations in slender nozzles with moist air as the medium was discovered and visualized by Schmidt [78]. Barschdorff [6, 7] continued this research and obtained frequency data in homogeneous condensing flow with moist air and steam. A similarity law for dimensionless frequency based on throat height, expansion rate, and stagnation conditions was derived by Zierep and Lin [110].
The first numerical 1-D results were performed by Saltanov and Tkalenko [77] which modeled unsteady two-phase nozzle flows with non-equilibrium condensation of water vapor. Guha and Young [34] also performed calculations for two different oscillation modes.
The first 2-D Euler unsteady results were performed by White and Young [102] for wet-steam flow in a slender Laval nozzle.
Mundinger [59] improved a numerical scheme to simulate unsteady 2-D condensation in circular arc nozzles. The method was applied to a systematic investigation of the frequency dependence on the relevant parameters; nozzle geometry, time - scale of expansion, and reservoir conditions.
Adam [1] performed experiments and numerically modeled unsteady transonic flow with non-equilibrium phase transition. The nozzle is called the A1 nozzle with a parallel outflow constant Mach number $M_{e,is.}$ =1.2. The nozzle characteristics are $2y^* = 90$ mm, radius of wall curvature at throat $R^* = 300$ mm, and cooling rate $-(dt/dx)^*_{exp} = 5.13$ K/cm. Flow patters in the supersonic nozzle include unsteady perfect symmetric shocks and unsymmetric moving oblique shock patterns. The difference between the A1 nozzle and circular

arc nozzles found in [81] is that the temperature gradient in the A1 nozzle after the throat decreases with a strong nonlinearity toward the exit compared to nearly constant for the circular arcs. From a detailed numerical study by Adam the following characteristics are determined for the plane A1 nozzle. At $\phi_0 < 40.0\%$ and with enough humidity thermal choking develops and a steady symmetric shock appears. At $40 < \phi_0 < 68.0\%$ the system is self excited and an unsteady symmetric shock moves to the throat disappears, reappears downstream of the shock and the process starts again. At $\phi_0 > 68.0\%$ there are two different frequencies for the same humidity. There is a frequency difference by a factor of 2 or more, where the higher frequency is an unsymmetric oblique shock system and the lower is the symmetric system. At $\phi_0 > 92\%$ there is only one oscillation pattern, the solution jumps immediately to the unsymmetric shock system. Since a numerical code can not model the unsymmetric oscillation in the hysteresis regime a linear disturbance for all primitive variables at one instant in time is applied to the symmetric solution, letting the code continue from there the unsymmetric solution evolves. To the right of the hysteresis regime the code is able to model the transition from a symmetric to unsymmetric mode, in a sense the symmetric mode is not stable or does not even exist at high enough humidities. It is possible that a disturbance is not needed if one is willing to wait for many days are if there is enough numerical error during the calculation, which means that one can use numerical error to amplify the inherent instability in the flow.
In regards to the experimental work of Adam, the hysteresis regime is much narrower compared to what was found from numerical simulations, but the structures (symmetric and unsymmetric) existed and were stable during the experiment.

Condensation on airfoils / wings

The photographs of condensation on airplanes reveal the flow structure on the plane and provide some fascinating pictures. What the pictures do not tell is how the performance of the plane is affected by the condensation, perhaps by talking with the pilot it is possible to learn, but for now the author must rely on numerical simulations. To begin the discussion of condensation on a wing lets start by examining some wonderful photographs of the different types of condensation.
Figure 1.2 shows two examples of a large supersonic region with condensation. The condensation front is produced due to large expansions, large temperature drop, followed by a sharp evaporation due to the shock that must occur to return to subsonic flow conditions.

Figure 1.2.: Left: Condensation on a F-14 Tomcat during level flight at $M_\infty = 0.9$ [13] Right: Condensation on a F-18 Hornet, photo by Nich Chinn, at Moffet Field airshow, 2001 [19]

Figure 1.3 is another clear example of the large supersonic region and it is occurring on a larger airplane, where the cooling rate and length are some of the important parameters for condensation. The F-14 has a swept back wing span around 11.55m where the B1-B Lancer has a swept back wing span around 24m. The chord lengths are more important for condensation but the wing span gives an idea of the magnitude of the wing size. Also in figs. 1.2 and 1.3 the canopy has a large expansion giving rise to condensation. It is postulated that the type of condensation occurring during this low-altitude level flight is heterogeneous condensation.

Figure 1.3.: Condensation on a B1-B Lancer, photo taken by Gregg Stansberry at Pensocola Beach, Florida, July 12, 2002 [90]

Lift-generated condensation usually occurs when the airplanes are at high angles of attack and large accelerations due to maneuvers. Figure 1.4 shows two examples of the condensation occurring on the wing. The flow is accelerated on the wing reaching local supersonic conditions, which coincides to large expansions thus enabling the water to condense. The water vapor is then terminated by a shock (compression increase in temperature). The shock is an adiabatic shock based on the assumption that the plane is traveling subsonic, therefore the flow must return to subsonic. For lift-generated condensation the type of condensation is most likely homogeneous, which is forming at the leading edge and then being convected downstream.

Figure 1.4.: Left: Lift condensation on a Tornado GR1 and Right: on a F-16 Falcon [90]

As the angle of attack is increased one can see a combination of lift-generated vortices and condensation on the top part of the wing appear, fig. 1.5. Cramer [19] uses the name Gullwing condensation cloud to describe the condensation on the top part of the wing in fig. 1.5 right.

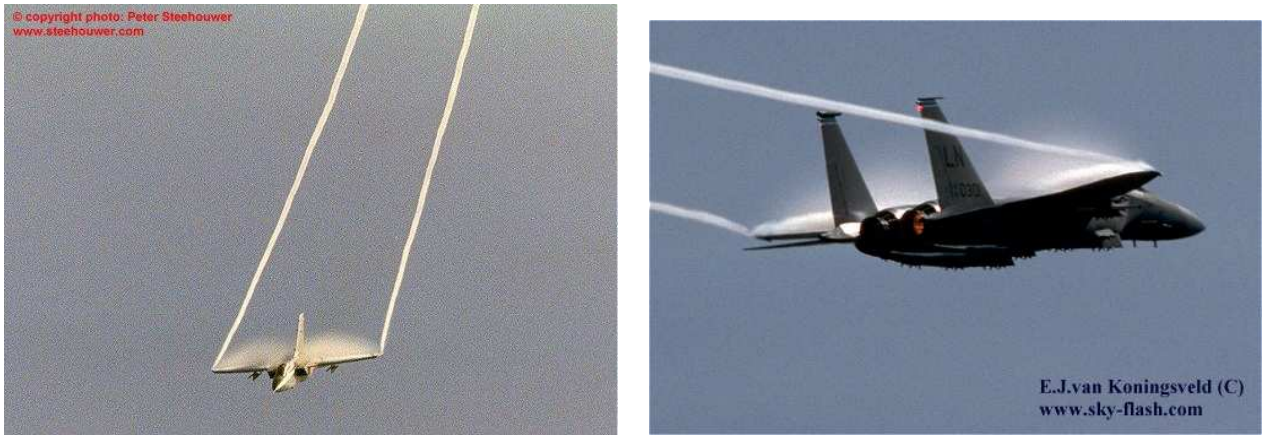

Figure 1.5.: Left: Condensation on a RAF Tornado, photo taken by Peter Steehouwer, at the International Air Tattoo. air show, 1998 [19] Right: Condensation on a F-15E Strike Eagle, [90]

Going to larger angles of attack the condensation cloud in fig. 1.6 starts to break up, most likely due to separation, also the wing tip vortices are visible in the figure on the right.

Figure 1.6.: Condensation on a F-18 Hornet at large angle of attack [90]

Figure 1.7.: Condensation on a F-J4J Phantom II. The following paragraph is text that was written on top of the photo: This one of a kind photo was shot by Mr. Harry Gann, of McDonnell Douglas, at the Point Mugu Naval Air Station on 23 October 1971. The aircraft, a McDonnell Douglas F-4J Phantom II "Black Bunny" from Navy flight test squadron VX-4, was captured on film while flying at near supersonic velocity. However, the local velocity on parts of the aircraft were supersonic, causing the two distinctive, diamond-shaped shock wave cones around the leading and trailing edges of the aircraft. A photograph like this is rare, it required split-second timing and a large amount of luck. "At the time, I was using a motorized Nikon F-2 camera, with a 300mm lens," states Mr. Gann, " I shot about four frames. The film was Ektachrome 400. As I remember, I was standing about 70 yards from the taxiway during the pass." [90]

Figure 1.7 is one of the best pictures in the authors view to describe condensation for a level flight at low altitudes. Below the figure is a description given by the photographer and most likely an employee of the former McDonnell Douglas. In fig. 1.7 with condensation one sees the supersonic expansion (sloped condensation front) followed by a strong normal shock at the trailing edge (nearly normal evaporation front), referred to as a diamond shock by the photographer. Again the canopy has condensation due to the flow expansion in the area. Noting that the region of condensation is not symmetric could mean that this is one frame from an unsteady behavior, where at the next second it is possible that the situation is reversed, (larger supersonic region on the top), which keeps the flight level. It is postulated that this type of condensation is dominated by heterogeneous effects.
The first set of numerical results for airfoils or wings with condensation to try to understand the effect on atmospheric flight was performed by Campbell, et.al.[13]. Side note: There is a long history of numerical condensation calculations in wind tunnels on airfoils

and such, but this was done for tunnel calibration, data accuracy, etc. In the Campbell paper they do not try to model the exact process of condensation but rather from the adiabatic solution they use relative humidity as a qualitative indicator for where condensation is to occur or evaporate. Thus the governing equations for fluid flow are decoupled from the transport equations for condensation. The numerical simulations include RAE2822 airfoil, NACA0012 airfoil, 76 degree slender delta wing, and a swept wing-body configuration (Boeing 747-200). The main focus of the paper is examining the different types of flow structures using condensation, shock waves, expansion, wing-body strake vortices, glove vortices. Schnerr and Dohrmann [82] coupled the Euler equations with 4 transport equations based on Hill [40] for homogeneous condensation. The test cases involved a circular arc and NACA0012 airfoil but with chord lengths based on wind tunnel models (0.08m and 0.1m). The purpose here was not to calibrate a wind tunnel but to simulate the change in drag due to homogeneous condensation. The main conclusion being an decrease in drag for the circular arc and an increase in drag due to condensation for the non-lifting NACA0012 airfoil. The decrease in drag is a result of a double shock forming which increases the pressure after the maximum thickness, thus reducing the drag. For the airfoil the heat addition occurs near the maximum thickness thus increasing the pressure, which increases the pressure drag. A different approach by Schnerr and Mundinger [84] couples the Euler equations with a similarity law where the heat source is specified by its strength and location. Comparisons are made with the coupled Euler and condensation transport equations. The main conclusions based on five different NACA profiles is that heat addition near stagnation points reduces the drag for non-lifting airfoils and around maximum thickness increases the drag. In another paper by Schnerr and Dohrmann [85] the same calculations for the circular arc and NACA0012 are performed but with the addition of a NACA0012 with a 1.5m chord with atmospheric flight parameters. Two different angles of attack were studied, 1.25° and 2.5°. The free stream humidity was set to 95% to achieve maximum effect. With the large angle of attack the supersonic region was increased, by shifting the shock further to the trailing edge. There is a slight decrease (5-10%) in lift for both angles of attack compared to the adiabatic conditions. Another technique examined was equilibrium condensation, this was performed by increasing the free stream Mach number from 0.8 to 0.834, which means the vapor becomes saturated in the free stream. In this case there is a lift increase of 30% but a drag increase of 200%. The missing link in the [85] paper is taking into account heterogeneous dominated or a mixture of homogeneous/heterogeneous condensation. So far we have discussed 2-D Euler flows for airfoils and now Yamamoto et. al. [105] brings turbulence as well as 3-D. The paper examines the RAE 2822 airfoil and ONERA M6 wing. The relative humidity is changed and results are compared with the adiabatic experiment. The geometries are model size scaled, for example a MAC of 0.646 m for the ONERA M6 wing. For both the RAE2822 and ONERA M6 wing the lift to drag ratio is decreased as the relative humidity is increased from 30 to 90%. Only homogeneous effects are considered. Another group Lee and Rusak [47] studied hetereogeneous/homogeneous condensation around a thin airfoil in atmospheric flight. The model is based on transonic small-disturbance theory with the addition of condensation parameters. For all the cases the freestream relative humidity is assumed to be a 100%

and thus comparisons are made by changing the free stream temperature. Lee and Rusak [47] state for each angle of attack there is a maximum lift coefficient for a given Mach number ($M_{\infty,max}$). The range of freestream Mach numbers evaluated are 0.3-0.9. If $M_\infty < (M_{\infty,max})$ then condensation will have the effect of increasing the lift and drag coefficient, on the other hand if $M_\infty > (M_{\infty,max})$ then there will be a decrease with the lift and an increase in the drag coefficient. Also comparisons are made between homogeneous and heterogeneous condensation on the NACA0012 airfoil with zero angle of attack. Compared to the adiabatic solution, heterogeneous condensation has the effect of moving the shock toward the trailing edge and increasing pressure drag, whereas homogeneous condensation is local, occurs ahead of the shock, with only a slight change of the shock wave position and pressure drag.

Turbulence Modeling

Heiler [39] was the first Ph.D. student in our group to bring together turbulence modeling and condensation. He implemented the Goldberg $k - R$ [31, 32] model with damping functions to be able to handle integration to the wall. Even though this was 4 years ago a lot has changed with turbulence models and computer hardware, thus enabling turbulence models to be applied to more advanced geometries and applications.

The 3-D solver that our current code is based on is from Benetschik [8] which uses a $k - \epsilon$ with two different low Reynolds approaches (Chien [14] and Biswas & Fukuyama [9]). It was decided not to implement a $k - \epsilon$ model because most of the flows in this thesis deal with walls and sometimes involve separation (due to a high pre-shock Mach number in transonic flow). It is well known that the $k-\epsilon$ model is not fit for separated flows and even though some of the fixes available could provide adequate results it was decided to go with $k - \omega$ based turbulence models. $k - \omega$ turbulence models are superior for wall bounded flows and separation, in fact the standard $k - \omega$ with no fixes can achieve superior results compared to a $k - \epsilon$ model. Also for a CFD code it is not advisable to have only one option for a turbulence model because each one has its advantages and disadvantages. For example the standard $k - \omega$ takes less time to calculate the source terms compared to the SST or EASM model, so in a simple unsteady flow it is advisable to use the $k - \omega$ model, but for a steady solution around a complex 3-D body then the EASM model is the model of choice. One disadvantage of turbulence modeling is that when this thesis is printed, it is likely that the turbulence models are outdated or have been improved whereas the classical nucleation theory for condensation still holds true after many decades.

The three turbulence models implemented in the code are the Wilcox $k - \omega$, SST, and EASM($k - \omega$). A distinction is made for EASM because there is also a $k - \epsilon$ version available. The SST model is a hybrid $k - \omega$-$k - \epsilon$ model but near a wall the mixing functions return to 100% the $k - \omega$ characteristics. Outside the boundary layer, the core flow, or in the wake, the SST model takes on $k - \epsilon$ characteristics. The details of the mentioned models can be found in chap 2, sec. 4.3.

1.3. Thesis Overview

The current two-phase, turbulent, 3-D Navier-Stokes CFD code pulls resources from many different fields and experiences. The quality of the condensation models found in phase CD are used [1, 23, 59, 39]. The RANS compressible equations are discretized using a 3-D node-centered finite volume method based on the work of Benetschik[8]. The code is written from a post-doctorial (Habilitation) report done by Benetschik which was developed for turbo machinery simulations at the RWTH Aachen. The report details how to determine the metrics, convective and diffusive fluxes, and boundary conditions. Thus Benetschik was used as a starting point for our code, where additions/alternations were added to accommodate for our research. Examples of additions include; k-ω based turbulence models compared to k-ϵ, condensation transport equations, boundary conditions for external flow, and the AUSMD scheme instead of the ROE scheme for the convective fluxes. The turbulence models [55, 75, 103] and upwinding AUSMD [97] scheme are found from journal articles and implemented with the EASM involving a few e-mails for clarification. The thesis involves validating the research code for condensation and turbulent test cases. The test cases for condensation involve nozzles with heat addition forming steady/ unsteady condensation shocks. The test cases for the turbulence model involve internal and external flow in the transonic regime. The test cases involve boundary layer flow with and without separation.
Chapter 2 covers the aspects of the physical models used to define a fluid with turbulence and heat addition. The equations and assumptions are presented in a way to give as much as possible the complete view of what was implemented.
Chapter3 shows how the physical models in chap. 2 are transformed to be solved numerically. Much work is needed to create a model and likewise the same amount of work is needed to solve them. The chapter also mentions where there are numerical problems and how they are solved.
In order to gain confidence in the results from the numerics, chap. 4 compares several test cases with known experimental data. To find and have an experiment is one aspect but it is also important to have all the information that is required by the numerical model. For example if the back pressure is not known for a nozzle flow with a shock, then this adds a degree of uncertainty because one can not compare the shock position if one can change the back pressure to match the correct shock position. Thus the test cases were chosen based on having enough information to begin a numerical test case.
Chapter 5 begins the first set of results for internal nozzle flow. The 2-D plane A1 nozzle used as a test case for validation in Chapter 4 is changed into a 3-D axisymmetric nozzle to see the effects of condensation when another degree of freedom is added to the system. For external flow chap. 6 examines the effect of homogeneous condensation around the 2-D circular arc ($t = 0.1$), NACA0012, and RAE2822 airfoils. The humidity is changed from 30-70% and a discussion follows as to why drag is either increasing or decreasing due to condensation. In chap. 7 two different wing configurations are examined, the ONERA M6 and the F-16 Falcon wing. For the ONERA M6 wing the effects of condensation are examined for different chord lengths and angles of attack. The ONERA M6 is a model size

test wing from a wind tunnel experiment, thus the chord length is changed to match that of atmospheric flight. Also with the ONERA M6 wing calculations are performed for a wind tunnel configuration, thus a smaller chord and different type of condensation occurs. The F-16 wing geometry is not changed because the actual wing size is used but the angle of attack is varied to see what different types of condensation occur.

2. Physical Modeling

2.1. Thermodynamic Principals For Moist Air

The main principles for moist air modeling are taken from the thesis of Adam [1] but for completeness a short description is given here. The system is a vapor/carrier gas mixture containing mostly dry air. Due to the high latent heat of water for a phase change from vapor to liquid, this can not be ignored in the energy equation. For example if there is stagnant moist air at 295 K with 50% relative humidity and 75% of the vapor were to condense to liquid the stagnation enthalpy would be increased by 5% based on a mixing ratio of 0.83% ($M_{v,0}/M$).
The air and water vapor are treated as perfect gases. The small vapor mass and high cooling rates give droplet radii on the order of 5x10^{-8} m, which allow for the approximation of neglecting the droplet volume and slip between the vapor/air and droplets [2].
The total mass of the system is given by the sum of the mass of air, vapor, and liquid

$$M = M_a + M_v + M_l \quad . \tag{2.1}$$

The fraction of liquid condensate to the total mass is defined

$$g = \frac{M_l}{M} = \frac{M_l}{M_a + M_v + M_l} \quad . \tag{2.2}$$

The possible maximum fraction of liquid condensate to total mass is

$$g_{max} = \frac{M_{v,0}}{M} \quad . \tag{2.3}$$

The relation between g_{max} and the absolute air humidity is

$$x = \frac{M_{v,0}}{M_a} = \frac{g_{max}}{1 - g_{max}} \quad . \tag{2.4}$$

The volume of liquid from condensation is magnitude orders less than the gas phase thus the total density can be assumed as function of air and vapor

$$\rho = \frac{\rho_a + \rho_v}{1 - g} \quad . \tag{2.5}$$

The components of the air density ρ_a and vapor density ρ_v are

$$\rho_v = (g_{max} - g)\rho \quad , \tag{2.6}$$

$$\rho_a = (1 - g_{max})\rho \quad . \tag{2.7}$$

For the gas phase one can make the following assumptions

$$T = T_a = T_v \quad , \tag{2.8}$$

$$p = p_a + p_v \quad . \tag{2.9}$$

The total pressure is the sum of the partial pressure of air and vapor where the temperature of the two phases are identical. The partial pressure can be obtained from the ideal gas equation for each component

$$p_a = \rho_a R_a T_a \quad , \tag{2.10}$$

$$p_v = \rho_v R_v T_v \quad . \tag{2.11}$$

The thermodynamic variables for the mixed state are defined by the following:

$$R_0 = (1 - g_{max})R_a + (g_{max} - g)R_v \quad , \tag{2.12}$$

$$c_{v0} = (1 - g_{max})c_{va} + (g_{max} - g)c_{vv} \quad , \tag{2.13}$$

$$c_{p0} = (1 - g_{max})c_{pa} + (g_{max} - g)c_{pv} \quad , \tag{2.14}$$

$$Pr_m = (1 - g_{max})Pr_{ma} + (g_{max} - g)Pr_{mv} \quad , \tag{2.15}$$

$$Pr_t = (1 - g_{max})Pr_{ta} + (g_{max} - g)Pr_{tv} \quad , \tag{2.16}$$

$$\gamma = (1 - g_{max})\gamma_a + (g_{max} - g)\gamma_v \quad . \tag{2.17}$$

It is more efficient in the numerical code to calculate the above thermodynamic variables only once at the beginning of the simulation (thus not a function of g). This means the caculation is based on the following simplified eqs. 2.18-2.23.

$$R_0 = (1 - g_{max})R_a + g_{max}R_v \quad , \tag{2.18}$$

$$c_{v0} = (1 - g_{max})c_{va} + g_{max}c_{vv} \quad , \tag{2.19}$$

$$c_{p0} = (1 - g_{max})c_{pa} + g_{max}c_{pv} \quad , \tag{2.20}$$

$$Pr_m = (1 - g_{max})Pr_{ma} + g_{max}Pr_{mv} \quad , \tag{2.21}$$

$$Pr_t = (1 - g_{max})Pr_{ta} + g_{max}Pr_{tv} \quad , \tag{2.22}$$

$$\gamma = (1 - g_{max})\gamma_a + g_{max}\gamma_v \quad . \tag{2.23}$$

The perfect gas equation is updated at each time step with the -g factor. The perfect gas equation for the mixture and specific enthalpy in the code are:

$$p = \rho T(R_0 - gR_v) \quad , \tag{2.24}$$

$$h = \frac{\gamma}{\gamma - 1}\frac{p}{\rho} - gL \quad . \tag{2.25}$$

For turbulent flow, the turbulent kinetic energy contributes to the mean pressure field, so instead of solving the turbulent term separately in the momentum equation it is added to the mean static pressure term

$$\bar{p} = \bar{\rho}\widetilde{T}(R_0 - gR_v) + \frac{2}{3}\bar{\rho}k \quad . \tag{2.26}$$

The pressure in the specific enthalpy equation must be the static pressure so the $\frac{2}{3}k$ term is subtracted out.

$$h = \frac{\gamma}{\gamma - 1}\left(\frac{\bar{p}}{\bar{\rho}} - \frac{2}{3}k\right) - gL \quad . \tag{2.27}$$

For the physical constants and thermodynamic functions refer to sec. 2.7.

In the case of nitrogen modeling the value of g_{max} is set to 1 and parameters that involve air go to zero and the parameters that involve vapor become the single gas phase N_2. The parameter absolute air humidity must also be switched off. The appropriate thermodynamics variables R_v, c_{vv}, c_{pv}, ..etc. must be changed, which are found in sec. 2.7.

2.2. Fluid Dynamic Equations

2.2.1. Conservation Equations

The compressible Navier-Stokes equations in vector form are:

$$\frac{\partial \mathbf{U}}{\partial t} + \frac{\partial \mathbf{E}}{\partial x} + \frac{\partial \mathbf{F}}{\partial y} + \frac{\partial \mathbf{G}}{\partial z} = 0 \quad , \tag{2.28}$$

where the vectors are given by

$$\mathbf{U} = \begin{vmatrix} \rho \\ \rho u \\ \rho v \\ \rho w \\ \rho E \end{vmatrix} \quad \mathbf{E} = \begin{vmatrix} \rho u \\ \rho u^2 + p - \tau_{xx} \\ \rho uv - \tau_{xy} \\ \rho uw - \tau_{xz} \\ (\rho E + p)u - u\tau_{xx} - v\tau_{xy} - w\tau_{xz} + q_x \end{vmatrix} \tag{2.29}$$

$$\mathbf{F} = \begin{vmatrix} \rho v \\ \rho vu - \tau_{xy} \\ \rho v^2 + p - \tau_{yy} \\ \rho vw - \tau_{yz} \\ (\rho E + p)v - u\tau_{xy} - v\tau_{yy} - w\tau_{yz} + q_y \end{vmatrix} \quad \mathbf{G} = \begin{vmatrix} \rho w \\ \rho wu - \tau_{xz} \\ \rho wv - \tau_{yz} \\ \rho w^2 + p - \tau_{zz} \\ (\rho E + p)w - u\tau_{xz} - v\tau_{yz} - w\tau_{zz} + q_z \end{vmatrix} \tag{2.30}$$

$$E = h - \frac{p}{\rho} + \frac{1}{2}(u^2 + v^2 + w^2) \quad , h = e + p/\rho \quad . \tag{2.31}$$

The components of the shear stresses and heat fluxes are given by

$$\tau_{xx} = \frac{2}{3}\mu(2\frac{\partial u}{\partial x} - \frac{\partial v}{\partial y} - \frac{\partial w}{\partial z}) \quad , \tag{2.32}$$

$$\tau_{yy} = \frac{2}{3}\mu(2\frac{\partial v}{\partial y} - \frac{\partial u}{\partial x} - \frac{\partial w}{\partial z}) \quad , \tag{2.33}$$

$$\tau_{yy} = \frac{2}{3}\mu(2\frac{\partial w}{\partial z} - \frac{\partial u}{\partial x} - \frac{\partial v}{\partial y}) \quad , \tag{2.34}$$

$$\tau_{xy} = \mu(\frac{\partial u}{\partial y} + \frac{\partial v}{\partial x}) = \tau_{yx} \quad , \tag{2.35}$$

$$\tau_{xz} = \mu(\frac{\partial u}{\partial z} + \frac{\partial w}{\partial x}) = \tau_{zx} \quad , \tag{2.36}$$

$$\tau_{yz} = \mu(\frac{\partial v}{\partial z} + \frac{\partial w}{\partial y}) = \tau_{zy} \quad , \tag{2.37}$$

$$q_x = -k\frac{\partial T}{\partial x} \quad , \tag{2.38}$$

$$q_y = -k\frac{\partial T}{\partial y} \quad , \tag{2.39}$$

$$q_z = -k\frac{\partial T}{\partial z} \quad . \tag{2.40}$$

2.2.2. Reynolds Averaged Navier-Stokes Equations

In order to solve a turbulent flow problem using equation 2.28, it requires direct numerical simulation of the entire turbulent spectrum. For the Reynolds number range and geometric length scale used in this study an approximation of the governing equations must be applied since the grid requirements are out of the scope of the resources available to the author. The dependent variables are thus cast into a mass averaged quantity and a random fluctuating quantity. The Favre mass-weighted operator is defined by

$$f = \tilde{f} + f'' \quad . \tag{2.41}$$

where $\tilde{f} = \frac{\overline{\rho f}}{\rho}$ is the mass-averaged part and f'' is the fluctuating part
The Favre operator can take on any scalar value of u, v, w, T, h, but ρ and p or treated without the multiplication of ρ, which is usually called Reynolds averaging. The mass weighted operator is then used to replace all the dependent variables in equation 2.28 and a time averaging on the entire equation is performed. Time averaging is appropriate for stationary turbulence, which means that the turbulent flow on average does not vary with time, which is acceptable for the flows encountered in this thesis. The continuity equation will be used to demonstrate the averaging procedure:

replace dependent variables,

$$\frac{\partial \overline{\rho}}{\partial t} + \frac{\partial \rho'}{\partial t} + \frac{\partial \overline{\rho}\tilde{u}_j}{\partial x_j} + \frac{\partial \tilde{u}_j\rho'}{\partial x_j} + \frac{\partial \overline{\rho}u_j''}{\partial x_j} + \frac{\partial \rho' u_j''}{\partial x_j} = 0 \tag{2.42}$$

time average entire equation,

$$\frac{\partial \overline{\overline{\rho}}}{\partial t} + \frac{\partial \overline{\rho'}}{\partial t} + \frac{\partial \overline{\overline{\rho}\tilde{u}_j}}{\partial x_j} + \frac{\partial \overline{\tilde{u}_j\rho'}}{\partial x_j} + \frac{\partial \overline{\overline{\rho}u_j''}}{\partial x_j} + \frac{\partial \overline{\rho' u_j''}}{\partial x_j} = 0 \tag{2.43}$$

using the following definitions, $\overline{\rho'} = 0; \overline{\rho f''} = 0; \overline{\tilde{f}} = \tilde{f}; \overline{\rho' \tilde{f}}, = 0;$

the second and fourth term in equation 2.43 are zero by definition and the last two terms can be combined to $\overline{\rho u_j''}$ which is also zero. From the above procedure the averaged continuity equation in tensor notation can be written as

$$\frac{\partial \overline{\rho}}{\partial t} + \frac{\partial \overline{\rho}\tilde{u}_j}{\partial x_j} = 0 \qquad . \tag{2.44}$$

The main advantage of mass averaging is that the term $\overline{\rho' u_j'}$ can be avoided, but it should be kept in mind that this is a mathematical technique not necessarily a physical one [103].

The mass averaged momentum equation in tensor notation is

$$\frac{\partial \overline{\rho}\tilde{u}_i}{\partial t} + \frac{\partial \overline{\rho}\tilde{u}_i\tilde{u}_j}{\partial x_j} + \frac{\partial \overline{p}}{\partial x_i} - \frac{\partial}{\partial x_j}(\overline{\tau}_{ij} - \overline{\rho u_i'' u_j''}) = 0 \qquad , \tag{2.45}$$

where $\overline{\tau}_{ij} = \bar{\mu}_m \left[\left(\frac{\partial \tilde{u}_i}{\partial x_j} + \frac{\partial \tilde{u}_j}{\partial x_i} \right) - \frac{2}{3}\delta_{ij} \frac{\partial \tilde{u}_k}{\partial x_k} \right]$

Equation 2.45 neglects fluctuations in molecular viscosity and a second simplification can be used to neglect all viscous terms involving fluctuations in the shear stress term based on order of magnitude arguments. The last term in equation 2.45 is a result of the time averaging process and is called the Reynolds-Stress tensor. A closure model must be provided which is usually the Boussinesq assumption, which states that the turbulent shearing stresses might be related by a mean strain through a scalar turbulent eddy viscosity [94]. This turbulent eddy viscosity is the reason for the need of a turbulence model which is explained in sec. 4.3. Equation 2.45 can be re-written after applying the Boussinesq assumption

$$\frac{\partial \overline{\rho}\tilde{u}_i}{\partial t} + \frac{\partial \overline{\rho}\tilde{u}_i\tilde{u}_j}{\partial x_j} + \frac{\partial \overline{p}}{\partial x_i} - \frac{\partial}{\partial x_j}((\overline{\tau}_{ij})_m + (\overline{\tau}_{ij})_{turb}) = 0 \qquad , \tag{2.46}$$

where $(\overline{\tau}_{ij})_m = \overline{\tau}_{ij} = \bar{\mu}_m \left[\left(\frac{\partial \tilde{u}_i}{\partial x_j} + \frac{\partial \tilde{u}_j}{\partial x_i} \right) - \frac{2}{3}\delta_{ij} \frac{\partial \tilde{u}_k}{\partial x_k} \right]$

$$(\overline{\tau}_{ij})_{turb} = \mu_t \left[\left(\frac{\partial \tilde{u}_i}{\partial x_j} + \frac{\partial \tilde{u}_j}{\partial x_i} \right) - \frac{2}{3}\delta_{ij} \frac{\partial \tilde{u}_k}{\partial x_k} \right] - \frac{2}{3}\rho k \delta_{ij} \quad .$$

The Reynolds averaged form of the energy equation is given by

$$\frac{\partial}{\partial t}(\overline{\rho}\widetilde{E}) + \frac{\partial}{\partial x_j}(\overline{\rho}\tilde{u}_j\widetilde{E} + \overline{p}\tilde{u}_j) + \frac{\partial}{\partial x_j}(\overline{\rho u_j'' h''} + \overline{q}_j) - \frac{\partial}{\partial x_j}(\overline{\tau}_{ij}\tilde{u}_i + \overline{u_i'' \tau_{ij}}) = 0 \qquad . \tag{2.47}$$

One of new terms from averaging equation 2.47 is $\overline{\rho u_j'' h''}$ which is called the Reynolds heat flux term. The closure model is given by

$$-\overline{\rho u_j'' h''} = \frac{c_p \mu_t}{Pr_t} \frac{\partial \widetilde{T}}{\partial x_j} \qquad . \tag{2.48}$$

Using the definition of $q_j = -k_m \frac{\partial \widetilde{T}}{\partial x_j}$ where k_m is the molecular part defined by $k = \frac{c_p \mu_m}{Pr_m}$,

making the same assumption for $\bar{\tau}_{ij}$ as in equation 2.45 and assuming that $\overline{u_i'' \tau_{ij}}$ is negligible, equation 2.47 can be rewritten as

$$\frac{\partial}{\partial t}(\overline{\rho}\widetilde{E}) + \frac{\partial}{\partial x_j}(\overline{\rho}\tilde{u}_j\widetilde{E} + \overline{p}\tilde{u}_j) - \frac{\partial}{\partial x_j}\left(c_p\left[\frac{\mu_m}{Pr_m} + \frac{\mu_t}{Pr_t}\right]\frac{\partial \widetilde{T}}{\partial x_j}\right) - \frac{\partial}{\partial x_j}(\overline{\tau}_{ij}\tilde{u}_i) = 0 \quad . \tag{2.49}$$

Summary of RANS

$Continuity$:

$$\frac{\partial \overline{\rho}}{\partial t} + \frac{\partial \overline{\rho}\tilde{u}_j}{\partial x_j} = 0 \quad , \tag{2.50}$$

$Momentum$:

$$\frac{\partial \overline{\rho}\tilde{u}_i}{\partial t} + \frac{\partial \overline{\rho}\tilde{u}_i\tilde{u}_j}{\partial x_j} + \frac{\partial \overline{p}}{\partial x_i} - \frac{\partial}{\partial x_j}((\overline{\tau}_{ij})_m + (\overline{\tau}_{ij})_{turb}) = 0 \quad , \tag{2.51}$$

$Energy$:

$$\frac{\partial}{\partial t}(\overline{\rho}\widetilde{E}) + \frac{\partial}{\partial x_j}(\overline{\rho}\tilde{u}_j\widetilde{E} + \overline{p}\tilde{u}_j) - \frac{\partial}{\partial x_j}\left(c_p\left[\frac{\mu_m}{Pr_m} + \frac{\mu_t}{Pr_t}\right]\frac{\partial \widetilde{T}}{\partial x_j}\right) - \frac{\partial}{\partial x_j}(\overline{\tau}_{ij}\tilde{u}_i) = 0. \tag{2.52}$$

2.3. Turbulence Modeling

Three complete turbulence models are presented, the Wilcox $k-\omega$, Menter shear stress transport (SST), and the EASM($k-\omega$) (explicit algebraic stress model). All three models are $k-\omega$ based because the simulations in this thesis involve wall-bounded flow with the potential for separation. Thus it has been shown by ([37],[55],[56],[103]) to name a few that the standard $k-\omega$ model is superior to the standard $k-\epsilon$ for wall bounded flow with separation. Of course with modifications and damping functions it is possible for the $k-\epsilon$ model to show improvements in separated flow. The Wilcox $k-\omega$ is the least complex of the other two models and the source terms require the least work units. The SST model involves a few more computations due to the blending functions, and the EASM is the most complex due to the cubic equation for turbulent eddy viscosity. The following equations are based on statistical quantities where the bar and tilde have been left out.

2.3.1. Wilcox $k-\omega$

The turbulent viscosity and two equation model are defined by [103]

$$\mu_t = \frac{\rho k}{\omega} \quad , \tag{2.53}$$

$$\frac{\partial(\varrho k)}{\partial t} + \frac{\partial(\varrho u_j k)}{\partial x_j} = \tau_{ij}\frac{\partial u_i}{\partial x_j} - \beta^*\rho\omega k + \frac{\partial}{\partial x_j}\left[(\mu + \sigma^*\mu_t)\frac{\partial k}{\partial x_j}\right] \quad , \tag{2.54}$$

$$\frac{\partial(\varrho\omega)}{\partial t} + \frac{\partial(\varrho u_j \omega)}{\partial x_j} = \alpha\frac{\omega}{k}\tau_{ij}\frac{\partial u_i}{\partial x_j} - \beta\rho\omega^2 + \frac{\partial}{\partial x_j}\left[(\mu + \sigma\mu_t)\frac{\partial \omega}{\partial x_j}\right] \quad . \tag{2.55}$$

The second term on the left hand side of equations 2.54 and 2.55 are the convection of turbulent kinetic energy (k) and specific dissipation rate (ω). The right hand side consists of two source terms and diffusion. The $\tau_{ij}\frac{\partial u_i}{\partial x_j}$ term is known as turbulent production and the turbulent portion of the stress tensor in the momentum equation 2.46 ($(\tau_{ij})_{turb}$) is used

$$\tau_{ij}\frac{\partial u_i}{\partial x_j} = P = \left[\mu_t\left[\left(\frac{\partial \tilde{u}_i}{\partial x_j} + \frac{\partial \tilde{u}_j}{\partial x_i}\right) - \frac{2}{3}\delta_{ij}\frac{\partial \tilde{u}_k}{\partial x_k}\right] - \frac{2}{3}\rho k\delta_{ij}\right]\frac{\partial u_i}{\partial x_j} \quad . \tag{2.56}$$

The closure coefficients and auxiliary relations are: [103]

$$\alpha = \frac{13}{25}, \quad \beta = \beta_o f_\beta, \quad \beta^* = \beta_o^* f_{\beta^*}, \quad \sigma^* = \sigma = 0.5 \quad ,$$

$$\beta_o = 0.072, \quad f_\beta = \frac{1+70\chi_w}{1+80\chi_w}, \quad \chi_w \equiv \left|\frac{\Omega_{ij}\Omega_{jk}S_{ki}}{(\beta_o^*\omega)^3}\right| \quad ,$$

$$\beta^* = 0.09, \quad f_{\beta^*} = \left\{1, \text{ if } \chi_k \le 0, \ \frac{1+680\chi_k^2}{1+400\chi_k^2}, \text{ if } \chi_k > 0\right\}, \chi_k = \frac{1}{\omega^3}\frac{\partial k}{\partial x_j}\frac{\partial \omega}{\partial x_j} \quad .$$

where: Ω_{ij} and S_{ij} are the mean rate of rotation and strain tensors

$$\Omega_{ij} = \frac{1}{2}\left(\frac{\partial u_i}{\partial x_j} - \frac{\partial u_j}{\partial x_i}\right), \quad S_{ij} = \frac{1}{2}\left(\frac{\partial u_i}{\partial x_j} + \frac{\partial u_j}{\partial x_i}\right) \quad .$$

The main difference between the closure coefficients above and an earlier version of the $k-\omega$ model [104] is the addition of f_β and f_{β^*}. These relations make improvements for free shear flows whereas in boundary layer flow ω is very large and thus the χ_w and χ_k terms will be very small.
The boundary conditions for k and ω will be described in chapter 3 section boundary conditions. For external flows with stagnation points the value of production eq. 2.56 and

ω must be limited due to the large jump in velocity and grid resolution. The limit on production is defined by [54]

$$P_k = \min(10\epsilon, P) \qquad . \tag{2.57}$$

The limit on ω is [58]

$$\omega = \max\left\{\omega, \frac{1}{\frac{1}{\beta^*}\sqrt{(3/8 \mid S_{ij}^2 \mid)}}\right\} \qquad . \tag{2.58}$$

One advantage of the $k-\omega$ model is that it can be provide a converged solution without any alteration when using the above relations in a Low Reynolds approach (integrating the fluid equations through the boundary layer). A $k-\epsilon$ model requires damping functions and they are usually a function of y^+ which can give problems for complex geometries, for example a wing-body junction. The author found that improved results can be gained by using a functional dependency of Re_t (turbulent Reynolds number) for β and β^* for boundary layer flow problems. The functional dependencies were derived for predicting transition but it also works for this Low-Reynolds approach. The Low Reynolds closure coefficients are: [103]

$$\alpha^* = \frac{\alpha_o^* + Re_t/R_k}{1 + Re_t/R_k} \qquad , \tag{2.59}$$

$$\alpha = \frac{13}{25}\frac{\alpha_o + Re_t/R_w}{1 + Re_t/R_w}\frac{1}{(\alpha^*)} \qquad , \tag{2.60}$$

$$\beta^* = \frac{9}{100}\frac{4/15 + (Re_t/R_\beta)^4}{(1 + Re_t/R_\beta)^4}(f_\beta^*) \qquad , \tag{2.61}$$

$$\beta = \frac{9}{125}f_\beta, \quad \sigma^* = \sigma = \frac{1}{2}, \quad \alpha_o^* = \frac{1}{3}\beta_o, \quad \alpha_o = \frac{1}{9} \qquad ,$$
$$R_\beta = 8, \quad R_k = 6, \quad R_w = 2.95 \qquad .$$

In the core or mean stream flow the functions return the fully turbulent value of the closure coefficients, but near the wall and at the start of a stagnation point the approach to the turbulent values is controlled by R_β, R_k, and R_w

2.3.2. Menter *SST*

The shear stress transport (SST) model is a combination of the $k-\epsilon$ and $k-\omega$ turbulence model. The idea is to combine the advantage of the $k-\epsilon$ free stream independence in

the far field and the $k-\omega$ near the wall behavior. Mixing relations are used to determine where in the flow field each model should be used.
The turbulent viscosity and two-equation model are defined by [55]

$$\mu_t = \frac{a_1 \rho k}{\max(a_1\omega; \Omega F_2)} \quad , \tag{2.62}$$

$$\frac{\partial(\varrho k)}{\partial t} + \frac{\partial(\varrho u_j k)}{\partial x_j} = \tau_{ij}\frac{\partial u_i}{\partial x_j} - \beta^* \rho\omega k + \frac{\partial}{\partial x_j}\left[(\mu + \sigma_k \mu_t)\frac{\partial k}{\partial x_j}\right] \quad , \tag{2.63}$$

$$\frac{\partial(\varrho \omega)}{\partial t} + \frac{\partial(\varrho u_j \omega)}{\partial x_j} = \frac{\rho\gamma}{\mu_t}\tau_{ij}\frac{\partial u_i}{\partial x_j} - \beta\rho\omega^2 + \frac{\partial}{\partial x_j}\left[(\mu + \sigma_\omega \mu_t)\frac{\partial \omega}{\partial x_j}\right] + 2(1-F_1)\rho\sigma_{\omega 2}\frac{1}{\omega}\frac{\partial k}{\partial x_j}\frac{\partial \omega}{\partial x_j} \quad . \tag{2.64}$$

The main differences between the $k-\omega$ and SST models are the last term in eq. 2.64, which is a cross-diffusion term from the transformation, the closure coefficients, and the definition of turbulent viscosity.
The model constants are defined by a linear mixing relation

$$\phi = F_1\phi_1 + (1-F_1)\phi_2 \quad , \tag{2.65}$$

where ϕ is a general term representing σ_k, σ_ω, β, β^*, and γ.
The constants for set 1 (Wilcox $k-\omega$) are

$$\sigma_{k1} = 0.85, \quad \sigma_{\omega 1} = 0.5, \quad \beta_1 = .075, \quad a_1 = 0.31$$
$$\beta^* = 0.09, \quad \kappa = 0.41, \quad \gamma_1 = \beta_1/\beta^* - \sigma_{\omega 1}\kappa^2/\sqrt{\beta^*} \quad .$$

The constants for set 2 (standard $k-\epsilon$) are

$$\sigma_{k2} = 1.0, \quad \sigma_{\omega 2} = 0.856, \quad \beta_2 = 0.0828$$
$$\beta^* = 0.09, \quad \kappa = 0.41, \quad \gamma_2 = \beta_2/\beta^* - \sigma_{\omega 2}\kappa^2/\sqrt{\beta^*} \quad .$$

The $\tau_{ij}\dfrac{\partial u_i}{\partial x_j}$ term in eqs. 2.63 and 2.64 is the same as in the $k-\omega$ model and is defined by eq.

2.56. The blending function F_1 used for the constants and cross-diffusion term is defined by

$$F_1 = \tanh(arg_1^4) \quad , \tag{2.66}$$

$$arg_1 = \min\left[\max\left(\frac{\sqrt{k}}{0.09\omega y}; \frac{500\nu}{y^2\omega}\right)\frac{4\rho\sigma_{\omega 2}k}{CD_{k\omega}y^2}\right] \quad , \tag{2.67}$$

where y is the distance to the next surface and $CD_{k\omega}$ is the positive portion of the cross diffusion term in eq. 2.64

$$CD_{k\omega} = \max\left(2\rho\sigma_{\omega 2}\frac{1}{\omega}\frac{\partial k}{\partial x_j}\frac{\partial \omega}{\partial x_j}; 10^{-20}\right) \quad . \tag{2.68}$$

The blending function F_2 in the turbulent viscosity definition is defined by

$$F_2 = \tanh(arg_2^2) \quad , \tag{2.69}$$

$$arg_2 = \max\left(2\frac{\sqrt{k}}{0.09\omega y}; \frac{500\nu}{y^2\omega}\right) \quad . \tag{2.70}$$

When integrating the SST model to the wall the Low Reynolds terms defined by eqs. 2.59 to 2.61 were found not to have any effect on the solution, which is most likely due to the definition of turbulent viscosity eq. 2.62. The limitation on production eq. 2.57 and ω eq. 2.58 are also used in the SST model. The ω limitation was written for the standard $k-\omega$ model but since it is used near a wall there is no danger of the correlation being used when the SST model coefficients are the standard $k-\epsilon$ model.

2.3.3. EASM($k-\omega$)

The explicit algebraic stress model (EASM) is a non-linear model in the sense that the turbulent stress tensor is a function of strain and two additional terms. The EASM model is the most complex and requires the most work units for an iteration compared to the Wilcox $k-\omega$ and Menter SST models.
The turbulent viscosity and two equation model are defined by [75]

$$\mu_t^* = C_\mu^* \frac{\rho k}{\omega} \quad , \tag{2.71}$$

$$\frac{\partial(\varrho k)}{\partial t} + \frac{\partial(\varrho u_j k)}{\partial x_j} = \tau_{ij}\frac{\partial u_i}{\partial x_j} - f_\beta^*\rho\omega k + \frac{\partial}{\partial x_j}\left[(\mu + \sigma^*\mu_t^*)\frac{\partial k}{\partial x_j}\right] \quad , \tag{2.72}$$

$$\frac{\partial(\varrho\omega)}{\partial t}+\frac{\partial(\varrho u_j\omega)}{\partial x_j} = \gamma\frac{\omega}{k}\tau_{ij}\frac{\partial u_i}{\partial x_j}-\beta\rho\omega^2+\frac{\partial}{\partial x_j}\left[(\mu+\sigma\mu_t^*)\frac{\partial\omega}{\partial x_j}\right] \quad . \tag{2.73}$$

At first glance the above equations look familiar to the Wilcox $k-\omega$ model but three main differences occur, in the definition of ω, the turbulent stress tensor, and the definition of turbulent viscosity. In the EASM model ω absorbs β^* or C_μ, (depending on which book or paper one chooses to read)

$$\omega_{EASM}=\omega_{Wilcox}\beta^* \quad . \tag{2.74}$$

This is very important to keep in mind when initializing the domain, boundary conditions, the ω limiter and so on.
The turbulent stress tensor is the same as in the first two turbulence models but with two additional terms [75]

$$\tau_{ij}=2\mu_tS_{ij}-\frac{2}{3}\rho k\delta_{ij}-a_2a_4(S_{ik}\Omega_{kj}-\Omega_{ik}S_{kj})+2a_3a_4(S_{ik}S_{kj}-\frac{1}{3}S_{kl}S_{lk}\delta_{ij}) \quad , \tag{2.75}$$

where Ω_{ij} and S_{ij} are defined above as the mean rate of rotation and strain. a_2 and a_3 are constants but a_4 is a function of the parameter (C_μ^*) in eq. 2.71 for turbulent viscosity. a_2 and a_3 are defined following the turbulent viscosity. Rumsey and Gatksi [75] rewrite the parameter C_μ^* as α_1/τ ($\tau\equiv 1/\omega$) and is obtained by solving the following cubic equation at each point in the flow field

$$(\alpha_1/\tau)^3+p(\alpha_1/\tau)^2+q(\alpha_1/\tau)+r=0 \quad , \tag{2.76}$$

where

$$p=-\frac{\gamma_1^*}{\eta^2\tau^2\gamma_0^*}$$

$$q=\frac{1}{(2\eta^2\tau^2\gamma_0^*)^2}\left(\gamma_1^{*2}-2\eta^2\tau^2\gamma_0^*a_1-\frac{2}{3}\eta^2\tau^2a_3^3+2R^2\eta^2\tau^2a_2^2\right)$$

$$r=\frac{\gamma_1^*a_1}{(2\eta^2\tau^2\gamma_0^*)^2} \quad .$$

The solution of α_1/τ is obtained by solving the smallest real root of eq. 2.76. A limiter on C_μ^* must be used in the form of

$$C_\mu^*=-(\alpha_1/\tau)=\min(0.187,\max(C_\mu^*,0.00005) \quad . \tag{2.77}$$

The remaining constants and parameters are defined by

$$\eta^2 \equiv S^2 = S_{ij}S_{ji}, \quad W^2 = \Omega_{ij}\Omega_{ji}, \quad R^2 = -W^2/S^2$$
$$a_1 = \frac{1}{2}(\frac{4}{3} - 0.36), \quad a_2 = \frac{1}{2}(2 - 0.4)$$
$$a_3 = \frac{1}{2}(2 - 1.25), \quad a_4 = \frac{\tau}{[\gamma_1^* - 2\gamma_0^*(\alpha_1/\tau)\eta^2\tau^2]}$$
$$\gamma_0^* = \frac{1.8}{2}, \quad \gamma_1^* = \frac{1}{2}3.4 + \left(\frac{1.83 - 1.44}{1.44 - 1}\right) \quad . \tag{2.78}$$

The same limitation for production eq. 2.57 and ω- eq. 2.58 are used.

2.4. Condensation Modeling

Two types of condensation models are implemented, homogeneous and heterogeneous condensation. Homogeneous condensation requires a specific cooling rate and length scale for droplets to suddenly form in an air water vapor mixture. Heterogeneous condensation requires the input of a number density of particles with a particle radius, to allow seeding of condensation to occur on the particles. It is also possible to have both types of processes simultaneously occurring.

2.4.1. Moist Air Homogeneous Condensation

Theory of Volmer, Frenkel, and Zel'dovich and Hertz-Knudsen
Two additional transport equations must be written to solve for homogeneous condensation, the equations are

$$\frac{\partial(\varrho g_{hom})}{\partial t} + \frac{\partial(\varrho g_{hom} u_j)}{\partial x_j} = \frac{4}{3}\pi\varrho_l\left(r_{hom}^{*\,3} J_{hom} + 3\varrho n_{hom}\overline{r}_{hom}^{\,2}\frac{d\overline{r}_{hom}}{dt}\right) \tag{2.79}$$

$$\frac{\partial(\varrho n_{hom})}{\partial t} + \frac{\partial(\varrho n_{hom} u_j)}{\partial x_j} = J_{hom} \quad . \tag{2.80}$$

Equations 2.79 and 2.80 are time dependent with convection of the condensate but no diffusion and the right hand sides consist of source/sink terms. In eq. 2.79 the source/sink

term consists of two parts where the first part is the critical volume times J, the nucleation rate which is purely a source term for g_{hom}, the second term takes into account the growth or decrease of a droplet that is already present. The source term for n_{hom} is the nucleation rate. The following source terms are defined below.
In order to model homogeneous condensation one must know a nucleation rate and a droplet growth to be able to predict the amount of condensate formed. The first step is to calculate all the thermodynamic parameters, liquid density ρ_l, saturation pressure p_s, and surface tension, σ_∞. In order for the water to condense numerically there must be a critical radius which is defined as

$$r^*_{hom} = \frac{2\sigma_\infty}{\rho_l R_v T ln(p_v/p_s)}, \quad if(p_v > p_s) \quad , \tag{2.81}$$

$$r^*_{hom} = 0, \quad if(p_v < p_s) \quad . \tag{2.82}$$

If there are droplets already present then the droplet radius is

$$\overline{r}_{hom} = \left(\frac{g_{hom}}{\frac{4}{3}\pi\rho_l n_{hom}} \right)^{1/3} \quad . \tag{2.83}$$

where n_{hom} is the droplet number per kg and g_{hom} is the homogeneous condensate mass fraction.
The classical nucleation theory of Volmer [96], Frenkel [28] , and Zel'dovich [109] was outlined in general form in sec. 1.2 eq. 1.3.

$$J = Z_{hom} D^*_{hom} C^*_{hom} \quad . \tag{2.84}$$

Z is the Zeldovich factor

$$Z = \frac{m_v}{\frac{4}{3}\pi r^{*3}_{hom}\rho_l} \sqrt{\frac{\Delta G^*}{3\pi k T}} \quad .$$

D^*_{hom} is the critical collision frequency for a vapor molecule on a critical droplet size for growth to begin

$$D^*_{hom} = \alpha 4\pi r^{*2}_{hom} \frac{p_v}{\sqrt{2\pi m_v k T}} \quad ,$$

C^*_{hom} represents the concentration of the critical droplet and is the most important term because the exponential term is the dominant factor in the theory of eq. 2.84

$$C^*_{hom} = \frac{\rho_v}{m_v} \exp\left(-\frac{\Delta G^*_{hom}}{kT} \right) \quad .$$

Combining all the terms and using the definition for ΔG^*

$$\Delta G^* = \frac{4}{3}\pi r_{hom}^{*2}\sigma_\infty$$

Equation 2.84 becomes

$$J = \sqrt{\frac{2}{\pi}\frac{\sigma_\infty}{m_v^3}}\frac{\rho_v^2}{\rho_l}e^{\left(\frac{-4\pi r^{*2}\sigma_\infty}{3R_v m_v T}\right)} \quad , \tag{2.85}$$

which is appropriate for the nucleation rate J in vapor/carrier gas mixtures for steady as well as unsteady flow [59].
J is the rate of nuclei formation per unit volume per unit time. The most important variable in eq. 2.85 is the surface tension σ because it is raised to the 3rd power when combining eq. 2.81 with eq. 2.85. In the past it was unknown if σ should be a free parameter in regards to liquid or solid condensate, but for the present only the σ function for liquid condensate is used. Also in eq. 2.85 m_v is the molecular mass of water vapor divided by Avogadro's number ($m_v = 2.991 \cdot 10^{-26}$ kg), also note that $R_v m_v$ is Boltzmann's constant.
The droplet growth rate is given by the Hertz-Knudsen formula

$$\frac{d\overline{r}_{hom}}{dt} = \frac{\alpha}{\rho_l}\frac{p_v - p_s}{\sqrt{2\pi R_v T}} \quad . \tag{2.86}$$

Dohrmann [23] and Mundinger [59] have shown by comparison with experiments the value of α should be set to 1 for moist air. The Hertz-Knudsen law is valid for a vapor/carrier gas mixture because 1) the droplet size remains smaller than the mean free path and 2) the high mass fraction of inert carrier gas keeps the temperature gradients to a minimum in the environment. From these two points the diffusion of the vapor molecules to the droplet surface is what controls droplet growth, thus a microscopic law is valid.

2.4.2. Moist Air Heterogeneous Condensation

With heterogeneous condensation only one additional transport equation is required because the number of particles is specified as an initial condition and remains constant. The transport equation for g_{het} is [39]

$$\frac{\partial\left(\varrho g_{het}\right)}{\partial t} + \frac{\partial\left(\varrho g_{het} u_j\right)}{\partial x_j} = 4\pi\rho_l\left(n_{het}\overline{r}_{het}^2\frac{d\overline{r}_{het}}{dt}\right) \quad . \tag{2.87}$$

In the time-dependent eq. 2.87, there is a convection term and one source term for the growth/evoporation of condensate on a particle. In Heiler [39] there is another more complicated model for heterogenous condensation based on the work of Kotake and Glass ([43],[44],[45]). Heiler [39] made comparisons between the two models in a nozzle with

moist air for different contact angles and particle densities. For a contact angle of 30° the results were identical but for 90° there were differences in which the effect of heterogeneous condensation would dominate over homogeneous. For the most part the two models showed the same trends and thus to reduce the complexity of parameters the simpler of the models was chosen.

The number of particles per m^3 (n_{het}) is

$$n_{het} = N_{het,0}\frac{\rho}{\rho_{01}} \quad , \tag{2.88}$$

where $N_{het,0}$ is a constant usually around $1 \cdot 10^{12}$ $[m^{-3}]$.
The radius of the droplet is given by

$$\overline{r}_{het} = \left(\frac{\rho g_{het}}{\frac{4}{3}\pi\rho_l n_{het}} + r_p^3\right)^{1/3} \quad . \tag{2.89}$$

Equation 2.89 is identical to 2.83 except for the value of r_p, which is the radius of the solid particle taken to be $1 \cdot 10^{-8}$ [m]. The droplet grow rate, $d\overline{r}_{het}/dt$ is based on the Hertz-Knudsen growth law, eq. 2.86. The radius of the particle with the addition of condensate is still smaller than the mean free path of the vapor/gas carrier mixture.

2.4.3. Nitrogen Homogeneous Condensation

The classical nucleation theory of Volmer [96], Frenkel [28] , and Zel'dovich [109] can also be used for nitrogen condensation with the appropriate change in parameters.

The most important term in the nucleation model is the value of σ. In the literature there are many different functions for (σ_∞ = f(T)), which are plotted in fig. 2.1. The Eötvös function can be found in [99], the ASHRAE comes from [50], the Dotson formulation from [24] and Düker and Koppenwallner [26]. Since the ASHRAE, Dotson, and Düker and Koppenwallner functions are nearly the same the ASHRAE function for surface tension is used. The applicable temperature range for the ASHRAE function is between 64 K – 125 K. If the temperature goes below 64 K a constant value of 0.0185 is used [26]. Since the interest lies in low temperature operation, values above 125 K are not encountered.

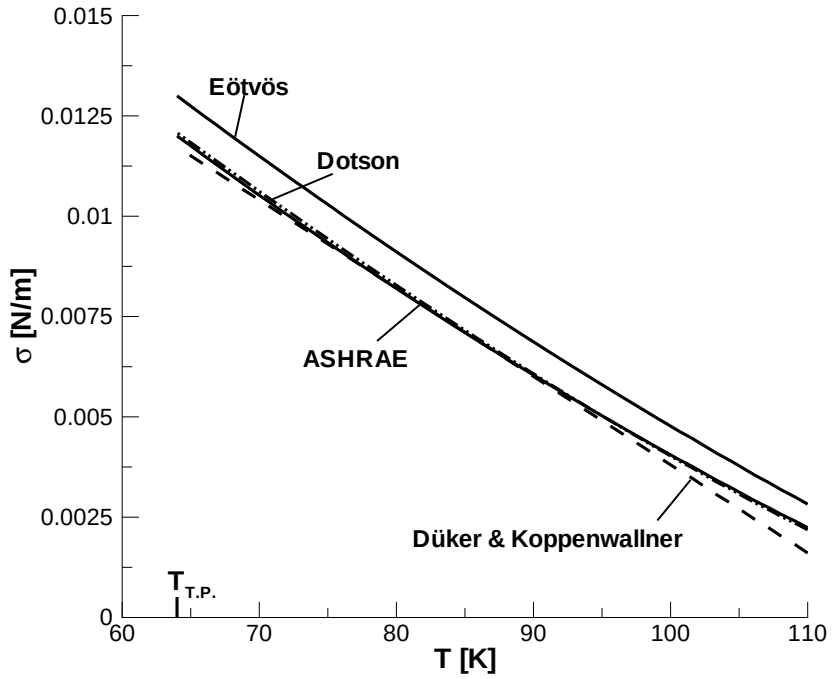

Figure 2.1.: Surface tension of N_2.

Since there is no carrier gas it is very likely that the mean free path of the gas is less than the droplet radius, thus a droplet growth law that takes into account a wider range of Kn numbers is required. Recall, to use the Hertz-Knudsen droplet growth law, $Kn >> 1$. One method is during the simulation to compare the droplet radius with the free mean path and if $\overline{r} < \lambda$ use Hertz-Knudsen, if $\overline{r} > \lambda$ then use [25, 87]

$$\frac{d\overline{r}}{dt} = \frac{k}{L\rho_l \overline{r}}(T_{s,r} - T) \quad , \tag{2.90}$$

where k is the conductivity (J/m-s-K), $\overline{r}$ is the Hill average droplet radius, and $T_{s,r}$ is the saturation temperature at the pressure of the gas corrected by Thompson-Gibbs formula

$$\frac{P_{s,r}}{P_{s,\infty}} = \frac{T_{s,r}}{T_{s,\infty}} = e^{\left(\frac{2\sigma}{\overline{r}} \frac{1}{\rho_l c R T}\right)} \quad , \tag{2.91}$$

assuming $\rho_{s,r} = \rho_{s,\infty}$.
Another method available is to use a droplet growth law established for a wider Kn number range, thus regardless if $\overline{r} \gtrless \lambda$. The modified Gyarmathy-Model is such a growth law [39]

$$\frac{d\overline{r}}{dt} = \frac{1}{\rho_l} f_{F-S}(Kn) \left(\frac{kRT^2}{L^2}\right) ln\left(\frac{p}{p_s}\right) \quad , \tag{2.92}$$

where the correction factor f_{F-S} is given by

$$f_{F-S}(Kn) = \frac{1+2Kn}{\overline{r}(1+3.42Kn+5.32Kn^2)}\left(1-\frac{r^*}{\overline{r}}\right) \quad . \tag{2.93}$$

2.5. Frozen Mach Number

Due to two phases the definition of the Mach number must be altered to what is called the frozen Mach number. The following relations were presented by Mundinger[59]. The definition of the speed of sound is

$$c^2 = \left(\frac{\partial p}{\partial \rho}\right)_{e,g} + \left(\frac{p}{\rho^2}\frac{\partial p}{\partial e}\right)_{\rho,g} \quad . \tag{2.94}$$

Equation 2.94 is equivalent to the frozen speed of sound

$$c_f^2 = \left(\frac{\partial p}{\partial \rho}\right)_{s,g} \quad . \tag{2.95}$$

By defining the latent heat as a function of temperature the above relation can be written as

$$c^2 = c_f^2 = \Gamma\frac{p}{\rho}, \tag{2.96}$$

$$\text{with} \quad \Gamma = \frac{c_{p0} - g(dL/dT)}{c_{v0} + g(R_v - (dL/dT))} \quad . \tag{2.97}$$

With the frozen speed of sound known the frozen Mach number can then be defined as

$$M_f = \frac{\sqrt{u^2+v^2+w^2}}{c_f} \quad . \tag{2.98}$$

For practical purposes in moist air the values of the frozen Mach number are nearly equivalent to that of the standard definition of Mach number.

2.6. Condensation Auxiliary Relations for Moist Air

Above it was mentioned that the first step in the condensation model is to calculate the thermodynamic variables of σ_∞, ρ_l, and p_s. The definition of these variables as a function of temperature are provided.

Surface tension

Dohrmann [23] matched the experimental results of Peters and Paikert [66] with the following functional relationship for surface tension for liquid condensation

$$\sigma_\infty(T) = \begin{cases} (76.1 + 0.155(273.15 - T)) \cdot 10^{-3}, \quad [N/m] \\ \quad \text{for} \;\; T \geq 249.39 \; K \\ ((1.1313 - 3.7091 \cdot 10^{-3}T)T^4 \cdot 10^{-4} - 5.6464)10^{-6} \quad [N/m] \\ \quad \text{for} \;\; T < 249.39 \; K \quad . \end{cases} \tag{2.99}$$

Liquid density

From Pruppacher and Klett [70] the liquid density is

$$\rho_l(T) = \begin{cases} \dfrac{A_0 + A_1 t + A_2 t^2 + A_3 t^3 + A_4 t^4 + A_5 t^5}{1 + B_0 t} \quad [kg/m^3] \quad \text{for} \quad t \geq 0^\circ \; C \\ A_6 + A_7 t + A_8 t^2 \qquad\qquad\qquad\qquad [kg/m^3] \quad \text{for} \quad t < 0^\circ \; C \end{cases} \tag{2.100}$$

with t in °C and the constants

$$\begin{array}{ll} A_0 = 999.83960 & A_5 = -393.2952 \cdot 10^{-12} \\ A_1 = 18.224944 & A_6 = 999.84 \\ A_2 = -7.922210 \cdot 10^{-3} & A_7 = 0.086 \\ A_3 = -55.44846 \cdot 10^{-6} & A_8 = -0.0108 \\ A_4 = -149.7562 \cdot 10^{-9} & B_0 = 18.159725 \cdot 10^{-3} \quad . \end{array} \tag{2.101}$$

Saturation pressure

The saturation pressure for water vapor is based on Sonntag and Heinze [92]

$$p_{s,\infty} = \exp\left(A_9 + A_{10}T + A_{11}T^2 + B_1 ln(T) + \frac{C_0}{T}\right) \quad [N/m^2] \quad , \tag{2.102}$$

with temperature in K and the constants

$$\begin{array}{ll} A_9 \;\; = 21.1250 & B_1 = 2.4576 \\ A_{10} = -2.7246 \cdot 10^{-2} & C_0 = -6094.4642 \\ A_{11} = 1.6853 \cdot 10^{-5} & \quad . \end{array} \tag{2.103}$$

Latent Heat

The latent heat of water vapor to liquid is best approximated by a linear equation. This allows the pressure to be calculated without having to do an iterative process, for example a Newton method. The Clausius-Clapeyron linear approximation is good for the temperature range of 200-300 K with the maximum error around 0.05% [1]. The latent heat equation is

$$L(T) = 3105913.39 - 2212.97T \quad [J/kg] \qquad , \tag{2.104}$$

with T [K].

Mean free path

A generic definition for the mean free path is

$$\lambda = \frac{1}{2}\frac{\mu_m\sqrt{2\pi R_0 T}}{p} \quad . \tag{2.105}$$

The gas-gas and gas-vapor collisions are neglected for water droplet growth and thus the pressure in the denominator of the mean free path is the vapor pressure. This assumption follows from Wegener and Mack [99]. The line of reasoning behind this is that the water droplet grows with respect to the vapor that it reacts with. The mean free path of the vapor is thus given by

$$\lambda_v = \frac{1}{2}\frac{\mu_m\sqrt{2\pi R_0 T_v}}{p_v} \quad , \tag{2.106}$$

where μ_m and R_0 are based on the mixture properties.
Knowledge of the droplet radius (r) with the definition of the mean free path the Knudsen number is defined as

$$Kn = \frac{\lambda_v}{2r} \quad . \tag{2.107}$$

Young and van Dongen state that neglecting the gas-gas collision is not valid and thus in eq. 4.4 the pressure should be based on the total pressure. Using the total pressure leads to a mean free path that is about 10 times smaller for a vapor/carrier gas mixture, which then puts the Knudsen number in the range of one. The Hertz-Knudsen droplet growth model would then in tendency be overpredicting droplet growth.

Physical Constants

The physical constants for air and water vapor are

$$\begin{array}{ll} R_a = 287.04 \ \ [J/kg-K] & R_v = 461.52 \ \ [J/kg-K] \\ c_{va} = 717 \ \ [J/kg-K] & c_{vv} = 1397.5 \ \ [J/kg-K] \\ c_{pa} = 1001 \ \ [J/kg-K] & c_{pv} = 1859 \ \ [J/kg-K] \\ \gamma_a = 1.4 & \gamma_v = 1.33 \quad . \end{array} \tag{2.108}$$

2.7. Condensation Auxiliary Relations for Nitrogen

Surface tension

The formulation for surface tension of liquid nitrogen is a curve fit from tabular values in ASHRAE [50]

$$\sigma_\infty(T) = \begin{cases} 0.0315687 - 0.000360049T + 8.49031\text{x}10^{-7}T^2, \quad [N/m] \\ \quad \text{for} \;\; T \geq 63.15.\; K \\ 0.0185 \quad [N/m] \\ \quad \text{for} \;\; T < 63.15\; K \quad . \end{cases} \tag{2.109}$$

Density

The formulation for density is from Wagner [98]

$$\rho(T) = \begin{cases} 1155.0 - 4.5T, \quad [kg/m^3] \qquad \text{for} \;\; T \geq 63.15.\; K \\ 1026.5, \qquad\quad [kg/m^3] \qquad \text{for} \;\; T < 63.15\; K \quad . \end{cases} \tag{2.110}$$

Düker and Koppenwallner [26] suggest a constant value of liquid density at 808.4 kg/m^3, but the difference between the temperature dependent function and a constant value have little effect on the solution.

Saturation pressure

The formulation for saturation pressure is given by Wagner [98]

$$p_{s,\infty}(T) = \begin{cases} 8705 \cdot 10^5 e^{-701.7/T}, \quad [Pa] \qquad \text{for} \;\; T \geq 63.15.\; K \\ 61970 \cdot 10^5 e^{-826.9/T}, \quad [Pa] \qquad \text{for} \;\; T < 63.15\; K \quad . \end{cases} \tag{2.111}$$

Latent Heat

For an ideal gas the latent heat of Nitrogen is assumed a constant, [98]

$$L = \begin{cases} 208093.5, \quad [J/kg] \qquad \text{for} \;\; T \geq 63.15.\; K \\ 245432.2, \quad [J/kg] \qquad \text{for} \;\; T < 63.15\; K \quad . \end{cases} \tag{2.112}$$

Dotson [24] uses a curve fit which is a function of temperature for the Latent heat of vaporization but to stay consistent with the ideal gas assumption the formulation from Wagner is chosen.

Mean free path

The definition for the mean free path of a pure substance is defined as

$$\lambda = \frac{1}{2}\frac{\mu_m\sqrt{2\pi R_0 T}}{p} \quad , \tag{2.113}$$

where all substances are defined for the gas phase.

Physical Constants

The physical constants for Nitrogen are

$$\begin{aligned} R &= 296.81 \ \ [J/kg-K] \\ c_{vN_2} &= 743.57 \ \ [J/kg-K] \\ c_{pN_2} &= 1041 \ \ [J/kg-K] \\ \gamma_{N_2} &= 1.4 \qquad . \end{aligned} \tag{2.114}$$

3. Numerical Methods

The Euler and the Navier-Stokes (N-S) equations will be solved depending on the type of flow problem. Some test cases can be solved with the Euler equations but if there is shock-boundary-layer interaction, separation, or wake flows to name a few, the N-S equations must be solved. Some major differences between the Euler and N-S is the requirement for fine meshes near the boundaries and the addition of the viscous terms. The fine meshes create large aspect ratios which produces larger truncation errors and decreases the rate of convergence [4]. Also in the N-S equations it is important to reduce the amount of numerical dissipation far below the physical dissipation, note condensation is also a form of physical dissipation.

3.1. Equation Transformation

The governing fluid equations (2.50, 2.51, 2.52), condensations models (2.79, 2.80, 2.87) and the choice of the turbulence model are cast into dimensionless form. The advantage being that one can independently vary Mach number, Reynolds number, or Prandtl number. Also this technique normalizes the flow variable between a limit of 0 and 1. The dimensionless form is done by the following relations

$$
\begin{aligned}
t^* = t\frac{c_{01}}{l} \ , \quad x^* = \frac{x}{l} \ , \quad y^* = \frac{y}{l} \ , \quad z^* = \frac{z}{l} \\
u^* = \frac{u}{c_{01}} \ , \quad v^* = \frac{v}{c_{01}} \ , \quad w^* = \frac{w}{c_{01}} \ , \\
p^* = \frac{p}{\rho_{01}c_{01}^2} \ , \quad T^* = \frac{T}{T_{01}} \ , \quad E^* = \frac{E}{c_{01}} \ , \quad \rho^* = \frac{\rho}{\rho_{01}} \ , \\
\mu^* = \frac{\mu}{\mu_{01}} \ , \quad k^* = \frac{k}{c_{01}} \ , \quad \omega^* = \omega\frac{l}{c_{01}} \ , \\
r_p^* = \frac{r_p}{l} \ , \quad n_{hom}^* = n_{hom}\rho_{01}l^3 \ , \quad n_{het,0}^* = n_{het,0}l^3 \ , \qquad .
\end{aligned}
\tag{3.1}
$$

where l is a characteristic length, examples include chord length, nozzle throat height, ..etc.

The Reynolds number can then be derived to give

$$
Re_{l,01} = \frac{\rho_{01}c_{01}l}{\mu_{01}} \qquad . \tag{3.2}
$$

It must be kept in mind that the above Reynolds number is purely a numerical one, for example when one calculates the flow around a wing, it makes no sense to report a Reynolds number based on total parameters, thus the physical Reynolds number should be reported but the numerical one must be used in the code to fit with the dimensionless procedure.

The physical domain on which the mesh was generated is transformed to the computational domain using a general transformation of the form

$$\xi = \xi(x, y, z) \quad , \quad \eta = \eta(x, y, z) \quad , \quad \zeta = \zeta(x, y, z) \qquad . \tag{3.3}$$

This procedure is done because one can have a general computational domain and at the same time it generates the volume and cell faces necessary for the finite volume method. For example, the inverse of the Jacobian of the transformation is the volume of the cell. Using the coordinates ξ, η, and ζ, the generalized transformation of the RANS equations, the turbulence model, and the condensation equations written in vector form is:

$$\frac{1}{J}\frac{\partial \mathbf{Q}}{\partial t} + \frac{\partial \mathbf{E}}{\partial \xi} + \frac{\partial \mathbf{F}}{\partial \eta} + \frac{\partial \mathbf{G}}{\partial \zeta} - \frac{1}{Re_{01}}\left(\frac{\partial \mathbf{E_v}}{\partial \xi} + \frac{\partial \mathbf{F_v}}{\partial \eta} + \frac{\partial \mathbf{G_v}}{\partial \zeta}\right) = \frac{\mathbf{S}}{J} \qquad . \tag{3.4}$$

where J is the determinate of the Jacobian

$$J = \xi_x(\eta_y\zeta_z - \zeta_y\eta_z) + \eta_x(\zeta_y\xi_z - \xi_y\zeta_z) + \zeta_x(\xi_y\eta_z - \eta_y\xi_z) \quad . \tag{3.5}$$

The metrics are:

$$\xi_x = \frac{\partial \xi}{\partial x} \ , \quad \xi_y = \frac{\partial \xi}{\partial y} \ , \quad \xi_z = \frac{\partial \xi}{\partial z} \tag{3.6}$$

$$\eta_x = \frac{\partial \eta}{\partial x} \ , \quad \eta_y = \frac{\partial \eta}{\partial y} \ , \quad \eta_z = \frac{\partial \eta}{\partial z} \tag{3.7}$$

$$\zeta_x = \frac{\partial \zeta}{\partial x} \ , \quad \zeta_y = \frac{\partial \zeta}{\partial y} \ , \quad \zeta_z = \frac{\partial \zeta}{\partial z} \tag{3.8}$$

The contravariant of the velocity components U, V, W are defined as

$$U = \xi_x u + \xi_y v + \xi_z w \ \ , \ \ V = \eta_x u + \eta_y v + \eta_z w \ \ , \ \ W = \zeta_x u + \zeta_y v + \zeta_z w \qquad . \tag{3.9}$$

To demonstrate the entire system of equations, the Wilcox k-ω turbulence model will be used and the SST and EASM models can be inferred. The time vector $\mathbf{Q}$, the convective vectors ($\mathbf{E,\ F,\ G}$), viscous vectors ($\mathbf{E_v}$, $\mathbf{F_v}$, $\mathbf{G_v}$) in the ξ, η, and ζ direction and the source/sink vector ($\mathbf{S}$) are:

$$\mathbf{Q} = \begin{pmatrix} \varrho \\ \varrho u \\ \varrho v \\ \varrho w \\ \varrho E \\ \varrho k \\ \varrho \omega \\ \varrho g_{hom} \\ \varrho n_{hom} \\ \varrho g_{het} \end{pmatrix}, \quad \mathbf{E} = \frac{1}{J} \begin{pmatrix} \varrho U \\ \varrho u U + \xi_x p \\ \varrho v U + \xi_y p \\ \varrho w U + \xi_z p \\ (\varrho E + p) U \\ \varrho k U \\ \varrho \omega U \\ \varrho g_{hom} U \\ \varrho n_{hom} U \\ \varrho g_{het} U \end{pmatrix}, \quad \mathbf{F} = \frac{1}{J} \begin{pmatrix} \varrho V \\ \varrho u V + \eta_x p \\ \varrho v V + \eta_y p \\ \varrho w V + \eta_z p \\ (\varrho E + p) V \\ \varrho k V \\ \varrho \omega V \\ \varrho g_{hom} V \\ \varrho n_{hom} V \\ \varrho g_{het} V \end{pmatrix}, \quad \mathbf{G} = \frac{1}{J} \begin{pmatrix} \varrho W \\ \varrho u W + \zeta_x p \\ \varrho v W + \zeta_y p \\ \varrho w W + \zeta_z p \\ (\varrho E + p) W \\ \varrho k W \\ \varrho \omega W \\ \varrho g_{hom} W \\ \varrho n_{hom} W \\ \varrho g_{het} W \end{pmatrix},$$

$$\mathbf{E_v} = \frac{1}{J} \begin{pmatrix} 0 \\ \xi_x \tau_{xx} + \xi_y \tau_{yx} + \xi_z \tau_{zx} \\ \xi_x \tau_{yx} + \xi_y \tau_{yy} + \xi_z \tau_{yz} \\ \xi_x \tau_{zx} + \xi_y \tau_{zy} + \xi_z \tau_{zz} \\ \xi_x (u\tau_{xx} + v\tau_{xy} + w\tau_{xz} + q_x) + \xi_y (u\tau_{yx} + v\tau_{yy} + w\tau_{yz} + q_y) + \xi_z (u\tau_{zx} + v\tau_{zy} + w\tau_{zz} + q_z) \\ \mu_k (\xi_x k_x + \xi_y k_y + \xi_z k_z) \\ \mu_\omega (\xi_x \omega_x + \xi_y \omega_y + \xi_z \omega_z) \\ 0 \\ 0 \\ 0 \\ 0 \end{pmatrix},$$

$$\mathbf{F_v} = \frac{1}{J} \begin{pmatrix} 0 \\ \eta_x \tau_{xx} + \eta_y \tau_{yx} + \eta_z \tau_{zx} \\ \eta_x \tau_{yx} + \eta_y \tau_{yy} + \eta_z \tau_{yz} \\ \eta_x \tau_{zx} + \eta_y \tau_{zy} + \eta_z \tau_{zz} \\ \eta_x (u\tau_{xx} + v\tau_{xy} + w\tau_{xz} + q_x) + \eta_y (u\tau_{yx} + v\tau_{yy} + w\tau_{yz} + q_y) + \eta_z (u\tau_{zx} + v\tau_{zy} + w\tau_{zz} + q_z) \\ \mu_k (\eta_x k_x + \eta_y k_y + \eta_z k_z) \\ \mu_\omega (\eta_x \omega_x + \eta_y \omega_y + \eta_z \omega_z) \\ 0 \\ 0 \\ 0 \\ 0 \end{pmatrix},$$

$$\mathbf{G_v} = \frac{1}{J}\begin{pmatrix} 0 \\ \zeta_x\tau_{xx} + \zeta_y\tau_{yx} + \zeta_z\tau_{zx} \\ \zeta_x\tau_{yx} + \zeta_y\tau_{yy} + \zeta_z\tau_{yz} \\ \zeta_x\tau_{zx} + \zeta_y\tau_{zy} + \zeta_z\tau_{zz} \\ \zeta_x(u\tau_{xx} + v\tau_{xy} + w\tau_{xz} + q_x) + \zeta_y(u\tau_{yx} + v\tau_{yy} + w\tau_{yz} + q_y) + \zeta_z(u\tau_{zx} + v\tau_{zy} + w\tau_{zz} + q_z) \\ \mu_k(\zeta_x k_x + \zeta_y k_y + \zeta_z k_z) \\ \mu_\omega(\zeta_x \omega_x + \zeta_y \omega_y + \zeta_z \omega_z) \\ 0 \\ 0 \\ 0 \\ 0 \end{pmatrix},$$

$$\mathbf{S} = \begin{pmatrix} 0 \\ 0 \\ 0 \\ 0 \\ 0 \\ P - \rho\beta^* k\omega \\ \alpha\frac{k}{\omega}P - \beta\omega^2 \\ \frac{4}{3}\pi\varrho_l\left(r^{*\,3}_{hom}J_{hom} + 3\varrho n_{hom}\overline{r}^{\,2}_{hom}\frac{d\overline{r}_{hom}}{dt}\right) \\ J_{hom} \\ 4\pi\rho_l(n_{het}\overline{r}^2_{het}\frac{d\overline{r}_{het}}{dt}) \end{pmatrix} \quad . \tag{3.10}$$

The source/sink terms can be found in chapter 2 sec. 2.3.1 and sec. 2.4. The shear stress and heat fluxes are defined in sec. 2.2.1, eq.2.32 - 2.40, but with the transformation the equations change, so it is helpful to examine at least one term of each and from that the others can be derived. The shear stress term τ_{xx} in Cartesian coordinates is

$$\tau_{xx} = \frac{2}{3}(\mu_m + \mu_t)\left[2\left(\frac{\partial u}{\partial x}\right) - \frac{\partial v}{\partial y} - \frac{\partial w}{\partial z}\right] \quad . \tag{3.11}$$

The shear stress term τ_{xx} transformed to general coordinates becomes

$$\tau_{xx} = \frac{2}{3}\frac{\mu_m + \mu_t}{J}\left\{2\left(\xi_x\frac{\partial u}{\partial \xi} + \eta_x\frac{\partial u}{\partial \eta} + \zeta_x\frac{\partial u}{\partial \zeta}\right) - \right. \quad ,$$
$$\left.\left(\xi_y\frac{\partial v}{\partial \xi} + \eta_y\frac{\partial v}{\partial \eta} + \zeta_y\frac{\partial v}{\partial \zeta}\right) - \left(\xi_z\frac{\partial w}{\partial \xi} + \eta_z\frac{\partial w}{\partial \eta} + \zeta_z\frac{\partial w}{\partial \zeta}\right)\right\} \quad . \tag{3.12}$$

The heat flux q_x in cartesian coordinates is

$$q_x = \left(\frac{\mu_m}{Pr} + \frac{\mu_t}{Pr_t} \right) \frac{1}{\gamma - 1} \frac{\partial T}{\partial x} \quad . \tag{3.13}$$

The heat flux q_x transformed to general coordinates becomes

$$q_x = \left(\frac{\mu_m}{Pr} + \frac{\mu_t}{Pr_t} \right) \frac{1}{\gamma - 1} \frac{1}{J} \left\{ \xi_x \frac{\partial T}{\partial \xi} + \eta_x \frac{\partial T}{\partial \eta} + \zeta_x \frac{\partial T}{\partial \zeta} \right\} \quad . \tag{3.14}$$

Note that the general trend of the transformation is to convert one partial derivative into a sum of three with the metrics in front.

3.2. Finite Volume Method 3-D

The finite volume method is implemented on eq. 3.4. The two main reasons for using a finite-volume method over a finite difference is because for complicated geometries the physical domain can be divided into small volumes and the mass, momentum, and energy equations are conserved when solved in integral form [4]. One of the main differences of this code from other codes is that it is a node-centered finite-volume scheme compared to a cell-centered, this means that there are nodes on the boundaries and no extrapolation is required (see fig. 3.2).

3.2.1. Fractional-Step-Method

The vector eq. 3.4 is split into a Fractional-Step-Method from Oran and Boris [61]. The two equations are

adiabatic equation:

$$\frac{1}{J}\frac{\partial \mathbf{Q}}{\partial t} + \frac{\partial \mathbf{E}}{\partial \xi} + \frac{\partial \mathbf{F}}{\partial \eta} + \frac{\partial \mathbf{G}}{\partial \zeta} - \frac{1}{Re_{01}}\left(\frac{\partial \mathbf{E_v}}{\partial \xi} + \frac{\partial \mathbf{F_v}}{\partial \eta} + \frac{\partial \mathbf{G_v}}{\partial \zeta}\right) = \frac{\mathbf{S}^{turb}}{J} \tag{3.15}$$

diabatic equation:

$$\frac{\partial \mathbf{Q}}{\partial t} = \mathbf{S}^{cond} \quad . \tag{3.16}$$

The $\mathbf{S}^{turb}$ is the two turbulent source/sink terms in row 6 and 7 of the $\mathbf{S}$ vector and the $\mathbf{S}^{cond}$ is the homogeneous and heterogeneous condensation terms in row 8, 9, 10 of the $\mathbf{S}$ vector. The Fractional-Step-Method is required because the growth of condensation in the beginning requires a very small time step and thus to impose such a small CFL number on the whole system of equations would be computationally too expensive. Thus, within each time iteration the condensation source term time interval is split according to the growth of droplets.

3.2.2. Time Integration

The compressible N-S equations are a mixture of hyperbolic-parabolic equations in time and the steady N-S equations are a hyperbolic-elliptic mixture. Due to this nature the steady solution is sought by marching in time to reach the steady solution, which is called a time-dependent approach. The solution of eq. 3.4 is sought explicitly in time. The different techniques available are, 1st order, 2nd order Runge-Kutta, and a 2nd order 4-stage low storage Runge-Kutta scheme.

3.2.2.1. Steady-State Solution 1st Order

The steady state solution is obtained by using a 1st order explicit technique. The 1st order approach on eq. 3.4 containing the RANS and turbulence model is

$$\begin{aligned}\mathbf{Q}_{i,j,k}^{(n+1)} = \mathbf{Q}_{i,j,k}^{(n)} - \frac{\Delta t_{i,j,k}}{\Delta V_{i,j,k}} \Big[& \mathbf{E}_{i+1/2,j,k}^{(n)} - \mathbf{E}_{i-1/2,j,k}^{(n)} + \mathbf{F}_{i,j+1/2,k}^{(n)} - \mathbf{F}_{i,j-1/2,k}^{(n)} \\ & + \mathbf{G}_{i,j,k+1/2}^{(n)} - \mathbf{G}_{i,j,k-1/2}^{(n)} + \frac{1}{\Delta V_{i,j,k} Re_{01}} \Big(\mathbf{E}_{v,\ i+1/2,j,k}^{(n)} - \mathbf{E}_{v,\ i-1/2,j,k}^{(n)} + \\ & \mathbf{F}_{v,\ i,j+1/2,k}^{(n)} - \mathbf{F}_{v,\ i,j-1/2,k}^{(n)} + \mathbf{G}_{v,\ i,j,k+1/2}^{(n)} - \mathbf{G}_{v,\ i,j,k-1/2,k}^{(n)} \Big) + \mathbf{S}_{i,j,k}^{turb,(n)} \Big] \quad .\end{aligned} \tag{3.17}$$

In order to obtain a stable solution for eq. 3.17 a proper Δt must be specified. Instead of specifying the Δt, a parameter called the CFL is given and a Δt is calculated from this. CFL stands for Courant-Friedrichs-Levy, sometimes it is referred to as the Courant number. The calculated Δt is thus

$$\Delta t_{i,j,k} = \frac{CFL}{\Big(\delta_x |u| + \delta_y |v| + \delta_z |w| + c_f \sqrt{\delta x^2 + \delta y^2 + \delta z^2} \Big)_{i,j,k}} \tag{3.18}$$

$$\text{with: } \delta_x = |\xi_x| + |\eta_x| + |\zeta_x|, \quad \delta_y = |\xi_y| + |\eta_y| + |\zeta_y|, \quad \text{and} \quad \delta_z = |\xi_z| + |\eta_z| + |\zeta_z| \quad .$$

There are empirical ways to calculate a maximum stable CFL number but the technique of set and see was used. The range of CFL numbers for explicit 1st order in space is around 0.4 - 0.7 and for 3rd order in space 0.1 - 0.3, where this range depends strongly on the mesh. Unfortunately one has a double penalty for finer meshes usually a smaller CFL number is required, the double penalty coming from a finer mesh already requires more CPU time. The most conservative approach would be to use the Δt that is the minimum from the entire domain, but for steady state it is possible to use a technique called *local time stepping*. Where each grid point is advanced in time by the Δt that was calculated for that volume.

With Δt defined above, the idea of fractional time stepping can be better understood. Recalling that the source term for the homogeneous condensate mass fraction is

$$\mathbf{S_8} = \frac{4}{3} \pi \rho_l \left(J r_{hom}^3 + \rho n_{hom} r_{hom}^2 \frac{dr}{dt} \right) \quad , \tag{3.19}$$

Δt_f is defined to be a fraction of the time step Δt from the CFL relationship. The time splitting is done according to an empirical relationship

$$\begin{aligned} \Delta t_f &= \min(1 \cdot 10^{-4}/\mathbf{S_8} \;\; ; \;\; 1 \cdot 10^{-4}/\mathbf{S_{10}}) \\ k &= \mathrm{INT}(\Delta t/\Delta t_f) + 1 \\ \Delta t_f &= \Delta t/k \quad . \end{aligned}$$

INT is an intrinsic FORTRAN subroutine that returns only the value of the integer from the division command. The values of g and n are updated in time according to

$$\begin{aligned} g_{hom} &= g_{hom} + \mathbf{S_8}\Delta t_f \qquad , \\ n_{hom} &= n_{hom} + \mathbf{S_9}\Delta t_f \qquad , \\ g_{het} &= g_{het} + \mathbf{S_{10}}\Delta t_f \qquad . \end{aligned}$$

The fractional time step is finished when the sum of Δt_f is equal to Δt

$$sum_{\Delta t_f} = sum_{\Delta t_f} + \Delta t_f \qquad . \tag{3.20}$$

To be consistent with the above notation in eq. 3.17, the 1st order scheme for the condensation model is

$$\begin{aligned} \mathbf{Q}_{i,j,k}^{(n+1)} = \mathbf{Q}_{i,j,k}^{(n)} - \frac{\Delta t_{i,j,k}}{\Delta V_{i,j,k}} \Big[\mathbf{E}_{i+1/2,j,k}^{(n)} - \mathbf{E}_{i-1/2,j,k}^{(n)} + \mathbf{F}_{i,j+1/2,k}^{(n)} - \mathbf{F}_{i,j-1/2,k}^{(n)} \\ + \mathbf{G}_{i,j,k+1/2}^{(n)} - \mathbf{G}_{i,j,k-1/2}^{(n)} + \frac{1}{\Delta V_{i,j,k} Re_{01}} \Big(\mathbf{E}_{v,\ i+1/2,j,k}^{(n)} - \mathbf{E}_{v,\ i-1/2,j,k}^{(n)} + \mathbf{F}_{v,\ i,j+1/2,k}^{(n)} - \\ \mathbf{F}_{v,\ i,j-1/2,k}^{(n)} + \mathbf{G}_{v,\ i,j,k+1/2}^{(n)} - \mathbf{G}_{v,\ i,j,k-1/2,k}^{(n)} \Big) \Big] + \frac{1}{\Delta V_{i,j,k}} \sum_{\Delta t_f = 0}^{\Delta t_f = \Delta t} \Delta t_f \mathbf{S}_{i,j,k}^{cond,(n)} \qquad . \end{aligned} \tag{3.21}$$

The main difference in eq. 3.21 compared to eq. 3.17 is that the **S** vector is outside the main bracket of $\Delta t/\Delta V$ which corresponds to the idea of having a fractional time step for the source term.

It is possible to calculate the steady state solution using higher order schemes in time, with the advantage that a higher CFL could be used, but usually the increase in CFL does not cover the extra cost of CPU time for higher order time schemes.

3.2.2.2. Unsteady Solution 2nd or 4th Order Runge-Kutta

For unsteady flows it is best to use a 2nd or higher order scheme for the time derivative. The 2nd order Runge-Kutta or improve Euler method which is given in [12]

To save space and to emphasize the technique let $\mathbf{R}$ equal the vectors ($\mathbf{E}$, $\mathbf{F}$, $\mathbf{G}$, $\mathbf{E_v}$, $\mathbf{F_v}$, $\mathbf{G_v}$) which also contains the differences on the cell faces.

RANS and turbulence model

$$\begin{aligned}
\mathbf{Q}_{i,j,k}^{(n+1/2)} &= \mathbf{Q}_{i,j,k}^{(n)} - \frac{\Delta t_{i,j,k}}{\Delta V_{i,j,k}} \left[\mathbf{R}^{(n)} + \mathbf{S}_{i,j,k}^{turb,(n)} \right] \quad , \\
\mathbf{Q}_{i,j,k}^{(n+1)} &= \mathbf{Q}_{i,j,k}^{(n)} - \frac{\Delta t_{i,j,k}}{2\Delta V_{i,j,k}} \left[\mathbf{R}^{(n+1/2)} + \mathbf{S}_{i,j,k}^{turb,(n+1/2)} + \mathbf{R}^{(n)} + \mathbf{S}_{i,j,k}^{turb,(n)} \right] \quad . \qquad (3.22)
\end{aligned}$$

Condensation model

$$\begin{aligned}
\mathbf{Q}_{i,j,k}^{(n+1/2)} &= \mathbf{Q}_{i,j,k}^{(n)} - \frac{\Delta t_{i,j,k}}{\Delta V_{i,j,k}} \mathbf{R}^{(n)} + \frac{1}{\Delta V_{i,j,k}} \sum_{\Delta t_f=0}^{\Delta t_f=\Delta t} \Delta t_f \mathbf{S}_{i,j,k}^{cond,(n)} \quad , \\
\mathbf{Q}_{i,j,k}^{(n+1)} &= \mathbf{Q}_{i,j,k}^{(n)} - \frac{\Delta t_{i,j,k}}{2\Delta V_{i,j,k}} \left[\mathbf{R}^{(n+1/2)} + \mathbf{R}^{(n)} \right] + \qquad (3.23) \\
&\quad \frac{1}{2\Delta V_{i,j,k}} \sum_{\Delta t_f=0}^{\Delta t_f=\Delta t/2} \Delta t_f \left[\mathbf{S}_{i,j,k}^{cond,(n+1/2)} + \mathbf{S}_{i,j,k}^{cond,(n)} \right] \quad .
\end{aligned}$$

In the above formulation two steps are taken noting the intermediate step by n+1/2, the scheme also requires an additional storage array to remember the fluxes at n and n+1/2. Since the diffusive fluxes take about 50% of the total CPU time for one time step it is possible to freeze the diffusive fluxes, so only calculate them at n and reuse them for n+1/2. Splitting the $\mathbf{R}$ vector into $\mathbf{R_c}$ (convective) and $\mathbf{R_v}$ (viscous) notation, eq. 3.22 can be written as

RANS and turbulence model

$$\begin{aligned}
\mathbf{Q}_{i,j,k}^{(n+1/2)} &= \mathbf{Q}_{i,j,k}^{(n)} - \frac{\Delta t_{i,j,k}}{\Delta V_{i,j,k}} \left[\mathbf{R_c}^{(n)} + \mathbf{R_v}^{(n)} + \mathbf{S}_{i,j,k}^{turb,(n)} \right] \quad , \\
\mathbf{Q}_{i,j,k}^{(n+1)} &= \mathbf{Q}_{i,j,k}^{(n)} - \frac{\Delta t_{i,j,k}}{2\Delta V_{i,j,k}} \left[\mathbf{R_c}^{(n+1/2)} + \mathbf{R_v}^{(n+1/2)} + \mathbf{S}_{i,j,k}^{turb,(n+1/2)} \right. \qquad (3.24) \\
&\quad \left. + \mathbf{R_c}^{(n)} + \mathbf{R_v}^{(n)} + \mathbf{S}_{i,j,k}^{turb,(n)} \right] \quad . \qquad (3.25)
\end{aligned}$$

This assumption can save CPU time without much risk in losing time accuracy. Equation 3.24 follows in the same way. It is also possible to use 4th order time accuracy for unsteady calculations. The Runge-Kutta method can also be obtained for 4th order but then memory must be allocated for 4 $\mathbf{R}$ vectors instead of two, for 3-D problems involving half million grid points this can degrade the performance of the calculation. Techniques have been developed for low storage 4th order schemes. The low storage 4th order scheme on the RANS and turbulent model, using freezing of the viscous terms is [57]

RANS and turbulence model

$$\begin{aligned}
\mathbf{Q}_{i,j,k}^{(1)} &= \mathbf{Q}_{i,j,k}^{(n)} - \frac{0.11\Delta t_{i,j,k}}{\Delta V_{i,j,k}} \left[\mathbf{R_c}^{(n)} + \mathbf{R_v}^{(n)} + \mathbf{S}_{i,j,k}^{turb,(n)} \right] \quad , \\
\mathbf{Q}_{i,j,k}^{(2)} &= \mathbf{Q}_{i,j,k}^{(n)} - \frac{0.2766\Delta t_{i,j,k}}{\Delta V_{i,j,k}} \left[\mathbf{R_c}^{(1)} + \mathbf{R_v}^{(n)} + \mathbf{S}_{i,j,k}^{turb,(1)} \right] \quad , \\
\mathbf{Q}_{i,j,k}^{(3)} &= \mathbf{Q}_{i,j,k}^{(n)} - \frac{0.5\Delta t_{i,j,k}}{\Delta V_{i,j,k}} \left[\mathbf{R_c}^{(2)} + \mathbf{R_v}^{(n)} + \mathbf{S}_{i,j,k}^{turb,(2)} \right] \quad , \\
\mathbf{Q}_{i,j,k}^{(n+1)} &= \mathbf{Q}_{i,j,k}^{(n)} - \frac{\Delta t_{i,j,k}}{\Delta V_{i,j,k}} \left[\mathbf{R_c}^{(3)} + \mathbf{R_v}^{(n)} + \mathbf{S}_{i,j,k}^{turb,(3)} \right] \quad .
\end{aligned} \tag{3.26}$$

The key points to notice in eq. 3.26 are the coefficients in front of the Δt / ΔV term and the next time step uses the solution from the previous step, so no additional storage is required. The author noticed that the 4th order scheme was not at a great advantage because the increase in CFL was not enough compensation in regards to taking 4 internal steps before one step in time. The flows encountered in this thesis were adequate for the 2nd order scheme to capture the unsteady behavior. The 4th order scheme was used only as a check at some conditions to validate the 2nd order scheme.

3.2.3. Calculation of the Fluxes - Integration in Space

In the above formulations for the time integration it is required to know the fluxes on each cell face. For example, $E_{i+1/2,j,k}$. The solution of the convective fluxes are done on each face at a time, (1-D numerical scheme) so first in the i, then j, and finally the k-direction. In the case of shocks it is important that the shock is somewhat normal and tangential to the grid lines for the 1-D numerical scheme assumption to be valid. The convective fluxes and diffusive fluxes will be described in the following sections.

Extrapolation – MUSCL-Technique

Before calculating the convective fluxes the primitive variables on the cell boundary must be extrapolated. The MUSCL (monotone upstream-centered schemes for conservation laws)

scheme is used to extrapolate the values on the cell boundaries to produce higher order schemes in space. The technique provides an extrapolation for the "left" and "right" state. The technique for the i-direction is given by [8]

$$\begin{aligned}\mathbf{Q}^L_{i+1/2,j,k} &= \mathbf{Q}_{i,j,k} + \\ &+ \left\{\chi/4\left[\left\{\frac{s_m}{s_i}+\kappa\left(2-\frac{s_m}{s_i}\right)\right\}\Delta_i + \left\{\frac{s_i}{s_m}-\kappa\left(2\frac{s_i}{s_m}-1\right)\right\}\Delta_m\right]\right\}_{i,j,k} \quad (3.27)\end{aligned}$$

$$\begin{aligned}\mathbf{Q}^R_{i+1/2,j,k} &= \mathbf{Q}_{i,j,k} + \\ &+ \left\{\chi/4\left[\left\{\frac{s_p}{s_i}+\kappa\left(2-\frac{s_p}{s_i}\right)\right\}(-\Delta_i) + \left\{\frac{s_i}{s_p}-\kappa\left(2\frac{s_i}{s_p}-1\right)\right\}\Delta_p\right]\right\}_{i,j,k} \quad (3.28)\end{aligned}$$

$$(\Delta_i)_{i,j,k} = \mathbf{Q}_{i+1,j,k} - \mathbf{Q}_{i,j,k} \quad (3.29)$$

$$(\Delta_m)_{i,j,k} = \mathbf{Q}_{i,j,k} - \mathbf{Q}_{i-1,j,k} \quad (3.30)$$

$$(\Delta_p)_{i,j,k} = \mathbf{Q}_{i+1,j,k} - \mathbf{Q}_{i+2,j,k} \quad (3.31)$$

$$s_i = \sqrt{((x_{i+1,j,k}-x_{i,j,k})^2 + (y_{i+1,j,k}-y_{i,j,k})^2 + (z_{i+1,j,k}-z_{i,j,k})^2)} \quad (3.32)$$

$$s_m = \sqrt{((x_{i,j,k}-x_{i-1,j,k})^2 + (y_{i,j,k}-y_{i-1,j,k})^2 + (z_{i,j,k}-z_{i-1,j,k})^2)} \quad (3.33)$$

$$s_p = \sqrt{((x_{i+1,j,k}-x_{i+2,j,k})^2 + (y_{i+1,j,k}-y_{i+2,j,k})^2 + (z_{i+1,j,k}-z_{i+2,j,k})^2)} \quad . \quad (3.34)$$

One main difference in the above MUSCL approach from the standard seen in the literature is the taking into account the grid spacing by s_i, s_m, s_p. The constant κ can be used to easily switch between different extrapolation techniques. For κ = -1 the scheme is 1^{st} order upwind, $\kappa = 1$ it is central difference 2^{nd} order, and for $\kappa = 1/3$ it is 3^{rd} order. The χ term is very important for the MUSCL scheme with discontinuities, because for a higher order scheme with shocks it will produce oscillations [4]. The χ term is called a limiter that switches the extrapolation technique to 1st order (upwinding) near discontinuities and retains the higher order in smooth regions. The limiter used is this case is called the Van Albada limiter [95]

$$\chi = \frac{2\frac{\Delta_i\Delta_m}{s_i s_m}+\varepsilon}{\left(\frac{\Delta_i}{s_i}\right)^2+\left(\frac{\Delta_m}{s_m}\right)^2+\varepsilon} \quad . \quad (3.35)$$

The parameter ε is used to avoid a division by zero and is $\varepsilon = 10^{-8}$.

3.2.3.1. Convective Fluxes AUSMD

The solution of the fluxes is known as solving the Riemann problem using one of two techniques Flux Difference Splitting (FDS) and Flux Vector Splitting (FVS). The FDS uses an approximation of the local Riemann problem, while the FVS splits the flux vector into an upstream and downstream travelling component. Of the FDS methods the Godunov [33] is the exact solution of the Riemann problem, but since this is a solution of a nonlinear equation it requires an iterative procedure. The most popular of the FDS schemes is the ROE scheme [74], which is the solution of the linearized Riemann problem. The advantage of the ROE scheme is that it can capture a single stationary discontinuity with no numerical dissipation. The disadvantage is, it can generate a nonphysical expansion shock, which can be fixed using an entropy fix. Another serious problem is the carbuncle phenomenon, which is a numerical instability in capturing strong shocks, but it is not the only scheme to suffer from this problem. Other FDS schemes include Osher and Solomon [62] and Harten-Lax-Van Leer-Einfeldt (HLLE)[38].
For the FVS schemes the flux function is split into a positive and negative portion

$$F(q) = F(q)^- + F(q)^+ \qquad . \tag{3.36}$$

Early schemes of FVS or Steger-Warming [93], were each portion of eq. 3.36 has a single propagation direction. The eigenvalues of the flux Jacobian matrix give the proper flux depending on the sign of the eigenvalues. These early schemes had problems at the sonic line and stagnation points. Another technique proposed by Van Leer [95] to compensate for the problems in the Steger-Warming scheme is by defining flux terms that were continuously differentiable through sonic and stagnation zones [4]. The Van Leer works but it has high numerical dissipation, which leads to significant errors in viscous calculations. A technique developed by Liou and Steffen called advection upstream splitting method (AUSM) [51], which uses a cell-face advection Mach number to define the upwind extrapolation. There is no numerical dissipation and it can capture strong shocks but behind the shock is has a numerical overshoot. A recent version of the AUSM scheme called AUSMD [97] redefines the mass flux difference which takes into account the density after the shock which it did not account for in earlier versions. The AUSMD scheme is used for the calculations in this thesis because of its robustness, lack of numerical dissipation, a linear problem, and its accuracy. The following is summary of the scheme [97]:
The mass flux is defined by

$$(\rho u)_{1/2} = u_L^+ \rho_L + u_R^- \rho_R \quad , \quad | \, (\rho u)_{1/2}) \, | = \mathrm{abs}((\rho u)_{1/2}) \; , \tag{3.37}$$

where u_L^+ and u_R^- are defined to yield a stationary and moving contact discontinuity

$$u_L^+ = \begin{cases} \alpha_L \left\{ \frac{(u_L + c_m)^2}{4c_m} \right\} + (1 - \alpha_L) \frac{u_L + \mid u_L \mid}{2}) & \text{if } \mid u_L \mid \leq c_m \quad , \\ \frac{u_L + \mid u_L \mid}{2} & \text{otherwise} \quad , \end{cases} \tag{3.38}$$

$$u_R^- = \begin{cases} \alpha_R \left\{ -\frac{(u_R - c_m)^2}{4c_m} \right\} + (1 - \alpha_R) \frac{u_R - \mid u_R \mid}{2}) & \text{if } \mid u_R \mid \leq c_m \quad , \\ \frac{u_R - \mid u_R \mid}{2} & \text{otherwise} \quad , \end{cases} \tag{3.39}$$

where

$$\alpha_L = \frac{2(p/\rho)_L}{(p/\rho)_L + (p/\rho)_R} \quad , \quad \alpha_R = \frac{2(p/\rho)_R}{(p/\rho)_L + (p/\rho)_R} \quad , \tag{3.40}$$

and

$$c_m = \max(c_L, c_R) \quad . \tag{3.41}$$

The pressure flux is thus defined by

$$p_{1/2} = p_L^+ + p_R^- \quad , \tag{3.42}$$

where

$$p_L^+ = \begin{cases} p_L \left\{ \frac{(u_L + c_m)^2}{4c_m} \right\} (2 - \frac{u_L}{c_m}) & \text{if } \mid u_L \mid \leq c_m \quad , \\ p_L \frac{u_L + \mid u_L \mid}{2u_L} & \text{otherwise} \quad , \end{cases} \tag{3.43}$$

$$p_R^+ = \begin{cases} p_R \left\{ \frac{(u_R + c_m)^2}{4c_m} \right\} (2 - \frac{u_R}{c_m}) & \text{if } \mid u_R \mid \leq c_m \quad , \\ p_R \frac{u_R + \mid u_R \mid}{2u_R} & \text{otherwise} \quad . \end{cases} \tag{3.44}$$

With the mass and pressure fluxes known, the numerical convective fluxes on the i or ξ cell face for the RANS equations, 2-equation turbulent model and condensation models are given by

$$
\begin{aligned}
E_\rho &= .5((\rho u)_{1/2}(1+1) - \mid ((\rho u)_{1/2}) \mid (1-1)) && (3.45)\\
E_u &= .5((\rho u)_{1/2}(u_L+u_R) - \mid ((\rho u)_{1/2}) \mid (u_R-u_L)) + \xi_x p_{1/2} && (3.46)\\
E_v &= .5((\rho u)_{1/2}(v_L+v_R) - \mid ((\rho u)_{1/2}) \mid (v_R-v_L)) + \xi_y p_{1/2} && (3.47)\\
E_w &= .5((\rho u)_{1/2}(w_L+w_R) - \mid ((\rho u)_{1/2}) \mid (w_R-w_L)) + \xi_z p_{1/2} && (3.48)\\
E_E &= .5((\rho u)_{1/2}(H_L+H_R) - \mid ((\rho u)_{1/2}) \mid (H_R-H_L)) && (3.49)\\
E_k &= .5((\rho u)_{1/2}(k_L+k_R) - \mid ((\rho u)_{1/2}) \mid (k_R-k_L)) && (3.50)\\
E_\omega &= .5((\rho u)_{1/2}(\omega_L+\omega_R) - \mid ((\rho u)_{1/2}) \mid (\omega_R-\omega_L)) && (3.51)\\
E_{g_{hom}} &= .5((\rho u)_{1/2}(g_{hom,L}+g_{hom,R}) - \mid ((\rho u)_{1/2}) \mid (g_{hom,R}-g_{hom,L})) && (3.52)\\
E_{N_{hom}} &= .5((\rho u)_{1/2}(N_{hom,L}+N_{hom,R}) - \mid ((\rho u)_{1/2}) \mid (N_{hom,R}-N_{hom,L})) && (3.53)\\
E_{g_{het}} &= .5((\rho u)_{1/2}(g_{het,L}+g_{het,R}) - \mid ((\rho u)_{1/2}) \mid (g_{het,R}-g_{het,L})) \quad , && (3.54)
\end{aligned}
$$

where h_L and h_R are the enthalpy, which can be calculated from

$$
\begin{aligned}
T_{L,R} &= \gamma p_{L,R}/\rho_{L,R} \qquad ,\\
g_{L,R} &= g_{hom,L,R} + g_{het,L,R} \qquad ,\\
h_{L,R} &= \frac{\gamma-1}{\gamma}(p_{L,R} - \frac{2}{3}\rho_{L,R}k_{L,R})/\rho_{L,R} - g_{L,R}L(T_{L,R}T_{01})/c_{01}^2 \quad . && (3.55)
\end{aligned}
$$

Remembering L is the function derived for latent heat (eq. 2.7) and since the function requires a temperature of K, the $T_{L,R}$ is multiplied by the total temperature and the L function thus returns a value with units which must be converted to dimensionless form by the speed of sound squared at total conditions.
The values of E are then related by +E for i and -E for i+1, then the next step in the i direction (i+1) it becomes +, thus closing the system. The same equations are used for the y or η direction **F** vector and z or ζ direction **G** vector with the only change being ξ $\rightarrow \eta$ or ζ in eqs. 3.46-3.48.
A numerical note is the convenance of the AUSMD scheme, the original paper did not discuss how to do the fluxes for a condensation or turbulence model but it is easy to infer. For example, u_L and u_R in eq. 3.46 become $g_{hom,L}$ and $g_{hom,R}$ eq. 3.52. Also what makes this scheme easy is the use of an explicit time step and naturally the perfect gas law helps.

3.2.3.2. Viscous Fluxes

When reading about how to implement the viscous fluxes it almost makes one rethink that Euler is not so bad, but once the initial shock is over and the pattern is seen it is a matter of just being consistent. The viscous fluxes $\mathbf{E_v}$, $\mathbf{F_v}$, $\mathbf{G_v}$ are calculated by using something called help cells, which is generated by translating the face ξ, η, or ζ in a half increment $\Delta\xi$ /2, $\Delta\eta$ /2,or $\Delta\zeta$ /2. The method is 2nd order accurate in space. The following numerical description of the viscous fluxes technique is a summary from [8]. A notation is used to represent the new coordinates of the help cells, N, S, E, W, T, and B. On a small note in [8] one would find a different notation for example O instead of E, where the German word for east is Ost.

Diffusive fluxes in ξ-direction

Figure 3.1 displays the geometry of the help cell and the location of the new coordinates. Important points are that the volume of the help cell is the average of the $V_{i,j,k}$ and $V_{i+1,j,k}$ and the new coordinates N, S, T, and B must be calculated from the surrounding points.

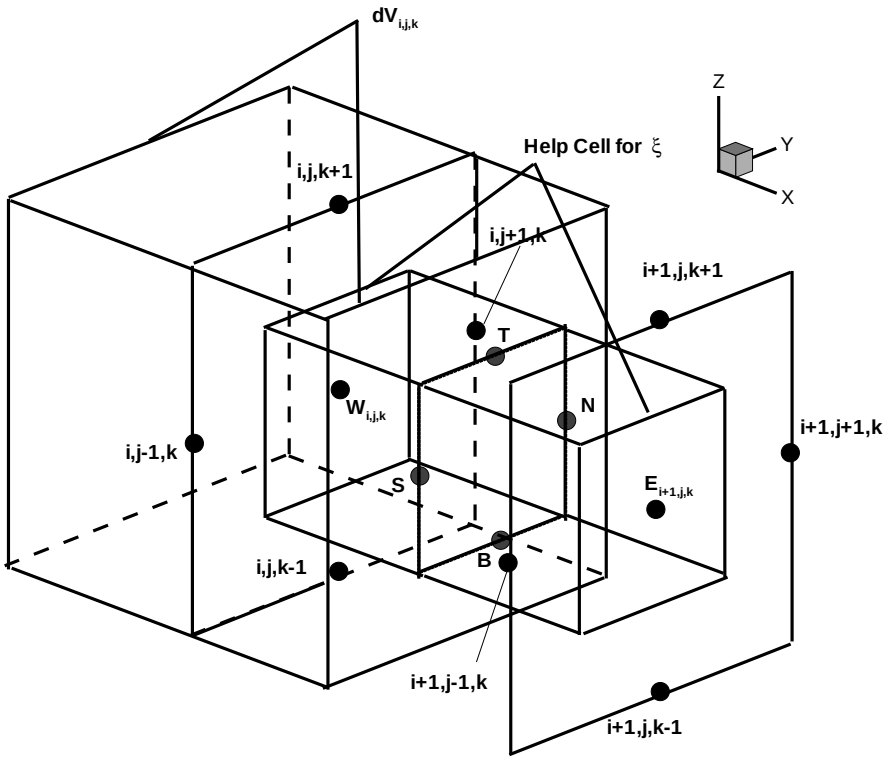

Figure 3.1.: Diagram of help cell for the discretization of the diffusive ξ - fluxes

Part of the interpolation for the new coordinates is as follows

$$
\begin{aligned}
Q_N^+ &= \frac{1}{2}(Q_{i,j+1,k} + Q_{i+1,j,k}) \qquad Q_N^- = \frac{1}{2}(Q_{i,j,k} + Q_{i+1,j+1,k}) \quad , \\
Q_S^+ &= \frac{1}{2}(Q_{i,j,k} + Q_{i+1,j-1,k}) \qquad Q_S^- = \frac{1}{2}(Q_{i,j-1,k} + Q_{i+1,j,k}) \quad , \\
Q_T^+ &= \frac{1}{2}(Q_{i,j,k+1} + Q_{i+1,j,k}) \qquad Q_T^- = \frac{1}{2}(Q_{i,j,k} + Q_{i+1,j,k+1}) \quad , \\
Q_B^+ &= \frac{1}{2}(Q_{i,j,k} + Q_{i+1,j,k-1}) \qquad Q_B^- = \frac{1}{2}(Q_{i,j,k-1} + Q_{i+1,j,k}) \quad .
\end{aligned}
$$

The new coordinates are determined by a binary factor r which determines the diagonal interpolation that is dominant. So for a 90° cube it does not matter but for a skewed volume the r factor will determine which interpolation to use, the + or the −. The equation for the coordinates is thus

$$
\begin{aligned}
Q_N &= r_{2N}^{m+} Q_N^+ + r_{2N}^{m-} Q_N^- \qquad Q_S = r_{2S}^{m+} Q_S^+ + r_{2S}^{m-} Q_S^- \quad , \\
Q_T &= r_{2T}^{m+} Q_T^+ + r_{2T}^{m-} Q_T^- \qquad Q_B = r_{2B}^{m+} Q_B^+ + r_{2B}^{m-} Q_B^- \quad .
\end{aligned} \tag{3.56}
$$

The binary factor r is defined in section A.1. With the help cell parameters determined the diffusive flux term $\mathbf{E_v}$ on the cell face $\xi_{i+1/2}$ is thus given by

$$
\begin{aligned}
\mathbf{E_v^m} = \tfrac{(\mu+\mu_t)_{i+1/2}}{V_{i+1/2}} \Big[& u_E\alpha_{2E}^{\xi m} - u_W\alpha_{2W}^{\xi m} + v_E\alpha_{3E}^{\xi m} - v_W\alpha_{3W}^{\xi m} + w_E\alpha_{4E}^{\xi m} - w_W\alpha_{4W}^{\xi m} \\
& + u_N\beta_{2N}^{\xi m} - u_S\beta_{2S}^{\xi m} + v_N\beta_{3N}^{\xi m} - v_S\beta_{3S}^{\xi m} + w_N\beta_{4N}^{\xi m} - w_S\beta_{4S}^{\xi m} \\
& + u_T\beta_{2T}^{\xi m} - u_B\beta_{2B}^{\xi m} + v_T\beta_{3T}^{\xi m} - v_B\beta_{3B}^{\xi m} + w_T\beta_{4T}^{\xi m} - w_B\beta_{4B}^{\xi m} \Big]_{i+1/2} \\
+ \left\{ \tfrac{1}{V} \left(\tfrac{\mu}{Pr} + \tfrac{\mu_t}{Pr_t} \right) \right\}_{i+1/2} & \tfrac{1}{\gamma - 1} \left(T_E\alpha_{5E}^{\xi m} - T_W\alpha_{5W}^{\xi m} + T_N\beta_{5N}^{\xi m} - T_S\beta_{5S}^{\xi m} + T_T\beta_{5T}^{\xi m} - T_B\beta_{5B}^{\xi m} \right) \\
+ \left\{ \tfrac{1}{V} \left(\mu + \tfrac{\mu_t}{\sigma_t} \right) \right\}_{i+1/2} & \left(k_E\alpha_{6E}^{\xi m} - k_W\alpha_{6W}^{\xi m} + k_N\beta_{6N}^{\xi m} - k_S\beta_{6S}^{\xi m} + k_T\beta_{7T}^{\xi m} - k_B\beta_{7B}^{\xi m} \right) \\
+ \left\{ \tfrac{1}{V} \left(\mu + \tfrac{\mu_t}{\sigma_t} \right) \right\}_{i+1/2} & \left(\omega_E\alpha_{7E}^{\xi m} - \omega_W\alpha_{7W}^{\xi m} + \omega_N\beta_{7N}^{\xi m} - \omega_S\beta_{7S}^{\xi m} + \omega_T\beta_{7T}^{\xi m} - \omega_B\beta_{7B}^{\xi m} \right) \quad .
\end{aligned} \tag{3.57}
$$

The parameters α and β are functions based on the metrics, which are given in completeness in section A.2. m is used as a short hand notation to represent the diffusive fluxes in the momentum (2-4), energy 5, and turbulence model 6, 7. As an example α_6^2 is zero because there is no diffusion of turbulent kinetic energy in the momentum equation.

Diffusive fluxes in η-direction

The technique for the η direction follows the same pattern as ξ, except now N and S are at j and j+1 and E, W, T, and B must be interpolated, with the help cell shifting in the j-direction instead of the x. The diffusive flux in the η-direction on the cell face $\eta_{j+1/2}$ is thus

$$\begin{aligned}\mathbf{F}_{\mathbf{v}}^{\mathbf{m}} = \tfrac{(\mu+\mu_t)_{j+1/2}}{V_{j+1/2}} \big[& u_N\alpha_{2N}^{\eta m} - u_S\alpha_{2S}^{\eta m} + v_N\alpha_{3N}^{\eta m} - v_S\alpha_{3S}^{\eta m} + w_N\alpha_{4N}^{\eta m} - w_S\alpha_{4S}^{\eta m} \\ & + u_E\beta_{2E}^{\eta m} - u_W\beta_{2W}^{\eta m} + v_E\beta_{3E}^{\eta m} - v_W\beta_{3W}^{\eta m} + w_E\beta_{4E}^{\eta m} - w_W\beta_{4W}^{\eta m} \\ & + u_T\beta_{2T}^{\eta m} - u_B\beta_{2B}^{\eta m} + v_T\beta_{3T}^{\eta m} - v_B\beta_{3B}^{\eta m} + w_T\beta_{4T}^{\eta m} - w_B\beta_{4B}^{\eta m} \big]_{j+1/2} \\ + \left\{ \tfrac{1}{V}\left(\tfrac{\mu}{Pr} + \tfrac{\mu_t}{Pr_t}\right)\right\}_{j+1/2} & \tfrac{1}{\gamma-1}\left(T_N\alpha_{5N}^{\eta m} - T_S\alpha_{5S}^{\eta m} + T_E\beta_{5E}^{\eta m} - T_W\beta_{5W}^{\eta m} + T_T\beta_{5T}^{\eta m} - T_B\beta_{5B}^{\eta m}\right) \\ + \left\{ \tfrac{1}{V}\left(\mu + \tfrac{\mu_t}{\sigma_t}\right)\right\}_{j+1/2} & \left(k_N\alpha_{6N}^{\eta m} - k_S\alpha_{6S}^{\eta m} + k_E\beta_{6E}^{\eta m} - k_W\beta_{6W}^{\eta m} + k_T\beta_{7T}^{\eta m} - k_B\beta_{7B}^{\eta m}\right) \\ + \left\{ \tfrac{1}{V}\left(\mu + \tfrac{\mu_t}{\sigma_t}\right)\right\}_{j+1/2} & \left(\omega_N\alpha_{7N}^{\eta m} - \omega_S\alpha_{7S}^{\eta m} + \omega_E\beta_{7E}^{\eta m} - \omega_W\beta_{7W}^{\eta m} + \omega_T\beta_{7T}^{\eta m} - \omega_B\beta_{7B}^{\eta m}\right) \quad . \end{aligned} \tag{3.58}$$

Diffusive fluxes in ζ-direction

The technique for the ζ direction follows the same pattern as ξ, except now T and B are at k and k+1 and E, W, N, and S must be interpolated, with the help cell shifting in the k-direction instead of the x. The diffusive flux in the ζ-direction on the cell face $\zeta_{k+1/2}$ is thus

$$\begin{aligned}\mathbf{G}_{\mathbf{v}}^{\mathbf{m}} = \tfrac{(\mu+\mu_t)_{k+1/2}}{V_{k+1/2}} \Big[& u_T\alpha_{2T}^{\zeta m} - u_B\alpha_{2B}^{\zeta m} + v_T\alpha_{3T}^{\zeta m} - v_B\alpha_{3B}^{\zeta m} + w_T\alpha_{4T}^{\zeta m} - w_B\alpha_{4B}^{\zeta m} \\ & + u_E\beta_{2E}^{z\eta m} - u_W\beta_{2W}^{\zeta m} + v_E\beta_{3E}^{\zeta m} - v_W\beta_{3W}^{\zeta m} + w_E\beta_{4E}^{\zeta m} - w_W\beta_{4W}^{\zeta m} \\ & + u_N\beta_{2N}^{\zeta m} - u_S\beta_{2S}^{\zeta m} + v_N\beta_{3N}^{\zeta m} - v_S\beta_{3S}^{\zeta m} + w_N\beta_{4N}^{\zeta m} - w_S\beta_{4S}^{\zeta m} \Big]_{k+1/2} \\ + \left\{ \tfrac{1}{V}\left(\tfrac{\mu}{Pr} + \tfrac{\mu_t}{Pr_t}\right)\right\}_{k+1/2} & \tfrac{1}{\gamma-1}\left(T_T\alpha_{5T}^{\zeta m} - T_B\alpha_{5B}^{\zeta m} + T_E\beta_{5E}^{\zeta m} - T_W\beta_{5W}^{\zeta m} + T_N\beta_{5N}^{\zeta m} - T_S\beta_{5S}^{\zeta m}\right) \\ + \left\{ \tfrac{1}{V}\left(\mu + \tfrac{\mu_t}{\sigma_t}\right)\right\}_{k+1/2} & \left(k_T\alpha_{6T}^{\zeta m} - k_B\alpha_{6B}^{\zeta m} + k_E\beta_{6E}^{\zeta m} - k_W\beta_{6W}^{\zeta m} + k_N\beta_{7N}^{\zeta m} - k_S\beta_{7S}^{\zeta m}\right) \\ + \left\{ \tfrac{1}{V}\left(\mu + \tfrac{\mu_t}{\sigma_t}\right)\right\}_{k+1/2} & \left(\omega_T\alpha_{7T}^{\zeta m} - \omega_B\alpha_{7B}^{\zeta m} + \omega_E\beta_{7E}^{\zeta m} - \omega_W\beta_{7W}^{\zeta m} + \omega_N\beta_{7N}^{\zeta m} - \omega_S\beta_{7S}^{\zeta m}\right) \quad . \end{aligned} \tag{3.59}$$

Programmers note: In writing the above diffusive fluxes, the $\mathbf{E}_{\mathbf{v}}$ was written and then cutting and pasting was done for the other two, so in writing the above equations there were errors and it took about 3-4 proof reads to find hopefully them all. This was a long process in debugging, thus going slow and reducing distractions is suggested when coding diffusive fluxes.

3.2.3.3. Source Terms

The source terms in the vector **S** can be found in chapter 2. The first 5 terms are zero, $\mathbf{S_6}$ and $\mathbf{S_7}$ can be found in sec. 4.3 depending on the turbulence model chosen and $\mathbf{S_8}$ - $\mathbf{S_{10}}$ can be found in sec. 2.4

3.2.4. Initial and Boundary Conditions

Initializing is very important in regards to starting with a stable solution and accelerating the calculation. For example if one were to initialize a nozzle with all values being zero it is likely the program would crash or even if just the velocity is zero and the thermodynamic variables are at total conditions. It is thus a question of what is the optimum starting point? The initialization of the domain depends on the type of flow problem (external or internal). For external flow the parameters are set to the free stream conditions. For internal flow the pressure on the inlet and outlet is used. A linear approximation is used between the two pressures to find the values in between, then the 1-D adiabatic compressible equations are used to solve for temperature, density, velocity and so on.
Boundary conditions in the authors view are the second most important factor in CFD, with the grid being number one. If the program is not working right, the first question, Is there a problem with the grid? For example, zero or negative volumes. The second question being are the boundary conditions implemented correctly.

3.2.4.1. Initial Conditions

Thermodynamic variables

In an external flow problem the initial conditions are quite simple. The variables are set to the free stream conditions calculated based on the 1-D compressible adiabatic relations between total, static, and free stream Mach number. With the total temperature, pressure, Mach number and angle of attack the domain can be initialized using the following relations:

$$T_\infty = T_{01}\left(1+\frac{\gamma-1}{2}M_\infty^2\right)^{-1} \quad , \tag{3.60}$$

$$p_\infty = p_{01}\left(1+\frac{\gamma-1}{2}M_\infty^2\right)^{\frac{\gamma-1}{\gamma}} \quad . \tag{3.61}$$

Density ρ_∞ is obtained from the perfect gas law and the velocity components are determined by the speed of sound and Mach number. The velocity components are given by

$$u_\infty = M_\infty\sqrt{\gamma p_\infty/\rho_\infty}\cos(\alpha) \quad , \tag{3.62}$$

$$v_\infty = M_\infty \sqrt{\gamma p_\infty / \rho_\infty} \sin(\alpha) \quad , \tag{3.63}$$

$$w_\infty = 0. \quad . \tag{3.64}$$

where α is the angle of attack and the w-component of velocity is simply set to zero. For internal flow the inlet Mach number is a parameter that is usually not known from experiment but it is approximated to get an inlet pressure. On the other hand the outlet pressure is usually known. Using eq. 3.61 with a guess for the Mach number the inlet and outlet pressure are used for a linear approximation to get the pressure throughout the nozzle. With pressure and total parameters known the following procedure for domain initialization is done:

$$\begin{aligned}
Do \;\; i &= 1 \,, \;\; Iend \\
p_i &= p_{inlet} - (i-1)\frac{p_{inlet} - p_{outlet}}{Iend - 1} \\
\rho_i &= \left(\frac{p_i}{p_{01}}\rho_{01}\right)^{\frac{1}{\gamma}} \\
T_i &= p_i/(\rho_i R_{gas}) \\
u_i &= \sqrt{2\left(h_{01} - \frac{\gamma}{\gamma - 1}\frac{p_i}{\rho_i}\right)} \\
v_i &= 0. \\
w_i &= 0. \\
END \;\; DO \quad ,
\end{aligned}$$

where $h_{01} = \frac{\gamma}{\gamma - 1}\frac{p_{01}}{\rho_{01}}$. For each level of j and if 3-D for each level of k this procedure is done. Another technique could be to use the compressible area relation equation to solve for the function of pressure as a function of area and then from pressure derive the other variables. No optimization tests were done to see if a better starting procedure would provide a faster converged solution, the above procedure worked and nothing further was done. Note if the outlet is supersonic then an outlet pressure is not needed but for initialization the outlet pressure is chosen to give a Mach number greater than 1, which can be calculated before starting the simulation.

Turbulence variables

The two turbulence parameters k and ω must also be specified in the entire domain for the calculation to properly begin without problems. The idea is to specify a relative turbulence

intensity (T'') and a ratio (E_{ratio}) of turbulent viscosity (μ_t) to molecular viscosity (μ_m). The turbulence intensity is related to k and given by

$$T'' \equiv 100\sqrt{\frac{2k_{init.}}{3u_{init.}^2}}\ [\%] \quad . \tag{3.65}$$

The range of relative turbulent intensities is around 1 to 0.5%. The value of $k_{init.}$ for most problems in transonic flow is around $2m^2/s^2$.
The initialization of ω follows from

$$\begin{aligned} \omega_{init.} &= \rho_{init.}k_{init.}/\mu_t \qquad \text{for } k-\omega \text{ or SST model} \quad , \\ \omega_{init.} &= 0.09\rho_{init.}k_{init.}/\mu_t \qquad \text{for EASM}(k-\omega) \text{ model} \quad . \end{aligned} \tag{3.66}$$

The turbulent viscosity μ_t is solved from the given ratio and μ_m is based on the Sutherland law which is a function of temperature

$$\begin{aligned} \mu_m &= \left(\frac{T_{init.}}{273.15}\right)^{1.5}\left(\frac{273.15+110.4}{T_{init.}+110.4}\right)1.71.^{-5} \quad , \\ \mu_t &= E_{ratio}\mu_l \quad . \end{aligned}$$

The E_{ratio} range is between 1 – 10 with higher values for the EASM model because of the 0.09 absorbed into ω. With this range there were no numerical problems after the initialization.

3.2.4.2. Boundary Conditions

One of the most important factors in CFD is putting boundaries on the numerical problem. Adding a wall, airfoil, wing to the problem creates a disturbance in the flow which must be handled, but also this disturbance is carried to other boundaries in the flow, being inlet or outlet and must also be taken into account.
One main feature of this code is that there are nodes on the boundary (node-centered scheme) compared to a cell-centered scheme so no extrapolation is required.

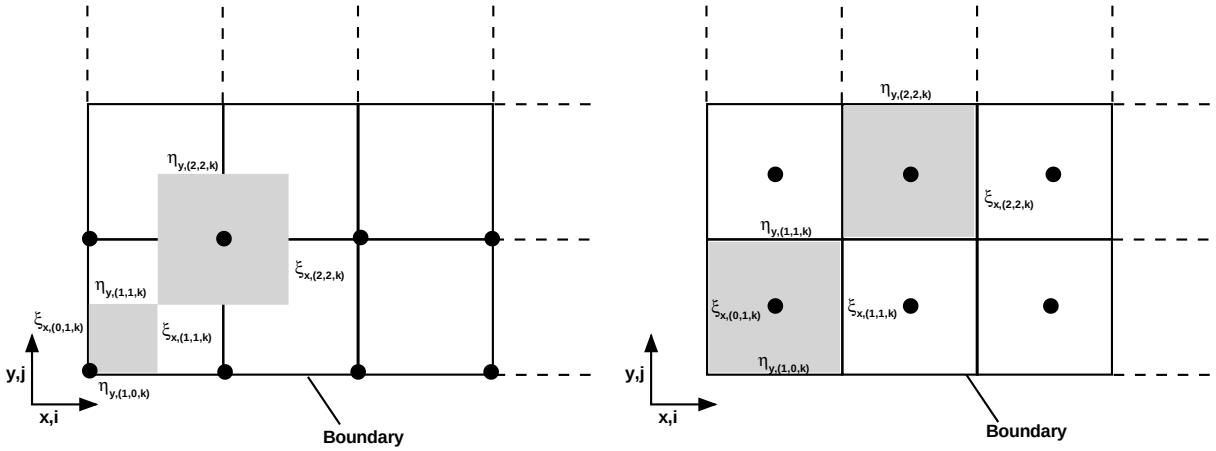

Figure 3.2.: Comparison between node-centered (left) and cell-centered scheme (right)

Figure 3.2 compares the difference between the node-centered and cell-centered scheme in 2-D, also the metrics are on the figure to give an idea of the notation used for counting and what they represent. If there are 5 nodes then there are 6 faces, which is the reason for the matrix to begin with 0 instead of 1. In this case fig. 3.2, ξ_y, ξ_z, η_x, and η_z are zero. The technique used in this code is to have a general boundary condition for the fluxes, thus for a wall, inlet, outlet, etc.. it is the same boundary condition and after the time integration is finished, the primitive variables are corrected according to the type of boundary. From a programming point of view this technique makes adding and subtracting boundary conditions very easy when using a module form.

Fluxes

In sec. 3.2.3.1 the fluxes were derived but only for cell faces on the interior. The general boundary condition for the fluxes at i=1 and i=NI is as follows:

$$UU = u\xi_{x,\,{}^{0}_{NI}} + v\xi_{y,\,{}^{0}_{NI}} + w\xi_{z\,{}^{0}_{NI}} \tag{3.67}$$

$$HH = h\rho + \frac{1}{2}\rho(u^2 + v^2 + w^2) \tag{3.68}$$

$$E_\rho = E_\rho \mp_{\substack{1\\NI}} \rho UU \tag{3.69}$$

$$E_u = E_u \mp_{\substack{1\\NI}} \rho uUU + \xi_{x,\,\substack{0\\NI}}\, p \tag{3.70}$$

$$E_v = E_v \mp_{\substack{1\\NI}} \rho vUU + \xi_{y,\,\substack{0\\NI}}\, p \tag{3.71}$$

$$E_w = E_w \mp_{\substack{1\\NI}} \rho wUU + \xi_{z,\,\substack{0\\NI}}\, p \tag{3.72}$$

$$E_E = E_E \mp_{\substack{1\\NI}} HHUU \tag{3.73}$$

$$E_k = E_k \mp_{\substack{1\\NI}} \rho kUU \tag{3.74}$$

$$E_\omega = E_\omega \mp_{\substack{1\\NI}} \rho\omega UU \tag{3.75}$$

$$E_{g_{hom}} = E_{g_{hom}} \mp_{\substack{1\\NI}} \rho g_{hom} UU \tag{3.76}$$

$$E_{N_{hom}} = E_{N_{hom}} \mp_{\substack{1\\NI}} \rho N_{hom} UU \tag{3.77}$$

$$E_{g_{het}} = E_{g_{het}} \mp_{\substack{1\\NI}} \rho g_{het} UU \quad . \tag{3.78}$$

At i = 1 (the index i = 0 is for the cell face), the flux is subtracted whereas at i= NI the flux is added, which follows from the closure scheme given in sec. 3.2.3.1. For the j and k-direction the only change is from $\xi \rightarrow \eta$ and ζ and keeping constant at j=1 and k=1 the flux is subtracted and at j=NJ and k=NK it is added. The general scheme makes the boundary condition for the fluxes very simple and easy to implement.

Inlet

For a subsonic inlet there are 4 characteristics for the Euler equations and one goes out in 3D Navier-Stokes (turbulence and condensation equations will be discussed at the end of the section). For both internal and external flow the total temperature T_{01} and total pressure p_{01} are usually known and thus they are two of the characteristics specified. For external flow the free stream Mach number is usually known, which can be the third characteristic. Specifying the total conditions and the free stream Mach number requires the inlet to be far away from the wing or airfoil, because this boundary condition acts like a wall, if the disturbance due to the wing or airfoil approaches the inlet it will be reflected. Having the boundary far from the body requires larger grids and thus more computation time, so a scheme that allows the free stream conditions to change at the inlet is an advantage. This is done by solving a set of 3 equations with 3 unknowns, which results in a non-linear equation that is solved with Newtons method. Even though this type of boundary condition takes more computational time, it is still at an advantage by using smaller grids. For example, an airfoil calculation usually requires an inlet that is 20 times the chord, but with the quasi "non-reflecting" boundary condition the inlet used is 8 times the chord. The following are the set of equations used for the inlet boundary condition:

$$u_N^* - 2\frac{c^*}{\gamma-1} = u_N - 2\frac{c}{\gamma-1} \quad \text{for Inlet at j=1} \tag{3.79}$$

$$u_N^* + 2\frac{c^*}{\gamma-1} = u_N + 2\frac{c}{\gamma-1} \quad \text{for Inlet at j=NJ} \tag{3.80}$$

$$\frac{p_{01}}{\rho_{01}^\gamma} = \frac{p}{\rho^\gamma} \tag{3.81}$$

$$\frac{\gamma}{\gamma-1}\frac{p_{01}}{\rho_{01}} = \frac{\gamma}{\gamma-1}\frac{p}{\rho} + \frac{1}{2}(u^2+v^2+w^2) \quad . \tag{3.82}$$

The * variables represent the primitive variables that were just solved at the recent time step and the primitive variables on the right hand side represent the corrected variables. Equation 3.79 or 3.80 is the normal momentum equation where u_N represents the velocity normal to the cell face. Equation 3.81 assumes there is no entropy production between the total and free stream (static) variables. Equation 3.82 assumes there is no energy loss between the total and free stream (static) variables. Since the shocks do not in general reach the inlet boundary and there is no heat addition the above assumptions are valid. The metrics are used to convert the normal velocity into its components and then the three equations are combined to reduce it to one unknown. Another assumption is that the w-component of velocity is zero, which is not entirely true for 3-D wing calculations but the magnitude of the w-component is much smaller than the u and v with an angle of attack. To include the w-component would require setting up another equation, most likely the tangential momentum equation. Using the metrics the normal velocity is

$$u_n = \eta_x u + \eta_y v + \eta_z w \quad . \tag{3.83}$$

The above equation is for an inlet of j=1, if it is i or k then the metrics are changed to ξ or ζ. The v-component of velocity is then related by

$$v = u\tan(\alpha) \quad . \tag{3.84}$$

Casting eqs. 3.79 or 3.80 - 3.82 into a function only of u and then using Newtons method, the primitive variables are updated by

$$u = u \tag{3.85}$$

$$v = u\tan(\alpha) \tag{3.86}$$

$$w = 0. \tag{3.87}$$

$$\rho = \frac{\gamma}{\gamma-1}\frac{p_{01}}{\rho_{01}} - \frac{\frac{1}{2}(u^2+v^2)}{\frac{\gamma}{\gamma-1}\frac{p_{01}}{\rho_{01}^\gamma}} \tag{3.88}$$

$$p = \frac{p_{01}}{\rho_{01}^\gamma}\rho^\gamma \tag{3.89}$$

The turbulence variables k and ω on the inlet can be specified by using the equations for the initialization, eq. 3.65 and eq. 3.66. Also different techniques were used where the value of k and ω at the inlet were set equal to the value at one cell in from the inlet or no correction at all was done. It seems for the test cases used in this thesis there was not a strong effect on how k and ω were specified on the inlet.
Since the inlet boundary conditions are based on adiabatic conditions the values of g_{hom}, g_{het}, and n_{hom} could be set to zero, but it was found that no correction also worked. No correction uses the idea that since there are nodes on the boundary, the governing equations for g_{hom}, g_{het}, and n_{hom} are being solved on the boundary and thus no correction is required.

Wall

Depending on the type of flow investigated (Euler or N.S) the wall boundary condition must be adapted. For Euler it is assumed there is slip between the wall and the fluid, in another words the wall has a velocity vector, but the mass flux is zero. The pressure and density is solved based on the tangential momentum equation and entropy. For N.S. the velocity is zero and thus slip between the wall and fluid, the pressure and density is based on conserving energy between the * states and entropy.

Euler Wall (Slip)
For an Euler wall the mass flux is zero and thus the velocity vector is tangent to the wall. The following set of equations define the boundary condition for an Euler wall:

$$
\begin{aligned}
T_T &= \sqrt{\eta_x^2+\eta_y^2+\eta_z^2} \quad , \\
T_X &= \eta_x/T_T \quad , \\
T_Y &= \eta_y/T_T \quad , \\
T_Z &= \eta_z/T_T \quad , \\
c^* &= \sqrt{\gamma\frac{p^*}{\rho^*}} \quad , \\
U_T^* &= T_X u^* + T_Y v^* + T_Z w^* \quad , \\
u &= u^* - T_X U_T^* \quad , && (3.90)\\
v &= v^* - T_Y U_T^* \quad , && (3.91)\\
w &= w^* - T_Z U_T^* \quad , && (3.92)\\
\rho &= \rho^* \left(\frac{c^* \pm \frac{\gamma-1}{2} U_T^*}{c^*} \right)^{2/(\gamma-1)} \quad , && (3.93)\\
p &= p^* \left(\frac{\rho}{\rho^*} \right)^{\gamma} \quad . && (3.94)
\end{aligned}
$$

The * represent the values of the primitive variables before correction. The $\pm$ in eq. 3.93 refers to a minus for the wall at j=1 and a plus for the wall at j=NJ. If the wall happens to be at the boundary of i or k then only η is changed to ξ or ζ, also the same rule is used for the $\pm$ sign in eq. 3.93.

N.S. Wall (No-Slip)
For a N.S. "adiabatic" wall all velocity components are set to zero and the pressure and density are defined by

$$
\begin{aligned}
S &= \frac{p^*}{\rho^{*\gamma}} \quad , \\
\rho &= \left(\frac{\frac{p^*}{\rho^*}\frac{\gamma}{\gamma-1} + \frac{1}{2}\left(u^{*2}+v^{*2}+w^{*2}\right)}{S^{\frac{\gamma}{\gamma-1}}} \right)^{\frac{1}{\gamma-1}} && (3.95)\\
p &= \rho^{\gamma} S \quad . && (3.96)
\end{aligned}
$$

With the use of a turbulence model the turbulent kinetic energy and specific dissipation rate must be corrected. The following is the method for correcting the turbulent parameters:[103]

$$k = 0. \tag{3.97}$$

$$dn = \sqrt{(x_{i,j,k} - x_{i,j\pm1,k})^2 + (y_{i,j,k} - y_{i,j\pm1,k})^2 + (z_{i,j,k} - z_{i,j\pm1,k})^2}$$

$$\mu_l = \left(\frac{1 + \frac{110.4}{T_{01}}}{T_w + \frac{110.4}{T_{01}}} \right) T_w^{1.5}$$

$$\omega = \frac{100\mu_l}{\rho dn^2} \qquad \text{for } k-\omega \text{ and SST} \tag{3.98}$$

$$\omega = \frac{100\mu_l}{\rho dn^2} 0.0895 \qquad \text{for EASM} \quad . \tag{3.99}$$

T_w is the temperature at the wall and the $\pm$ sign in the dn equation is plus at j=1 and minus at J=NJ, if the wall is at i or k then the only change is in the dn term, which will be i$\pm$1 or k$\pm$1.

Outlet

At the subsonic outlet there are 3 outgoing characteristics and 1 is incoming for the 3D Navier-Stokes equations, so 1 characteristic must be specified. The turbulent and condensation equations do not require a boundary condition at a subsonic outlet. The typical parameter at the outlet is the pressure. The pressure being the free stream (static) or back pressure for a nozzle. For internal flow the given back pressure is set constant for the entire outlet geometry. For external flow the outlet back pressure is more difficult because of the vortex or wake from the trailing edge of the airfoil or wing. In this case the average pressure on the outlet is the free stream pressure, thus allowing for a variation in pressure on the outlet[39]. The first step is to solve for the average pressure on the outlet

$$\overline{p} = \frac{1}{l} \int_0^l p(y)\, dy \approx \frac{\sum_{j=1}^{NJ} p(j)(\xi_x)_j}{\sum_{j=1}^{NJ} (\xi_x)_j} \quad . \tag{3.100}$$

The above equation is only valid for an outlet geometry that is perpendicular to the x-axis, but simple adjustments can be made to account for a general outlet geometry.
The local pressure is then related by

$$p_{(i,j,k)} = p_{(i\pm1,j,k)} \frac{p_{\infty,out}}{\overline{p}} \quad . \tag{3.101}$$

Once the pressure is known the other primitive variables can be derived by the following procedure

$$\begin{aligned}
T_T &= \sqrt{\xi_x^2 + \xi_y^2 + \xi_z^2} \\
T_X &= T_X/TT \\
T_Y &= T_Y/TT \\
T_Z &= T_Z/TT \\
U_T^* &= u^* T_X + v^* T_Y + w^* T_Z \\
c^* &= \sqrt{\frac{\gamma p^*}{\rho^*}} \\
\rho &= \rho^* \left(\frac{p}{p^*}\right)^{\frac{1}{\gamma}} \qquad (3.102) \\
c &= \sqrt{\frac{\gamma p}{\rho}} \\
W_N &= (U_T^* \pm \frac{2}{\gamma - 1}(c^* - c)) \\
u &= u^* - T_X(U_T^* - W_N) \qquad (3.103) \\
v &= v^* - T_Y(U_T^* - W_N) \qquad (3.104) \\
w &= w^* - T_Z(U_T^* - W_N) \quad . \qquad (3.105)
\end{aligned}$$

The $\pm$ sign in the definition of W_N is minus for i=1 and plus for i=NI. If the outlet boundary lies in j or k instead then the only change is from ξ to η or ζ.
The above scheme for the outlet is independent of Euler or N.S.. For supersonic outflow the technique of do nothing is required, simply comment out the call to this subroutine and that is the outlet boundary condition. For turbulent calculations the question arises what to do for the boundary layer because it is partially subsonic. One idea was to find the sonic point, extrapolate pressure and then use the above routine for points that were subsonic. So far the author found that also doing nothing was adequate for the calculations in this thesis. A physical interpretation of the doing nothing technique for a subsonic boundary layer outlet is thought to be equivalent to zero gradient.

The technique for specifying the value of k and ω on the outlet was the do nothing technique, which means k and ω follow from the solution of the time step. This is one of the advantages of having a node-centered scheme.

Periodic

The periodic boundary condition is the easiest to implement. This boundary condition is needed in the c-grid connection after the trailing edge. An example of how it works is to examine an airfoil boundary for a c-grid, which might run from i=35 to i=179, there is then two nodes at the same x, y, z location. The boundary condition is simply to average the two values and then set them both equal to their average. When zooming into the connection a small kink is noticed, many techniques were implemented to try to remove this kink but in the end it was found to have little affect on the solution.

3.2.5. Coupling the System of Equations

The numerical procedure requires the solution of 5 equations for Euler, 7 for turbulence, 8 for Euler-condensation, and 10 for turbulence-condensation. The system of equations is closed through the definition of pressure, which is a relation between static pressure, turbulent kinetic energy, and the fraction of condensed water.

3.3. Implementation and Program Structure

The following is a summary of the program structure.

Begin Program
  Read INPUT and *GRID* files
  Initialize domain or read RESTART file
  CALL **NONDIM** (cast into dimensionless terms)
  CALL **GEOMETRY** (calculate metrics and volume)
    Begin Time Iteration
    CALL **TIMESTEP** (calculate global minimum or local time step for each volume)
      IF (Navier-Stokes) then
        IF (Turbulence) then
          IF (*WILCOX*) *CALL* **WILCOX**
          IF (*MENTER*) *CALL* **MENTER**
          IF (*EASM*) *CALL* **EASM**
        ENDIF
      CALL **FLXIDIFF**
      CALL **FLETDIFF**
      CALL **FLZEDIFF**
      ENDIF
    CALL **FLXICONV**
    CALL **FLETCONV**
    CALL **FLZECONV**
    Update primitive variables in time
    CALL **XI1** (boundary condition for ξ at i=1)
    CALL **XIM** (boundary condition for ξ at i=NI)
    CALL **ET1** (boundary condition for η at j=1)
    CALL **ETM** (boundary condition for η at j=NJ)
    CALL **ZE1** (boundary condition for ζ at k=1)
    CALL **ZEM** (boundary condition for ζ at k=NK)
    Update thermodynamic variables $(T, p_{vap}, \rho_{vap}, h)$
    End Time Interation
  CALL **NONDIM** (cast into dimensional terms)
  Write RESTART file
  Write OUTPUT data file
End Program

4. Validation

4.1. Steady flow with Condensation

4.1.1. S1 Nozzle - Euler

4.1.1.1. Geometry and Grids

The S1 nozzle was developed by Schnerr [81] as one of many nozzles to test and understand the physics of shocks due to heat addition, steady as well as unsteady. The S1 nozzle has a high curvature and thus is good for Euler simulations due to the boundary layer growth is suppressed by wall curvature. Figure 4.1 shows the geometry of the nozzle and appropriate boundary conditions. Since it is an Euler simulation it is not needed to model the full geometry of the nozzle and channel test section, for example the curvature of the nozzle is terminated by a parallel wall in the experiment. Likewise a short parallel section is only needed before the nozzle curvature begins. The Euler assumption is tested in sec. 4.4.

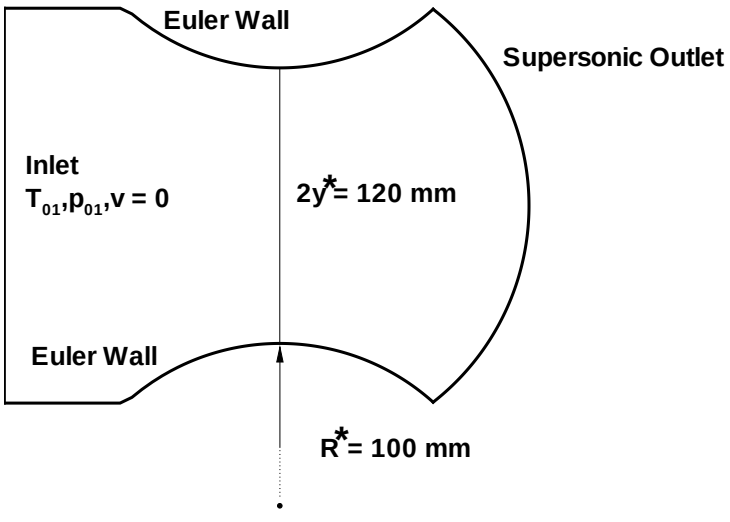

Figure 4.1.: S1 nozzle geometry

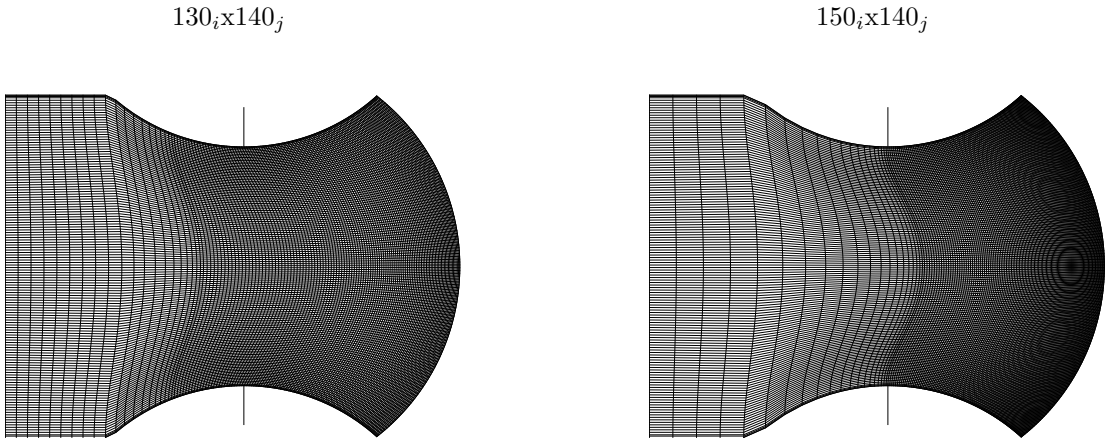

Figure 4.2.: S1 nozzle Euler grids

After the first condensation calculation using the 130_ix140_j grid, good results were obtained with experiment and since most of the condensation is occurring after the throat it was decided to change the density of the grid after the throat rather than just doubling the whole grid to check grid independence. Figure 4.3 shows a closeup of the two grids after the throat, thus one can see the Δx is $\sim \frac{1}{2}$ in the 150_ix140_j grid. The main reason for checking grid independence is to see if there is a difference in the Schlieren picture between the two grids, which is the reason why only the i-component of the grid was changed.

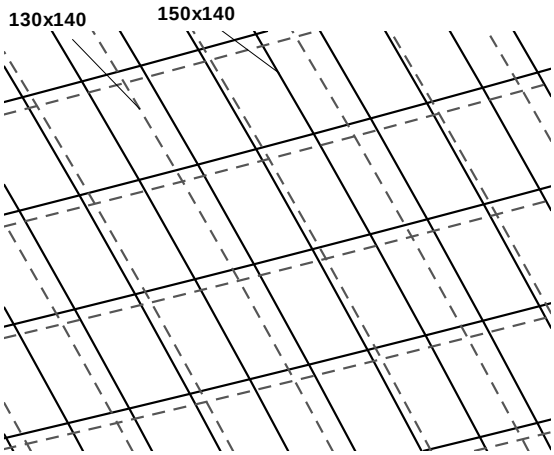

Figure 4.3.: Grid comparison: solid line 150_ix140_j, dotted line 130_ix140_j

4.1.1.2. Adiabatic

Figure 4.4 left, shows a numerical Schlieren picture of the adiabatic expansion flow in the S1 nozzle. The adiabatic flow field with no back pressure (supersonic outlet) is very simple, smooth gradients and is used as a template to show there are no underlining errors when going to flows with complex structures due to heat addition. Figure 4.4 right is the Mach number and temperature gradient distribution at the centerline. At Mach one the 2-D numerical temperature gradient is 6.52 K/cm, where the 1-D approximation is 8.14 K/cm, and the experiment is 6.85 K/cm.

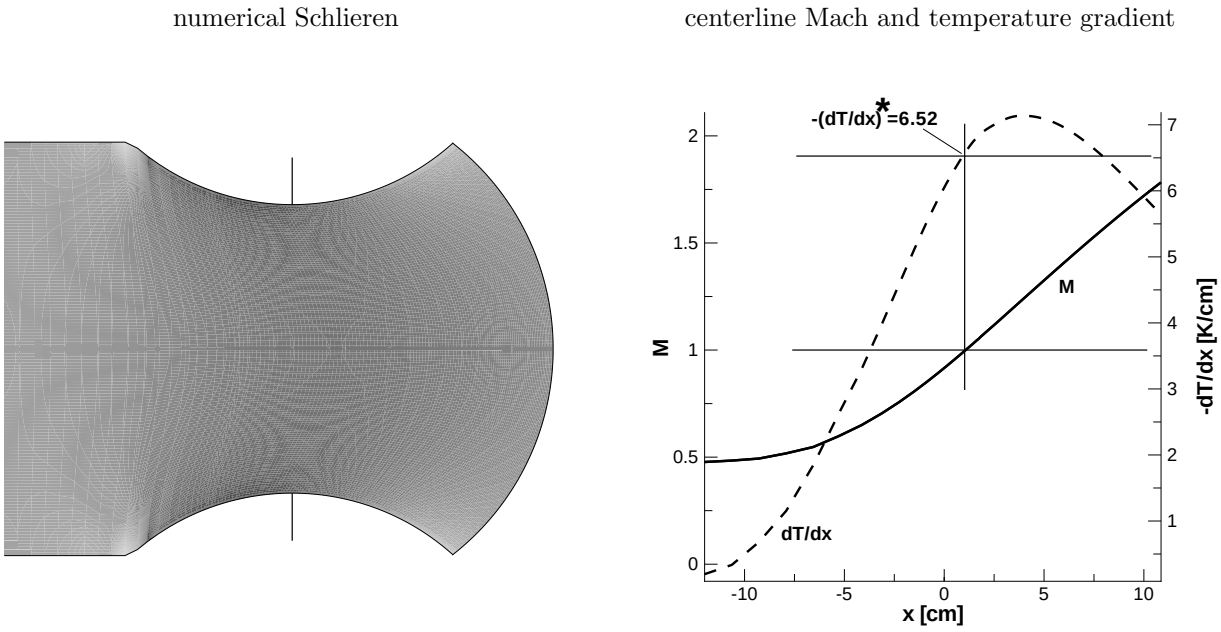

Figure 4.4.: Expansion adiabatic flow, left: numerical Schlieren picture, right: along center line, [$T_{01} = 295$ K, $p_{01} = 1$ bar].

In the following figs.4.5-4.6 the features due to heat addition in the numerical Schlieren picture are not as distinct or sharp as the experimental pictures. The former code PhaseCD was better at capturing the features of heat addition in a nozzle. For example in fig. 4.6 the shock is weaker compared to the experiment. A possible reason for this difference is that PhaseCD was a 2-D code compared to the current 3-D code that requires two cell volumes in the z-direction. The two side walls require a boundary condition which adds error to the numerical simulation by having a w-component of velocity that is non-zero. This small difference in velocity could effect the peak value or location of nucleation rate, where if a little more condensate is produced, the shock due to heat addition would be stronger.

4.1.1.3. $\phi_0 = 37.2\%$

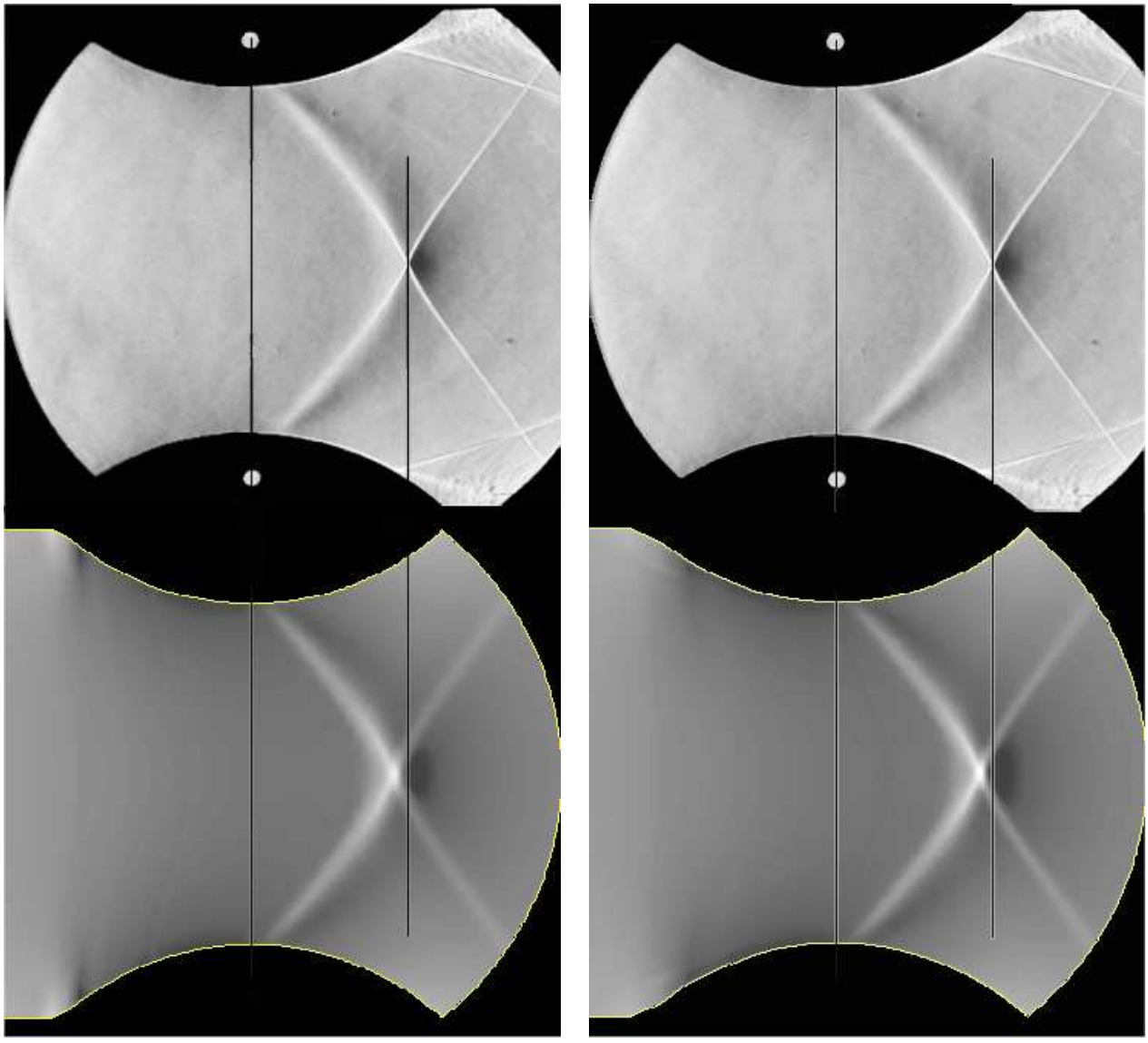

grid 130_ix140_j grid 150_ix140_j

Figure 4.5.: S1 nozzle comparison between experiment and different grid densities, [$T_{01} = 295$ K, $p_{01} = 1$ bar, $\phi_0 = 37.2\%$, humid air].

top : experiment [81]
bottom : numerical Schlieren picture

At $\phi_0 = 37.2\%$ the classical "X-Shock" is produced. Due to the high latent-heat release of water vapor condensing in air, weak oblique shocks extend from the nozzle wall just after the throat. At the centerline a weak normal shock exist, marking the center of the "X-Shock". Downstream of the weak normal shock are again oblique shocks due to heat addition. The numerical Schlieren results (fig.4.5 bottom) reproduce the 2-D structure found in the experimental Schlieren photograph (fig.4.5 top).

4.1.1.4. $\phi_0 = 71.3\%$

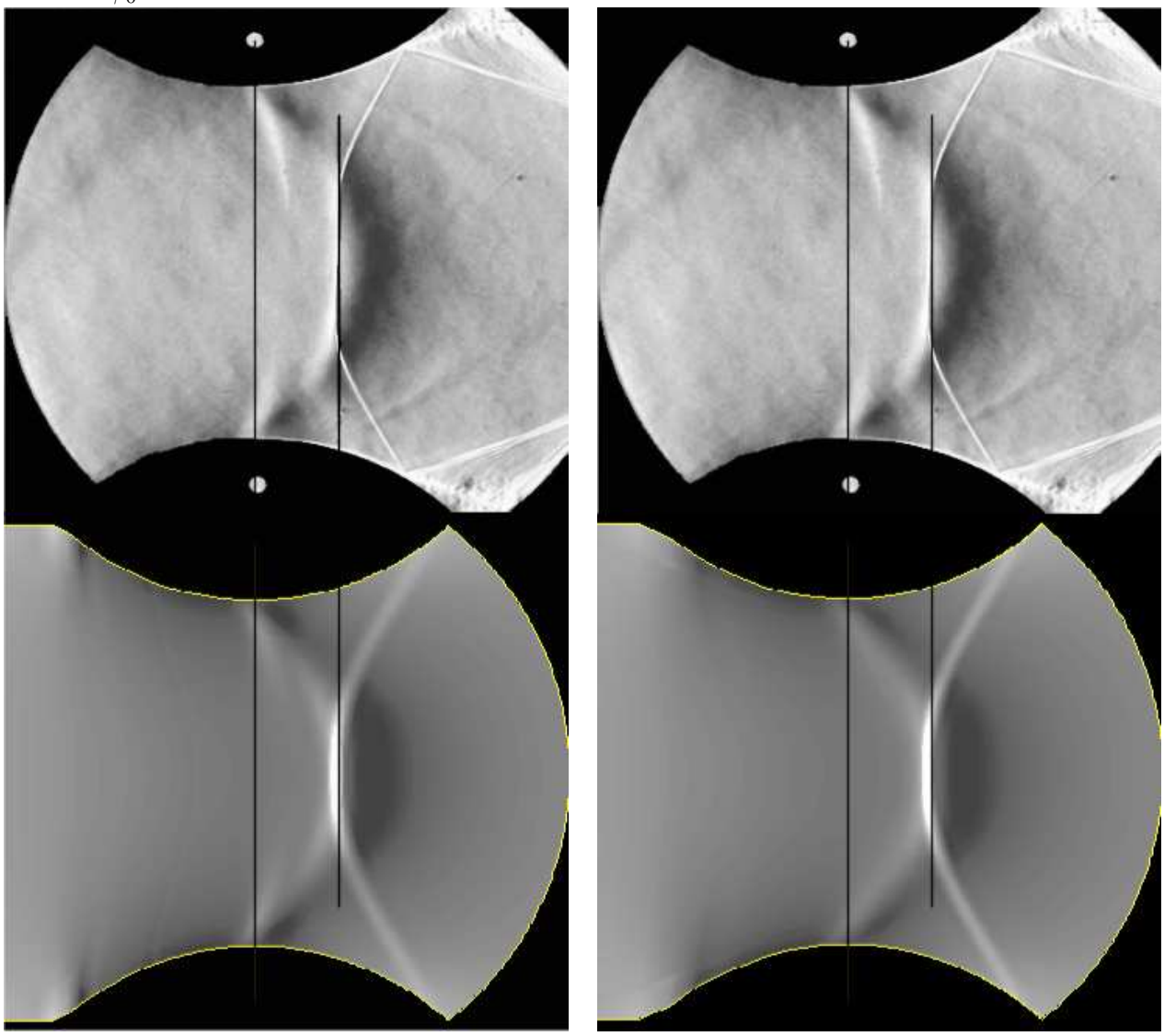

grid 130_ix140_j grid 150_ix140_j

Figure 4.6.: S1 nozzle comparison between experiment and different grid densities, [$T_{01} = 286.8$ K, $p_{01} = 1$ bar, $\phi_0 = 71.3\%$, humid air].

top : experiment [81]
bottom : numerical Schlieren picture

As the humidity or water content of the air is increased the formation of compression waves extend from the wall before the throat [83], fig. 4.6. This occurrence was previously pointed out by Bratos and Meier [11]. The compression wave is characterized by subcritical heat addition, it is not a shock. The shock due to heat addition occurs further downstream (normal and oblique components), also present are weak compressions before the normal shock. Again the numerical code is able to capture all the 2-D structures found in the experimental Schlieren photograph.

4.1.2. A1 Nozzle - Euler

4.1.2.1. Geometry and Grid

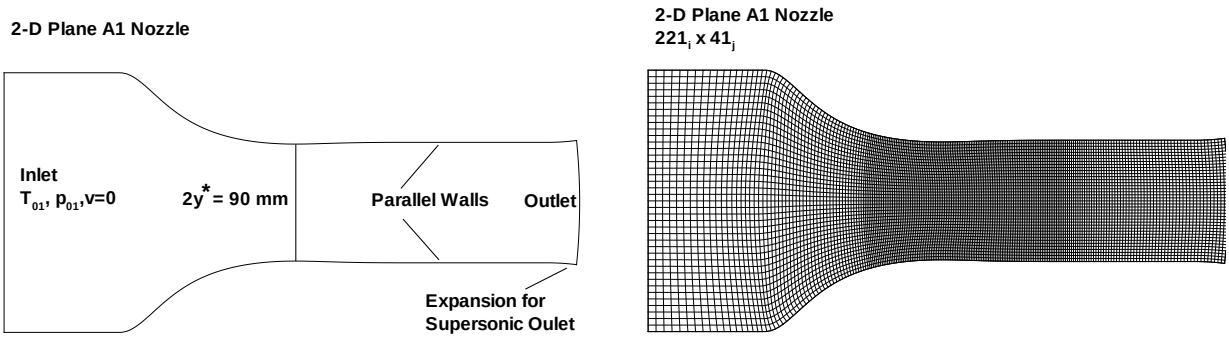

Figure 4.7.: A1 plane nozzle geometry and grid.

The A1 nozzle consists of a relatively small curvature after the throat with a parallel outflow constant Mach number of $M_{e,is.}$ =1.2. The nozzle characteristics are $2y^* = 90$ mm, radius of wall curvature at throat $R^* = 300$ mm, and temperature gradient $-(dt/dx)^*_{exp} = 5.13$ K/cm. The grid in fig. 4.7 (right) is one of the grids used by Adam in his thesis. Adam also did a grid study using 440_ix40_j and 440_ix80_j, but found at maximum a 2% difference in frequency. The small expansion on the outlet is used to obtain a supersonic outlet since the back pressure is not known. In Adam [1, 2] comparisons were made with and without this small expansion, no differences in frequency or flow structure were found.

4.1.2.2. Adiabatic

The adiabatic flow through the nozzle is simply a smooth expansion followed by a constant outlet Mach number. A side note, notice there is no large bump or small compression when the expansion ends which shows that Adam designed an efficient nozzle. The numerical Schlieren fig. 4.8 right shows the smooth features of the nozzle and there is no background numerical error. Figure 4.8 (right) shows the centerline Mach number and temperature gradient, which compares quite well with the experimental value of 5.13 K/cm.

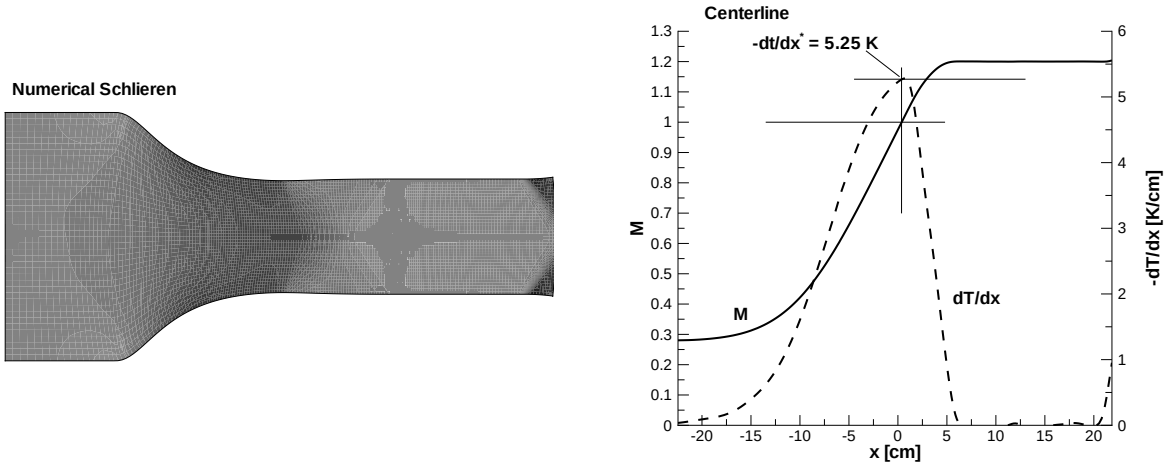

Figure 4.8.: Expansion adiabatic flow in the A1 nozzle, left: numerical Schlieren picture, right: along center line, [$T_{01} = 295$ K, $p_{01} = 1$ bar, humid air].

4.1.2.3. $\phi_0 = 35.6\%$

The steady case for the A1 nozzle, using a relative humidity of 35.6% obtains a steady shock due to heat addition near the throat. The experimental Schlieren picture fig. 4.9 (top) shows a slightly higher curvature in the shock wave than the numerical but position, expansion (dark area before shock), and shock wave agree with experiment. Also note that the numerical solution is Euler, which shows that good agreement can be obtained since there is no separation.

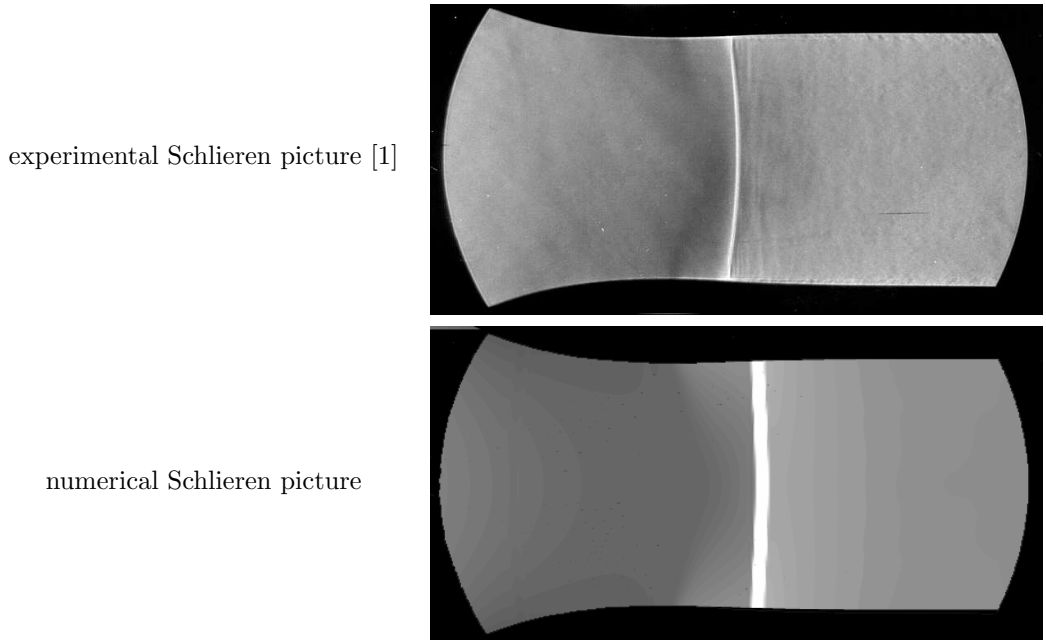

Figure 4.9.: Steady shock due to heat addition, [$T_{01} = 298.7$ K, $p_{01} = 1$ bar, $\phi_0 = 35.6$, humid air].

The Schlieren pictures provide a qualitative comparison whereas the pressure distribution (fig. 4.10) shows if the model is obtaining the correct shock strength and back pressure. Unfortunately the model is over predicting the strength of the shock wave by having a larger compression, but the rounding of the pressure followed by the linear decrease in pressure is obtained in the model. Since the shock strength is larger, the back pressure is also higher by this amount. Also in fig. 4.10 is a comparison of the present model with that of Adam [1].

centerline pressure ratio distribution

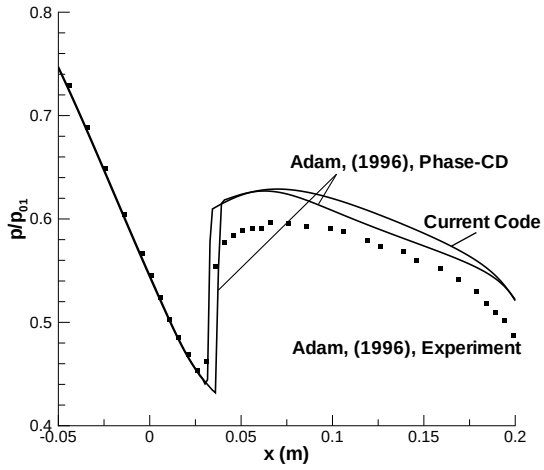

centerline nucleation rate and wetness fraction

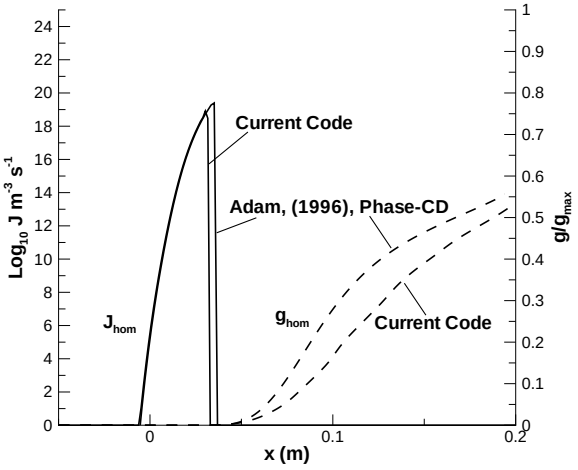

Figure 4.10.: Steady diabatic flow in the A1 nozzle, [$T_{01} = 298.7$ K, $p_{01} = 1$ bar, $\phi_0 = 35.6\%$].

4.1.2.4. Unsteady

To test the unsteady part of the code the A1 nozzle is an excellent test case. Adam [1] has done extensive experiments and numerical simulations on this nozzle and thus only a small part of what Adam has done is reproduced to test the unsteadiness. The unique geometric feature of the A1 nozzle compared to other nozzles of our group is the parallel outflow section that produces a constant exit Mach number. Also the stability limit is lower due to the lower temperature gradient at the throat which comes from the nozzle shape compared to circular nozzles.

experimental Schlieren pictures [1] numerical Schlieren pictures

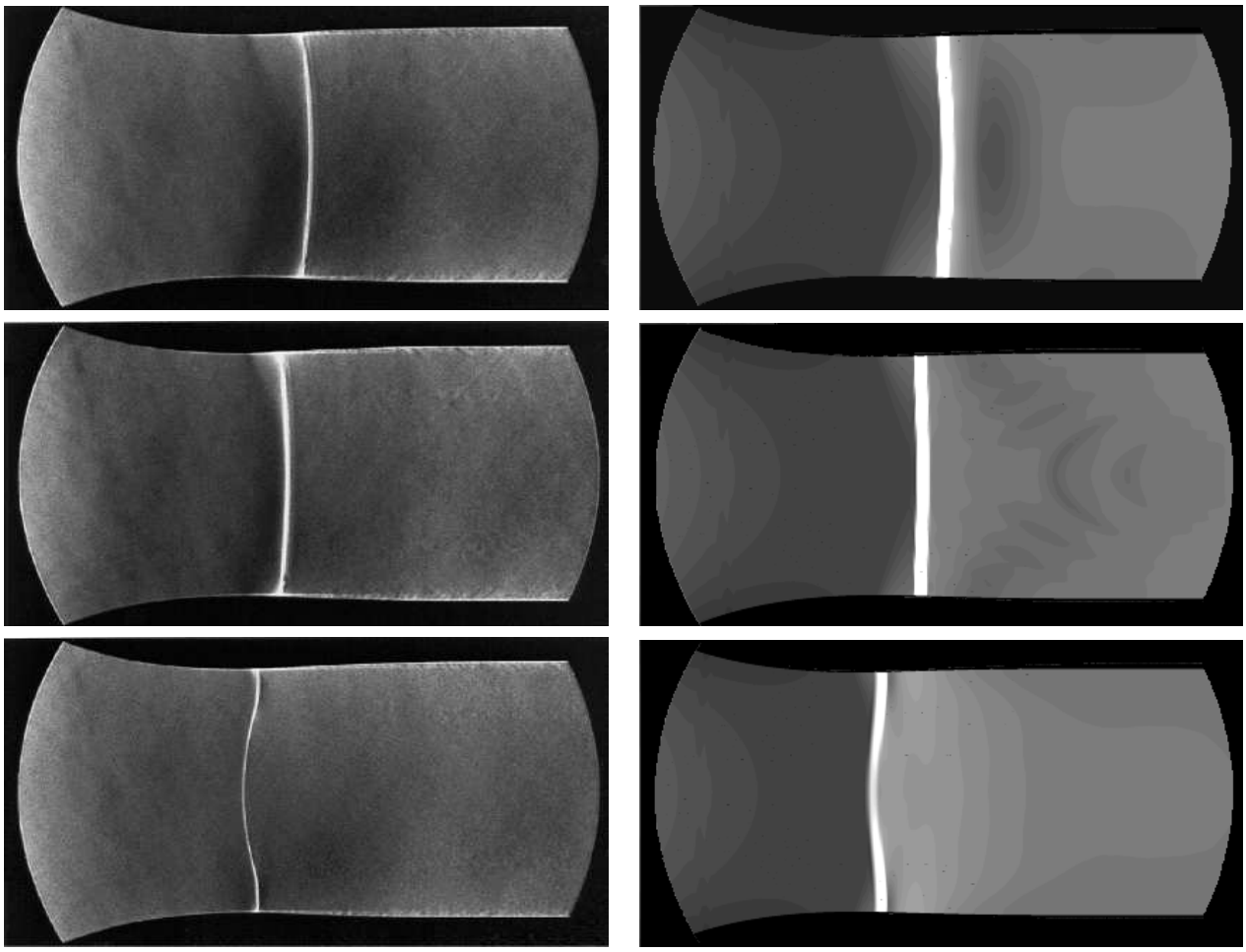

Figure 4.11.: Unsteady symmetric oscillation in the A1 nozzle, [$f_{num.} = 262$ Hz, $f_{exp.} = 225$ Hz, $T_{01} = 292.8$ K, $p_{01} = 0.998$ bar, $\phi_0 = 51.6\%$, humid air].

Figure 4.11 compares experimental and numerical Schlieren pictures for the symmetric flow oscillation. The symmetric oscillation is well established, it is due to the strong latent heat release which produces shocks that then move upstream into the nucleation zone. The interaction with the nucleation zone reduces the amount of condensate which allows for higher supersaturation downstream, which forms a new shock to start the process again [86]. The shocks in the numerical Schlieren pictures fig. 4.11 (right) are not as resolved as the experimental photographs but the trend and structure match with the experiment. The frequency is not well captured compared to other test cases, a likely reason is due to the weaker instabilities are harder to duplicate.

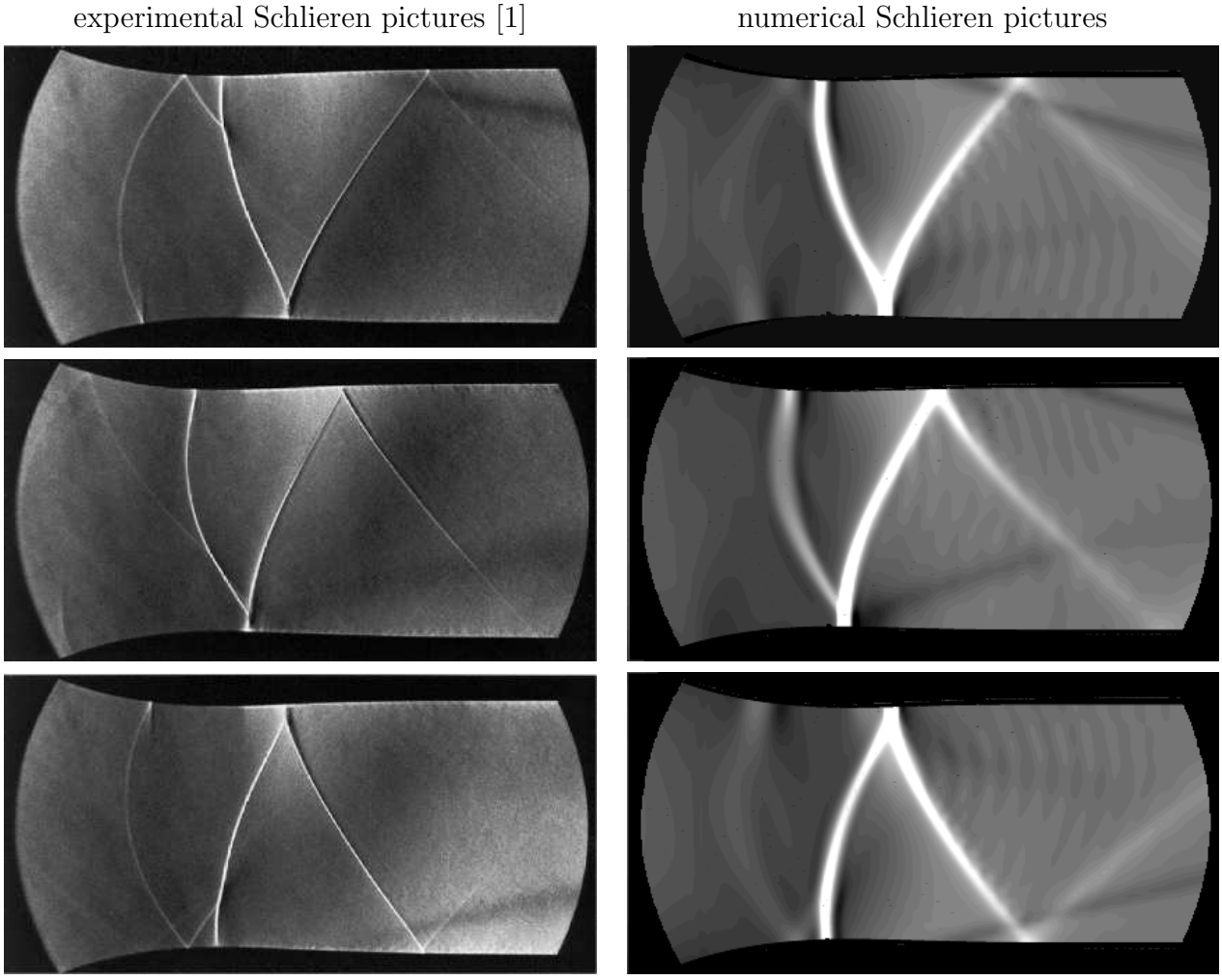

Figure 4.12.: Unsteady unsymmetric oscillation in the A1 nozzle, [$f_{num.} = 843$ Hz, $f_{exp.} = 905$ Hz, $T_{01} = 288.2$ K, $p_{01} = 1$ bar, $\phi_0 = 82\%$, humid air].

Figure 4.12 compares the experiment and numerical Schlieren for the unsymmetric oscillation. At the time of Adam's doctorate work this was a new type of phenomenon with unsteady condensation in nozzles. The pattern here is a Mach reflection in the region of the nozzle throat before the upstream shock becomes more curved. The shock weakens and dies out as it travels upstream through the throat. The process alternates between the upper and lower wall [86]. Again the numerical Schlieren is not as resolved as the photographs but the 2-D structure is evident and the frequency is that of the experimental range.

A very important numerical point here is that a linear disturbance eq. 5.1 was applied to the symmetric oscillation mode found at the above operating conditions in fig. 4.12. This linear disturbance enabled the unsymmetric oscillation to evolve. It is possible due to numerical error that the system would involve into the unsymmetric oscillation given enough time, but the disturbance equation is a better control mechanism.

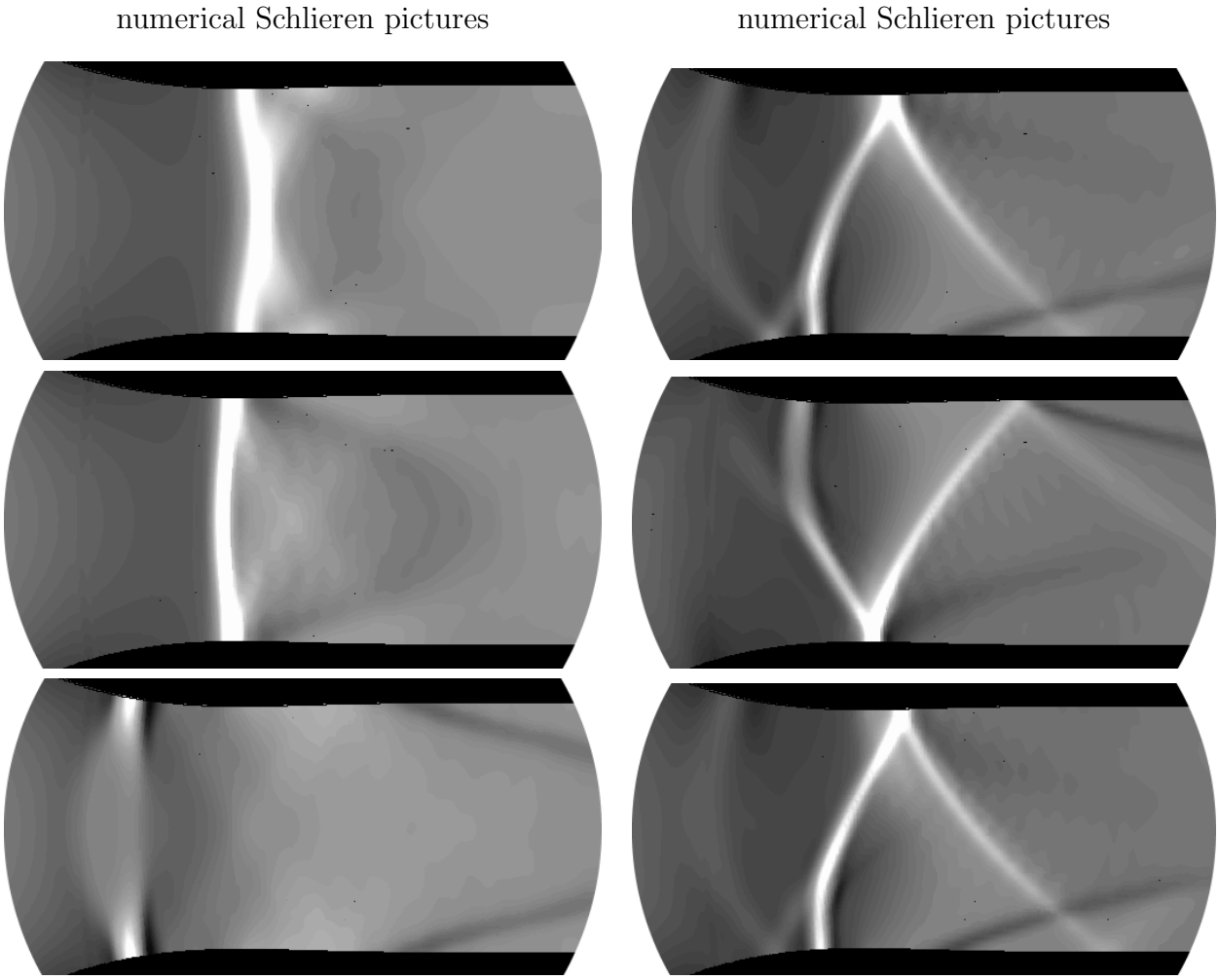

Figure 4.13.: Unsteady flow pattern in the A1 nozzle, [, T_{01} = 295 K, p_{01} = 1 bar, ϕ_0 = 90%, humid air].

left	:	symmetric	$f_{num.}$ = 446 Hz, $f_{num.,Adam}$=447 Hz
right	:	unsymmetric	$f_{num.}$ = 1091 Hz, $f_{num.,Adam}$=1068 Hz

A unique flow feature in the A1 nozzle occurs at a certain threshold value of ϕ_0, where there are two possible oscillation structures at identical reservoir conditions. The two structures being a symmetric and unsymmetric flow oscillation. In fig. 4.12 there was also a symmetric oscillation but only the unsymmetric was shown.

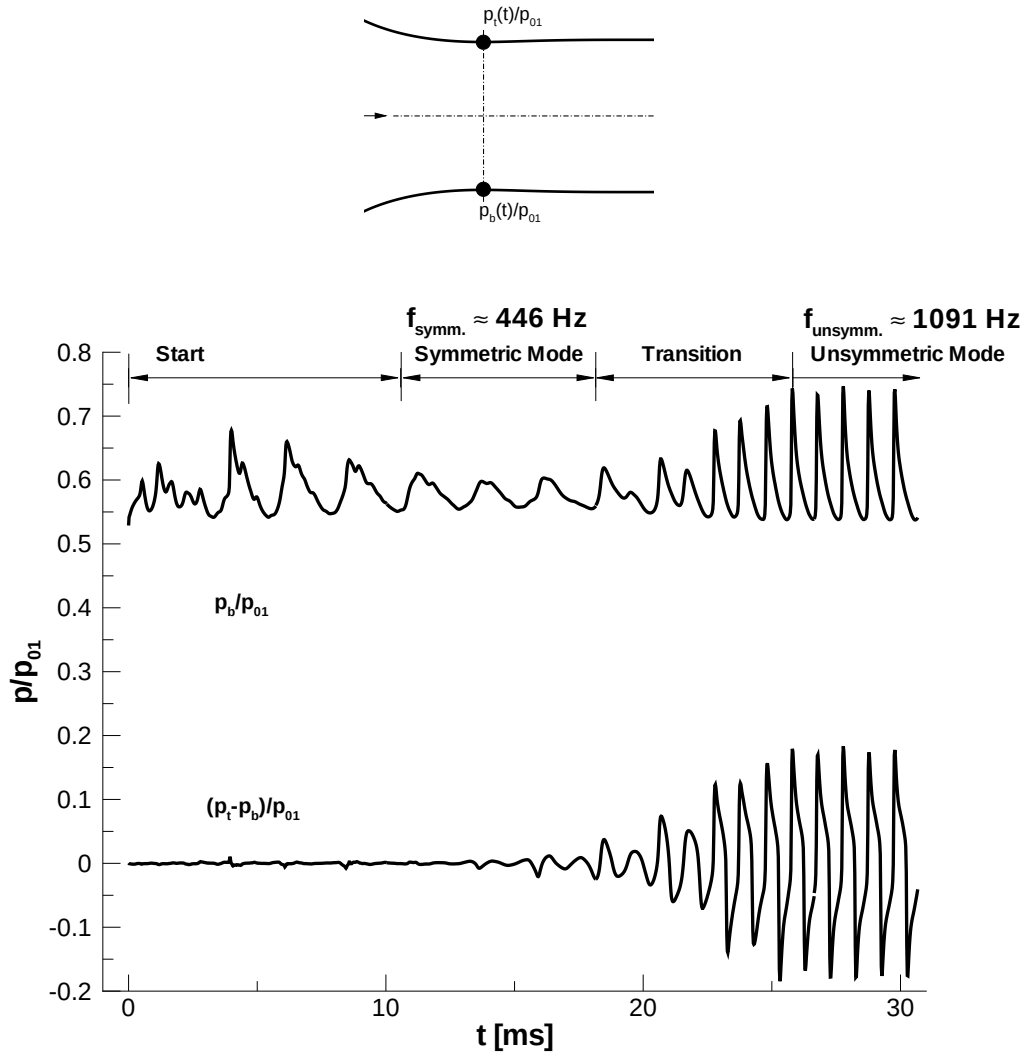

Figure 4.14.: Pressure fluctuations at the throat, bottom wall in the A1 nozzle, [T_{01} = 295 K, p_{01} = 1 bar, ϕ_0 = 90%, humid air].

top	:	locations where data is sampled for frequency curve
bottom	:	top half of the graph shows the frequency history of the pressure ratio at the bottom station
bottom	:	bottom half of the graphs shows the frequency history of the pressure ratio "difference" between top and bottom station

Figure 4.14 displays the graphs from which the frequency is derived. A numerical station is placed at the throat to write out pressure ratio measurements every 150 iterations at the top and bottom wall. The top time series shows the pressure fluctuations at the bottom wall from the start of the simulation to the unsymmetric oscillation. The bottom time series shows the pressure difference, which is zero until the start of the transition

region and then reaching a consistent pattern that matches the unsymmetric oscillation. The physical interpretation of the bifurcation is the instability of the interaction between transonic flow with homogeneous condensation [2, 86]. The case of 90% humidity is at the border of the upper end of the hysteresis regime. The hysteresis regime is only found from numerical simulations, whereas in the experiment it is either symmetric or unsymmetric, it was not possible to add a disturbance during the experiment to see if the unsymmetric oscillation would evolve. From Adam's numerical simulations at 90% humidity there are both solutions but for this case. In figs. 4.13-4.14 no disturbance was needed, because at this high humidity or water content the additional transport equations for condensation add numerical uncertainty into the time scheme that the flow can go directly to the unsymmetric mode without a disturbance. Whereas for 82% humidity and T_{01} =288.2 K, a disturbance was needed to obtain the unsymmetric oscillation.

4.2. Nitrogen

4.2.1. CAST-10 Airfoil - Turbulent

To go from a moist air model to a pure nitrogen system is relatively easy, it is only a matter of changing the thermodynamic functions and realizing there is no longer p_v and p_{air} but just p_{vN_2}, no carrier gas, thus the blending functions for c_{p_0}, c_{v_0}, ..etc are not needed. Since there is no carrier gas the assumption of the Hertz-Knudsen droplet growth model may not be valid because the droplet radii are greater than the mean free path of the nitrogen gas. The experimental data for a transonic numerical test case with nitrogen condensation is very limited and if one is found it usually dates back to the early 80's. The first test case found was by Hall [36] at the NASA Langley 0.3m cryogenic wind tunnel. The main problem with using this as a test case, is because heterogeneous condensation is speculated to play a role because the onset of condensation occurs with a small supercooling, ($\Delta T \approx 3°$). Also these experiments were some of the first results, based on the prototype wind tunnel. Two more experiments from Düker [25](European Transonic Wind tunnel ETW) and Wegener [101] (NASA Langley 0.3m) are for a nozzle with nitrogen condensation. Here the problem is, the expansion of nitrogen goes below the triple point, thus it is likely the condensate is a solid particle. It is of interest to study this type of condensation but for the ONERA M6 wing the focus will be on operating above the triple point. The experiment of Dotson [24] is based on the CAST-10 airfoil at the NASA Langley 0.3m cryogenic wind tunnel, the conditions are above the triple point and since the ONERA M6 will be studied an airfoil is an ideal test case compared to a nozzle. It is not to say that this test case is problem free, but the problems can be worked around.

Figure 4.15 shows the geometry and grid used for the CAST-10 airfoil. The transonic airfoil is unsymmetric with a 12.18% thickness and 0.152m chord.

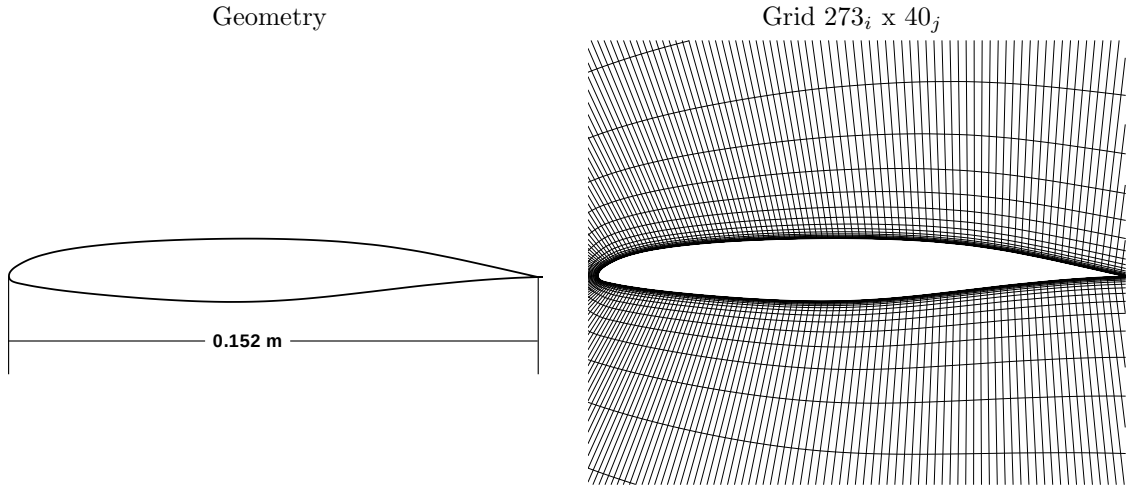

Figure 4.15.: CAST-10 geometry and grid around the airfoil, the trailing edge is similar to the RAE2822 airfoil, see fig.4.37 right.

Table 4.1.: Total and free stream conditions for the CAST-10 airfoil simulation.

Total	Freestream	Miscellaneous
$T_{01}^{\dagger} = 99$ K	T_{∞}= 91.29 K	$c^{\dagger}$=0.152 m
$p_{01}^{\dagger} = 5.066$ bar	p_{∞}= 3.81 bar	$\alpha_{exp.} = 6.^{\circ}$ $\alpha_{corr.} = 4.75^{\circ}$
$s_0 = 0.706$	$M_{\infty}^{\dagger}$= 0.65	$Re_{c,\infty} = 43.79$ million
	$s_{\infty} = 0.968$	

† specified by experiment [24]

Table 4.1 lists the conditions from the experiment and the values used in the simulation.The first problem encountered was trying to match the adiabatic experimental data. The problem is the airfoil is at a 6° angle of attack with a chord of 0.152m inside a 0.3m octagonal test section. It is not known for sure if the 2-D plane channel was installed at this time of the experiment but for sure wall interference correction was later than 1983. Thus the airfoil was modeled under free stream conditions and the angle of attack was slowly changed to match the experimental data. Changing the angle of attack is much better than actually modeling the wind tunnel because 1st, the exact geometry of the tunnel is not known (even if for sure it is the octagonal shape there are still gaps between the plates that are unknown and 2nd it increases computation time because now it is a 3-D problem instead of 2-D. Figure 4.16 compares the adiabatic free stream solution with the experimental data. Pressure data was not given for the complete airfoil because they were only interested in the onset of condensation, which should occur near the leading edge. By adjusting the angle of attack the correct expansion is modeled with a slight deviation before the shock, but with all the uncertainties this is a good match.

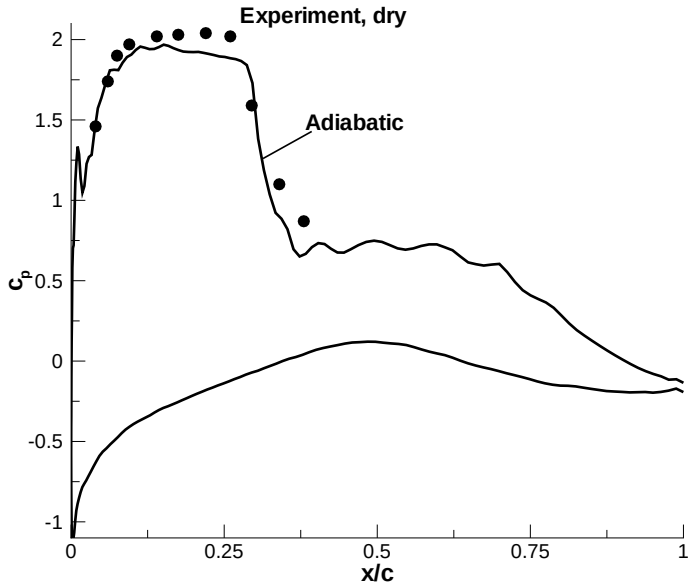

Figure 4.16.: Adiabatic calculated pressure coefficient and experimental data [24],[N_2, T_{01}=99 K, $p_{01} = 5.066$ bar, $M_\infty = 0.65$, c =0.152 m, $Re_{c,\infty,99K} = 43.79$ million, $\alpha = 4.75°$]

Now turning on the condensation model, there was no condensation regardless of the droplet model until the Tolman correction factor was used in the nucleation equation

$$\sigma = \sigma_\infty \frac{1}{1 + \frac{2\delta}{r^*}} \quad . \tag{4.1}$$

The use of the Tolman correction decreases the value of sigma which in turn increases the nucleation rate which forms condensate. The value of δ was regarded as a free parameter that was changed until the right amount of condensation occurred. The value found is 0.5x10^{-10}m. Wegener and Mack [99] regard δ as the constant for a given liquid which is approximately equal to the intermolecular distance of the liquid with a value of 1.x10^{-10}m. Although Dotson [24], also changed the value of δ to 0.25x10^{-10}m.
The results in fig. 4.17 (left) are based on the modified Gyarmathy droplet growth model, with the value of 0.5x10^{-10}m for δ in the Tolman correction term. The y-axis is the difference in the pressure coefficient between the adiabatic and diabatic case

$$\Delta c_p = c_{p,ad.} - c_{p.di.} \quad . \tag{4.2}$$

Changing the total temperature to 101 K produced no condensation in the experiment and fig. 4.17 (right) shows the model without any further changes is able to predict when no condensation should occur. The bottom line in fig. 4.17 (right) is the pressure difference on the pressure side, it should be zero since no condensation occurs there. Two possible reasons for this is that the condensation on the top surface causes an upstream disturbance that

slightly alters the angle of attack or most likely numerical noise because the same situation occurs for the $T_{01} = 101$ K case without condensation.

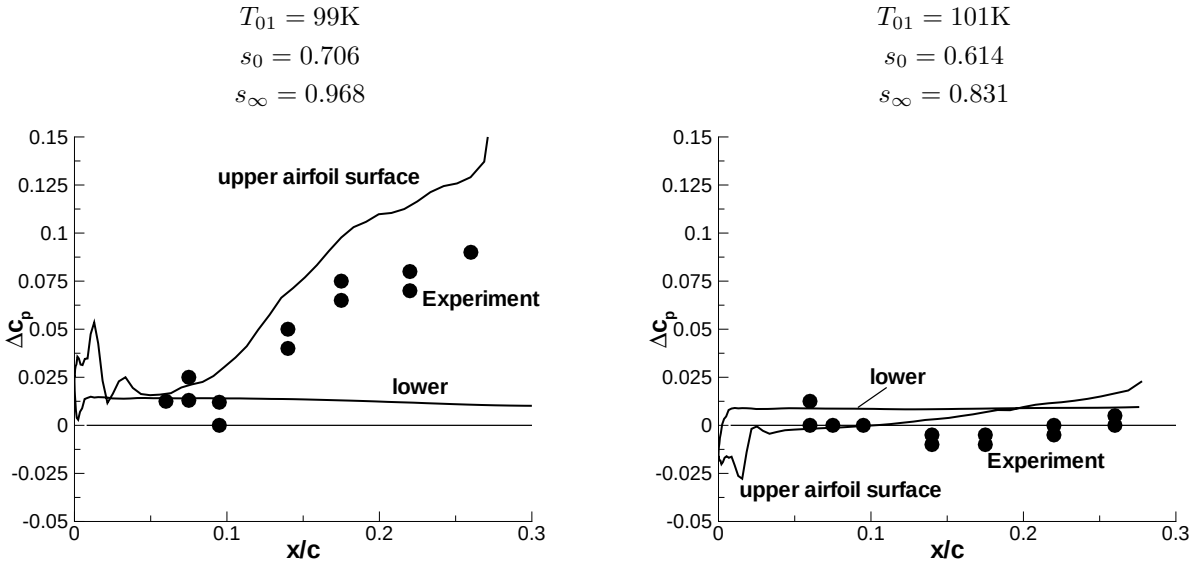

Figure 4.17.: Pressure coefficient difference between adiabatic and diabatic case, [N_2, $p_{01} = 5.066$ bar, $M_\infty = 0.65$, $Re_{c,\infty,99K} = 43.79$ million, $Re_{c,\infty,101K} = 42.47$ million].

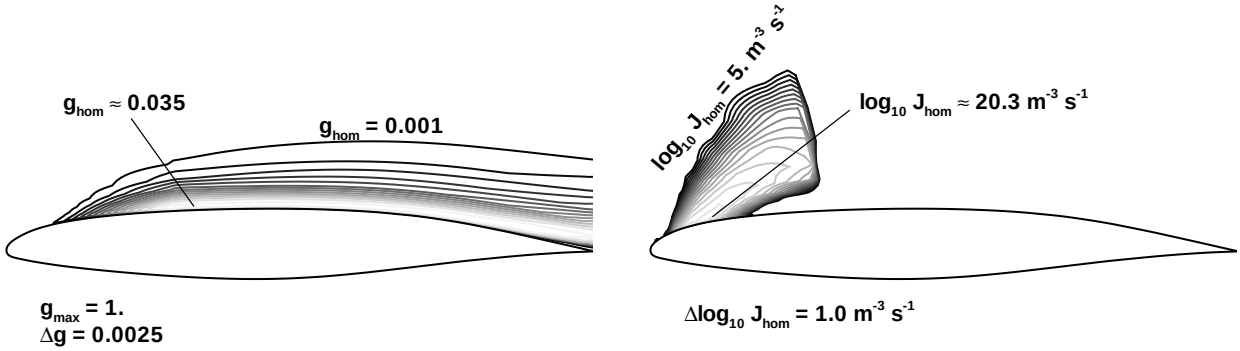

Figure 4.18.: Homogeneous condensate and nucleation rate, [N_2, T_{01}=99 K, $p_{01} = 5.066$ bar, $M_\infty = 0.65$, c =0.152 m, $Re_{c,\infty,99K} = 43.79$ million, $\alpha = 4.75$, $s_0 = 0.706$, $s_\infty = 0.968$].

Figure 4.18 shows the amount of homogeneous condensate formed and where, with the corresponding nucleation rate. Figure 4.19 verifies the use of the modified Gyarmathy droplet growth model because the droplet radius is greater than the mean free path of the gas phase. The values of λ_v , $\overline{r}_{hom}$, and r^* are from the streamline in fig. 4.22 (top left)

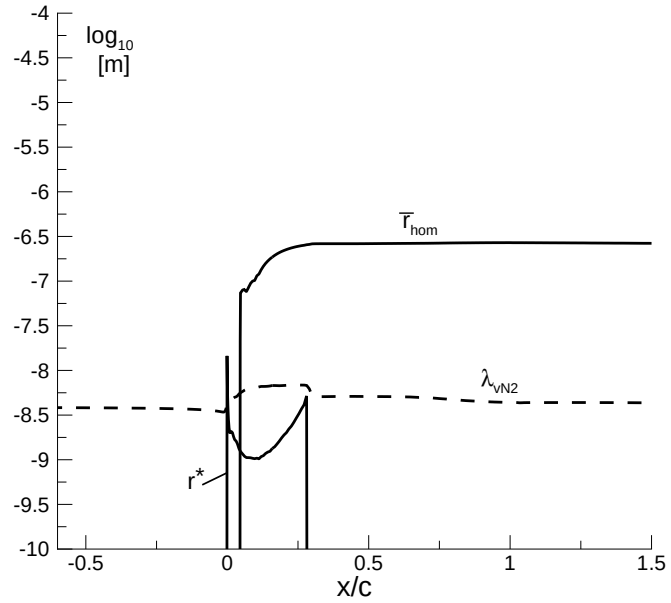

Figure 4.19.: Verification of modified Gyarmathy droplet growth model due to the average homogeneous droplet radius is greater than the mean free path of the N_2.

Another set of experimental results consists of a lower total temperature and pressure, T_{01} = 94, 96 K and p_{01} =3.6 bar. Without changing the model, fig. 4.20 shows good agreement with the experimental data for condensation and again predicts when no condensation should occur.

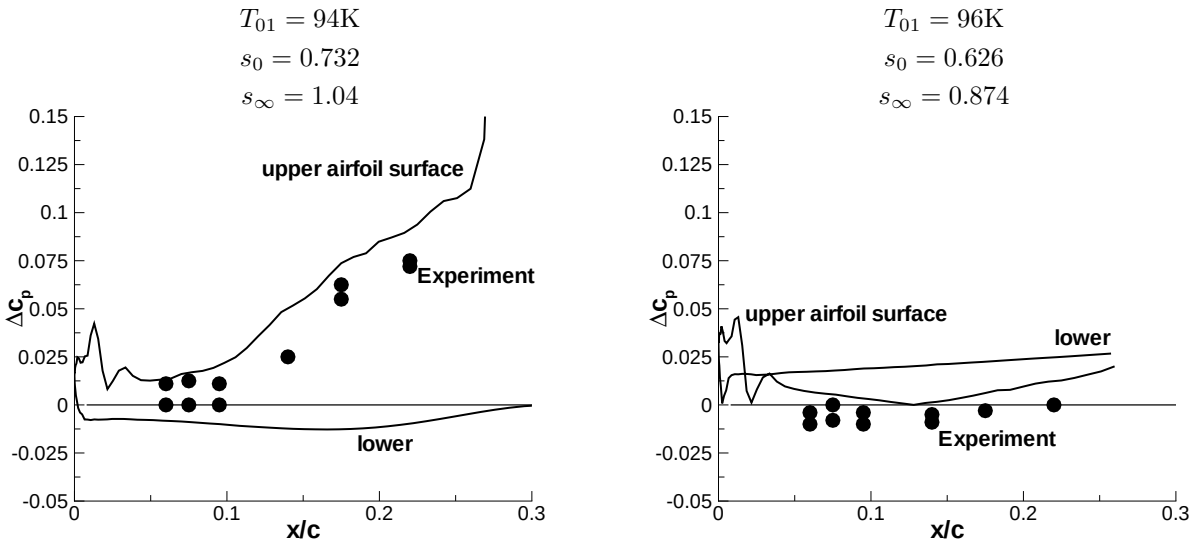

Figure 4.20.: Pressure coefficient difference between adiabatic and diabatic case, [p_{01} = 3.648 bar, $M_\infty = 0.65$, $Re_{c,\infty,94k}$ = 34.14 million, $Re_{c,\infty,96K}$ = 33.05 million].

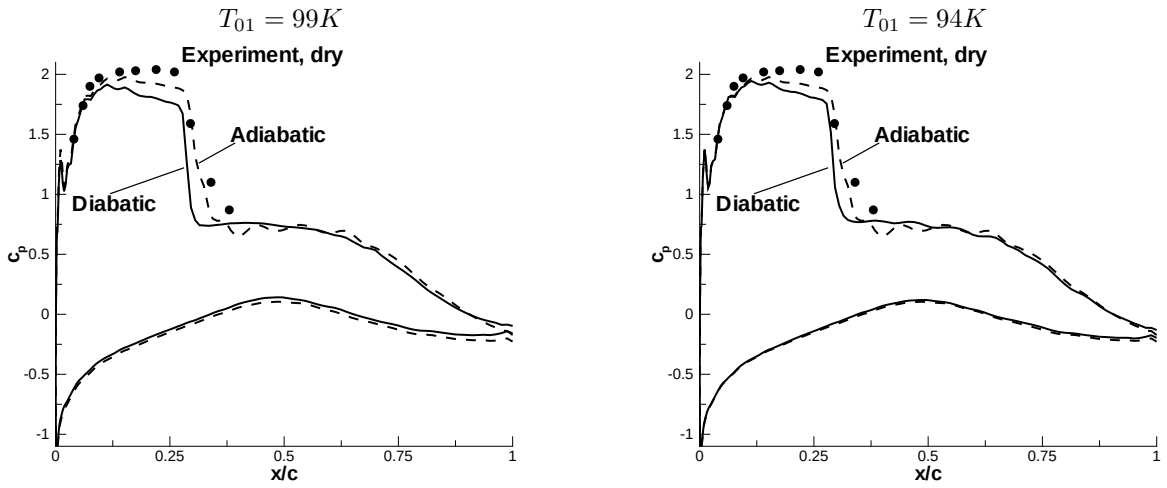

Figure 4.21.: Pressure coefficient for the two cases with homogeneous condensation.

Figure 4.21 gives a complete picture of the difference between the adiabatic and diabatic test case for the temperatures that produce condensation. From the c_p plot it is seen that the effect of condensation is small but present. Also at 99K the pressure decrease is slightly greater than 94K.
To understand better the physics of condensation a Mach, J, and g distribution as well as a p-T diagram based on the values extracted from a streamline near the boundary layer edge fig. 4.22, are constructed. The main difference between the two cases of 99K and 94K is that the total condition for the 94K test case is already super-saturated, by noting that the 01 point is left of the saturation line. Due to the pressure difference of 5.1bar and 3.6bar, the bottom right figure is shifted below the bottom left. An important similarity is that both have approximately the same amount of supercooling, $\Delta T_{99K} = 22.3$K and $\Delta T_{94K} = 22.6$K. For both cases after the shock (point 4), the flow is still super-saturated also with respect to $\overline{r}$, thus the condensate remains and flows into the free stream past the trailing edge (point 5). The amount of supercooling in fig. 4.22 indicates the condensation is purely homogeneous, even if foreign nuclei are present they would not influence the amount of condensation because the time scale of cooling for this chord length is comparable to the time scale of nucleation.

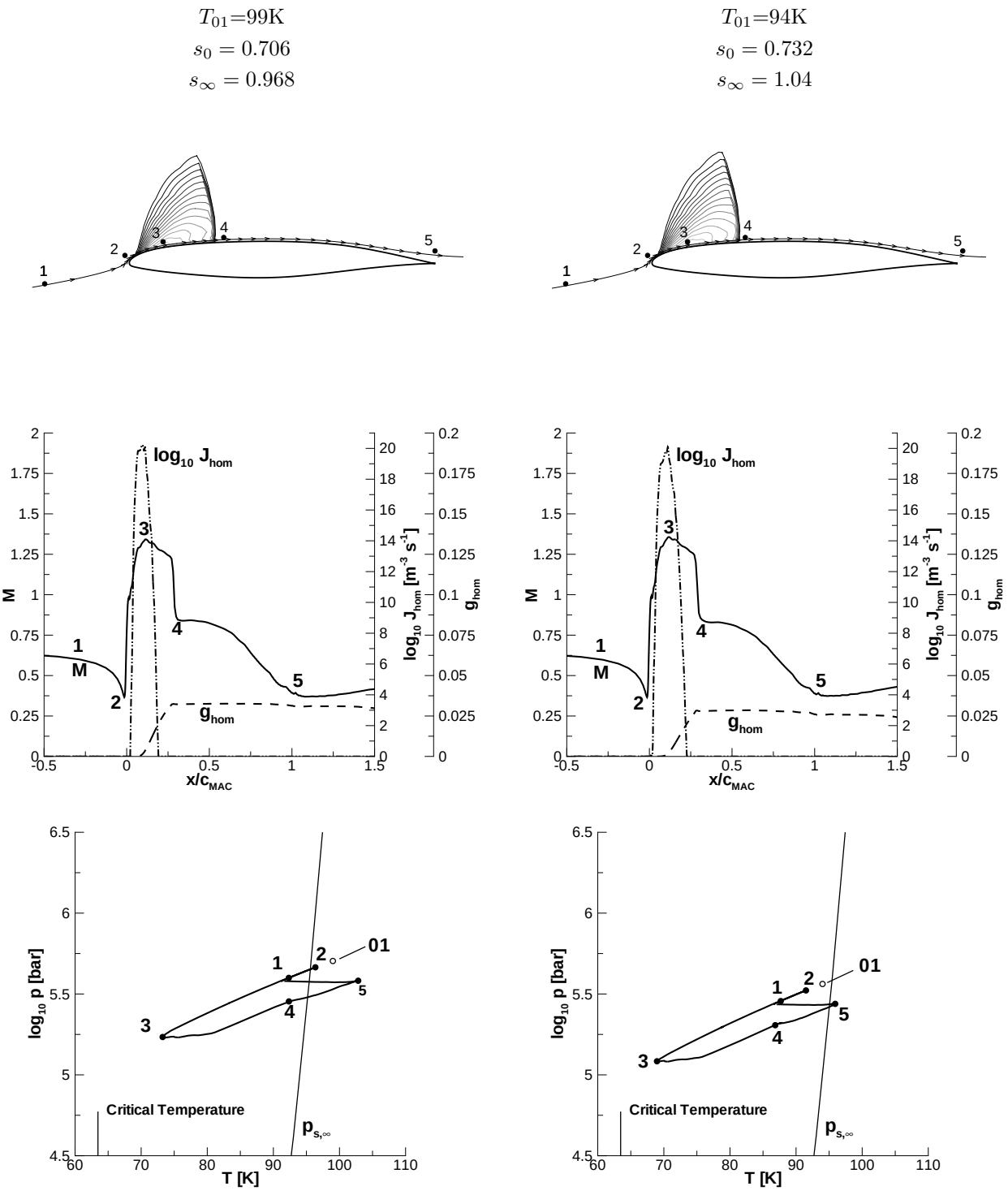

Figure 4.22.: Thermodynamic discussion of the two cases with condensation.

top : Mach contour ($M > 1$) with streamline near boundary layer edge
middle : Mach, J_{hom}, and g_{hom} values extracted from streamline.
bottom : p-T diagram based on streamline.
T_{01}=99K - $p_{01} = 5.066$ bar, $Re_{c,\infty} = 43.79$ million
T_{01}=94K - $p_{01} = 3.648$ bar, $Re_{c,\infty} = 34.14$ million

To understand why a 2° change in the total conditions did not produce condensation the same thermodynamic plot as fig. 4.22 is used. Figures 4.23 and 4.24 (right) shows a distinct difference between the 99-101K and 94-96K test cases. One difference being at the Wilson point in the p-T diagram the higher temperature decompresses nearly along the expansion line. Also note 2° increase is at a constant pressure. The main reason for no condensation is "not" found in the p-T diagram but rather in examining the nucleation rates, (figs. 4.23 and 4.24 (left), here for the higher temperatures nucleation is present but not high enough to produce a sufficient high concentration of critical clusters for the formation of droplets.

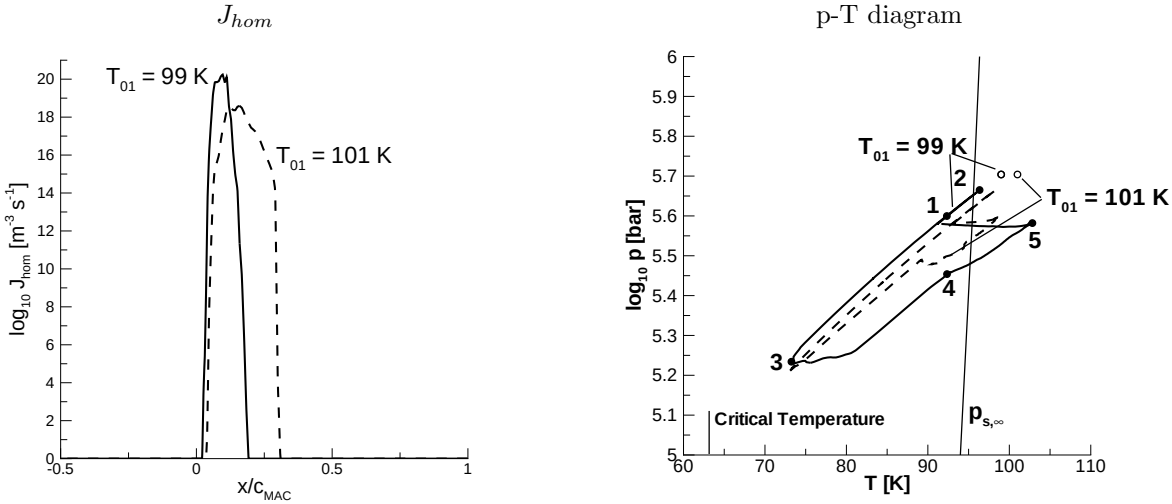

Figure 4.23.: J_{hom} distribution and p-T diagram comparison between two different total conditions, [$p_{01} = 5.066$ bar, $M_\infty = 0.65$, $Re_{c,\infty,99K} = 43.79$ million, $Re_{c,\infty,101K} = 42.47$ million].

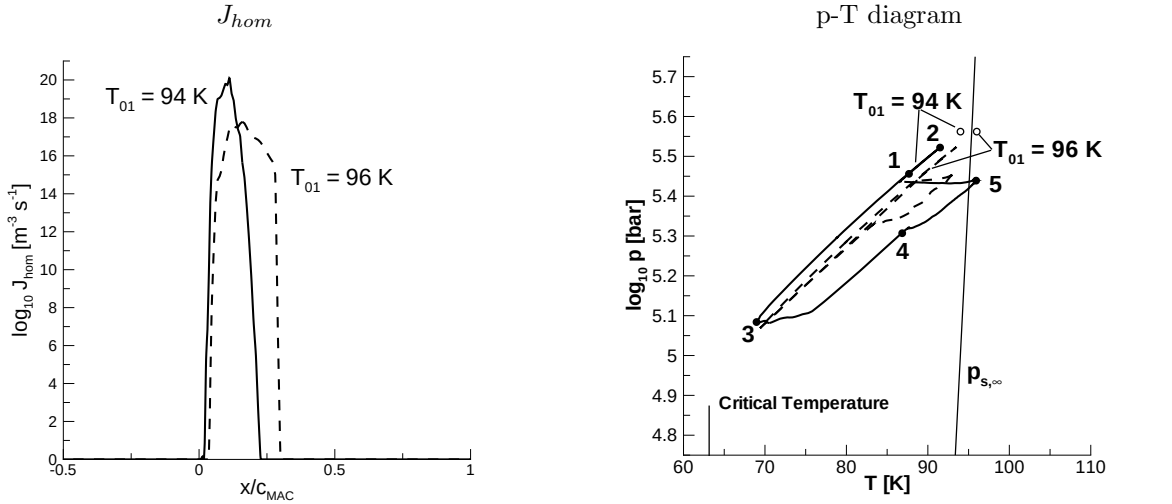

Figure 4.24.: J_{hom} distribution and P-T diagram comparison between two different total conditions, [$p_{01} = 3.648$ bar, $M_\infty = 0.65$, $Re_{c,\infty,94k} = 34.14$ million, $Re_{c,\infty,96K} = 33.05$ million].

A comparison is now made between the current model and a previous modeling technique, see subsec. 4.2.2 for details of the model differences.

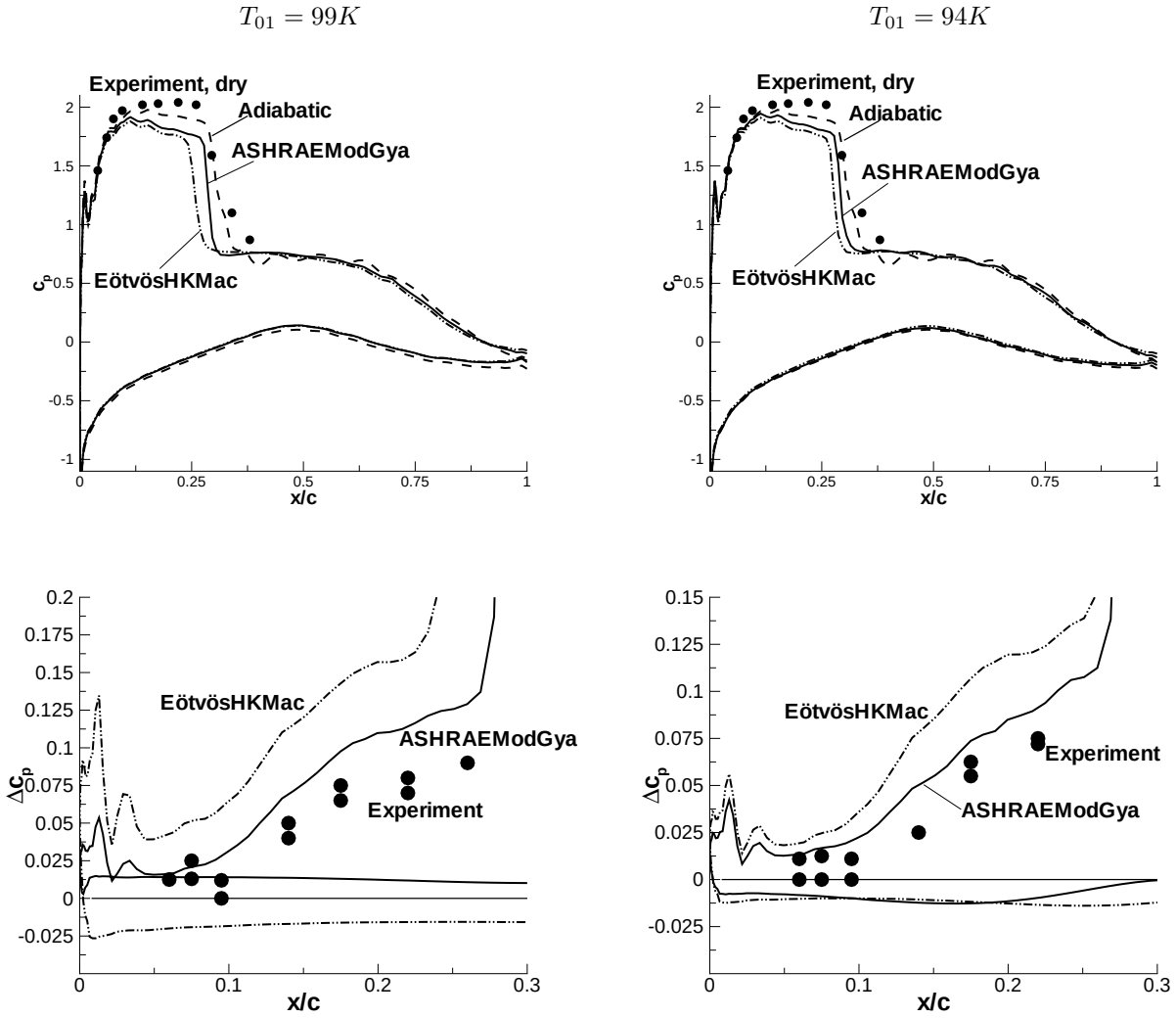

Figure 4.25.: Pressure coefficient/difference for the two cases with homogeneous condensation.
T_{01}=99K - $p_{01} = 5.066$ bar, $s_0 = 0.706$, $Re_{c,\infty} = 43.79$ million
T_{01}=94K - $p_{01} = 3.648$ bar, $s_0 = 0.732$, $Re_{c,\infty} = 34.14$ million

The main conclusion from fig. 4.25 is that the EötvösHKMac models tend to overestimate the effect of condensation by producing more condensate, which increases the pressure in the c_p plots.

4.2.2. BAII–Nozzle - Euler

The BAII is a circular arc nozzle that has been used as a test case for moist air [59] and nitrogen [87]. The name comes from Barschdorff which follows BAI that was used for steam calculations and by Zierep for humid air. The geometry and grid are shown in fig. 4.26. A comparison is now made between the model calibrated with the experiment using the CAST-10 airfoil (sec. 4.2.1) and the modeling technique used by Schnerr and Dohrmann given in [87]. Important note: The numerical code for Nitrogen is not used from Schnerr and Dohrmann, thus a replica is generated from the models specified in the paper. The main difference between the two models is the use of the σ relationship and the droplet growth law. In the CAST-10 validation the ASHRAE σ (fig. 2.1) function is used with the modified Gyarmathy model eq. 2.92, whereas from [87] the Eötvös σ (fig. 2.1) function is used and depending on the mean radius size a macroscopic law (eq. 2.90) or the Hertz-Knudsen formula is applied. For notation to distinguish between the results the following is used

- ASHRAEModGya: σ function ASHRAE, $\frac{dr}{dt}$ modified Gyaramthy model
- EötvösHKMac σ function Eötvös, $\frac{dr}{dt}$ Hertz-Knudsen $\overline{r} < \lambda$ or macroscopic law $\overline{r} > \lambda$

One last very important difference between the two modeling techniques is the value of the Tolman constant δ in eq. 4.1. For the ASHRAEModGya model the value is set at $0.5\text{x}10^{-10}$ and for EötvösHKMac it is $1.\text{x}10^{-10}$.

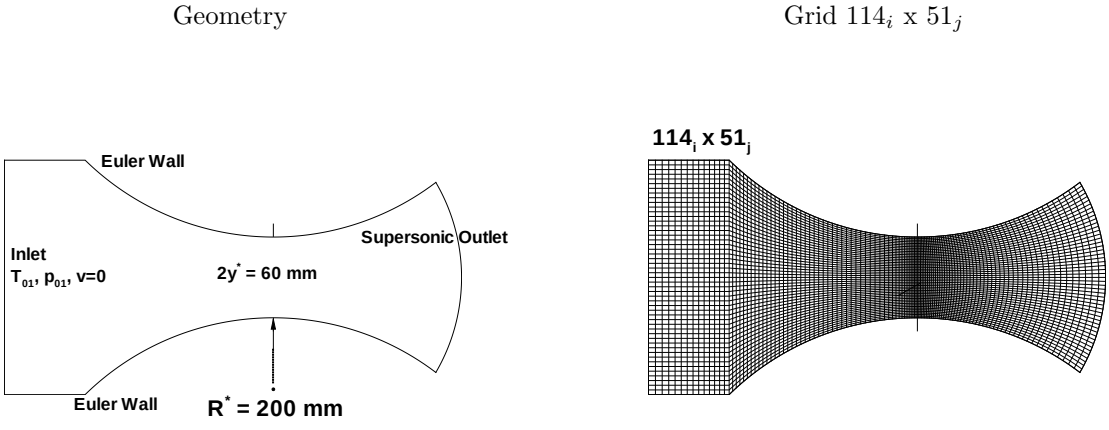

Figure 4.26.: BAII geometry and grid.

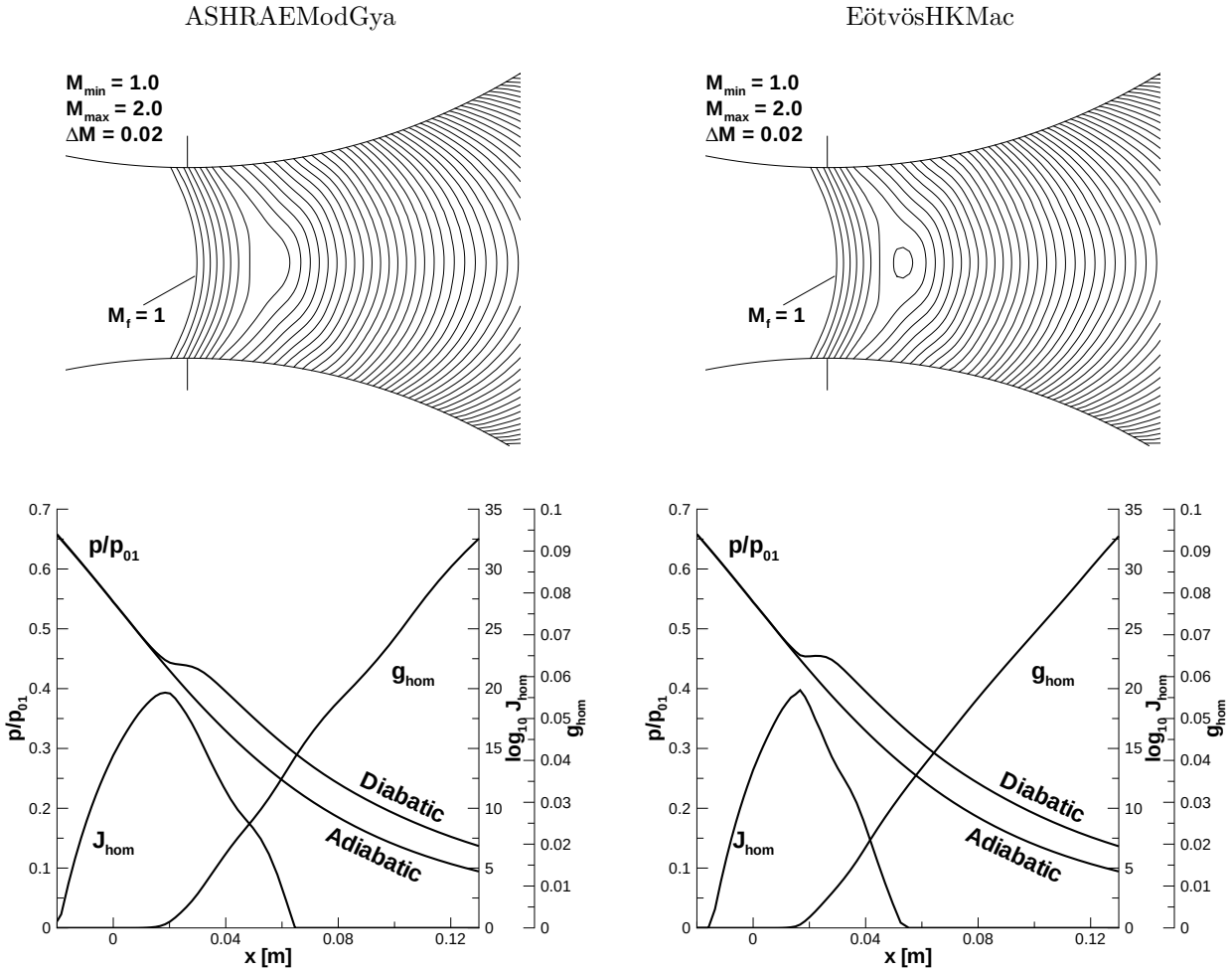

Figure 4.27.: Mach contour and p, J_{hom}, g_{hom} center line distribution,[T_{01}=91.1 K, p_{01}=3.604 bar, ϕ_0=91.7%].

Figure 4.27 compares the Mach contour and centerline pressure, nucleation, and wetness fraction for the BAII nozzle. The differences are minor with nucleation starting earlier for the ASHRAEModGya and having a larger envelope, but the peak values are nearly identical. It is interesting that the peak values are the same because of the different σ functions used but what is important is that the Tolman correction term is changed, which compensates this difference thus producing somewhat equal nucleation rates. At the peak value of nucleation (J_{hom}) the growth of g_{hom} starts and also the deviation from the adiabatic expansion. The location for the start of g_{hom} is identical but the deviation for the EötvösHKMac models is slightly greater at the beginning which is noted by the plateau region in pressure. In regards to the original results from Schnerr and Dohrmann [87] the compression is slightly stronger than what has been calculated (fig.4.27, right) using the current code with the same condensation models as [87]. Also the nucleation zone is larger in fig.4.27 (right) compared with [87]. In [87] the nucleation rate ends at about 0.3m, which means the growth of g_{hom} is not as strong, which relates to the weaker compression

found in the current simulation. Although the peak value of the nucleation rate and the location of condensate formation are the same as [87]. The most likely reason for a slight difference is because the FVS scheme is not the same, Schnerr and Dohrmann [87] use a 2nd order upwind flux-extrapolation technique without any additive dissipation compared to the 3rd order upwind AUSMD scheme used in the current code, also something as small as approximating the metrics could make this small difference.

4.2.3. S1–Nozzle - Euler

The geometry (fig. 4.1) and grid (fig. 4.2, right) for the S1 nozzle used in the N_2 calculation is the same as in subsec. 4.1.1.

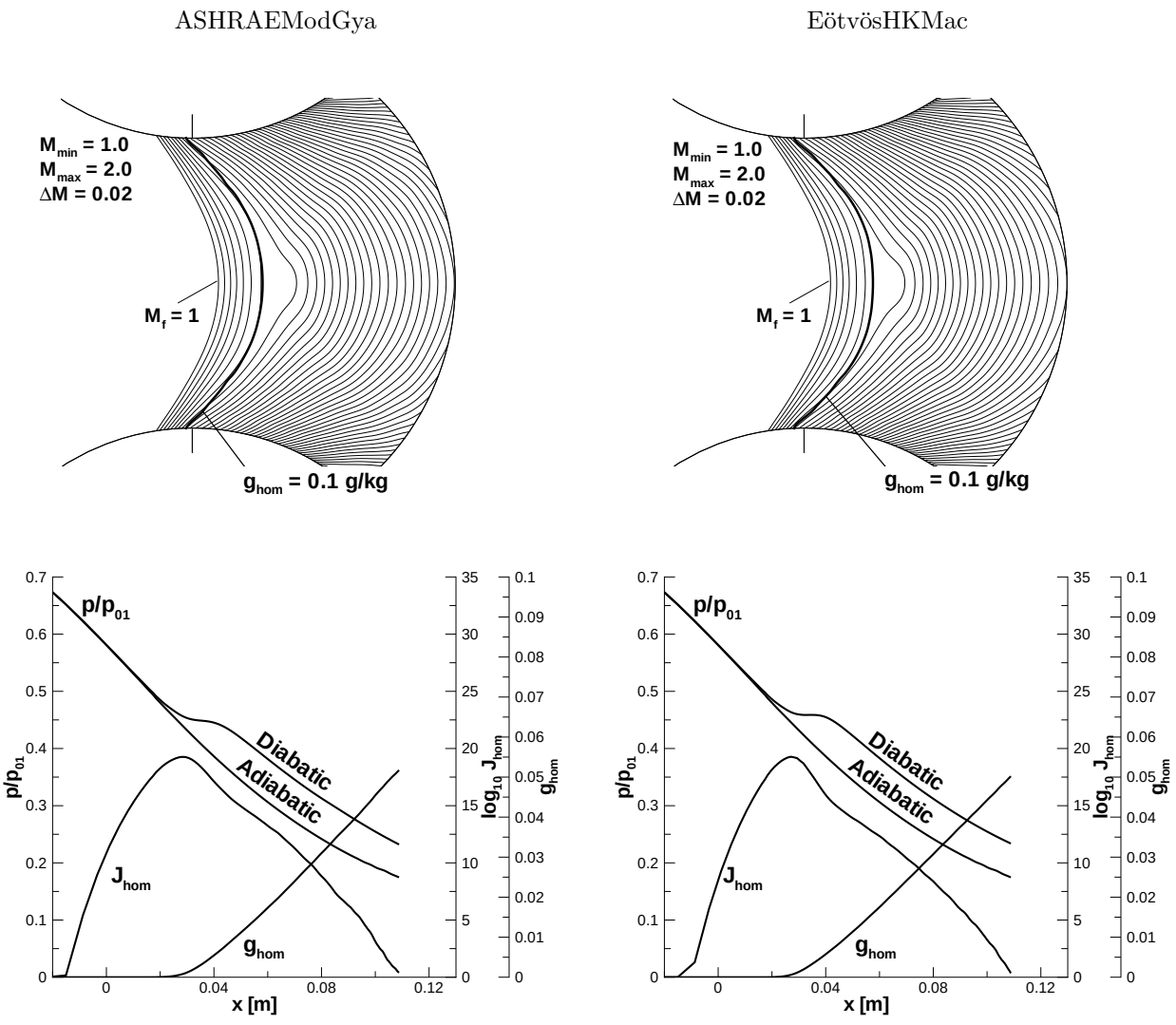

Figure 4.28.: Mach contour and p, J_{hom}, g_{hom} center line distribution,[T_{01}=91.1 K, p_{01}=3.604 bar, ϕ_0=91.7%].

For the S1 nozzle (fig. 4.28) both models predict very similar results compared with the BAII nozzle in the previous subsection. The peak values of nucleation are the same with slightly different distributions. Like in the BAII nozzle the EötvösHKMac models shows a greater plateau in the diabatic pressure distribution which results from slightly higher condensate formation.
Comparing the original calculation from Schnerr and Dohrmann [87] for the S1 nozzle, the Mach contour plot of the EötvösHKMac model in the current code agrees with [87], except for a slightly larger compression then the current code. This difference is similar to the BAII nozzle comparison. The reason for the difference follows the same line of reasoning presented at the end of subsection 4.2.2.

4.3. Turbulence Modelling

The notation Sarkar(k-ω) in the following figures, represents the Wilcox k-ω model presented in chap. 2 sec. 3 with the Sarkar correction given in [103].

4.3.1. Sajben Transonic Diffusor

The Sajben transonic diffusor experiment was conducted by McDonnell Douglas Corporation in the 80's to study the effects of unsteady, transonic flow in diffusors. The experiments also provided data for steady results involving weak and strong shocks, where the strong shock produces a separation bubble which is valuable for turbulence modeling testing.

4.3.1.1. Geometry and Grid

The 2-D plane converging-diverging duct has a maximum divergence angle of 8.8°. The experimental data include time mean wall static pressure on the top and bottom wall, velocity profiles at 4 locations in the diffusor, and the separation and reattachment locations were obtained with oil flow techniques.
Figure 4.29 displays the geometry and grid used for the transonic diffusor. At first glance it would appear to be only half of a nozzle but the bottom wall is a Navier-Stokes wall, not a symmetry boundary. The grid seems coarse but adequate results can be obtained and thus it is a very good test case to get quick results when checking new ideas for a turbulence model, also using this grid, results can be compared with other CFD codes. The geometry, grid, and electronic form of the experimental data was obtained from [91] but for a hard copy reference one could look into [10] or [76].

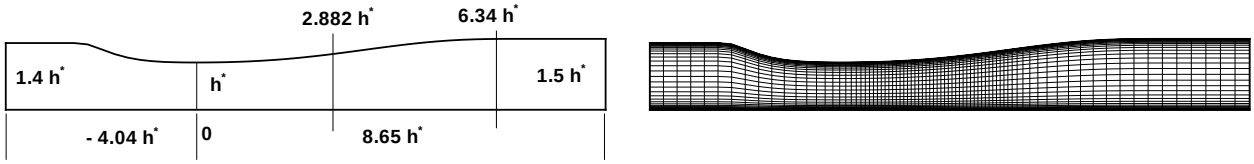

Figure 4.29.: Sajben transonic diffusor geometry and grid (81_ix51_j), h^*=.044m, plane 2-D.

4.3.1.2. Weak Shock **pre-shock** $M \approx 1.21$

The first test case is a weak shock, which is obtained by specifying a back pressure of 1.11 bars, $R = 0.862$, where R is the ratio of exit plane static pressure to reservoir total pressure. To get acquainted with the flow, fig. 4.30 is plot of the Mach and numerical schlieren contour. The maximum Mach number is around 1.22, which occurs downstream of the throat and the numerical Schlieren relieves a normal shock.

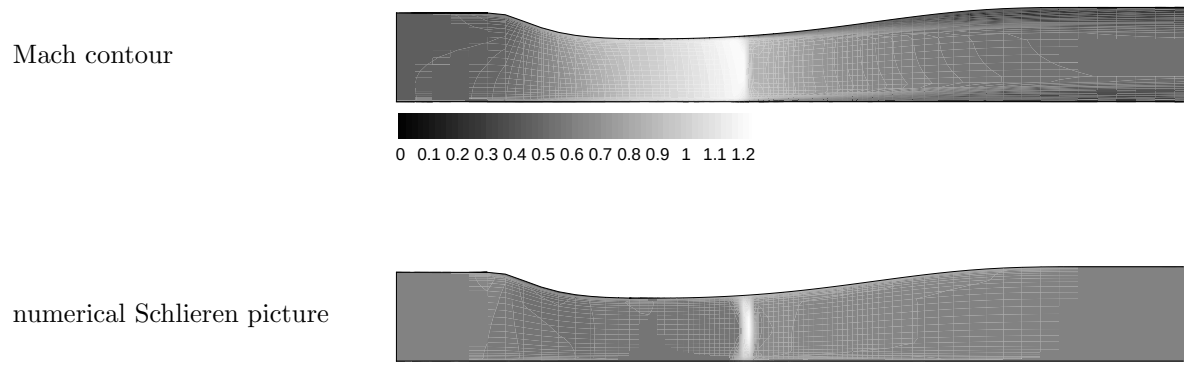

Figure 4.30.: Mach contour and numerical Schlieren picture using the k-ω turbulence model, [T_{01}=277.8 K, p_{01} =1.35 bar, p_{out}=1.11 bar, $Re_{h^*,01}$ = 1.42 million].

Figures 4.31 and 4.32 are the pressure distribution on the top and bottom wall and two velocity profiles at x/h^* of 2.822 and 6.34. All turbulence models are able to capture the correct pressure distribution. The peak in Figs. 4.31 and 4.34 (right) is due to the coarse grid and skewed grid cell near the wall which can be seen in fig.4.29 (right). The rise in pressure at the beginning is because the inlet boundary condition requires the total energy to be constant and since the wall boundary condition requires the velocity to be zero, the pressure ratio must approach 1, where as in the experiment it is not a numerical inlet/wall boundary condition. The velocity profiles for both locations are underestimated by all turbulence models by about 4%, similar velocity profiles were obtained with the WIND and NPARC code [106].

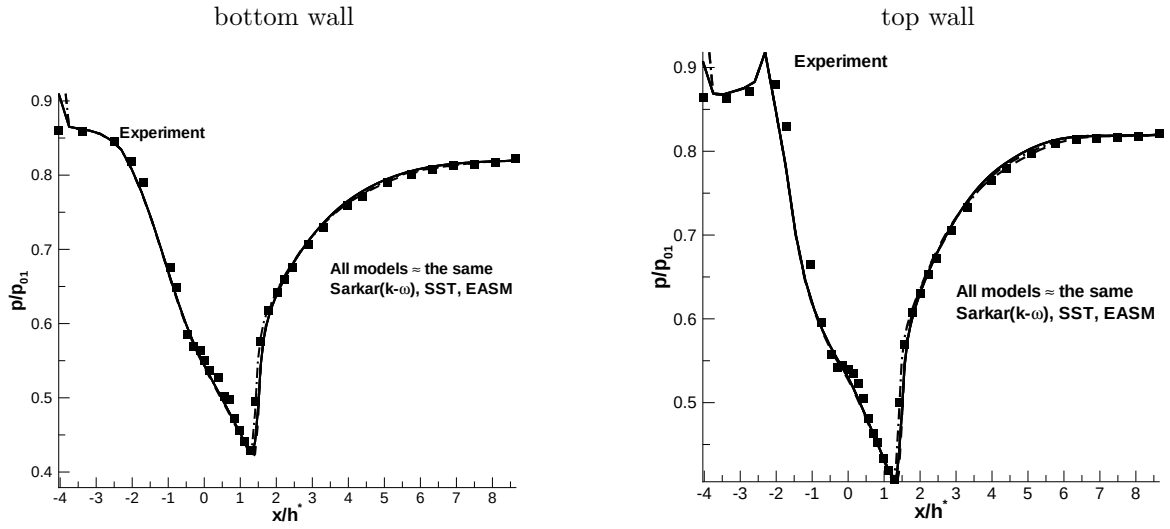

Figure 4.31.: Comparison of pressure distribution between experiment and turbulent models, [T_{01}=277.8 K, p_{01} =1.35 bar, p_{out}=1.11 bar, $Re_{h^*,01}$ = 1.42 million].

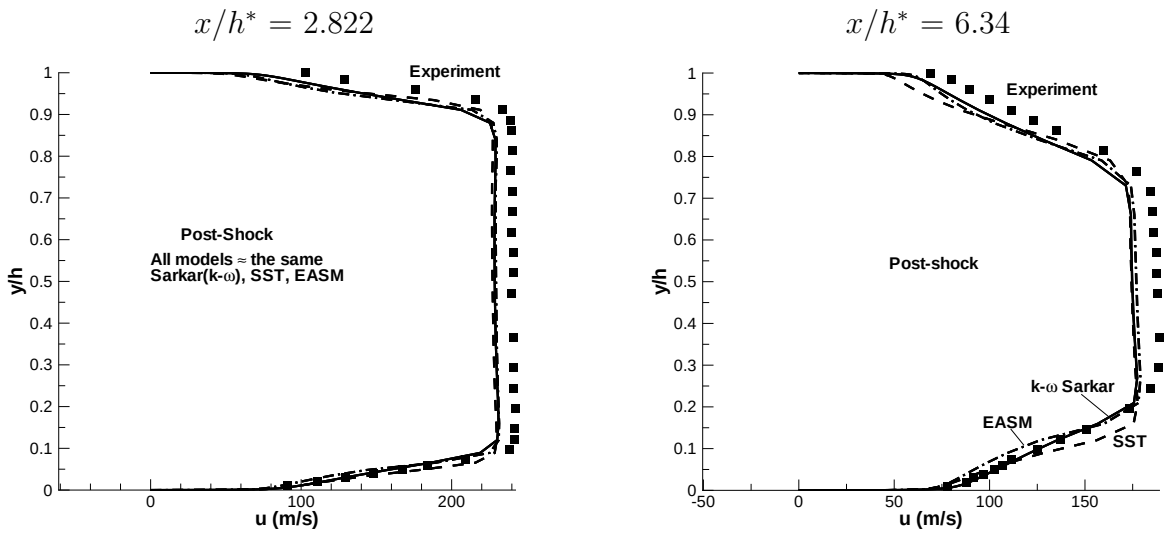

Figure 4.32.: Comparison of two velocity profiles in the nozzle between experiment and turbulent models, [T_{01}=277.8 K, p_{01} =1.35 bar, p_{out}=0.97 bar, $Re_{h^*,01}$ = 1.42 million].

4.3.1.3. Strong Shock pre-shock $M \approx 1.35$

The strong shock case is obtained by lowering the back pressure to 0.97 bar, R=0.722, which moves the shock further downstream of the throat which increases the supersonic region, thus pre-shock Mach number. Figure 4.33 is again a plot of the Mach and numerical Schlieren contour. Here a larger pre-shock Mach number of 1.38 and a large separation

region on the top wall occurs. The numerical Schlieren also reveals a change in the shock structure which looks to be the beginning of a lambda shock.

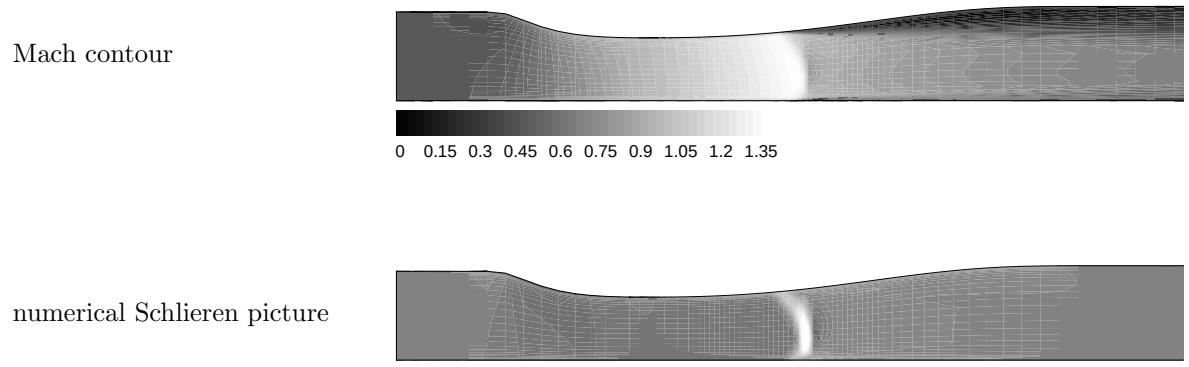

Figure 4.33.: Mach contour and numerical Schlieren picture using the k-ω turbulence model, [T_{01}=277.8 K, p_{01} =1.35 bar, p_{out}=0.97 bar, $Re_{h^*,01}$ = 1.42 million].

In fig. 4.34 left, all turbulence models have a slight curvature to the pressure distribution on the top wall after the shock in the separation region. From pressure it seems all models have the same results but looking at the separation and reattachment location and velocity profiles, different trends are present.

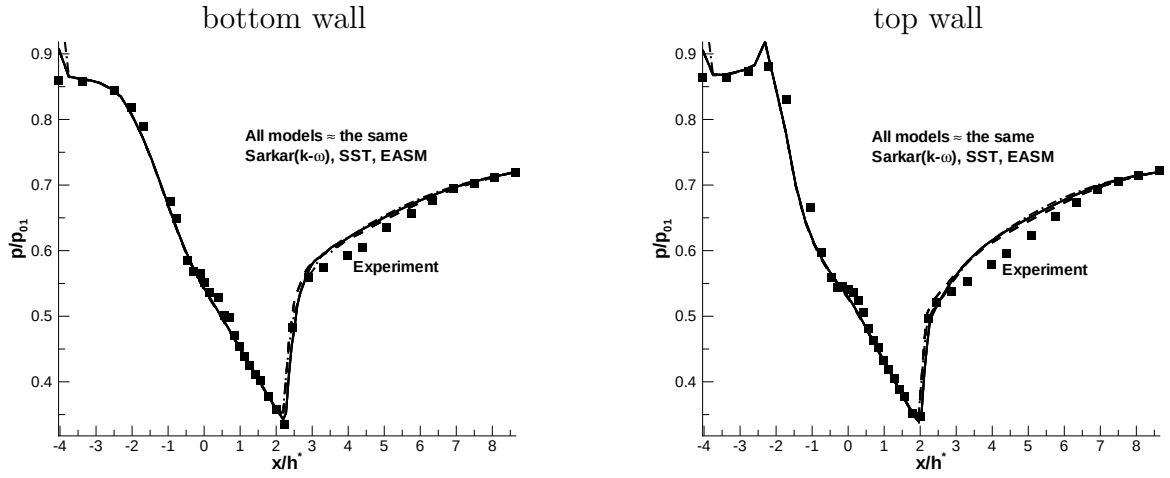

Figure 4.34.: Comparison of pressure distribution between experiment and turbulent models, [T_{01}=277.8 K, p_{01} =1.35 bar, p_{out}=0.97 bar, $Re_{h^*,01}$ = 1.42 million].

Figure 4.35 left is just after the separation point, here on the top wall all models have the negative velocity, with the EASM having a slight advantage with reproducing the core

flow. In fig. 4.35 (right), the flow has reattached but the SST model still has the separation region which can be seen by the negative velocity. All turbulence models have a slightly different slope for the velocity distribution from the top wall to the core flow, fig 4.35(right).

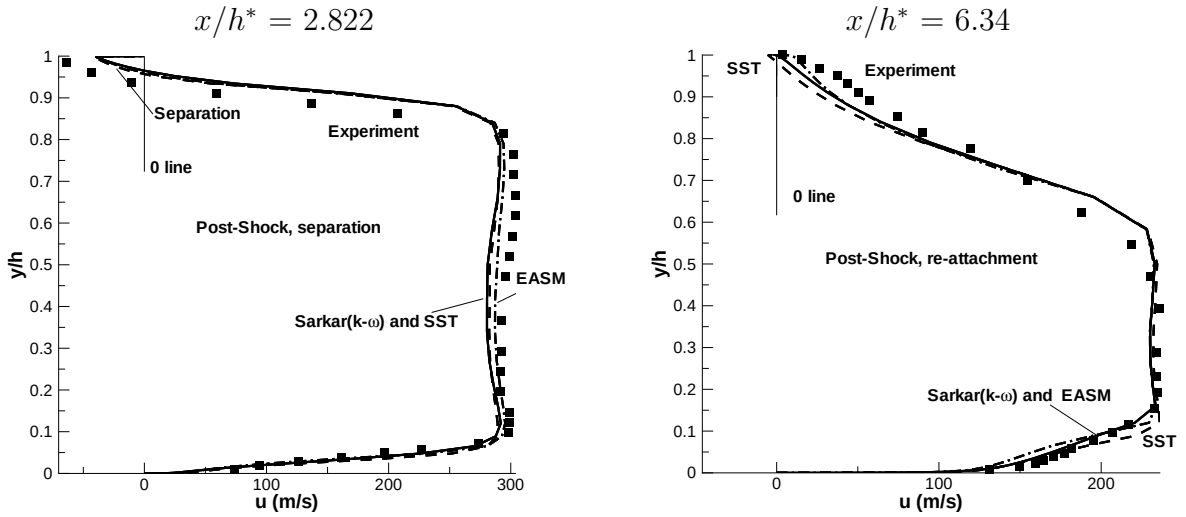

Figure 4.35.: Comparison of two velocity profiles in the nozzle between experiment and turbulent models, [T_{01}=277.8 K, p_{01} =1.35 bar, p_{out}=,0.97 bar, $Re_{h^*,01}$ = 1.42 million].

Table 4.2 compares the different turbulent models used in this code and with the Wind model of NPARC. For both codes using the SST model, the separation point is predicted but reattachment is too far down stream. For the $k-\omega$ model without the Sarkar correction the separation zone is greatly reduced and with the Sarkar correction there is much improvement in increasing the separation region. The EASM gives the best overall results for predicting separation and reattachment points. An interesting point is that for the Wind model it uses a 2nd order ROE scheme for the convective fluxes, with a minmod limiter for extrapolation and still the same results are obtained for the SST model using AUSMD with Van Albada limiter.

Table 4.2.: Separation and reattachment locations for various compressible correction correlations and turbulence models.

	Separation	Reattachment	Length	%Length Error
$k-\omega$ Sarkar	2.13	6.44	4.31	7.31
$k-\omega$ Wilcox	2.41	5.50	3.09	-23.21
$k-\omega$ Zeman	2.31	5.63	3.31	-17.57
$k-\omega$ No Correction	2.41	5.35	2.94	-26.90
SST	2.07	6.78	4.70	+16.92
$EASM(k-\omega)$	2.10	5.95	3.85	-4.23
$k-\epsilon$[106]	2.20	5.96	3.76	-6.17
SST[106]	2.00	6.79	4.79	+19.15
Experiment	2.00	6.0	4.02	

4.3.2. RAE 2822 Airfoil

The RAE2822 airfoil is a classical test case for external flow, it is based on the experiments of [18]. The experiments involved changing free stream Mach number and angle of attack. The two test cases involve a normal shock with and without boundary layer separation. The data includes surface pressure measurements and mean flow boundary layer and wake profiles. The tests were conducted in the RAE 8ft. by 6ft. continuous, closed circuit transonic wind tunnel.

4.3.2.1. Geometry and Grid

The RAE2822 supercritical airfoil has a nose radius of 0.00827 chord and a maximum thickness of 0.121 chord, the experimental chord length is 0.61m.

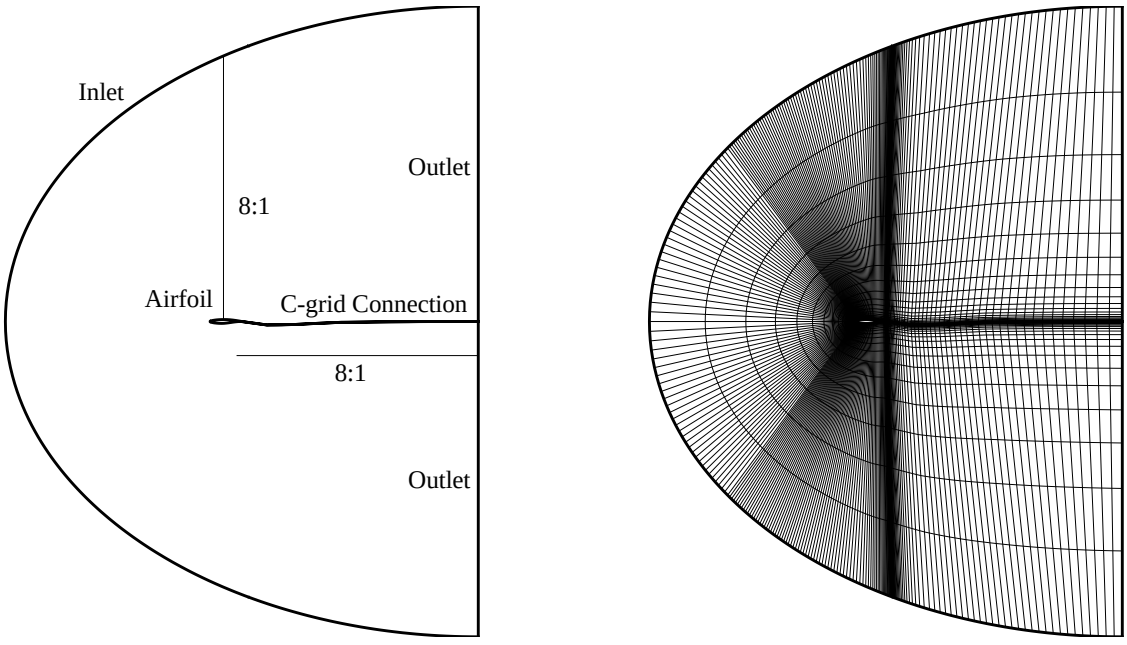

Figure 4.36.: RAE2822 geometry and grid (349_ix40_j),plane 2-D, 8:1 ratio based on chord length.

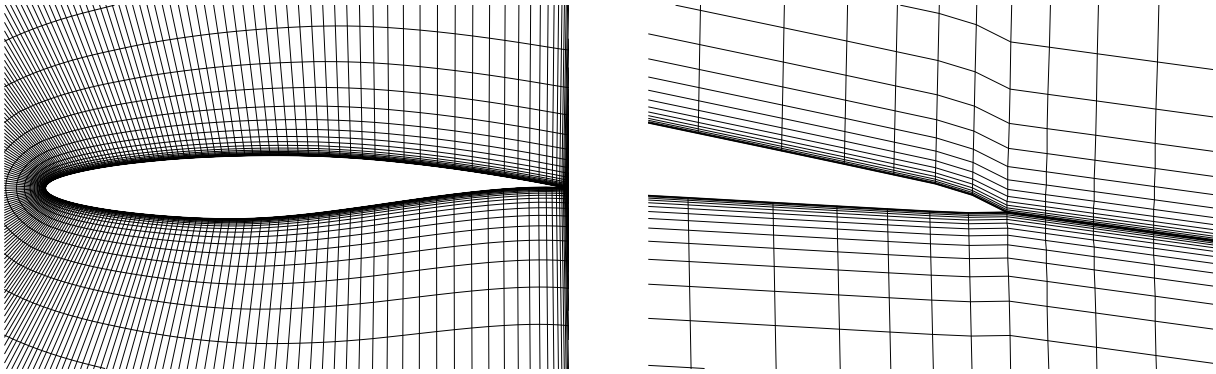

Figure 4.37.: Closeup of RAE2822 airfoil grid

4.3.2.2. Case 6 pre-shock $M \approx 1.23$

Table 4.3 lists the conditions for case 6, note the change in α from experiment to corrected, which is a correction for calculating free stream conditions. The correction is an empirical relationship based on the lift, momentum coefficient, channel height, and constants derived for this particular wind tunnel. The chord length was changed to 0.1m only for convenance. A stagnation temperature of 293K was chosen based on the information that the tunnel operates in the range of 290 K to 323 K, with the Mach number and specified Reynolds number the total and static pressure were calculated.

Table 4.3.: Parameters used to describe case 6 of Cook [18].

Total	Freestream	Other
T_{01} = 293 K	T_∞= 265.1 K	c=0.1 m
p_{01} = 4.95 bar	p_∞= 3.49 bar	$\alpha^\dagger_{exp.}$ = 3.92 $\alpha_{corr.}$ = 2.31
	$M^\dagger_\infty$= 0.725	$Re^\dagger_{c,\infty}$ = 6.5 million

† specified by experiment

Figure 4.38 compares the experimental pressure coefficient with three different turbulence models. The shock for the EASM model is a little further to the right and for the SST there is a small decrease in the pressure near the trailing edge. For this case the Wilcox $k-\omega$ with Sarkar compressible correction gives the best pressure distribution.

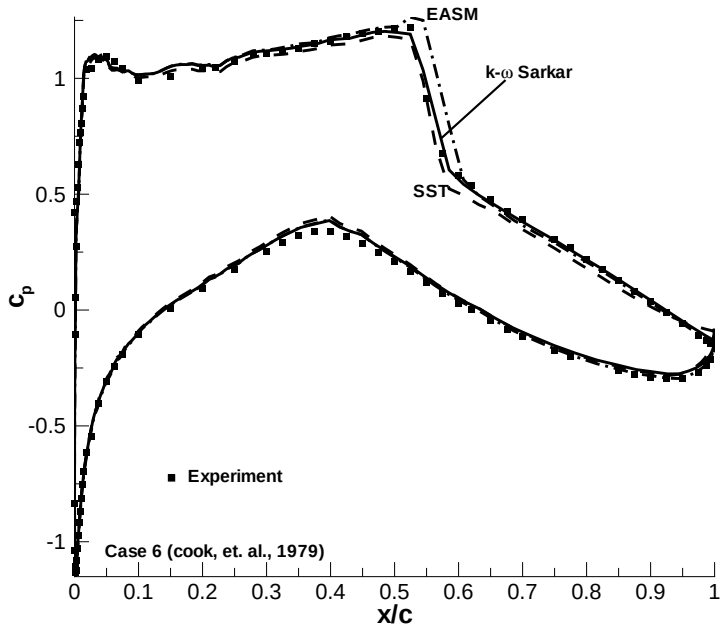

Figure 4.38.: Comparison of turbulence models with experiment using the pressure coefficient.

Examining the total velocity profiles in the boundary layer before and after the shock, fig. 4.39, the SST model slightly over predicts the velocity but for velocity profiles all three models are adequate. The kinks in the velocity profiles indicate mesh points, which shows the number of grid points in the boundary layer are at a minimum. Knowing the minimum in the 2D case will help create an optimum grid for the 3D case in regards to quality versus computational time.

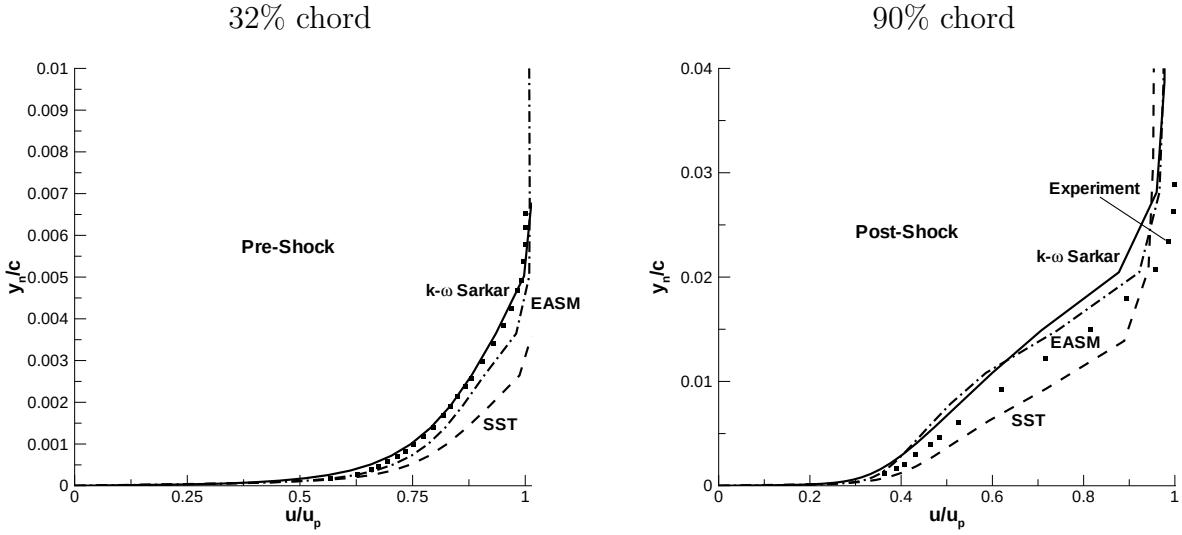

Figure 4.39.: Comparison of turbulence models with experiment using the total velocity on the suction side of the airfoil.

4.3.2.3. Case 10 pre-shock $M \approx 1.30$

Table 4.4.: Parameters used to describe case 10 of Cook [18]

Total	Freestream	Other
T_{01} = 293 K	T_∞= 263.4 K	c=0.1 m
p_{01} = 4.63 bar	p_∞= 3.19 bar	$\alpha^\dagger_{exp.} = 3.19$ $\alpha_{corr.} = 2.8$
	$M^\dagger_\infty$= 0.75	$Re^\dagger_{c,\infty}$ = 6.2 million

† specified by experiment

Case 10 is a stronger pre-shock Mach number compared to case 6, which introduces a small separation region. Figure 4.40 shows a plot of c_p around the airfoil, the SST model predicts a much larger separation region, where EASM($k-\omega$) gets the correct shock position but the recovery pressure is too high. The k-ω model with Sarkar correction does a slightly better job with the recovery pressure but the shock position is wrong. Surprisingly all three models predict a slightly different pressure side distribution. Figure 4.41 examines the total velocity before and after the shock, The SST does the best job due to the large separation region and the $k-\omega$ model with Sarkar correction and EASM($k-\omega$) are over predicting velocity because the recovery is too soon. Here is a fine example of the difficulties in modeling, good pressure distribution but wrong velocity, good velocity but wrong pressure, but since the interest is more in pressure drag than viscous drag and lift for this airfoil, the one with the best pressure distribution is needed.

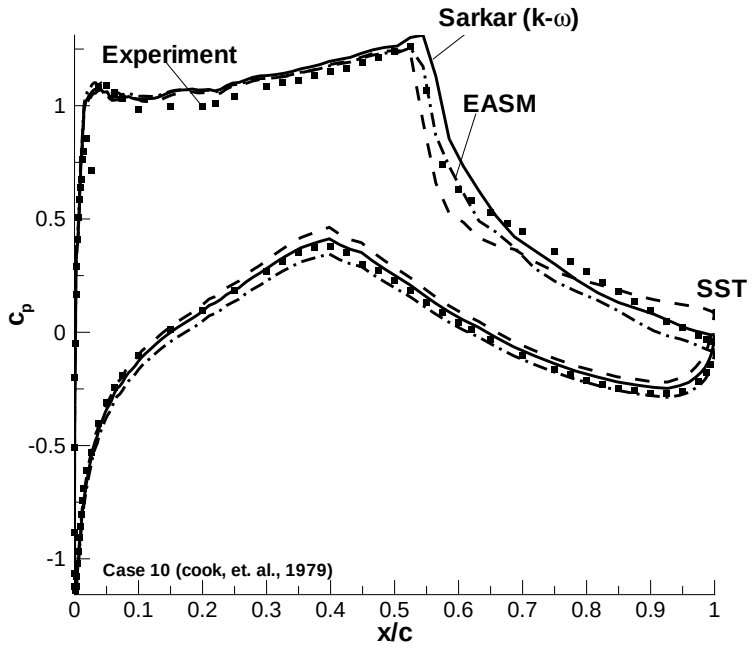

Figure 4.40.: Comparison of turbulence models with experiment using the pressure coefficient.

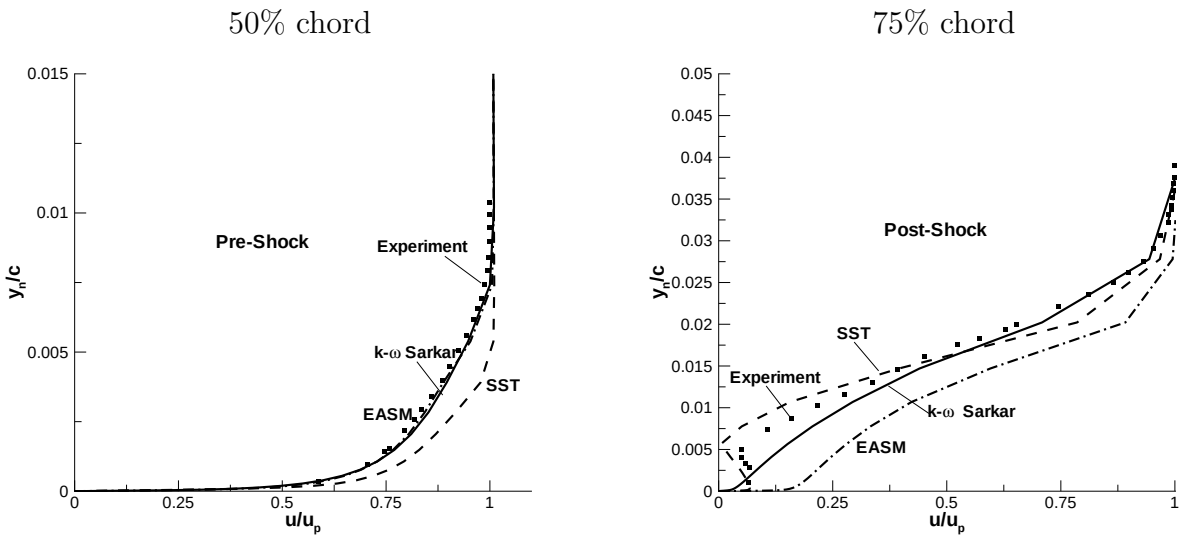

Figure 4.41.: Comparison of turbulence models with experiment using the total velocity on the suction side of the airfoil.

4.3.3. 3-D Skewed Bump

The final adiabatic turbulent test case is based on the experiment of [68] where the goal of the experiment was to study the effect of shock-wave/boundary-layer interaction and provide a test case for CFD and turbulence models. The experimental data was sent by electronic form, which included wall pressure distributions on the top and bottom wall and a 3 component LDV system giving mean velocity, velocity fluctuations, and turbulent shear stresses at ten longitudinal planes ($z = 10$ to 110 mm). From the journal paper [68], computed skin-friction line patterns were scanned to compare flow topology with computed results. The journal paper also had surface flow visualization by oil-flow technique but the quality from the paper was too low to make a comparisons with.

4.3.3.1. Geometry and Grid

Figure 4.42 displays the geometry and grid used for this simulation. The geometry is a skewed bump enclosed in a rectangular channel (120mm x 100mm), the bump creates a 1st throat and then a 2nd throat is used to accelerate the flow to supersonic. The contoured bump is swept 30° from the upstream flow condition which aids in creating 3-D effects. The strong interaction between boundary layer and shock wave is induced by the second throat which can be adjusted to provide the right blockage effect.
The grid dimensions are comparable to simulations performed by Leschziner et. al. [49], 120_ix55_jx60_k. For the top and bottom wall there is approximately 12-14 grid points in the boundary layer when it was not separated, with the first grid point Δy_1 of 5x10^{-6}m

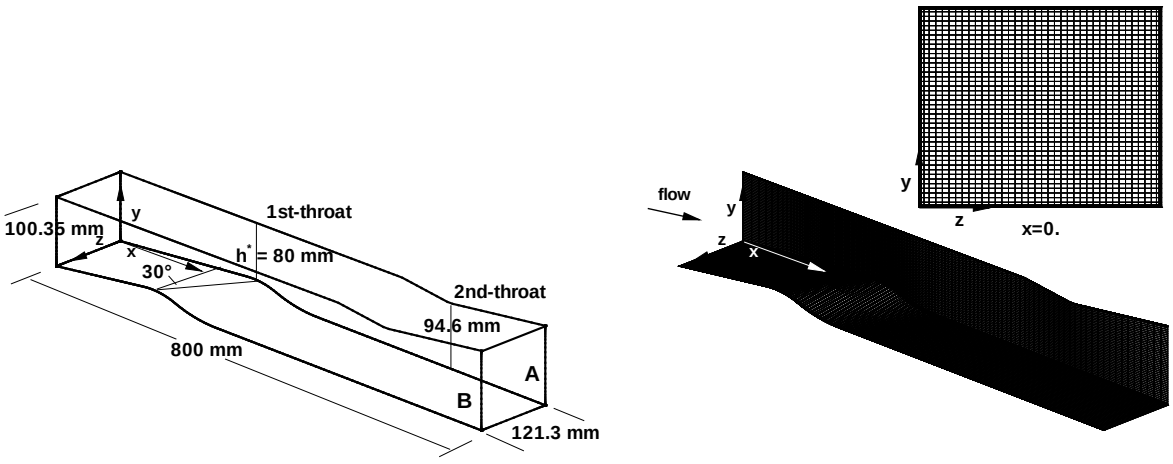

Figure 4.42.: Geometry and grid (114_ix60_jx53_k) sections of the skewed bump.

4.3.3.2. Test Case Results

Table 4.5 list the parameters used for the skewed bump test case. With the given throat height and total conditions a transonic flow problem is established. Before beginning with the main results tab. 4.6 list the average y^+ value for all 4 surfaces and the different turbulence models. The larger y^+ values on the side walls is because the first grid point is 1x10^{-5}m instead of 5x10^{-6}m for the top and bottom wall. The reason for the larger distance is because the flow is less complicated (no separation) on the side walls and the width is about 20mm wider than the height.

Table 4.5.: Parameters used to describe the skewed bump test case [68].

Total	Misc.
T_{01} = 300 K	h^*=0.08 m
p_{01} = 0.92 bar	$Re_{h^*,01}$ = 1.613 million

Table 4.6.: Summary of average y^+ values on all 4 surfaces of the skewed bump channel.

Surface	EASM($k-\omega$)	SST	Sarkar($k-\omega$)	$k-\omega$
Bottom	1.36	1.35	1.37	1.37
Top	1.29	1.28	1.30	1.30
Wall B	2.33	2.32	2.36	2.41
Wall A	2.24	2.27	2.34	2.33

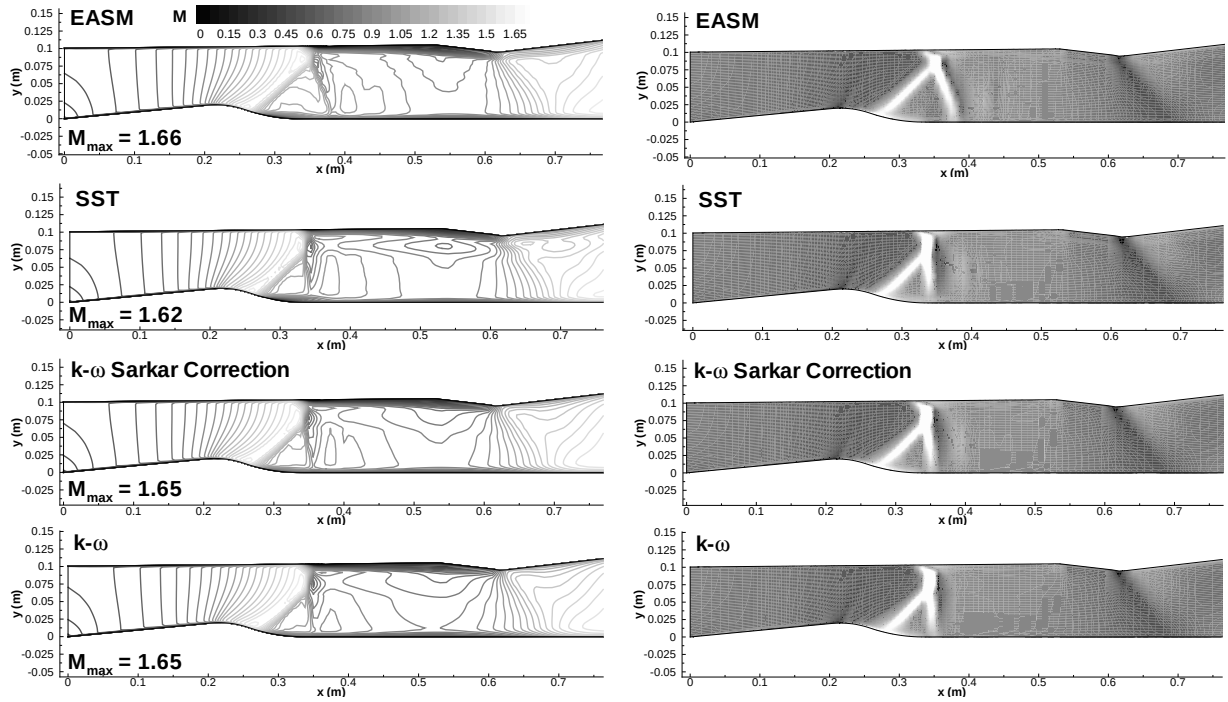

Figure 4.43.: Mid-plane Mach and numerical Schlieren contour.

Figures 4.43 - 4.45 examine the physics of the flow at the mid-span. Near the bottom wall there is an expansion terminated by an oblique shock, then another expansion terminated by the normal leg of the lambda shock, small expansion but due to the second throat a weak compression and then expansion to a supersonic outlet. The top wall pressure experiences a expansion terminated by a normal shock but there is separation as seen by the small plateau in pressure (fig. 4.45 right), then a weak compression terminated by a Prandtl-Meyer expansion to supersonic outlet. The lambda shock is reproduced in all turbulence models and the maximum Mach number is nearly the same. Figure 4.44 shows a closeup and comparison with experiment of the Mach contour in the region just after the bump. The SST model shows a much smaller area of separation on the top wall and the lambda shock for the EASM($k-\omega$) model does not have the normal foot like the experiment.

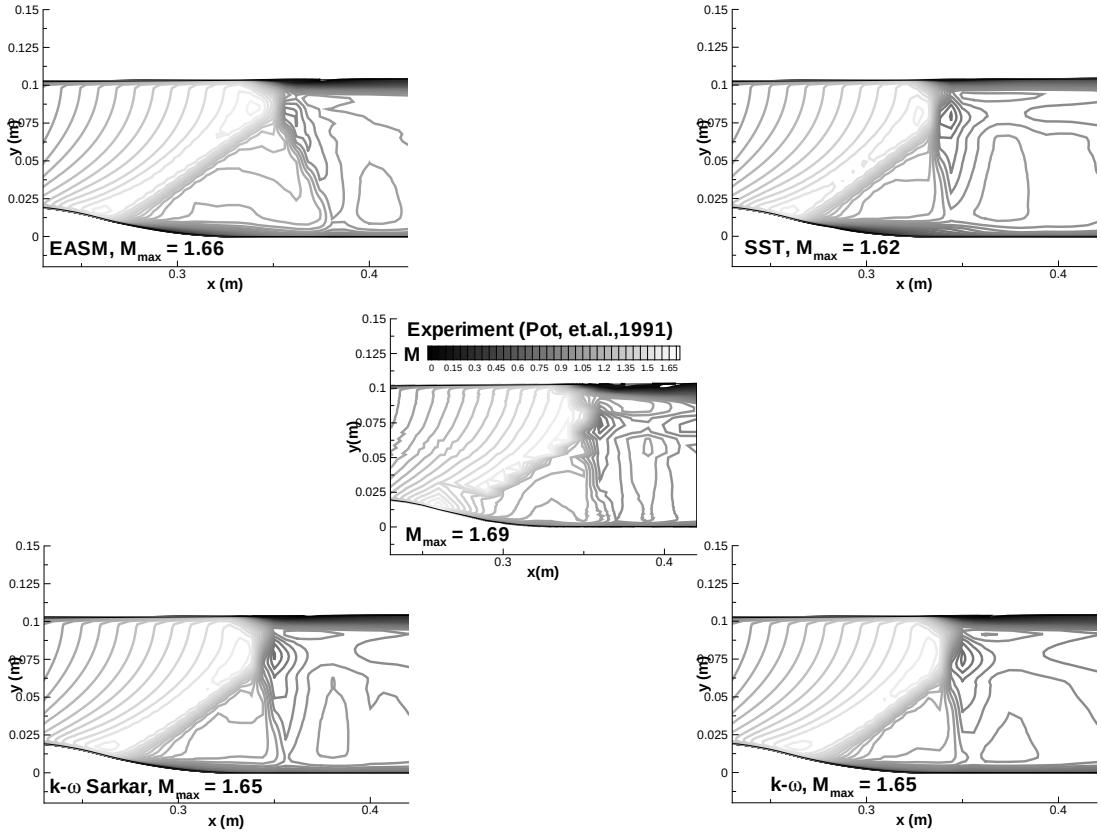

Figure 4.44.: Closeup view of the Mach number distribution and comparison with experiment at the mid-plane, M_{max} is the maximum Mach number reached at the mid-plane.

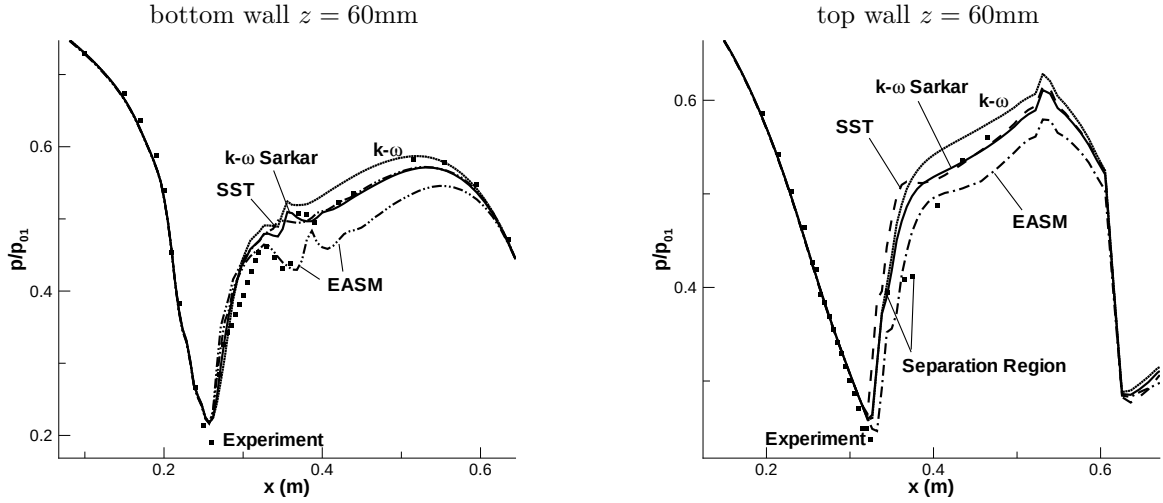

Figure 4.45.: Mid-plane pressure distribution on the top and bottom wall.

On the top wall fig.4.45 (left) only the EASM($k-\omega$) model shows a slight flat region of pressure in the separation zone. In fig.4.45 (right) the EASM($k-\omega$) model is not able to reproduce the correct post-shock recovery pressure but the EASM($k-\omega$) model does predict the second and third expansion line for the bottom wall. The Wilcox $k-\omega$ model with Sarkar correction almost reproduces the two peaks and it does capture the correct recovery pressure.
Figure 4.46 examines the u-component of velocity at the mid-span. The EASM($k-\omega$) model overall matches the data best, especially in the region of the lambda shock but it is over predicting velocity after the shock.

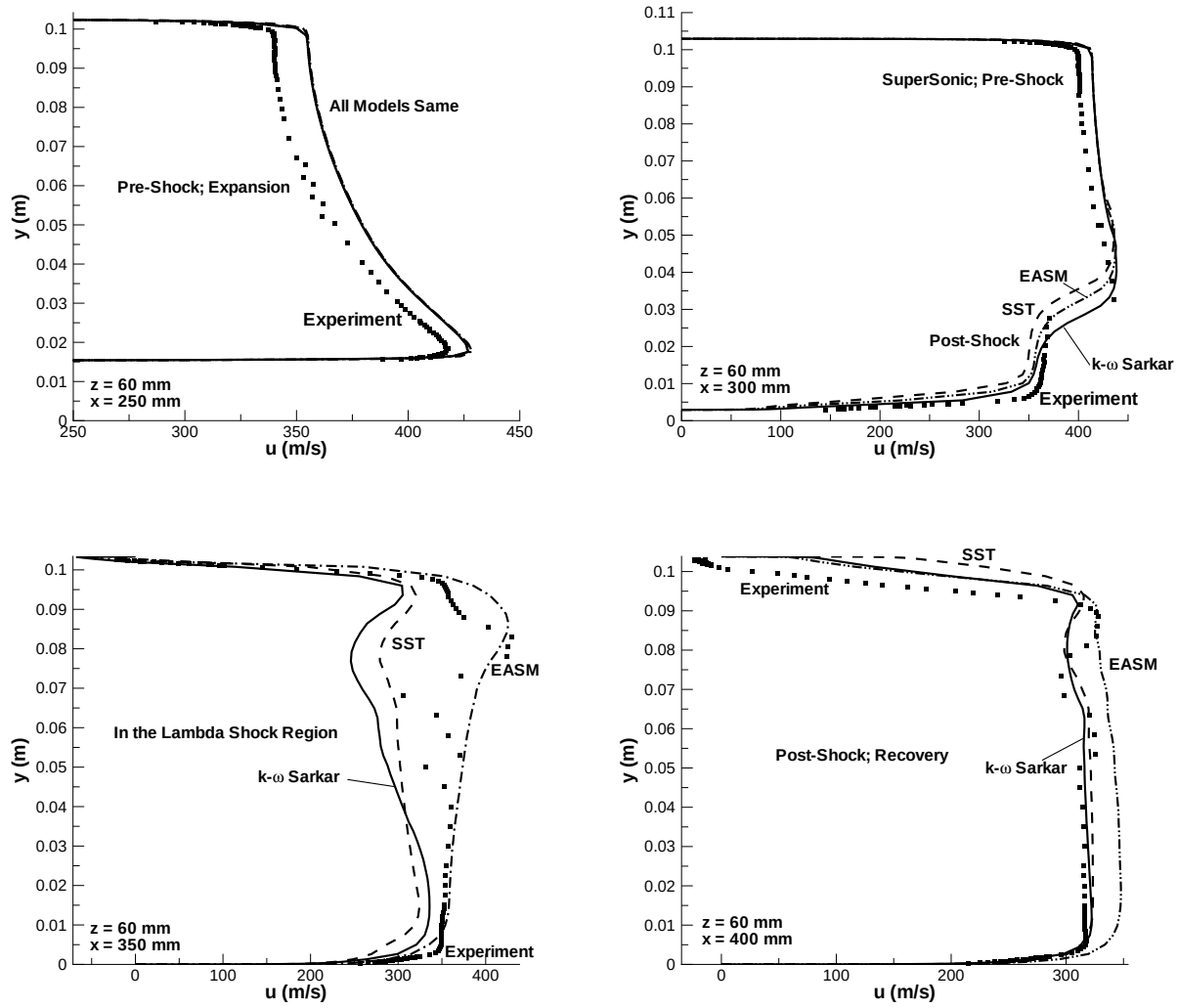

Figure 4.46.: Mid-plane u-component velocity distribution at 4 different stations.

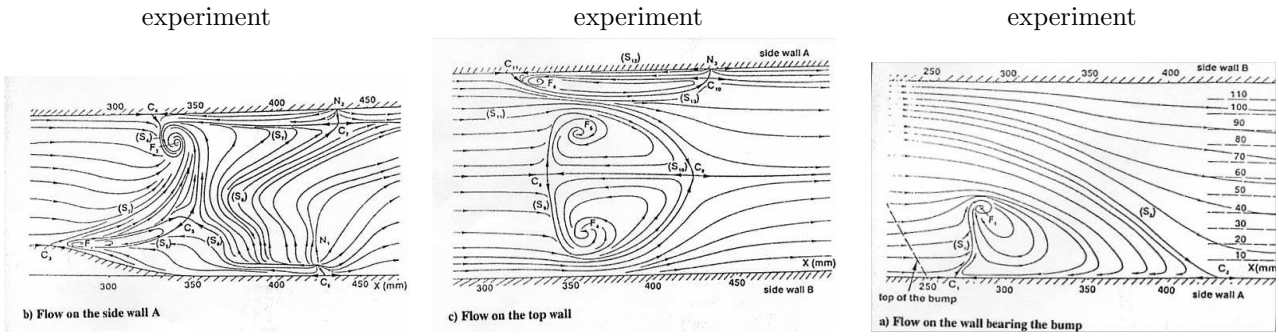

Above: Topological interpretation of the surface flow visualizations [68]

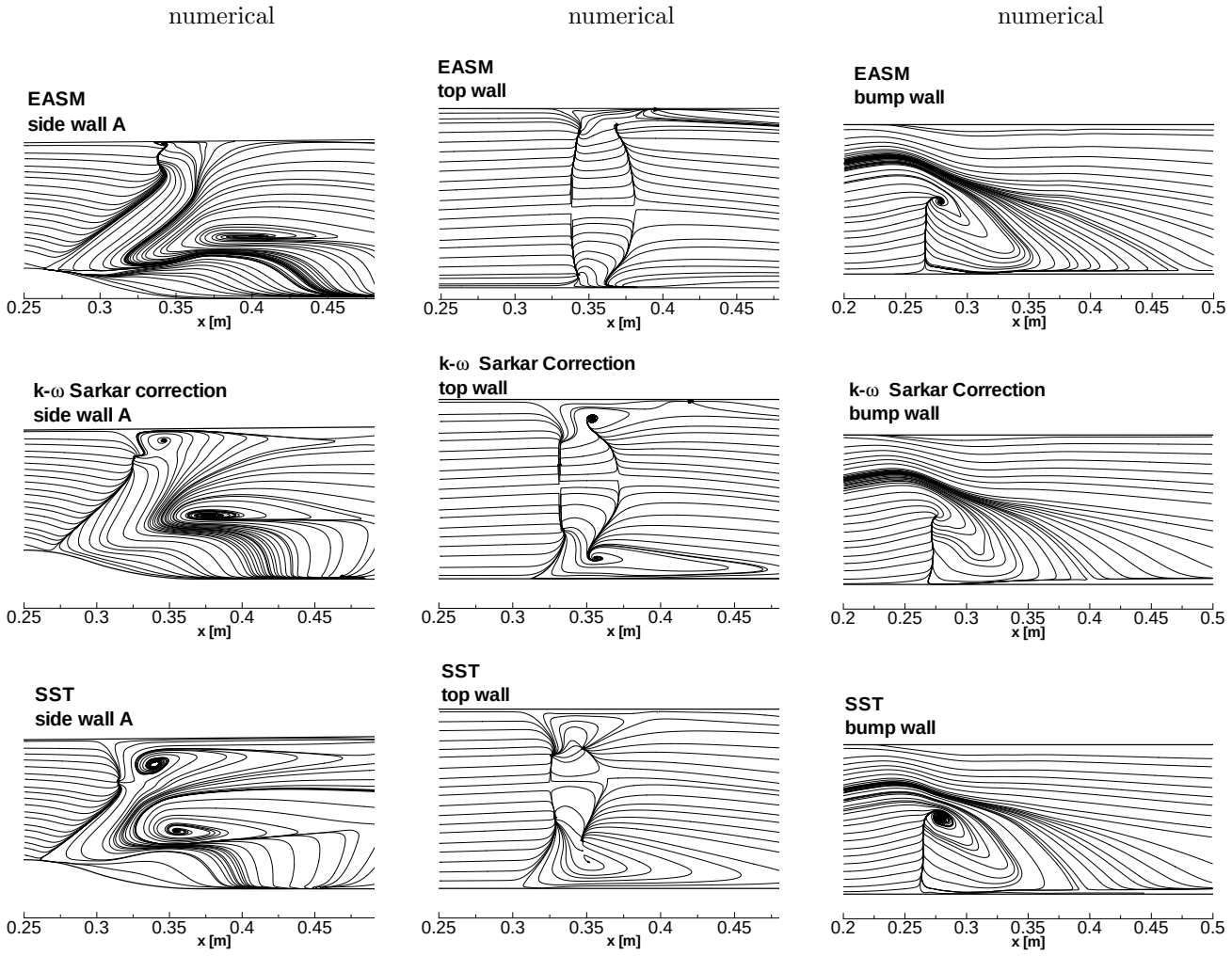

Above: Computed skin-friction lines calculated from the wall shear stress eqs. 2.35-2.37 which are then cast into the three vector components where streamlines are drawn from.

Figure 4.47.: Flow topology on the front wall (left), top wall (middle), and bump wall (right).

Examining the flow topology is important to see if the turbulence models can reproduce the flow structure on surfaces. The computed skin friction lines are calculated based on the wall shear stress eqs. 2.35-2.37. In fig. 4.47 (left) all models have relatively the same structure with the half saddle point on the bump, the half saddle point on the top wall but the second one is missing or it has been combined somewhere. For the second half saddle point on the bottom, the $k-\omega$ does the best job reproducing this one. Also in the topological interpretation is a full saddle point but for the turbulence models, it seems to be producing a focus point. For the focus point near the top, the SST model shows a good representation.
On the top wall fig. 4.47 (middle) there are three foci with two symmetric in the core flow and two half saddle points on side wall A. The $k-\omega$ does the best overall job in reproducing the top wall, the foci are not in the correct location but compared to the other two models it is in good agreement. The models lack to show the continuous flow at side wall B and the focus near side wall A. Figure 4.47 (right) shows us that all three turbulence models can reproduce the focus on the bump wall and at the same position. Although the shape of the focus is better with the EASM($k-\omega$) and SST models. The models also capture the two half saddle points on the bump wall but at different locations, with SST the shortest and EASM($k-\omega$) the furthest. Figure 4.48 shows the complete 3-D view of the computed skin friction lines on the bump wall compared to the top view in fig. 4.47 (right).

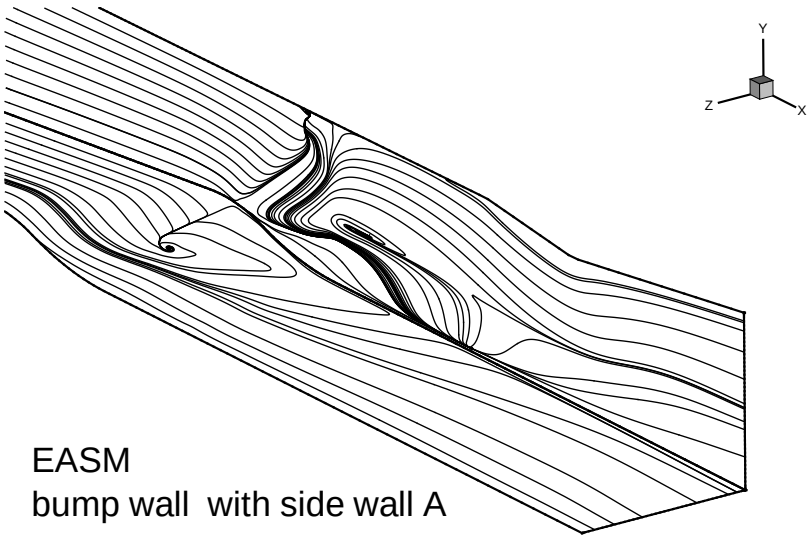

Figure 4.48.: 3-D flow topology view.

4.4. Turbulence and Condensation

4.4.1. S1 Nozzle

The S1 grid and geometry must change for the turbulent case to capture the oblique shock and separation region. With Euler the geometry stopped somewhere along the line of the wall curvature, but for a turbulent simulation more of the real geometry must be modeled because the parallel wall acts like a stagnation point causing the separation to occur, not any effects due to heat addition. From the experimental Schlieren picture the location of the parallel wall is approximated by knowing one real dimension in the picture (throat height). Figure 4.49 displays the grid for the turbulent calculation. Unfortunately the real geometry from the experiment is not known outside the Schlieren picture, so a certain distance of parallel wall is assumed, followed by an expansion to create a supersonic outflow, which is useful because the back pressure is not known. In regards to grid density, the same grid density in the core flow is used for the turbulent and Euler calculation, only more points near the wall and for the extended geometry are required.

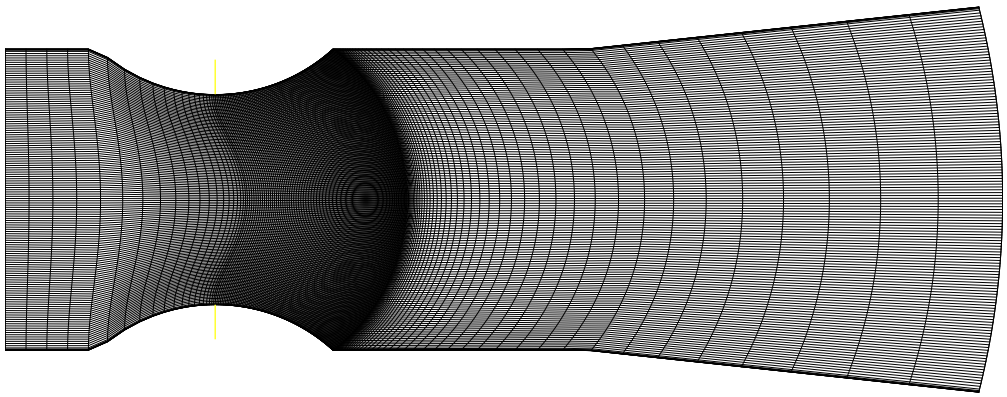

Figure 4.49.: S1 nozzle grid for the turbulent calculation (195_ix150_j)

In sec. 4.1.1 the S1 nozzle was computed using Euler, which was adequate because the main condensation occurs in the core flow and the high wall curvature suppresses boundary layer growth. In the experimental picture fig. 4.50 (top) there is a region of separation which is also captured in the turbulent calculation, but in both cases of humidity the separation

point is independent of the amount of water content in the air. Therefore, this is not the best test case to compare the effects of turbulence with condensation because they are occurring independent of each other. On the other hand this test case shows that the turbulence model is not effecting the condensation solution and it is again able to capture a separation point with the right angle for the oblique shock.

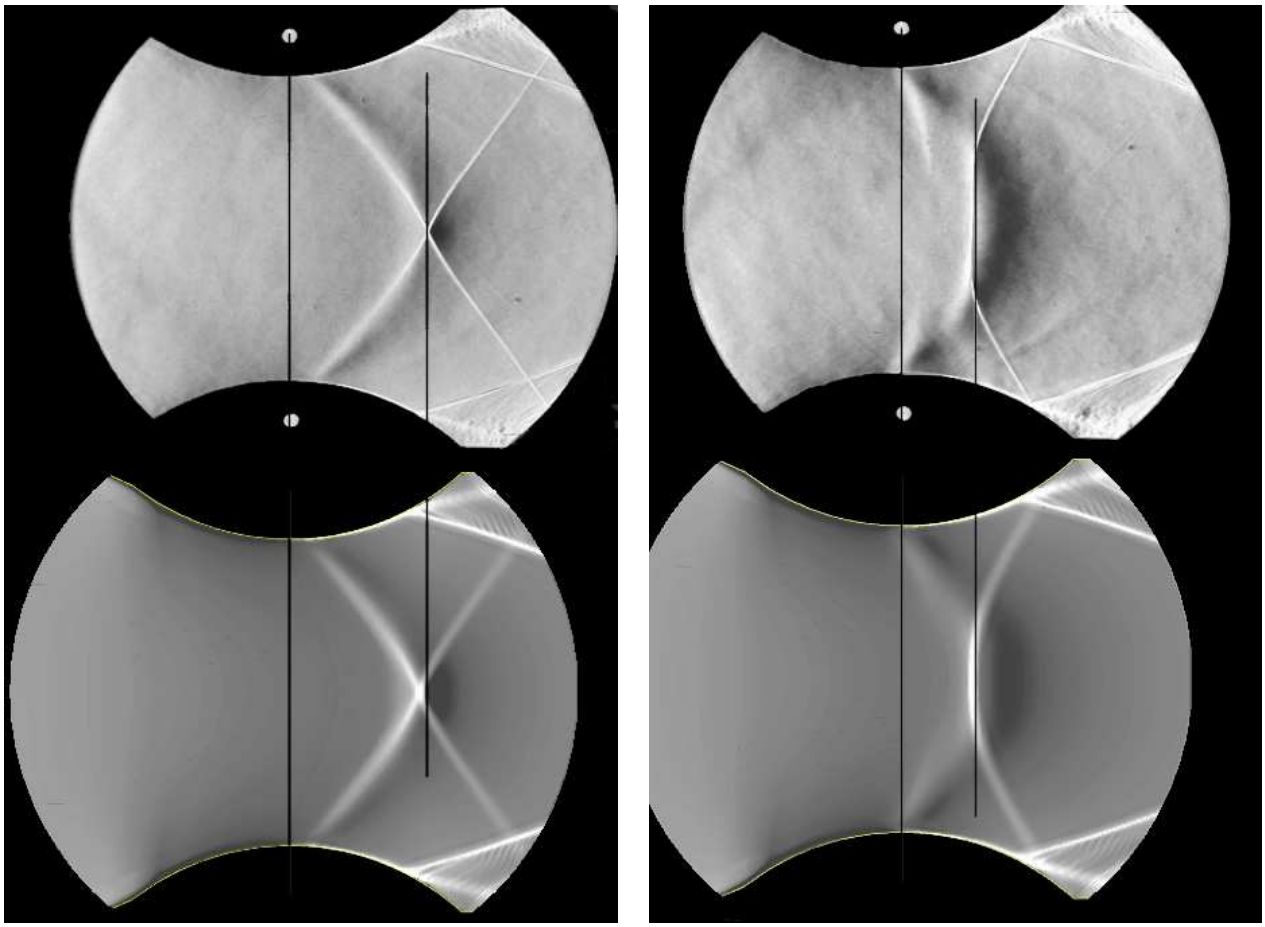

Figure 4.50.: S1 nozzle comparison between experiment and turbulent (EASM($k-\omega$)) simulation. [Top: experiment [81], $h^* = 0.12$ m, $p_{01} = 1$ bar Left: $T_{01} = 295$ K $\phi_0 = 37.2\%$, $Re_{01,h^*} = 2.69$ million, Right: $T_{01} = 286.8$ K $\phi_0 = 71.3\%$, $Re_{01,h^*} = 2.79$ million]

4.5. Validation of Hertz-Knudsen Model

The Hertz-Knudsen droplet growth model chap. 2 sec. 2.4 is normally applied for flows which are dominated by homogeneous condensation with large cooling rates and most important in a vapor/carrier gas mixture. The Hertz-Knudsen model is now extended to an application for homogeneous / heterogeneous condensation under atmospheric flight conditions. Heiler [39] has applied the Hertz-Knudsen droplet growth law to flows in nozzles with various particle densities. The main concern is that since the fluid contains particles of a finite diameter, is the radius of the particles with condensation below the mean free path of the vapor?
A generic definition for the mean free path is

$$\lambda = \frac{1}{2}\frac{\mu_m\sqrt{2\pi R_0 T}}{p} \quad . \tag{4.3}$$

The gas-gas and gas-vapor collisions are neglected for water droplet growth and thus the pressure in the denominator of the mean free path is the vapor pressure. This assumption follows from Wegener and Mack [99]. The line of reasoning behind this is that the water droplet grows with respect to the vapor that it reacts with. The mean free path of the vapor is thus given by

$$\lambda_v = \frac{1}{2}\frac{\mu_m\sqrt{2\pi R_0 T_v}}{p_v} \quad , \tag{4.4}$$

where μ_m and R_0 are based on the mixture properties.
Knowledge of the droplet radius (r) with the definition of the mean free path the Knudsen number is defined as

$$Kn = \frac{\lambda_v}{2r} \quad . \tag{4.5}$$

Young and van Dongen state that neglecting the gas-gas collision is not valid and thus in eq. 4.4 the pressure should be based on the total pressure. Using the total pressure leads to a mean free path that is about 10 times smaller for a vapor/carrier gas mixture, which then puts the Knudsen number in the range of one. The Hertz-Knudsen droplet growth model would then in tendency be over predicting droplet growth.

Two different wings, ONERA M6 and F-16 Fighting Falcon were calculated under atmospheric flight conditions. Since both simulations involve the same conditions of temperature, pressure, angle of attack, particle radius, and particle density, only the F-16 is analyzed to show the Hertz-Knudsen is a valid model for droplet growth in atmospheric flight.
For a nozzle one would show the centerline distribution of mean free path λ, critical radius r^*, and particle radius $\overline{r}$, but for a wing a streamline must be used. A streamline is created close to the boundary layer edge on the suction side of the wing. The starting point for the streamline is near the nose at 38% and 77% span, which are then projected into a 2-D plane. The values of λ, r^*, and $\overline{r}$ are extracted from the streamline and presented in a 2-D plot.

Figure 4.51 shows the streamline around the wing at two cross-sections, 38% and 77% span, which are to scale with the 77% about 2/3 the size of 33%. As a backdrop for the streamlines, is the Mach contour ($M > 1$).
Figure 4.52 shows that the particle radius with and without condensation is less than the free mean path of the vapor. Note the horizontal portion of $\overline{r}_{het}$ corresponds to $R_p = 10^{-8}$m. Since the effect of condensation can increase with a higher angle of attack the simulations for $\alpha = 3$ and 6° are checked. Figures 4.53 and 4.55 show the contour plot and streamline from which the data is extracted and plotted in figs. 4.54 and 4.56. The same trend exists for a streamline further from the boundary. At 77% span a portion of homogeneous condensation occurs which is seen by the appearance of $\overline{r}_{hom}$ in fig. 4.54 right. At $\alpha = 6^\circ$ for both cross-sections the homogeneous portion is also present, but most important is that both $\overline{r}_{hom}$ and $\overline{r}_{het}$ are less than the mean free path of the vapor.

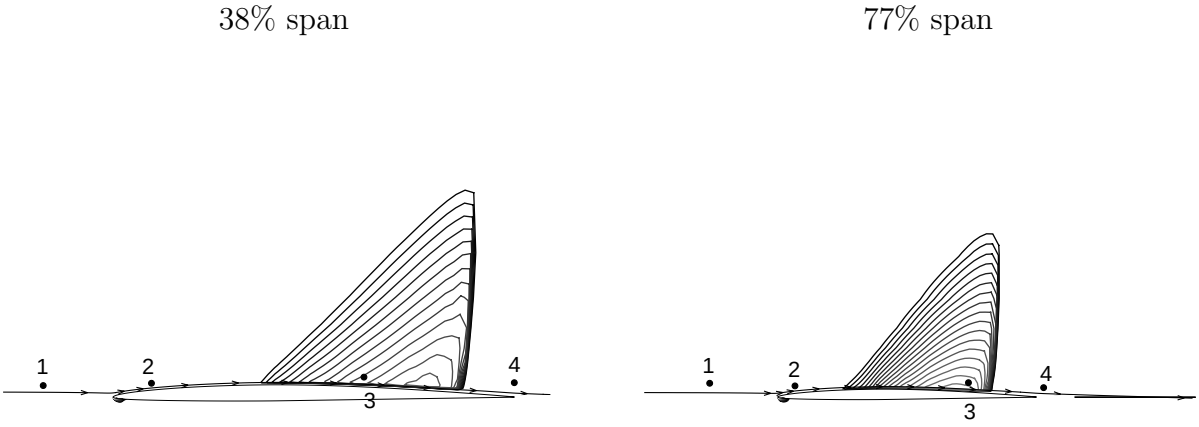

Figure 4.51.: Projected streamlines around two cross-sections of the F16 wing, [$T_\infty = 295$ K, $p_\infty = 1$ bar, $M_\infty = 0.9$, $\alpha = 0°$, $\phi_\infty = 90\%$, $N_{het,0} = 10^{12}$ m^{-3}, $R_p = 1\text{x}10^{-8}$m].

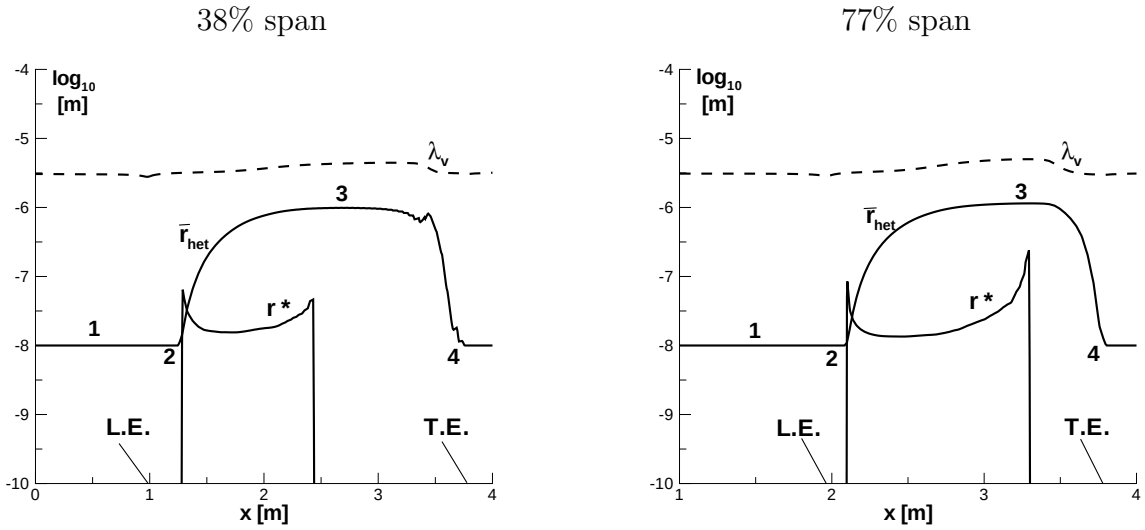

Figure 4.52.: Streamline values of free mean path λ, critical radius r^* and average particle radius $\overline{r}_{het}$ close to the boundary layer, [$T_\infty = 295$ K, $p_\infty = 1$ bar, $M_\infty = 0.9$, $\alpha = 0°$, $\phi_\infty = 90\%$, $N_{het,0} = 10^{12}$ m^{-3}, $R_p = 10^{-8}$m, $c_{44\%} = 2.79$ m, $c_{80\%} = 1.81$ m].

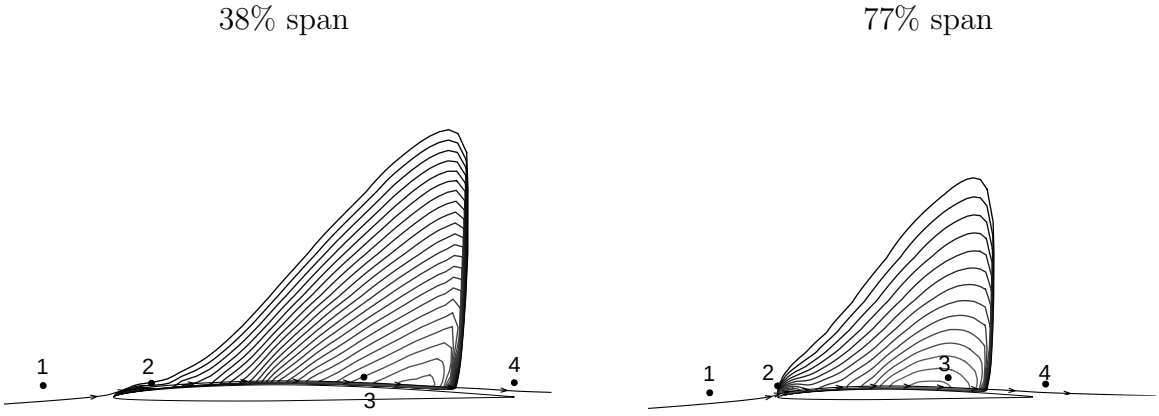

Figure 4.53.: Projected streamlines around two cross-sections of the F16 wing, [$T_\infty = 295$ K, $p_\infty = 1$ bar, $M_\infty = 0.9$, $\alpha = 3°$, $\phi_\infty = 90\%$, $N_{het,0} = 10^{12}$ m^{-3}, $R_p = 1\text{x}10^{-8}$m].

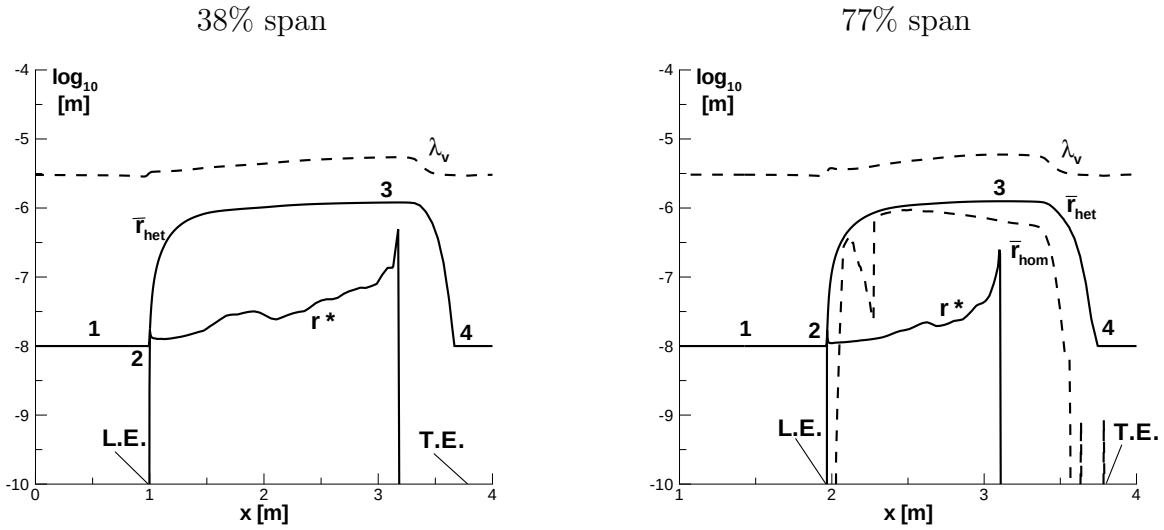

Figure 4.54.: Streamline values of free mean path λ, critical radius r^* and average particle radius $\overline{r}_{het}$ close to the boundary layer, [$T_\infty = 295$ K, $p_\infty = 1$ bar, $M_\infty = 0.9$, $\alpha = 3°$, $\phi_\infty = 90\%$, $N_{het,0} = 10^{12}$ m^{-3}, $R_p = 10^{-8}$m, $c_{44\%} = 2.79$ m, $c_{80\%} = 1.81$ m].

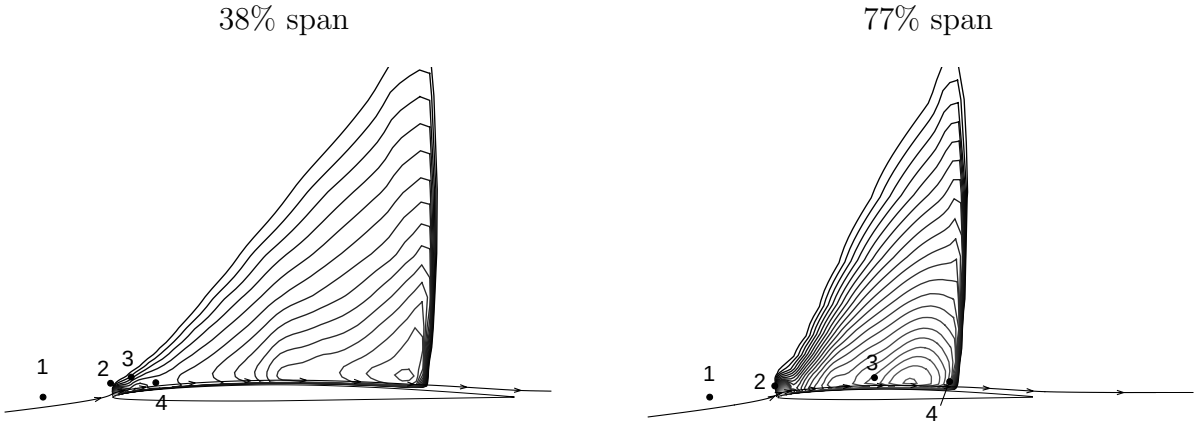

Figure 4.55.: Projected streamlines around two cross-sections of the F16 wing, [$T_\infty = 295$ K, $p_\infty = 1bar$, $M_\infty = 0.9$, $\alpha = 6°$, $\phi_\infty = 90\%$, $N_{het,0} = 10^{12}m^{-3}$, $R_p = 1\text{x}10^{-8}$m].

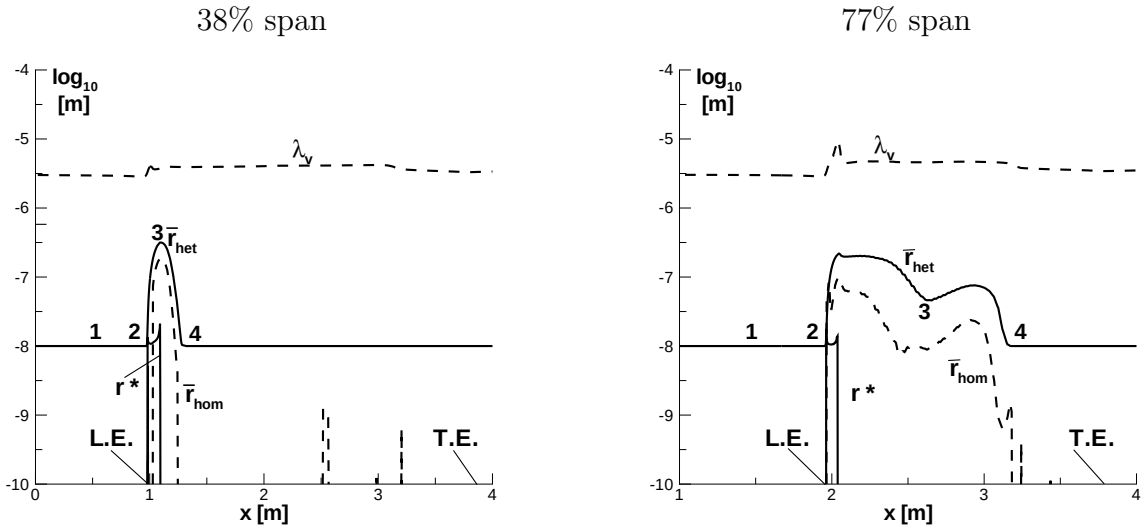

Figure 4.56.: Streamline values of free mean path λ, critical radius r^* and average particle radius $\overline{r}_{het}$ close to the boundary layer, [$T_\infty = 295$ K, $p_\infty = 1bar$, $M_\infty = 0.9$, $\alpha = 6°$, $\phi_\infty = 90\%$, $N_{het,0} = 10^{12}m^{-3}$, $R_p = 10^{-8}$m, $c_{44\%} = 2.79$ m, $c_{80\%} = 1.81$ m].

4.6. Validation Summary

From the validation of the condensation models to the turbulence models a short summary is in order before moving onto the main results. For the condensation models it is sufficient to use the classical nucleation theory of Volmer, Frenkel, and Zel'dovich for steady as well as unsteady simulations as seen from the results with the S1 and A1 nozzle. In regards to atmospheric flight with particles the Hertz-Knudsen droplet growth model is adequate since the mean free path of the vapor is larger than the droplet radius.
In regards to the turbulence models, the three produced adequate results with all the test cases with the EASM($k-\omega$) having slight advantages in some areas. The Sarkar compressible correction is able to obtain benefits when it is needed and remain neutral when not. The $k-\omega$ model with Sarkar seems to have an advantage over the SST and EASM($k-\omega$ with regards to the post shock recovery pressure, especially in areas of separation. For an unsteady calculation involving Low Reynolds, the best model would be the $k-\omega$ because it involves less work units to calculate the source terms and provides adequate results. For steady 3D flows involving complex geometries the EASM($k-\omega$ model is the best out of the ones tested because there are no blending functions dependent on geometry and it seems to be more stable for flows with non-optimum grids. The current version of the code can only handle a single block, thus comprises must be made when creating 3-D grids. For example creating the grid around the tip of the wing, which results in grid cells that have angles which are skewed.

5. Internal Flow

5.1. 3-D Channel with Skewed Bump - Turbulent

In chap. 4 sec. 4.3 the skewed bump channel was used as a test case for turbulence models but it is also of interest to see how condensation will effect the 3-D structures in the flow. The same total conditions are used from tab. 4.5 [T_{01} = 300 K, p_{01} = 0.92 bar, h^* = 0.08 m, $Re_{h^*,01}$ = 1.613 million] with the only addition of adding 50% relative humidity to the air. This is also a good case for humidity because the throat is only 80mm which corresponds to temperature gradients for homogeneous condensation. Table 5.1 compares the temperature gradient at Mach 1 for 3 different streamlines starting along the z-axis (spanwise with bump).

Table 5.1.: Computed temperature gradient at Mach 1

Start of streamline	x = 0mm z = 30mm	y = 50mm z = 60mm	z = 90mm
$-\left(\frac{dT}{ds}\right)^*$ [K/cm]	4.31	4.25	3.92
x-location at M=1	0.216 m	0.211 m	0.207 m

The trend of the temperature gradient matches that of the geometry of the skewed bump because the throat is further downstream for z=30mm compared to z=90mm, which allows for a larger expansion slope and thus a higher temperature gradient. Figure 5.1 starts by comparing the Mach and numerical Schlieren picture distribution at the mid-plane. A distinct difference has occurred due to condensation where the shock has weakened and moved closer to the throat and a disappearance of the lambda shock which is seen in the numerical Schlieren picture. Before the shock it seems a weak compression is formed because of the heat addition. Looking at the pressure distribution on the top and bottom wall, fig.5.2 the condensation has smoothed out the two expansions in the adiabatic case (bottom wall) and the weak compression due to heat addition is seen on the top wall. Very important is that on the bottom wall the shock has moved further to the throat which has increased the separation zone but due to the increase in pressure, reduction in Mach number, the separation zone on the top wall has been reduced. Figure 5.3 shows

the u-component of velocity at 4 different x locations. At 250mm the station is on the downward slope of the bump but before the shock, already the effect of heat addition can be seen by the decrease in the core flow velocity. 300mm is the end of the bump with the shock already occurring at the bottom wall but still not on the top wall, for the diabatic simulation, the velocity on the bottom is recovering from the separation. At 350mm the adiabatic portion is in the lambda shock region the diabatic case is already recovering from the shock at the top wall. 400mm downstream from the entrance the flow is recovering from the shock system and preparing for expansion to supersonic.

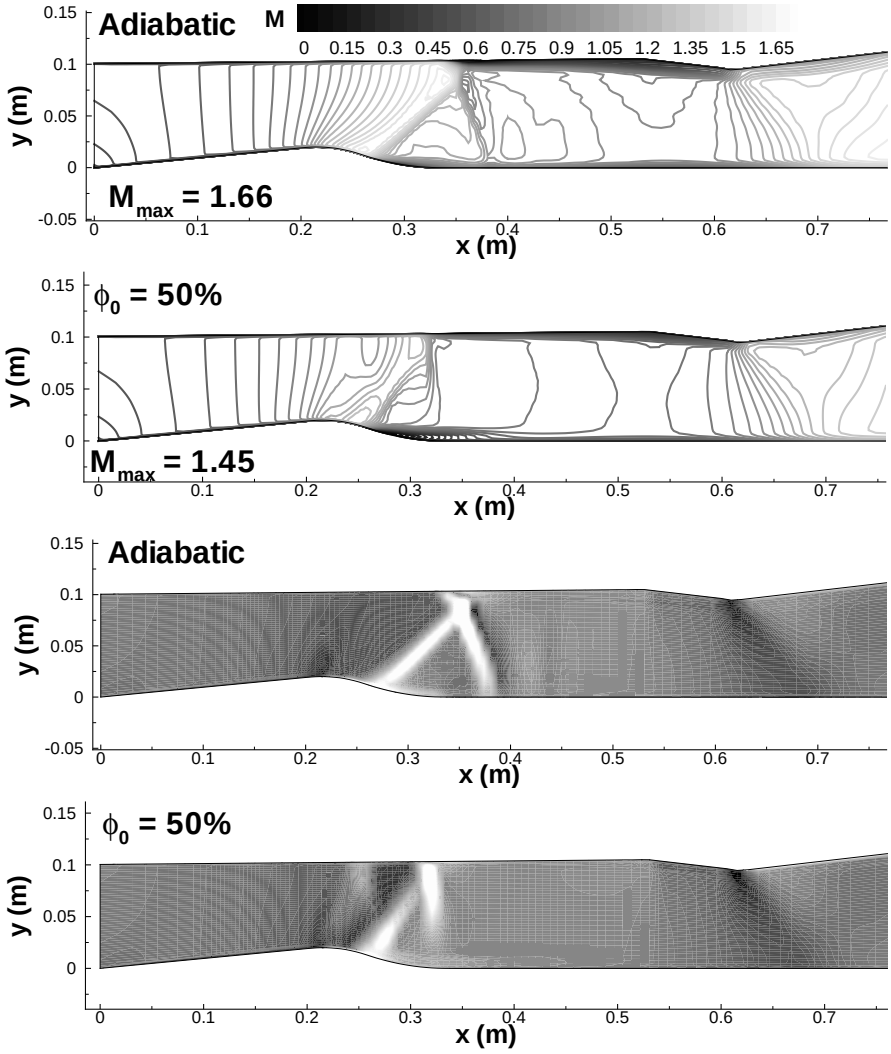

Figure 5.1.: Mid-plane Mach and numerical Schlieren contour $\frac{\partial \rho}{\partial x}$, [$T_{01} = 300$ K, $p_{01} = 0.92$ bar, h^*=0.08 m, $Re_{h^*,01} = 1.613$ million, ϕ_0=50%], M_{max} is the maximum Mach number reached at the mid-plane.

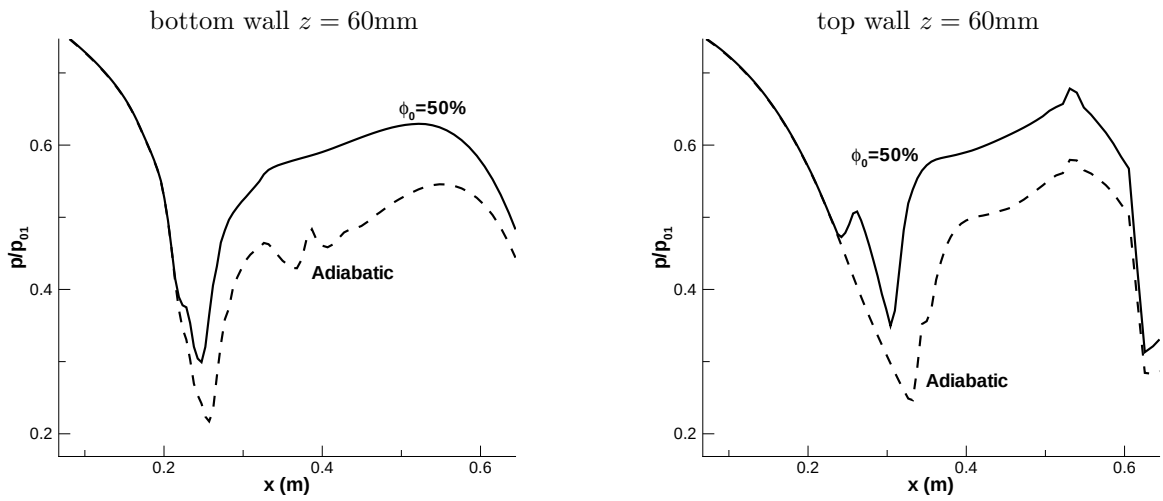

Figure 5.2.: Mid-plane pressure distribution on the top and bottom wall, [T_{01} = 300 K, p_{01} = 0.92 bar, h^*=0.08 m, $Re_{h^*,01}$ = 1.613 million, ϕ_0=50%].

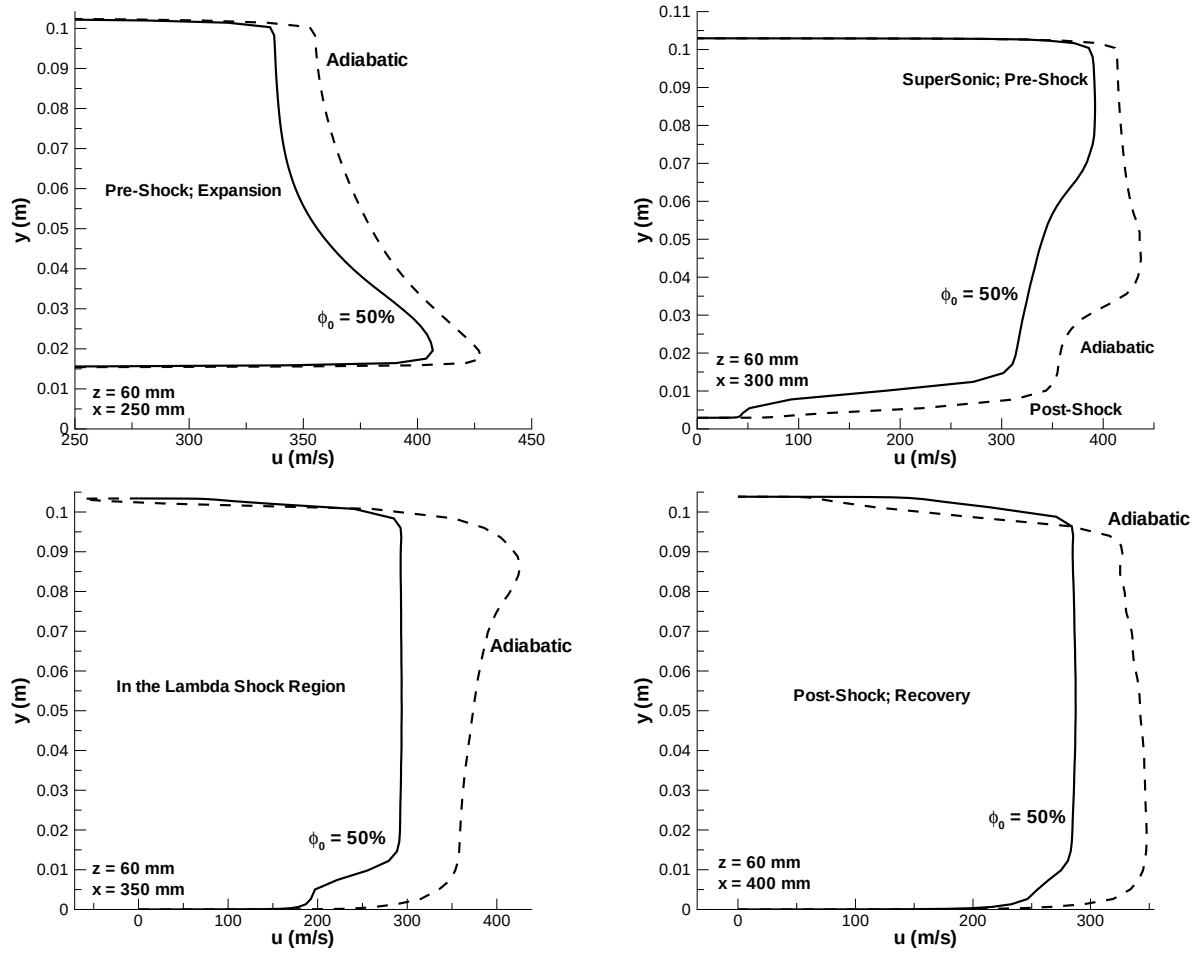

Figure 5.3.: Mid-plane u-component velocity distribution at 4 different stations, [T_{01} = 300 K, p_{01} = 0.92 bar, h^*=0.08 m, $Re_{h^*,01}$ = 1.613 million, ϕ_0=50%].

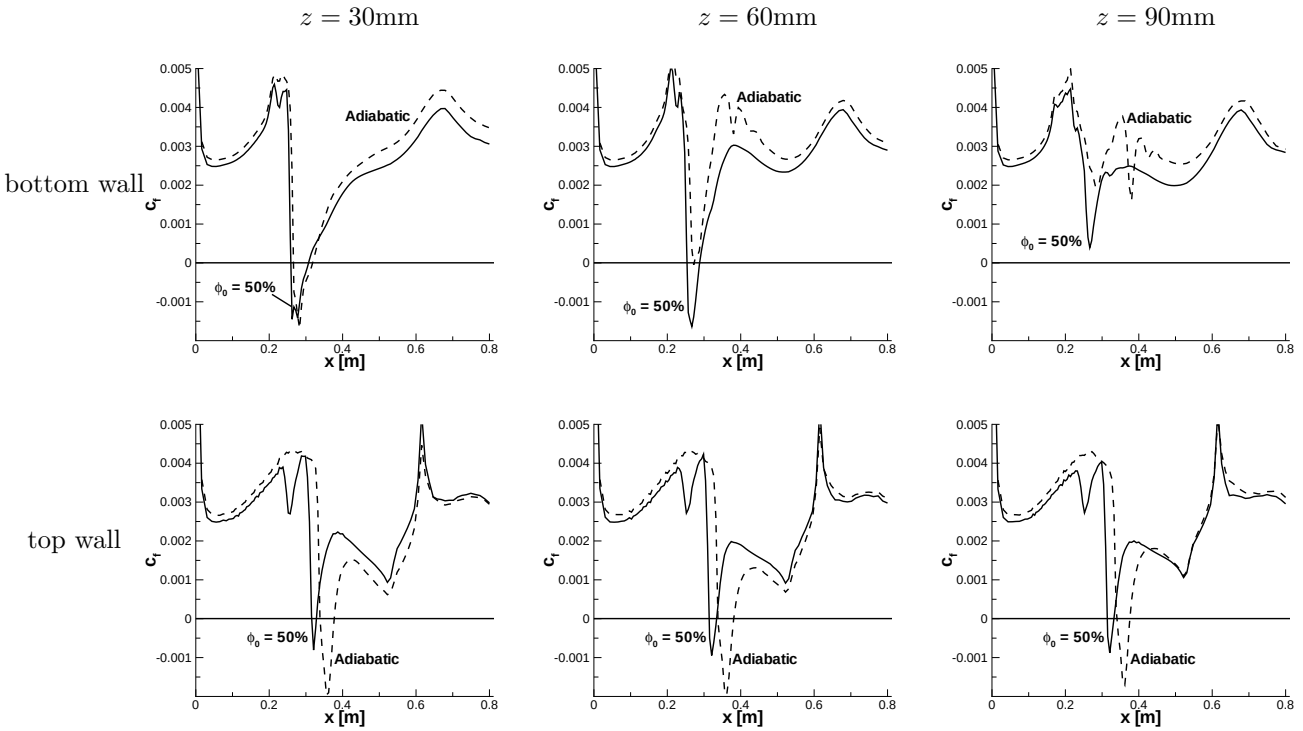

Skin friction c_f distribution on the top and bottom wall at three different spans.

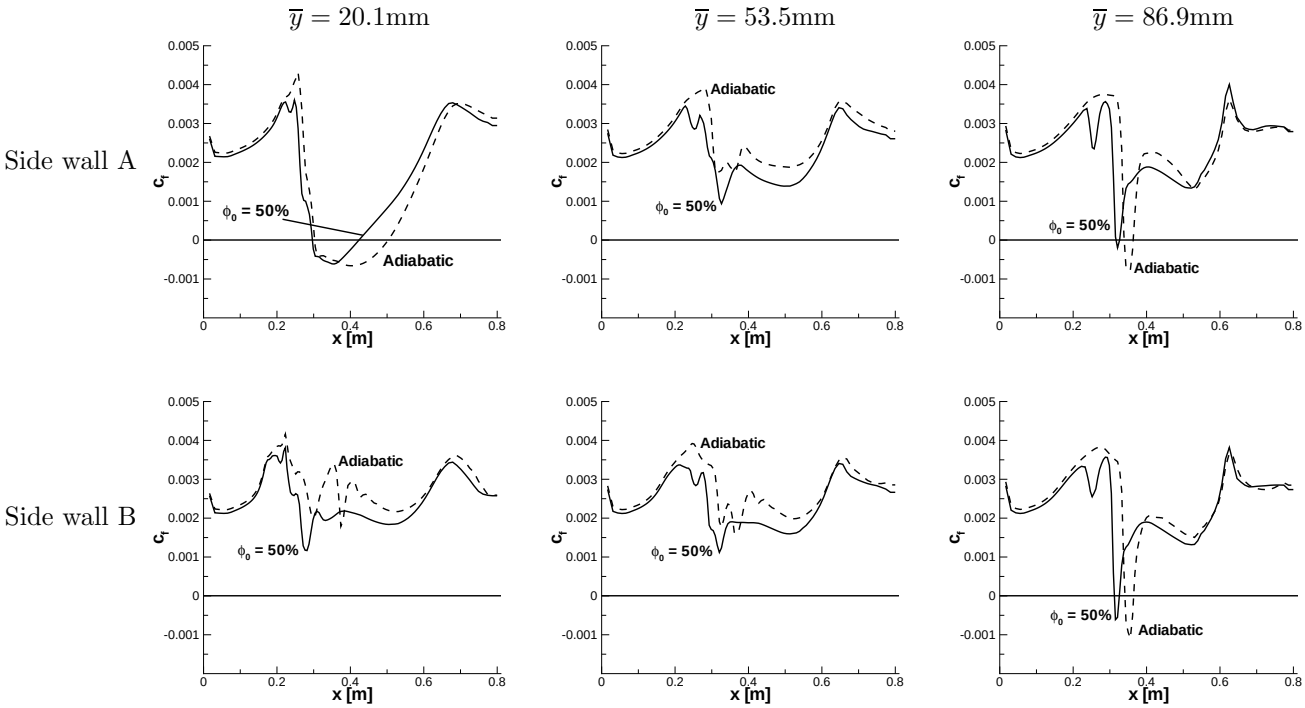

Skin friction c_f distribution on the front and back wall at three different average heights.

Figure 5.4.: Skin friction c_f distribution on the four channel walls, [T_{01} = 300 K, p_{01} = 0.92 bar, h^*=0.08 m, $Re_{h^*,01}$ = 1.613 million, ϕ_0=50%]

Another way to examine the flow is to look at c_f on all 4 surfaces at different cross sections. Figure 5.4 (top-half) shows c_f on the bottom (bump wall) and top wall, whereas the bottom-half is the two flat side walls. The most interesting result is that c_f is increased due to condensation on the top surface because of the increase in static pressure which is also a decrease in pre-shock Mach number. On the bottom wall, bump surface c_f is decreased. The decrease is a result of the shock being moved closer to the throat or higher on the bump surface. Like the top wall the pre-shock Mach number on the bottom wall is less but since this is occurring on a curved surface compared to a flat surface, the separation zone is increased. Refer again to fig. 5.1 Mach contour at the mid-plane to see the increase in separation. On the side walls condensation is mainly decreasing c_f only for $\overline{y}$=86.9 m is it increasing and the effect of condensation is moving the peak value closer to the throat. An average height is used in fig. 5.4 (bottom-half) because the c_f plot on the side walls follows from 1 grid line, j=15, j=30, and j=45, due to the bump these grid lines are not at constant height. Figure 5.5 helps to determine why the shock has moved closer to the throat and why there exists a weak compression before the shock in the numerical Schlieren picture. Nucleation starts before the throat and with the growth of g there is a weak compression but not a diabatic shock, the diabatic static pressure deviates from the adiabatic one with this growth of g, the shock occurs at a smaller pre-shock Mach number compared to the adiabatic case which usually decreases the separation zone but since the shock is occurring on a curved surface it increases the separation region by occurring earlier on the bump. The shock for the diabatic case is moved to the left of the adiabatic one because condensation increases the static pressure, it acts like a higher back pressure on the nozzle exit, which can be seen on fig. 5.5 (bottom).

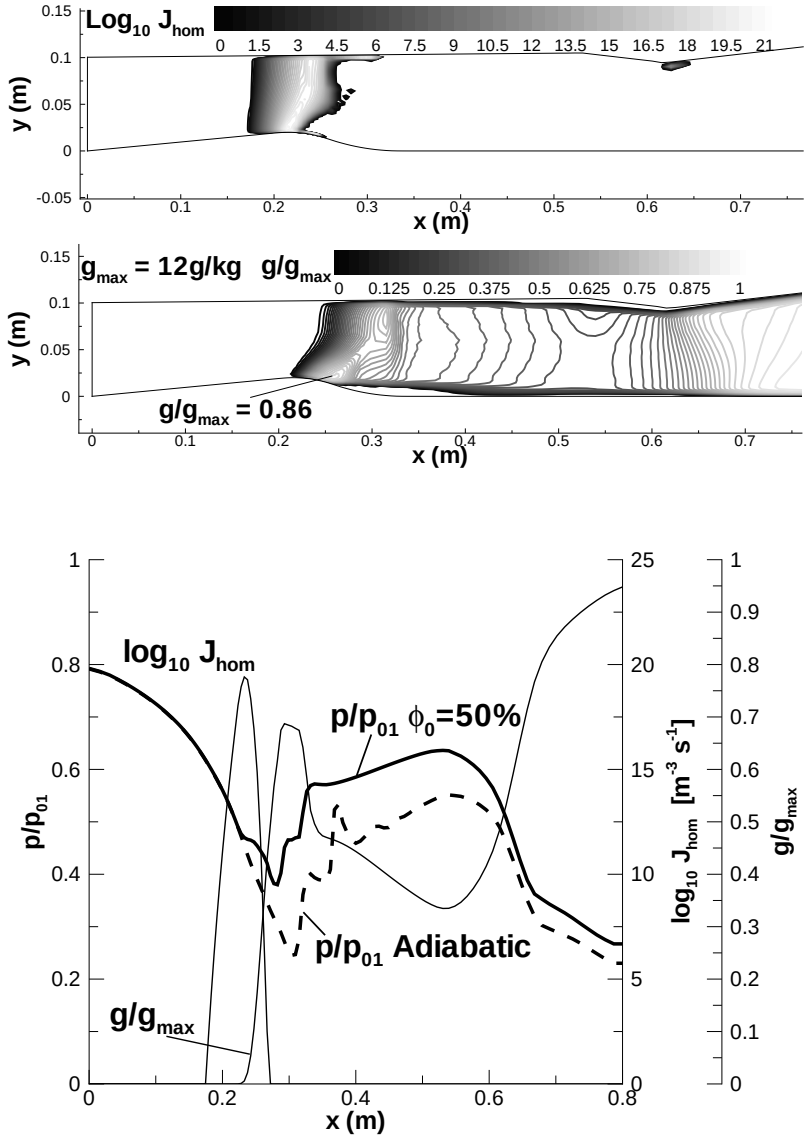

Figure 5.5.: Mid-plane nucleation and condensate mass fraction contour (top), mid-plane centerline pressure, nucleation, and condensate mass fraction distribution (bottom),[T_{01} = 300 K, p_{01} = 0.92 bar, h^*=0.08 m, $Re_{h^*,01}$ = 1.613 million, ϕ_0=50%].

A final comparison between the adiabatic and diabatic solution uses the computed skin friction lines to observe the flow topology on the four surfaces of the nozzle (fig. 5.6). For the most part the structure of the adiabatic case is repeated in the diabatic with a slight shift to the left. On the bump surface the large focus has shifted to the right but the separation line has shifted to the left and extended higher into the core flow. On the top wall the structure has been decreased in width, which corresponds to the decrease in c_f on the top. The start of the shock position is given for the bump and top wall to show the shift and relation to the separation line. The two side walls show very similar patterns with only a slight shift.

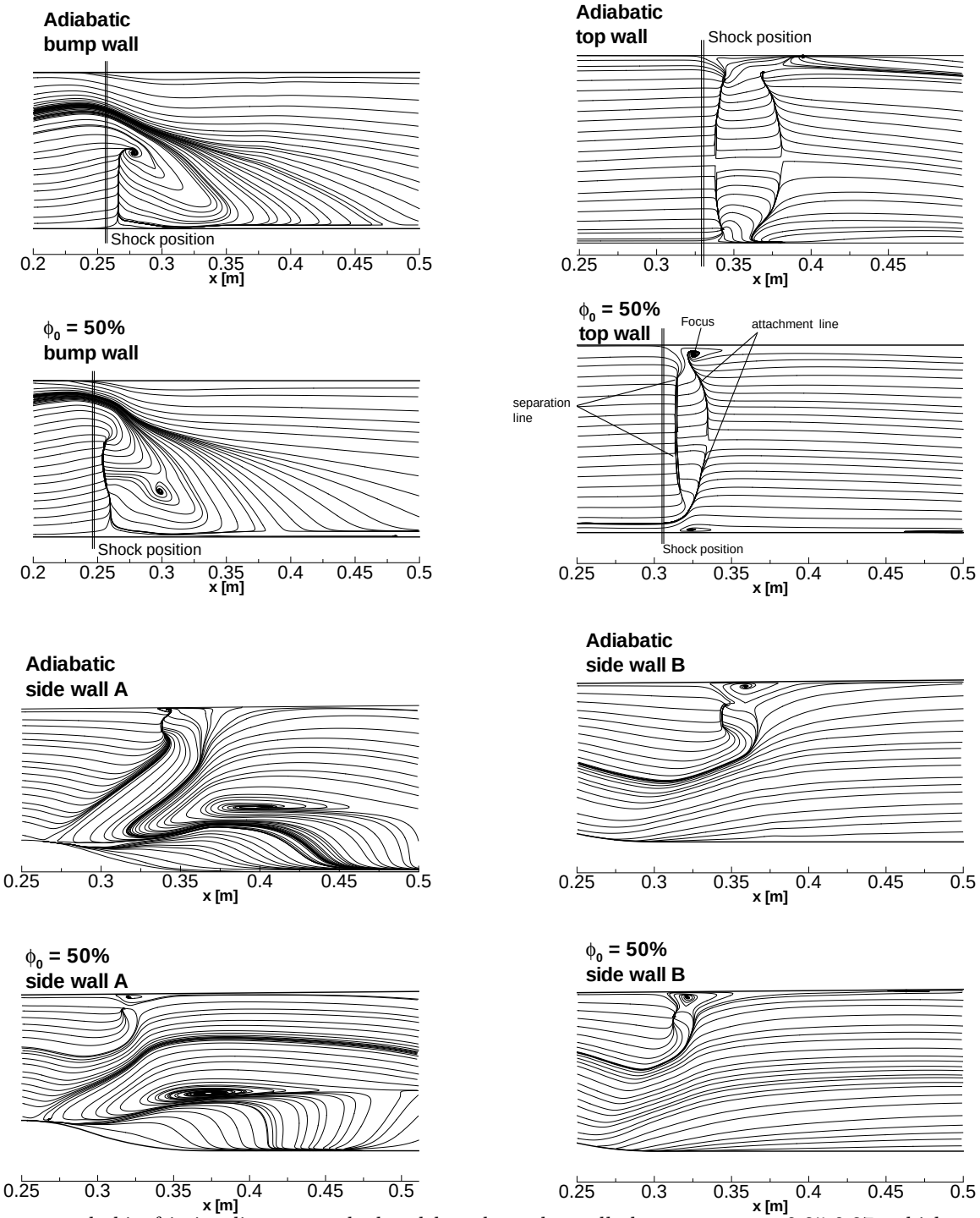

The computed skin friction lines are calculated based on the wall shear stress eqs. 2.35-2.37, which are then cast into the three vector components where streamlines are drawn from.

Figure 5.6.: Computed skin-friction lines, [T_{01} = 300 K, p_{01} = 0.92 bar, h^*=0.08 m, $Re_{h^*,01}$ = 1.613 million, ϕ_0=50%], refer to fig.4.42 for location of side wall A and B.

5.2. 3-D Axisymmetric A1 Nozzle - Euler

5.2.1. Geometry and Grid

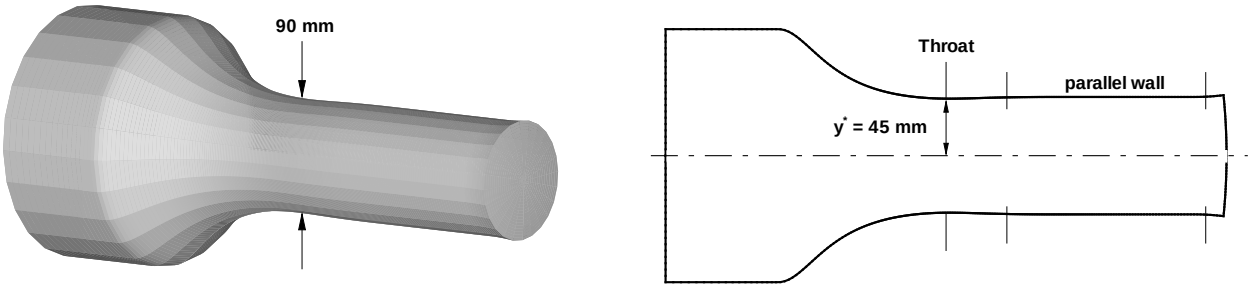

Figure 5.7.: 3-D A1 nozzle geometry.

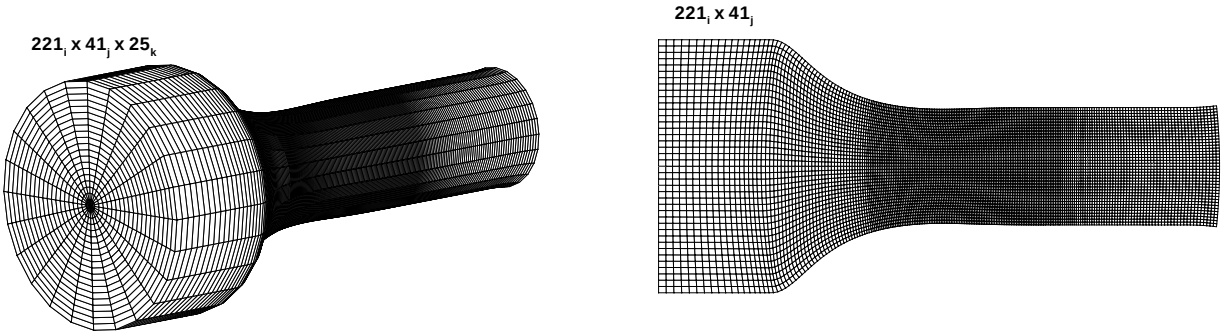

Figure 5.8.: 3-D A1 nozzle grid.

The geometry (fig.5.7) and grid (fig.5.8) of the 3-D A1 nozzle is obtained by rotating the 2-D plane A1 nozzle found in chap. 4 subsec. 4.1.2. The full 3-D grid is calculated because unsymmetric solutions are sought. One numerical note is that for a structured grid there must be no overlap or identical nodes, thus it appears that in fig.5.8 (left) the grid comes to a point at the centerline axis but in fact there is a small circle there. In a sense it can be thought of as a cylinder or rod, which requires a boundary condition. An Euler wall was not chosen because this would eliminate the chance for flow to cross the rod, thus it is assumed that all variables on the rod are equal, this is done by finding the average value

around the rod and then setting the nodes equal to this value. More sophisticated codes handle this problem by having an o-grid on the outside and an h-grid for the inside, with interpolation techniques to handle the interface between the two grid types.

5.2.2. Steady

Adiabatic

The adiabatic pressure gradient for the 3-D A1 nozzle is compared with the 2-D plane in fig. 5.9 (right-top). The conclusion from this figure points out that the 3-D A1 nozzle as a higher slope compared with the 2-D plane. Also the static pressure is lower for the 3-D nozzle which means a higher Mach number is achieved in the parallel section of the nozzle. Table 5.2 compares the $M = 1$ temperature gradient between the 2-D and 3-D A1 nozzle. The larger temperature gradient means that the flow in the 3-D nozzle has a higher stability limit, which translates too, it takes higher humidities to get the flow in the nozzle to become unsteady. Figure 5.9 (left-top) shows the numerical Schlieren picture in one plane for the axisymmetric nozzle, the importance here is the smooth gradients toward the throat, but in the pressure plot after the throat the 3-D axisymmetric pressure distribution is wavy until the outlet. When looking at a close up of the numerical Schlieren picture and a smaller contour range of the density gradient from the throat to the outlet fig. 5.9 (bottom), waves are picked up. The white areas are small compressions which corresponds to the small peaks in the pressure distribution from the throat to the outlet.

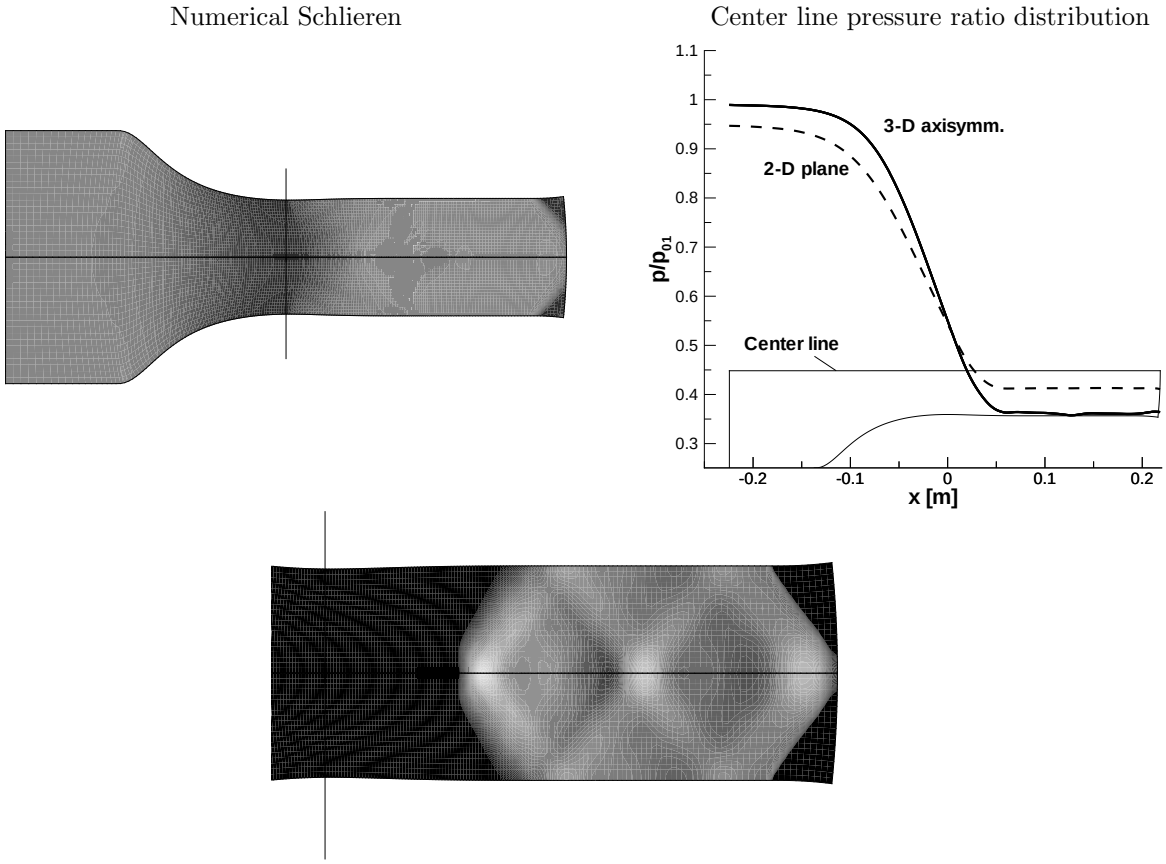

Figure 5.9.: Supersonic adiabatic flow in the 3-D A1 nozzle, $[T_{01} = 295K, p_{01} = 1bar]$.

top left : numerical Schlieren of one plane in the 3-D axisymm. nozzle
top right : center line pressure ratio distribution between 2-D plane and 3-D axisymm. nozzles
bottom : numerical Schlieren closeup view of the outlet of the 3-D axisymm. nozzle.

Table 5.2.: Comparison of the temperature gradient at $M = 1$ along the centerline for the plane and axisymmetric A1 nozzle, $[T_{01} = 295K, p_{01} = 1bar]$.

Nozzle	$\left(-\frac{dT}{dx}\right)^*_{1-D}$ [K/cm]	exp. $\left(-\frac{dT}{dx}\right)^*_{2-D}$ [K/cm]	num. $\left(-\frac{dT}{dx}\right)^*_{2-D}$ [K/cm]
2-D plane	5.43	5.13	5.25
3-D axisymm.	7.68	N/A	7.30

Humidities

Three humidities of 35, 45 and 55% are plotted in fig. 5.10, all are steady results. At the lowest humidity weak compressions are present, with a 10% increase resulting in a shock due to heat addition that is moved closer to the throat at 55%.

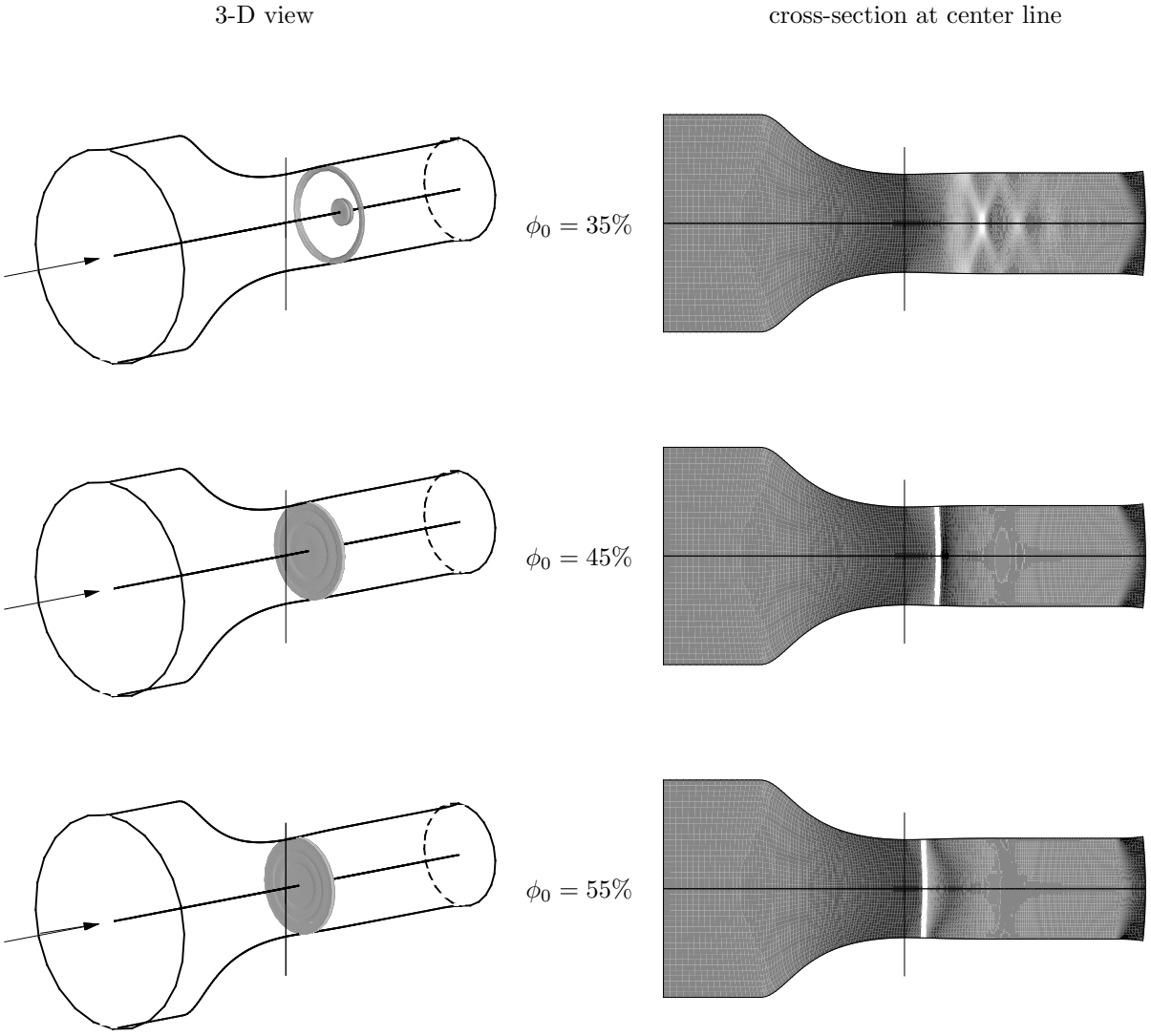

Figure 5.10.: Steady numerical Schlieren for different humidities, [$T_{01} = 295$ K, $p_{01} = 1$ bar].

5.2.3. Unsteady Oscillation

Before going into the results of the unsteady oscillations, a discussion on the disturbance must be made. For the symmetric oscillation no disturbance is required, the system is self-excited. As seen in the 2-D case it is not necessary to add a disturbance to go to the unsymmetric oscillation if high enough humidity is used. For the case of the 3-D A1 nozzle due to the higher temperature gradient at the throat, the system is more stable in regards to getting to the second unsymmetric oscillation. Figure 5.11 shows 4 out of 25 of the k planes.

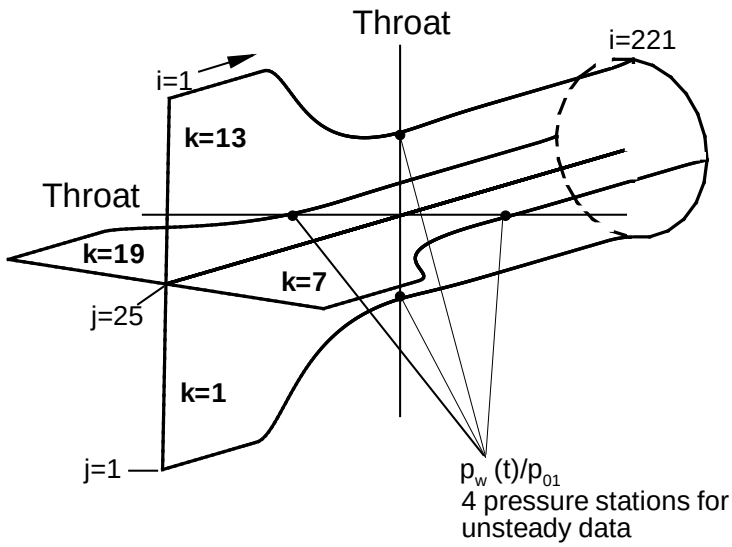

Figure 5.11.: Graphical view of 4 out of the 25 k planes in the 3-D A1 nozzle, also shown are the pressure stations from which data is sampled during the unsteady simulation, at the throat on the wall.

The first attempt at reaching the unsymmetric oscillation was to add a linear disturbance in the k=1,13 plane fig. 5.12. The disturbance is added at one instance in time throughout the entire plane. Figure 5.12 shows an example with ρ using a contour plot before and after including the distribution at the inlet, throat, and outlet. The same disturbance is added to u, v, w, p. Also important is that the disturbance was added to a solution that contains a shock due to heat addition. For example taking the symmetric solution at $\phi_0 = 95\%$. For the linear disturbance in the k=1,13 plane the system went back to the symmetric oscillation (see fig.5.14).

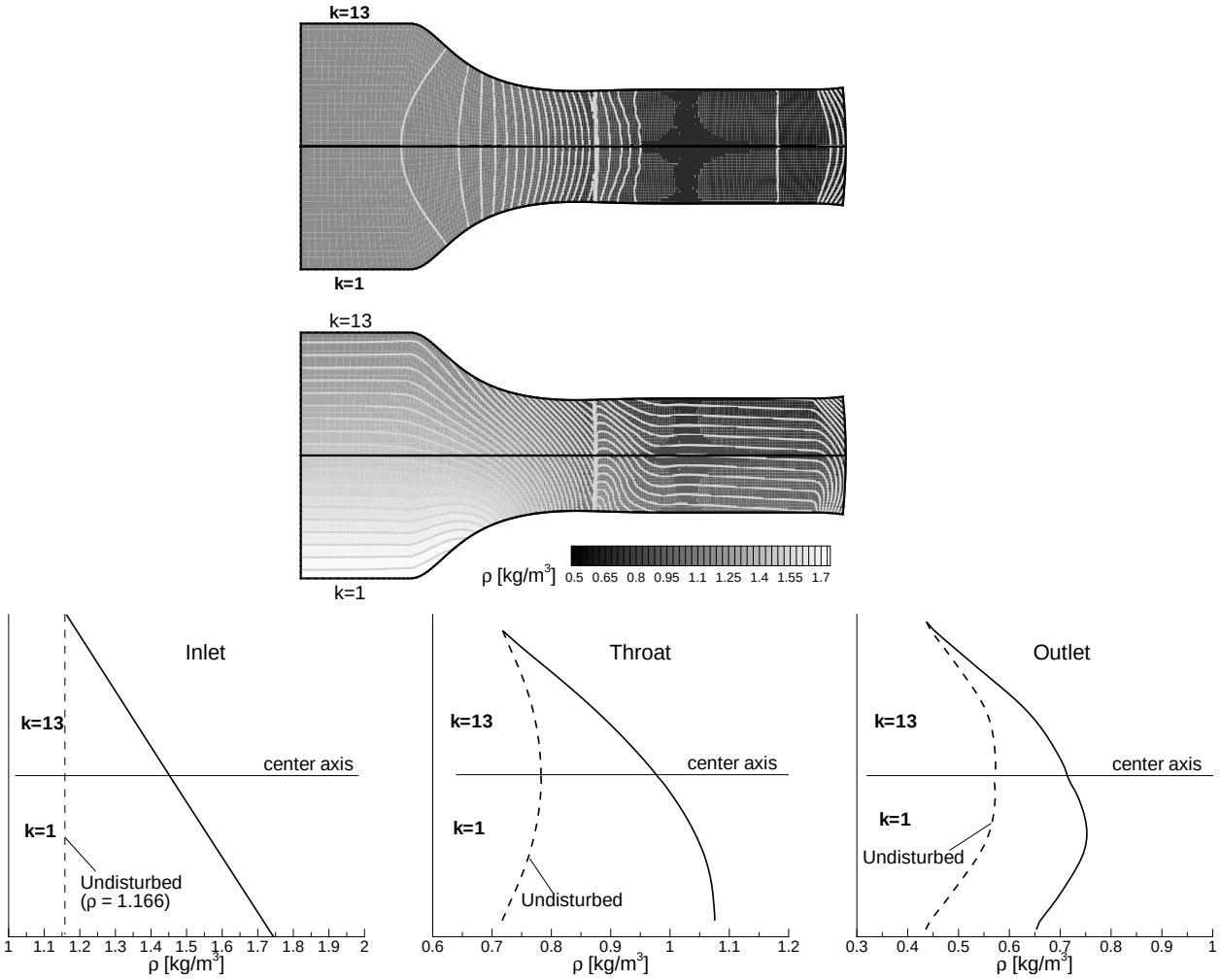

Figure 5.12.: Visual means to show the procedure for a linear disturbance in one plane, [T_{01}=295 K, p_{01}=1 bar, $\phi_0 = 95\%$, $ajj = 0.5$].

top	:	contour plot of ρ before the linear disturbance
middle	:	contour plot of ρ after the linear disturbance
bottom	:	linear disturbance at the inlet, throat, and outlet

The next step was to add a linear disturbance in the k=1,13 and k=7,19 plane, for example a cross, again the system went back to the symmetric oscillation at $\phi_0 = 95\%$. In both of the cases the linear disturbance was only a function of j. Equation 5.1 represents the disturbance factor (DF), which takes on the simple form

$$
\begin{aligned}
DF &= (1 + ajj) - \frac{ajj/2}{nj - 1} \cdot (j - 1) \quad \text{for } k < 7 \text{ and } k \geq 19 \\
DF &= 1 + \frac{ajj/2}{nj - 1} \cdot (j - 1) \quad \text{for } k \geq 7 \text{ and } k < 19
\end{aligned} \tag{5.1}
$$

$$\text{where:} \quad ajj \longrightarrow 0.1 - 0.5 \quad .$$

The next step for the linear disturbance is to go from f(j) to one of f(j,k). The disturbance equations then become

$$
\begin{aligned}
akk &= 1. + (k + 6)/48 \qquad \text{for } k < 7 \\
akk &= 1. + (k - 18)/48 \qquad \text{for } k \geq 19 \\
DF &= akk \left(1.5 - \frac{0.25}{nj - 1} \cdot (j - 1) \right) \qquad \text{for } k = 1, 6 \,\&\, k = 19, 25
\end{aligned} \tag{5.2}
$$

$$
\begin{aligned}
akk &= 1. + (k - 6)/48. \qquad \text{for } k \geq 7 \text{ and } k < 19 \\
DF &= akk \left(1. + \frac{0.25}{nj - 1} \cdot (j - 1) \right) \qquad \text{for } k = 7, 18 \quad .
\end{aligned} \tag{5.3}
$$

Important point in eq. 5.2 is that the disturbance is the same at $k = 1$ and $k = 25$ since these planes are identical, similar to the c-grid connection after the airfoil. The value of 48 was chosen arbitrary resulting in a maximum value of $akk = 1.25$ at the k=6 and k=18 plane, with a minimum value of 1.02 at k=7 and k=19. Note that the disturbance does not uniformly increase as one goes from the k=1 plane to the k=24 plane but rather there are smooth changes from the k=1 to k=6 plane with an abrupt change between k=6 and k=7. Figure 5.13 is similar to Fig.5.12 which shows the disturbance in two planes k=1,13 and k=7,19, this shows the distinct difference which creates the unsymmetrical flow field. With this type of disturbance (eqs. 5.2-5.3) the unsymmetric oscillation was achieved for humidities above 90%. In the authors view there are certainly other possible combinations for a disturbance in the j and k plane to create the unsymmetric pattern, but it is not likely that a different disturbance structure will change the value of the humidity where the unsymmetric pattern first occurs.

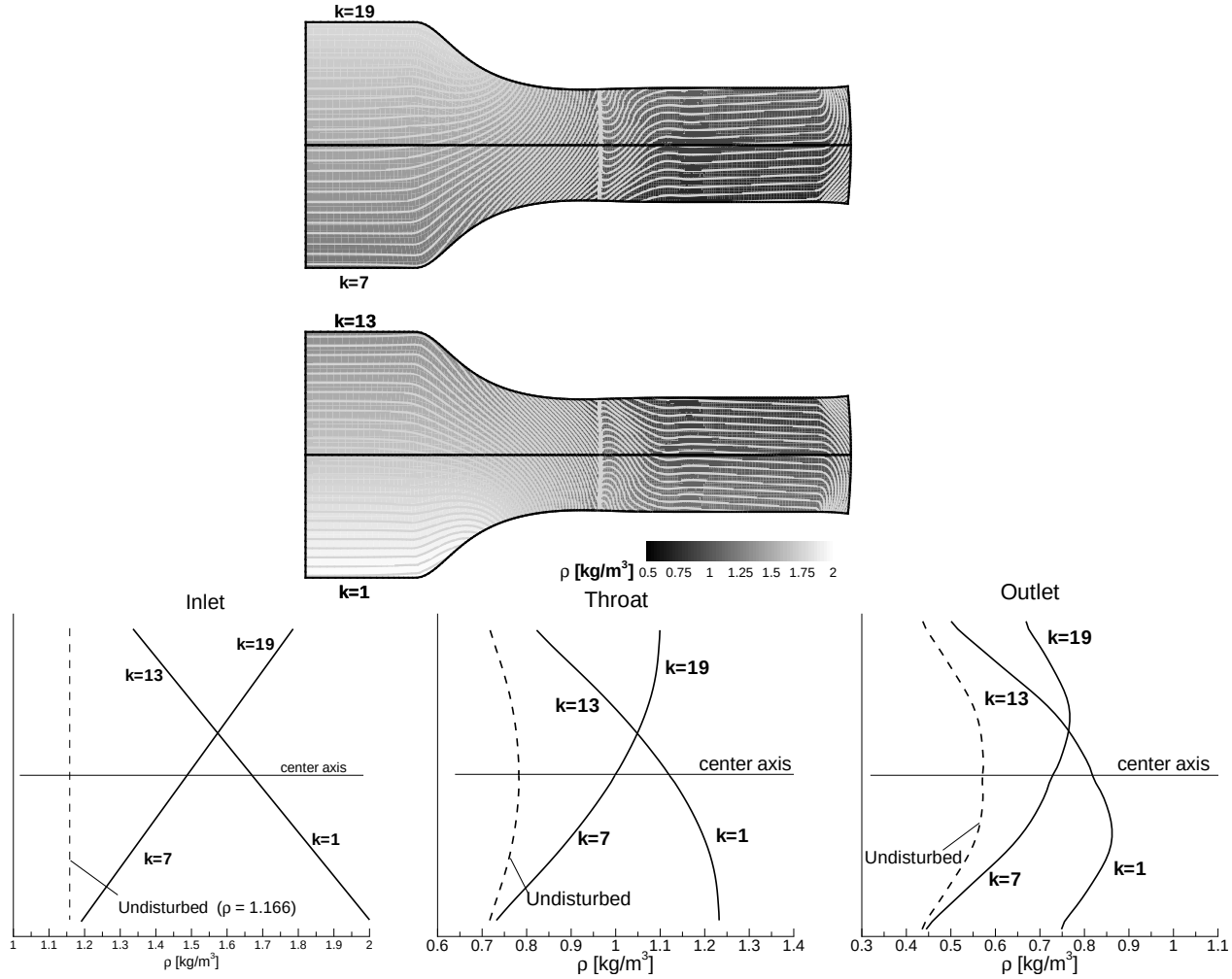

Figure 5.13.: Visual means to show the procedure for a linear disturbance according to Eqs. 5.2-5.3 in two planes, [T_{01}=295 K, p_{01}=1 bar, $\phi_0 = 95\%$, $ajj = 0.5$].

a) : contour plot of ρ in the k7-k19 plane using Eq.5.2
b) : contour plot of ρ in the k1-k13 plane using Eq.5.3
c) : linear disturbance at the inlet, throat, and outlet

The unsteady data was taken at 4 different stations at the throat in the k=1,7,13, and 19 plane. Figure 5.11 shows a plot of the four stations.
Figure 5.14 shows two humidities of 75 and 85% where the disturbance was added but the solution returned to the symmetric oscillation. At a close look the symmetric oscillation after the disturbance is not as perfect as before, but the frequency and amplitude are the same. The main reason for this is that the numerics are not able to fully recover after such a disturbance. A disturbance has been added to an Euler system thus there is no way for

it to die out over time, thus this noise remains.

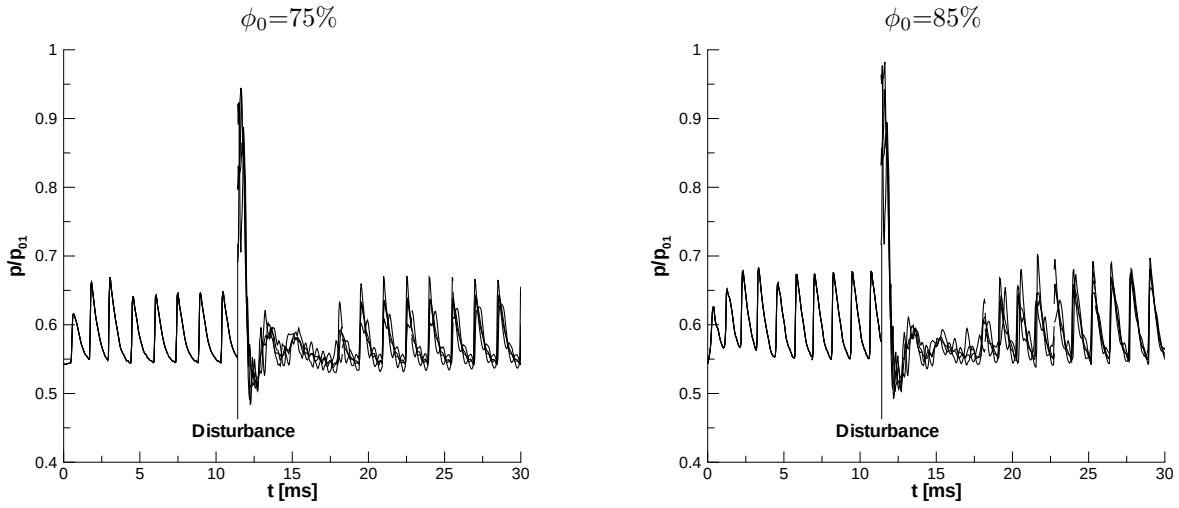

Figure 5.14.: Pressure ratio at throat-wall versus time, {symmetric - disturbance - return to symmetric}.

Moving to a higher humidity of ϕ_0=95% fig. 5.15 (left) the time series after the disturbance takes on a new unsteady repeating pattern. Also important is that by cutting the disturbance in half fig. 5.15 (right), it still results in the same unsteady unsymmetric pattern. This unsymmetric pattern is a shock that forms in half of one plane, then spirals into other planes and through the throat. A graphical view is presented in fig. 5.19. A closeup view of the unsymmetric part in fig. 5.15 (left) is shown in fig. 5.16. The trend is that the peaks in each plane are separated, thus showing the shock due to heat addition is spiraling throughout the 3-D nozzle.
Figure 5.17 is a summary of the main features of the 3-D nozzle for operating at total conditions of 295K and 1 bar. After 60-65% the flow becomes unsteady with a symmetric oscillation, at 87.5-90% humidity there is the lower branch of the hysteresis regime where the system can have more than one solution. If the total temperature was increased by $10-15°$ it is likely that the stability limit and beginning of the hysteresis would shift to the left. In the 2-D plane nozzle at higher humidities $\gtrsim$95% the symmetric solution no longer exist and goes straight to the unsymmetric oscillation, but for the 3-D nozzle since the temperature gradient is higher it is not possible to solve for the upper end of the hysteresis regime. It is then an open question in fig.5.17 if there exist an upper limit in the hysteresis. When going to humidities above 100% it is likely that subsonic heat addition occurs and the shock due to heat addition near the throat would not occur, which is driving this interesting flow field. With the 2-D A1 plane nozzle the symmetric frequency was around 446Hz for 90% humidity and for the 3-D nozzle it is $\approx$ 850 Hz, unsymmetric 2-D is $\approx$ 1091 Hz and 3-D is $\approx$ 1350 Hz. The frequency for the unsteady oscillations are greater for the 3-D nozzle. The reason for this is because of the higher cooing rate in the 3-D nozzle. This

trend of a higher frequency also agrees with the reduced frequency formula found in Adam [1]

$$F_1 \sim \frac{f}{\left(-\frac{1}{T}\frac{dT}{dt}\right)^*} \quad .$$

Since the 3-D nozzle has a higher cooing rate it thus must also have a higher frequency to have the same F_1 value as the 2-D plane nozzle.
Figures 5.18 and 5.19 show a time series of the symmetric and unsymmetric oscillation. The full 3-D nozzle is shown by creating a numerical Schlieren picture with limits that only show the shock structure, where the time series on the right shows a full numerical Schlieren picture of a 2-D cross-section.

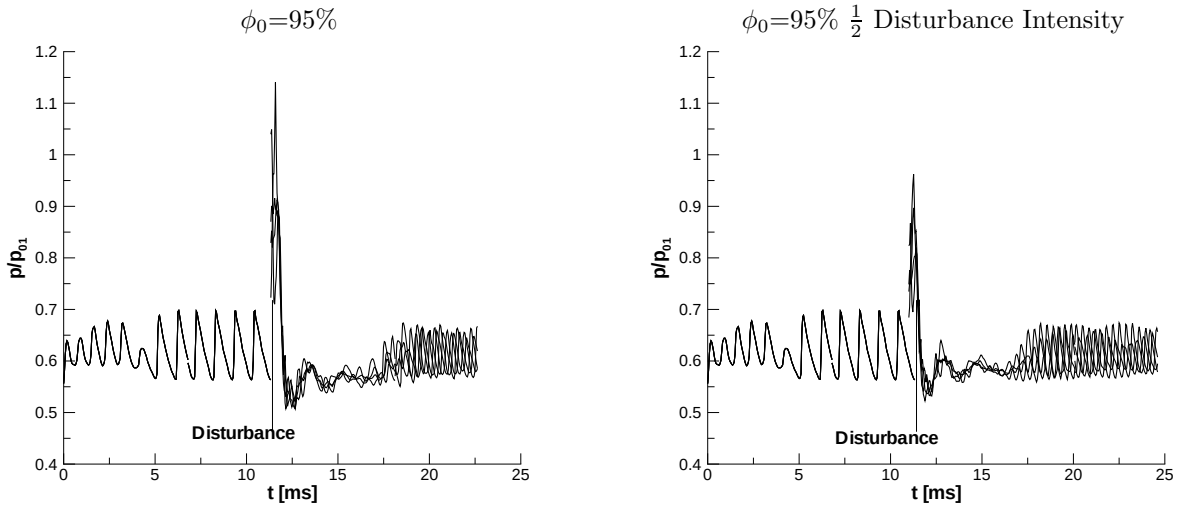

Figure 5.15.: Pressure ratio at throat-wall versus time for two different disturbance intensities, {symmetric - disturbance - unsymmetric}.

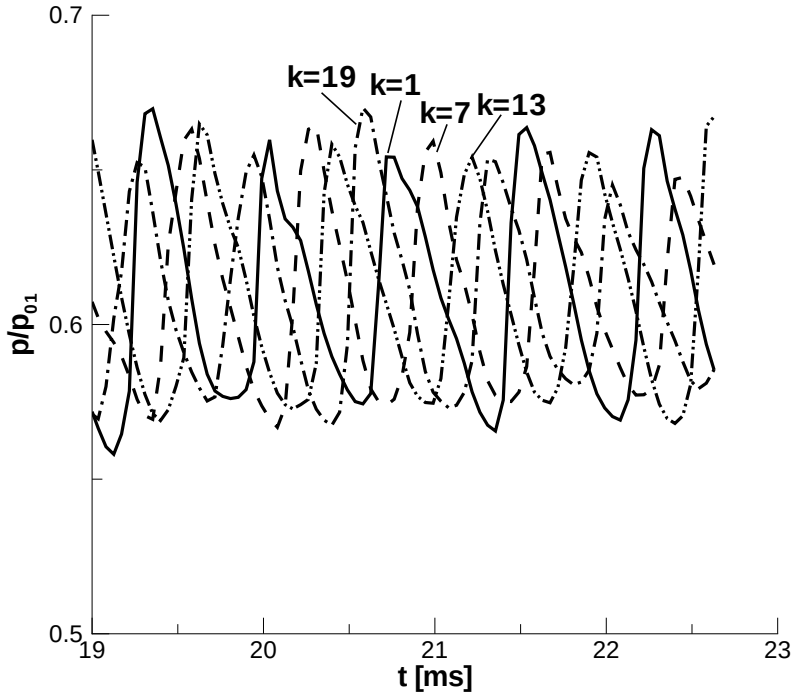

Figure 5.16.: Close up of the pressure ratio at throat center line versus time for unsymmetric pattern.

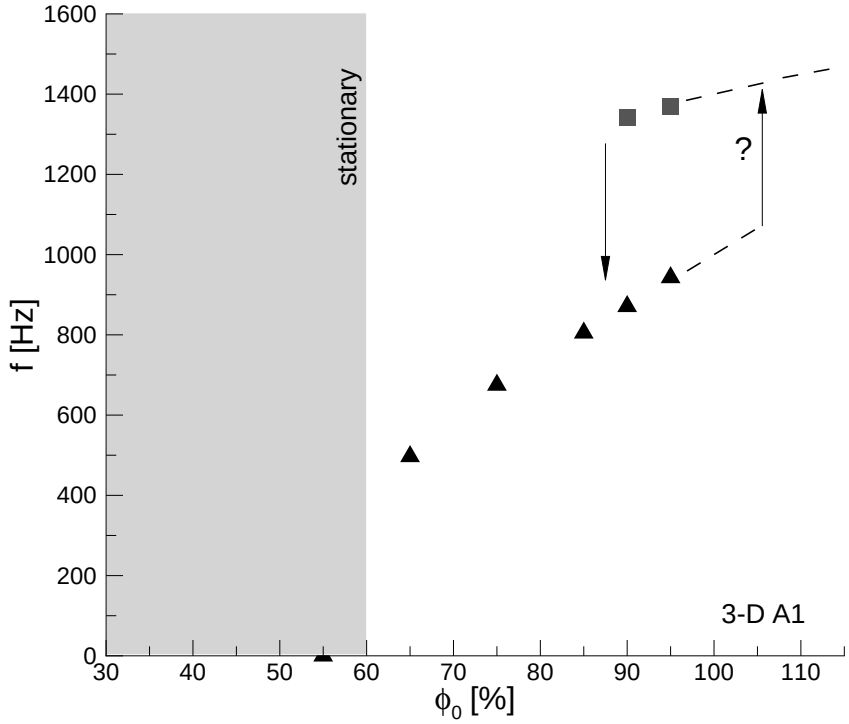

Figure 5.17.: Frequency versus humidity for the 3-D A1 nozzle, [$T_{01} = 295$ K, $p_{01} = 1$ bar].

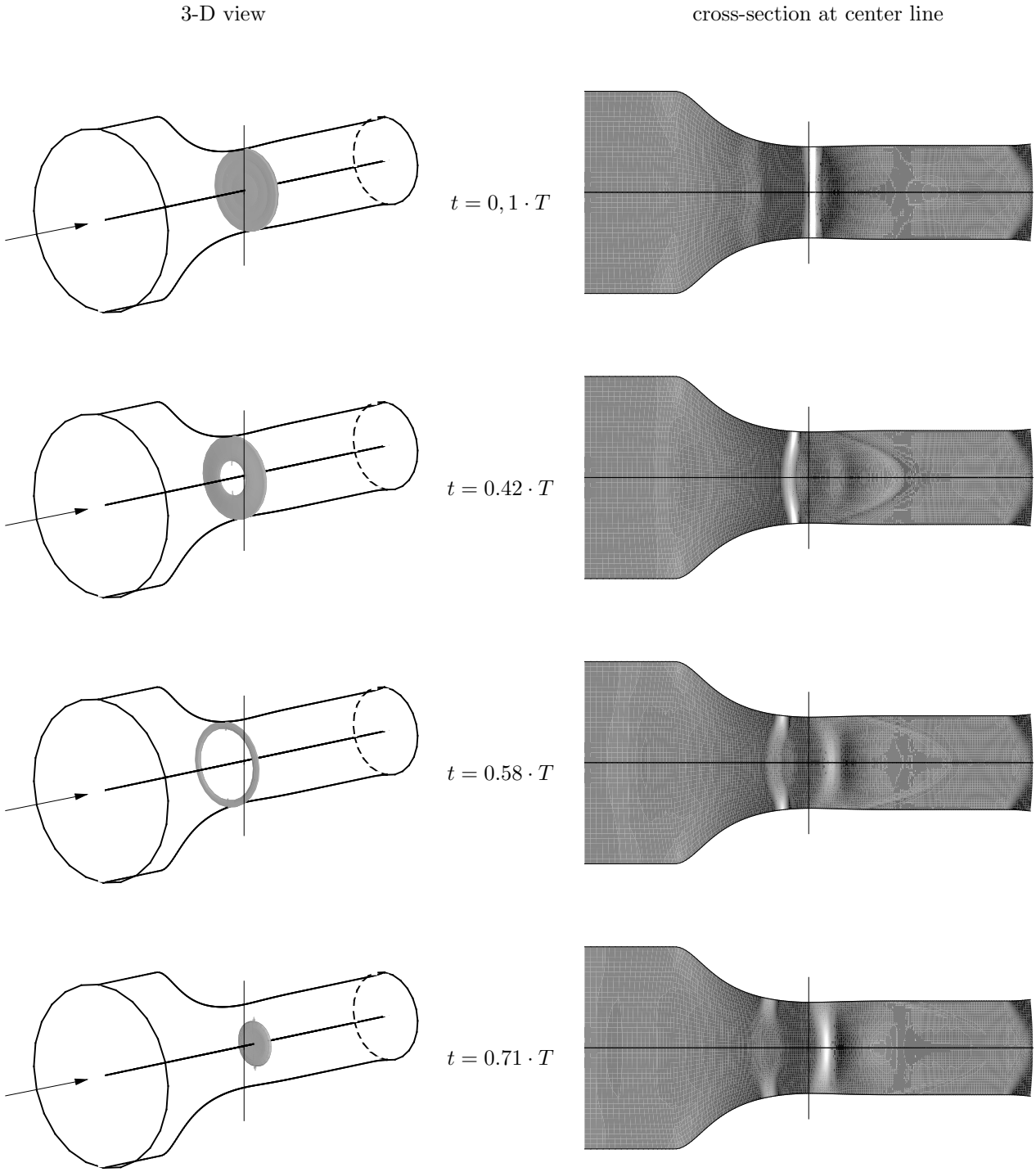

Figure 5.18.: Unsteady symmetric oscillation, [$T_{01} = 295$K, $p_{01} = 1$ bar, $\phi_0 = 95\%$, $\mathbf{f \approx 942Hz}$].

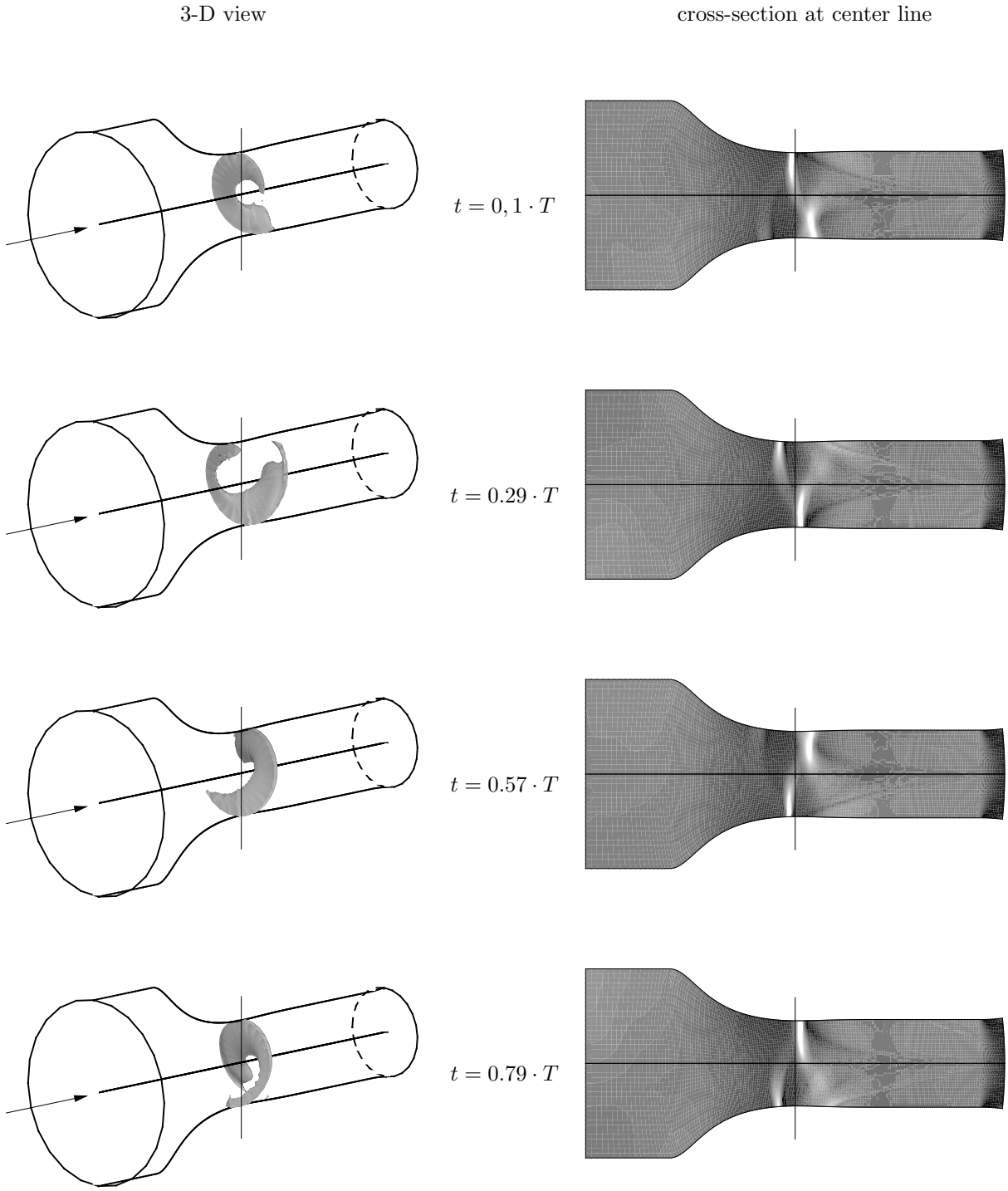

Figure 5.19.: Unsteady unsymmetric oscillation, [$T_{01} = 295$ K, $p_{01} = 1$ bar, $\phi_0 = 95\%$, $\mathbf{f \approx 1350Hz}$].

In fig. 5.19 the shock rotated in the counter clockwise direction looking in the direction of the flow, when the disturbance method was created this was not taken into account, thus to see if the shock can rotate in the clockwise direction the disturbacne was rotated by 45°. The disturbance equations (eqs. 5.4-5.5) then become

$$\begin{aligned} akk &= 1. + (k)/48 \qquad \text{for } k \geq 7 \text{ and } k < 13 \\ akk &= 1. + (k-12)/48 \qquad \text{for } k \geq 13 \text{ and } k < 19 \\ DF &= akk\left(1.5 - \frac{0.25}{nj-1} \cdot (j-1)\right) \qquad \text{for } k = 7, 18 \end{aligned} \tag{5.4}$$

$$\begin{aligned} akk &= 1. + (k)/48. \qquad \text{for } k < 7 \\ akk &= 1. + (k-12)/48. \qquad \text{for } k \geq 19 \\ akk &= 1. + (k-24)/48. \qquad \text{for } k = 25 \\ DF &= akk\left(1. + \frac{0.25}{nj-1} \cdot (j-1)\right) \qquad \text{for } k = 1, 6 \,\&\, k = 19, 25 \quad . \end{aligned} \tag{5.5}$$

Now the maximum values of akk are at the k=12 and k=24 plane compared to k=6 and k=18 in eqs. 5.2-5.3. Figure 5.20 compares the original disturbance and the rotated. It can be seen that the same intensity is used but the k=1 plane becomes the k=7 plane and the k=13 becomes k=19.

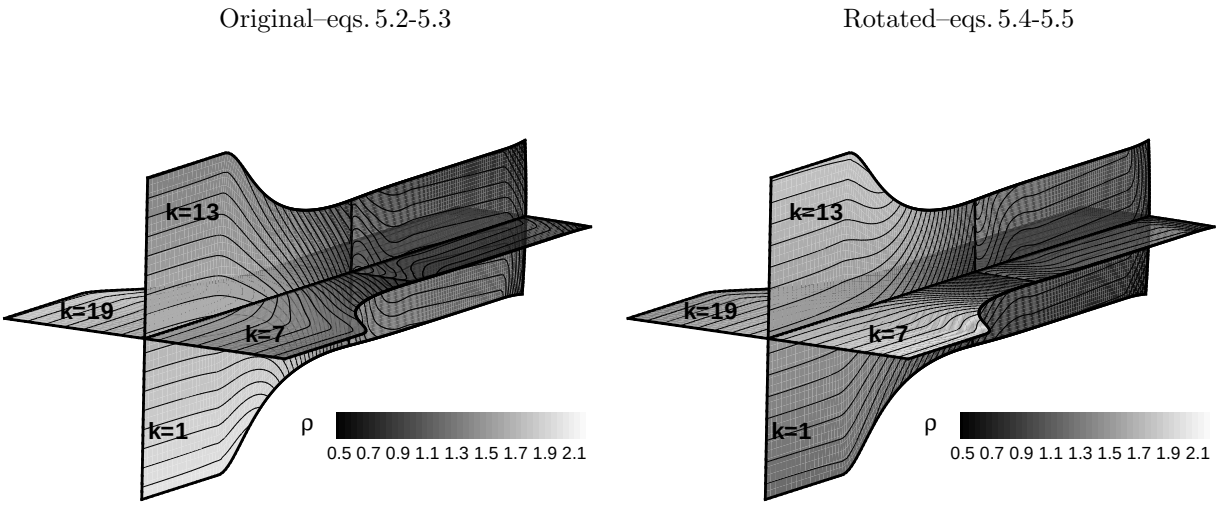

Figure 5.20.: Comparison between two different types of disturbances using a contour plot of ρ.

From the rotated disturbance the shock now rotates (fig. 5.21) in the clock wise direction with the same frequency.

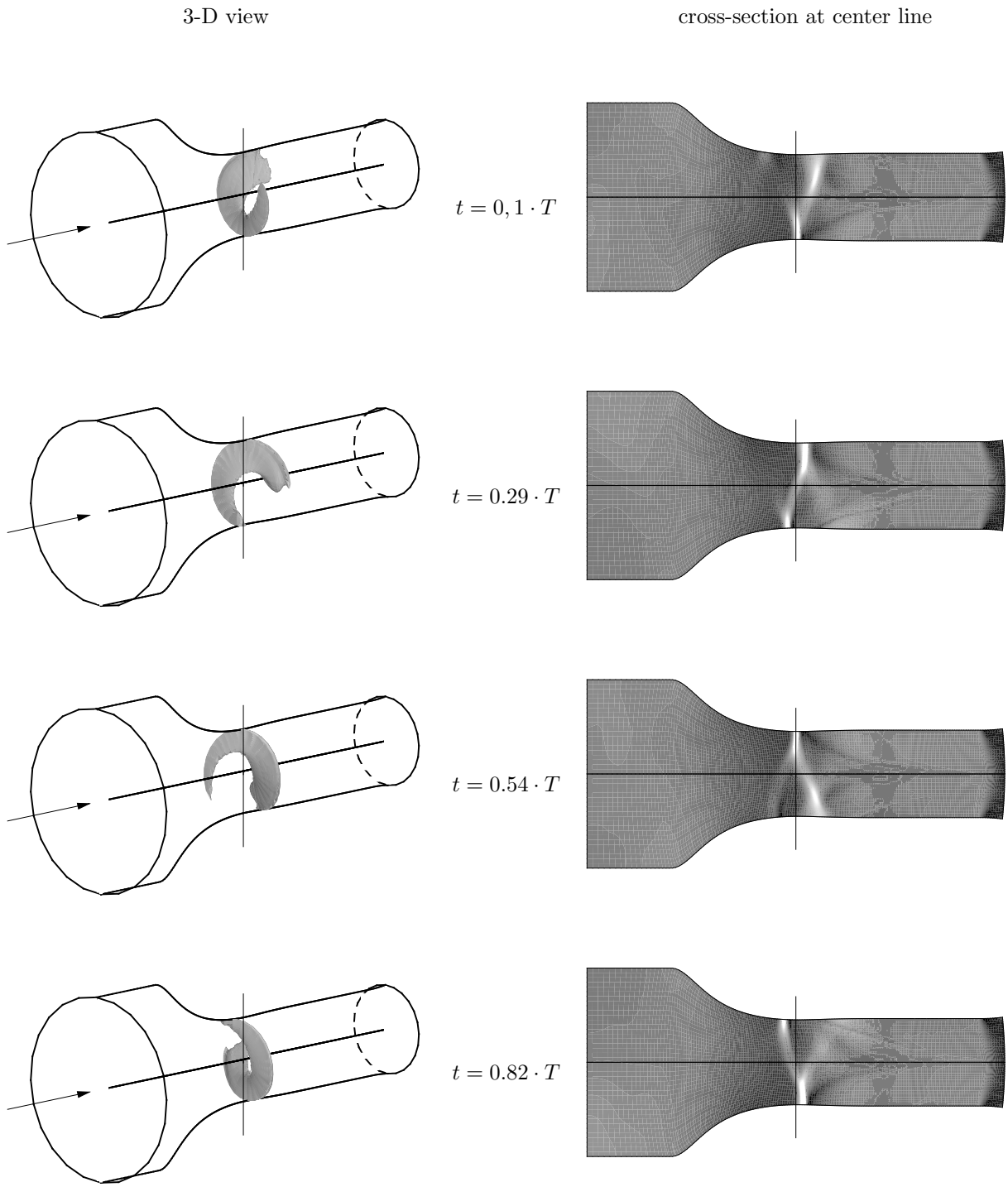

Figure 5.21.: Unsteady unsymmetric oscillation, rotated disturbance, [$T_{01} = 295$ K, $p_{01} = 1$ bar, $\phi_0 = 95\%$, $\mathbf{f \approx 1350Hz}$].

6. Airfoil Condensation

6.1. Circular Arc - Euler

6.1.1. Geometry and Grids

Previous work by Dohrmann and Schnerr [23], [81], [82], and [85] have done extensive 2-D Euler numerical simulations and experiments of homogeneous condensation on the circular arc bump with thickness (t=0.06, 0.1, 0.12) for zero angle of attack. It is the purpose here to recalculate the t=0.1 condition for a range of humidities to verify the new 3-D code predicts the same trends as the previous PhaseCD code used by Dohrmann. Important note is that the comparison is made between two numerical solutions, no experimental data is available for the conditions specified, but on the other hand there has been extensive experimental work on the circular arc in a transonic wind tunnel, which shows the structures seen in the numerical prediction. The purpose here is not to validate the code is able to predict the wind tunnel conditions, ex. top and side wall interference, back pressure, non-uniform inlet velocity...etc, but rather to predict the structures that were seen in the experiments.

The grid used by Dohrmann [23] is not available and no pictures of the grid could be found, but what is stated in [23] is that it was an O-grid, which was generated by a Poisson equation, with clustering at the stagnation regions. In this case an H-grid will be used on half the domain, the top boundary was made to slope slightly, thus taking on the characteristics of a c-grid, where the inlet curves around the airfoil. Figure 6.1 shows the boundary relations and grid used for the simulation. The ratios are consistent with what the code has demonstrated to handle and using a H-grid is a very simple way to achieve high grid quality around the arc fig. 6.2. Since the angle of attack is zero only half the domain is calculated and with Euler it is possible to use an Euler wall before and after the circular arc. Another technique would be to use an H-grid where the top boundary is the bottom side of the arc and the bottom boundary is the top surface, using periodicity for the line before and after the circular arc, but in this case it is not needed.

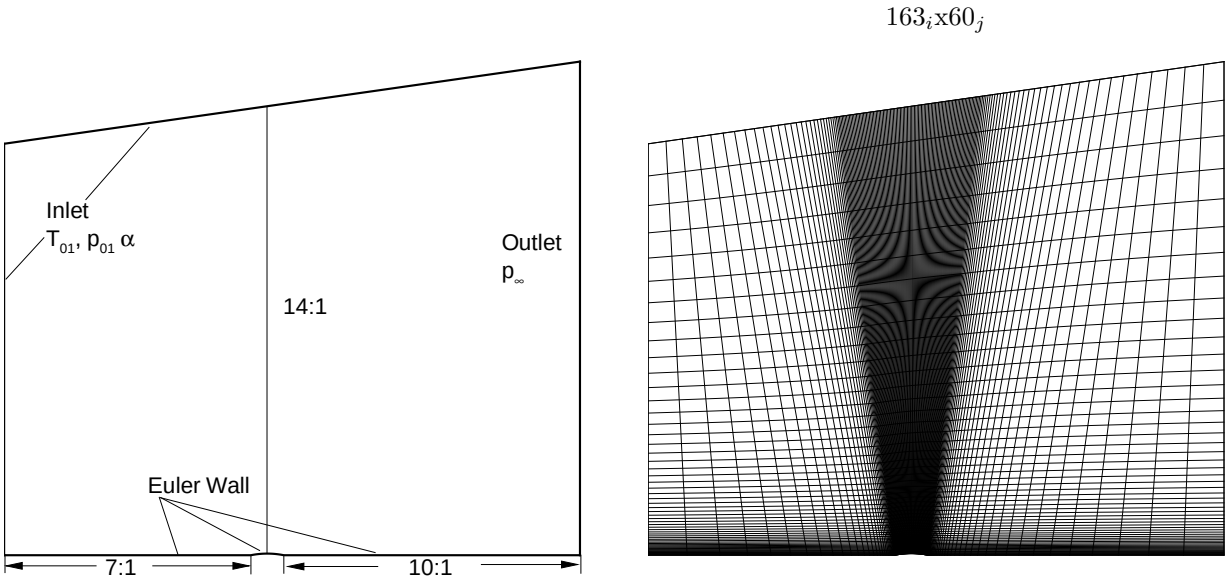

Figure 6.1.: CA-1 circular arc geometry with relation to boundaries and grid.

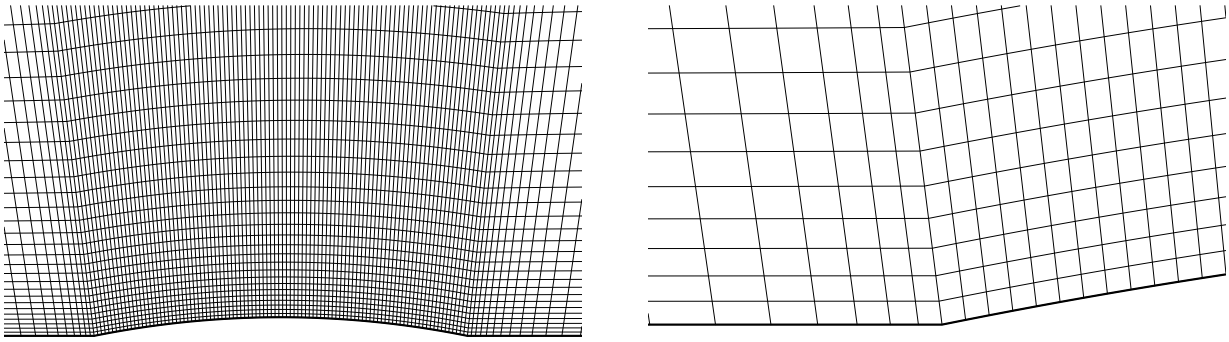

Figure 6.2.: CA-1 grid around the circular arc.

6.1.2. Adiabatic

The adiabatic solution for the CA-1 at $M_\infty = 0.87$ is presented in fig. 6.3. The shock strength and position match exactly with Dohrmann [23] or [82]. The predicted drag is also similar to Dohrmann with a 2% difference. The supersonic Mach contour shows the shock is normal at the wall which is then curved to match with the streamlines, where the shock is always perpendicular to the flow.

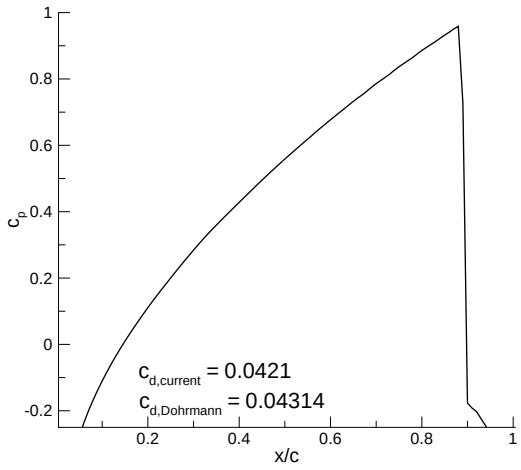

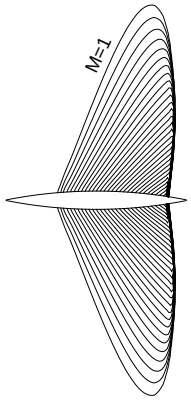

$\Delta M = 0.015$, $M_{max} = 1.43$

Figure 6.3.: c_p distribution and mirrored supersonic Mach contour around the CA-1 airfoil, [$T_{01} = 293$ K, $p_{01} = 1$ bar, $c = 80$ mm, $M_\infty = 0.87$, $\alpha = 0°$]

6.1.3. Diabatic

Moving to flow with heat addition the total conditions are kept constant and the humidity is increased from 30-65%. Figure 6.4 shows the supersonic Mach contour for the different humidities and the maximum Mach number reached. The adiabatic case is put in the center as a reference. As the humidity is increased it has the effect of increasing the pressure which lowers the maximum Mach number. At 30% the shock is reduced and shifted to the left, with a disturbance in the Mach contour near the shock from heat addition. At 40% the pattern is similar to 30%. At 50% the formation of the double shock is becoming present, also the structure of the adiabatic shock is altered. The double shock system is present at 65% with the first shock due to heat addition and the second shock the adiabatic shock. The maximum Mach number between 50% and 65% is similar where a minimum was reached at 60% (not shown). In all cases except at 65% the supersonic Mach contour matches that of Dohrmann [85]. The main difference at 65% is that in the current simulation the shock due to heat addition does not extend to the airfoil, this is also seen in Dohrmann but not as distinct in the current code, in that the Mach 1 line is continuous compared to the double shock seen on the NACA0012 airfoil(fig.6.10).

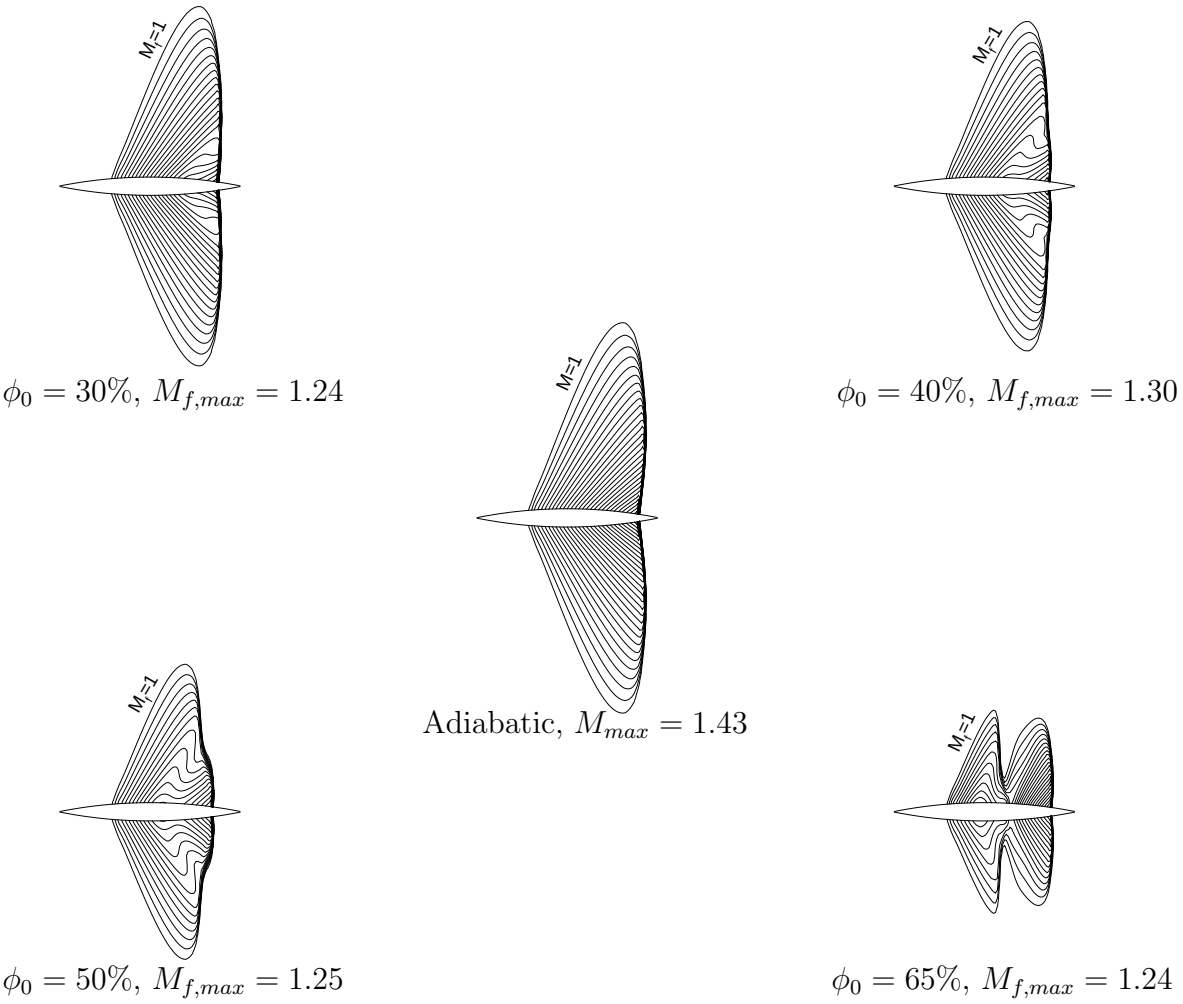

Figure 6.4.: Supersonic Mach contour mirrored around the CA-1 airfoil, [$T_{01} = 293$ K, $p_{01} = 1$ bar, $c = 80$ mm, $M_\infty = 0.87$, $\alpha = 0°$, $\Delta M_f = 0.015$].

Figure 6.5 examines a p-T diagram and Mach, J_{hom}, and g_{hom} distribution from a streamline close to the airfoil surface. Two humidities of 50 and 65% are compared. At 50% the freestream is super-saturated which then compresses back to 2 but not to the 01 point because for the circular arc the sharp leading edge has not a real stagnation point and the streamline is not intersecting this point. Again an expansion around the airfoil to point 3, but condensation starts before the shock, so there is a slight increase in temperature and decrease in Mach number to point 4. The shock, compression is after 4, which passes the saturation line causes the growth of g_{hom} to be cut off. Finally a small compression at 5 where g_{hom} decreases due to the trailing edge, but eventually increases and reaches a constant value in the wake.

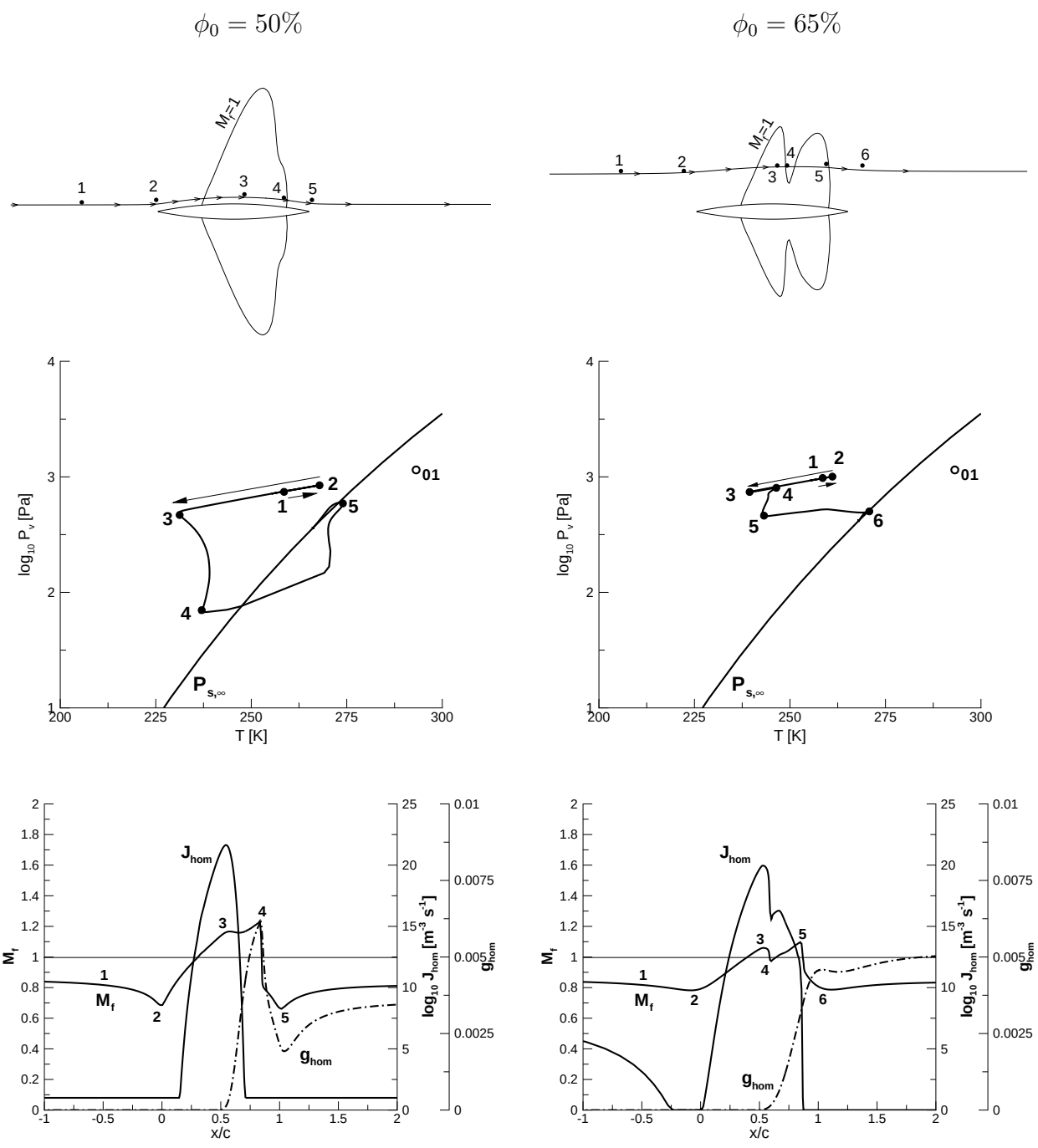

Figure 6.5.: Thermodynamic discussion along a streamline near the airfoil, [$T_{01} = 293$ K, $p_{01} = 1$ bar, $c = 80$ mm, $M_\infty = 0.87$, $\alpha = 0°$]

top	:	Mach l line and streamline near airfoil from which data is extracted
middle	:	p-T diagram with saturation line
bottom	:	Mach, J_{hom}, and g_{hom} distribution along streamline

For the case of 65% humidity the streamline was moved further away from the profile to pick up the double shock system. The main difference from 50% is the existence of a weak shock due to heat addition from 3-4. The weak shock cuts off the growth of J_{hom}, but then another expansion from 4-5 with the growth of g_{hom}, the heat addition increases the temperature like in the p-T diagram 3-4 for 50% but is less in the p-T for 65%, thus the temperature is decreasing due to the expansion. The adiabatic shock from 5-6 does cuts off the growth of g_{hom} but does not decrease or cause evaporation but rather a constant value that flows into the freestream. The reason for g_{hom} not to decrease is because the streamline is further from the profile, also the maximum value of g_{hom} is smaller for the 65% case but that is also because of the streamline location.

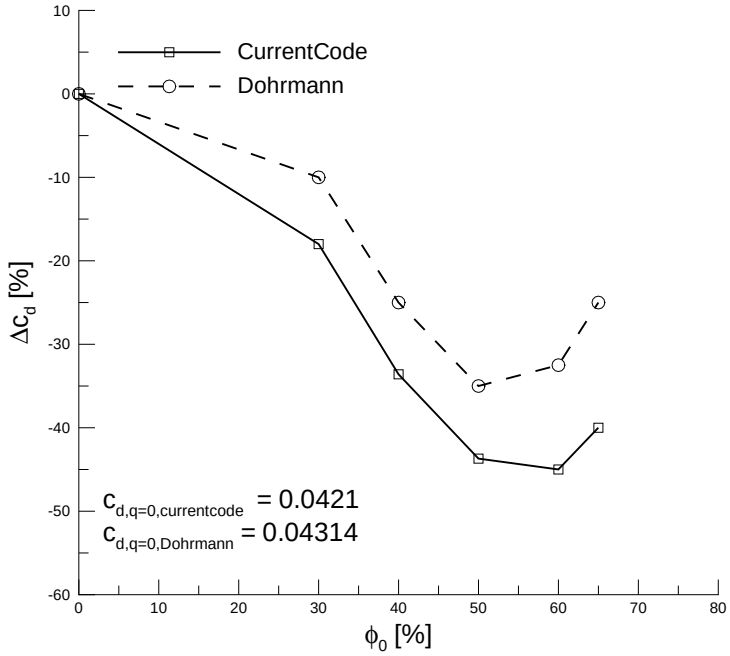

$$\Delta c_d = \frac{c_{d,q>0} - c_{d,q=0}}{c_{d,q=0}}$$

Figure 6.6.: Pressure drag increase due to homogeneous condensation on the CA-1 airfoil, [T_{01} = 293 K, $p_{01} = 1$ bar, $c = 80$ mm, $M_\infty = 0.87$, $\alpha = 0°$].

Figure 6.6 is a comparison to the former work of Dohrmann [85] in regards to the pressure drag coefficient. The main conclusion is that due to homogeneous condensation the pressure drag is decreasing for all humidities, which is the opposite trend for the NACA0012 (fig. 6.12). The reason for the decrease in drag is because the heat addition is causing the shock to occur earlier and the heat addition is occurring after the maximum thickness (see

fig.6.5 bottom). The movement of the shock causes an area of high pressure to increase after the maximum thickness. Also the heat addition is occurring in supersonic flow which results in a static pressure increase, thus also helping to increase drag. Unfortunately the drag comparison between Dohrmann [85] and the current code is remarkably different compared to the NACA0012 case (fig.6.12). The adiabatic drag comparison is in good agreement thus the use of a different grid is most likely not the reason. At 50% Dohrmann reports a drag coefficient of $c_{d,p}$=0.03281, the current code calculates $c_{d,p}$=0.0237, making a difference 0f 30%. In the NACA0012 drag the current code was consistently calculating higher drag values which means the effects of condensation were higher which matches the theme here because if condensation is higher the reduction is greater. Since the pre-shock Mach numbers are much higher than the NACA0012 case any small change in the shock location will have a much larger effect on drag. Thus it is not the case that the NACA0012 case is showing a better comparison than the circular arc case but instead the difference is amplified in the circular arc case. Looking into differences between the modeling of Dohrmann and the current code, there are no differences in the physical parameters, σ, ρ_l, L,..etc or in the use of droplet growth law and classical nucleation theory. The only difference in the condensation models is Dohrmann used 4 additional transport equations based on the work of Hill [40], where the current code uses two additional transport equations based on the condensate mass and droplet number from Heiler [39]. The most likely reason for the difference is in the calculation of the thermodynamic variables themselves, thus in using 3rd order in space for the convective fluxes instead of 2nd order and the AUSMD scheme instead of the flux interpolation scheme of Eberle [27]. A small difference in the calculation of density and pressure changes the amount of condensate formed, where a small difference in heat addition for the strong shocks relates to large differences in drag.

6.2. NACA0012 - Euler

6.2.1. Geometry and Grids

Previous work by Dohrmann and Schnerr [23],[82], and [85] have done extensive 2-D Euler numerical simulations of homogeneous condensation on the NACA0012 airfoil for zero and small angles of attack. It is the purpose here to recalculate some of the conditions to verify the new 3-D code predicts the same trends as the previous PhaseCD code used by Dohrmann. Important note is that the comparison is made between two numerical solutions, no experimental data is available. On the other hand there has been many experiments that show the development of a double shock on a curved surface in a wind tunnel. Besides the comparison with previous work it is also an important issue for completeness in the thesis, thus before going to a complex solution of condensation on a 3-D swept wing it is important to examine the physics of condensation on a 2-D airfoil.
The grid used by Dohrmann [23] is not available but what is known is that it was an O-grid which used 192_ix64_j nodes. Figure 6.7 shows the boundary relations to the NACA0012 airfoil and the grid. Due to early inexperience in grid production, the boundary relations are not typical for a freestream calculation of an airfoil because the outflow is shorter than the inflow. Although, with the boundary conditions used for the inlet and outlet see subsec. 3.2.4.2 the simulations provide good results in relation to adiabatic shock position and drag. Figure 6.8 shows a closeup of the Euler grid near the airfoil and around the nose.

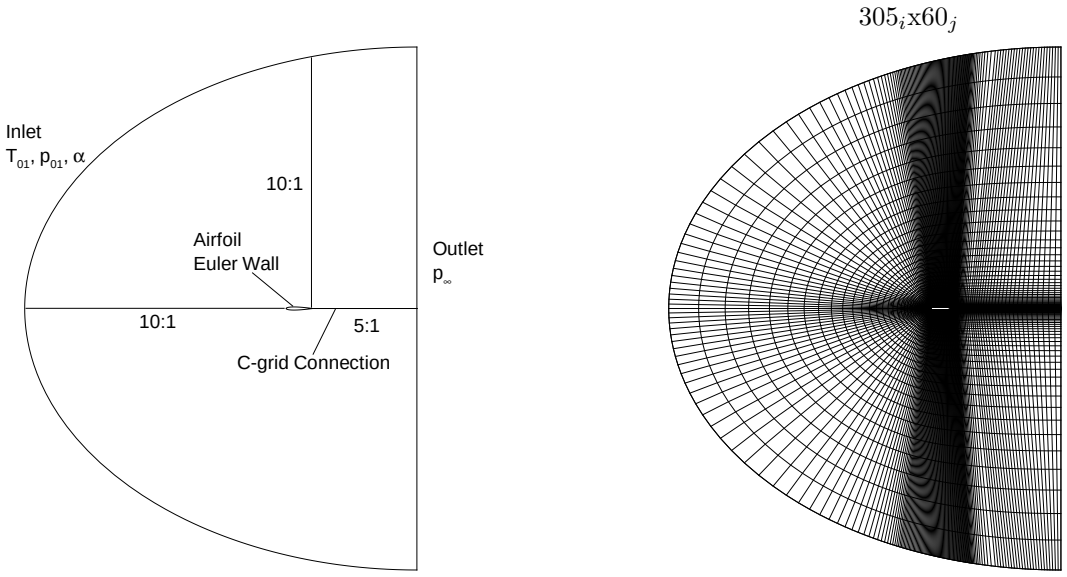

Figure 6.7.: NACA0012 geometry with relation to boundaries and grid

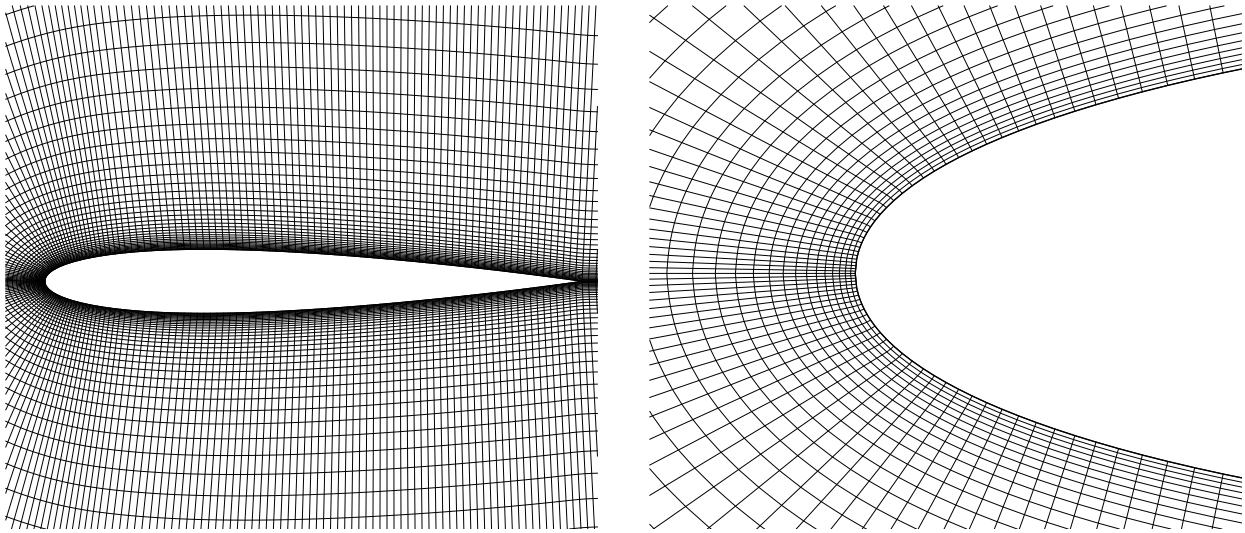

Figure 6.8.: NACA0012 grid around the airfoil

6.2.2. Adiabatic

The adiabatic solution for the NACA0012 at $M_\infty = 0.8$ is a well known test case for the shock position and drag (tab. 6.1). The shock occurs at 50% chord, the grid and numerical code are able to capture the correct position of the shock, which can also be seen in fig.6.9 (left). Figure 6.9 (right) shows the supersonic Mach contour around the airfoil, which gives an idea of the supersonic region and the quality of the code to resolve a shock.

Table 6.1.: Comparison of the pressure drag coefficient with other researchers.

	Current Code	Dohrmann[82]	Jameson[42]
c_d	0.00862	0.00845	0.0086

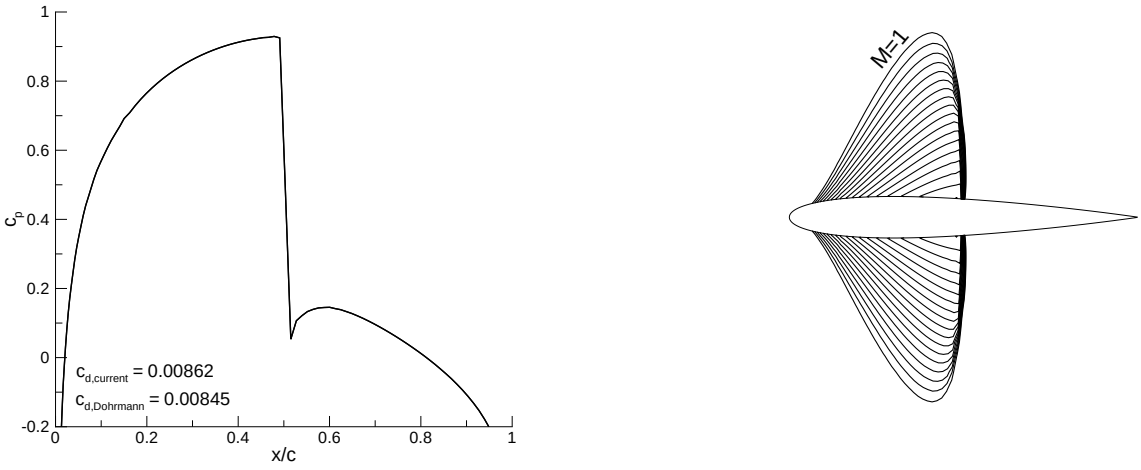

Figure 6.9.: c_p distribution and supersonic Mach contour around the NACA0012 airfoil, [T_{01} = 293 K, $p_{01} = 1$ bar, $c = 100$ mm, $M_\infty = 0.8$, $\alpha = 0°$]

6.2.3. Diabatic

Moving to flow with heat addition the total conditions are kept constant and the humidity is increased from 30-70%. Figure 6.10 shows the supersonic Mach contour for the different humidities and the maximum Mach number reached. The adiabatic case is put in the center as a reference. As the humidity is increased it has the effect of increasing the static pressure which lowers the Mach number, at 50% a distinct difference has occurred with 60% starting to show the double shock system. The trends found in fig. 6.10 matches that of Dohrmann [85]. Up to 60% the shock is an adiabatic shock due to the freestream condition is subsonic and the local supersonic flow on the airfoil must return to subsonic, but at 70% a weak shock due to heat addition first appears and then the flow re-accelerates to supersonic, followed by an adiabatic shock.
Figure 6.11 examines a p-T diagram and Mach, J_{hom}, and g_{hom} distribution from a streamline close to the airfoil surface. Two humidities of 50 and 70% are compared. At 50% the freestream is super-saturated which then compresses back to the saturation line at 2 but not exactly to the 01 point because the streamline is not going into the stagnation point. Again an expansion around the airfoil to point 3, but condensation starts before the shock, so there is a slight increase in temperature and decrease in Mach number. The shock, compression is from 4-5, which passes the saturation line causes the growth of g_{hom} to be cut off. Finally a small compression at 6 where g_{hom} decreases due to the trailing edge, but eventually increases and reaches a constant value in the wake.

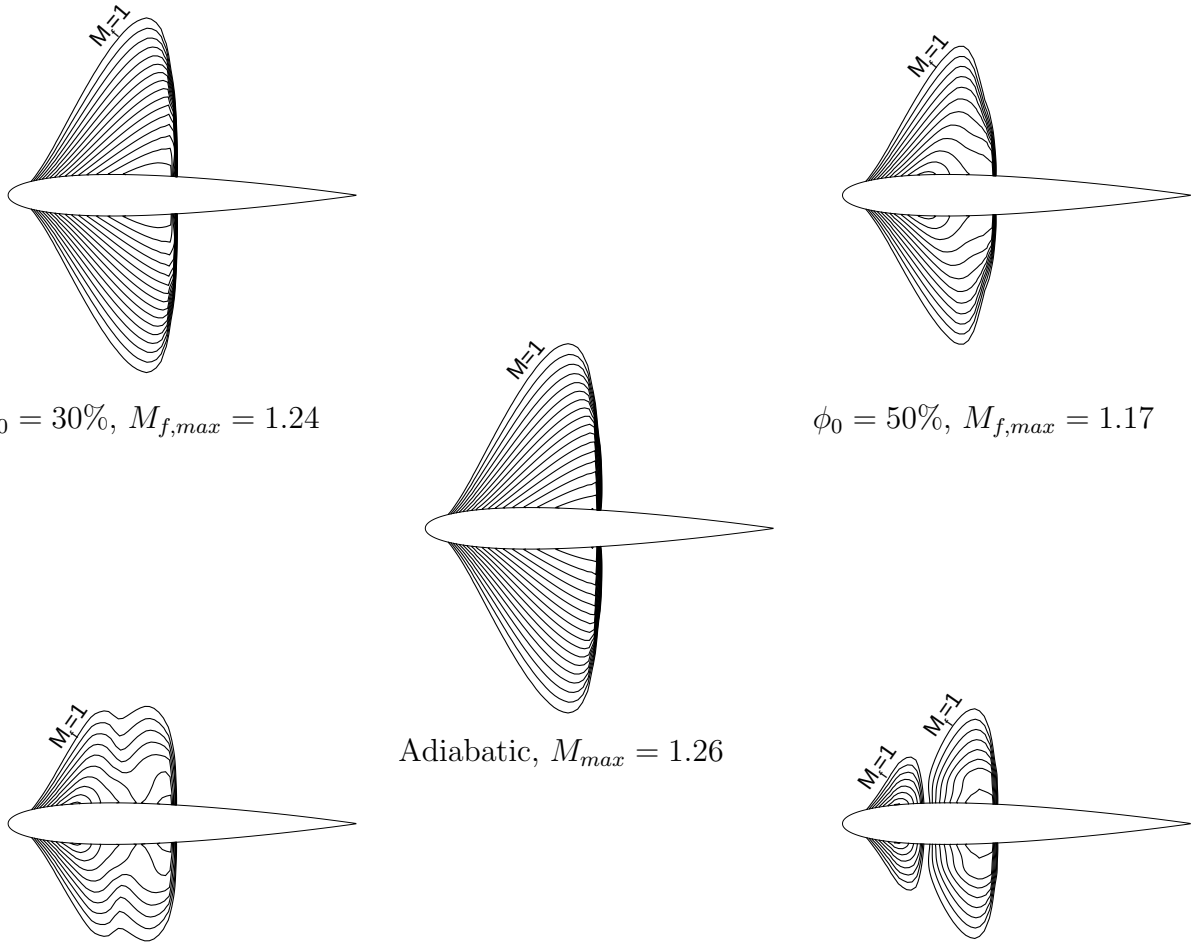

$\phi_0 = 30\%$, $M_{f,max} = 1.24$

$\phi_0 = 50\%$, $M_{f,max} = 1.17$

Adiabatic, $M_{max} = 1.26$

$\phi_0 = 60\%$, $M_{f,max} = 1.14$

$\phi_0 = 70\%$, $M_{f,max} = 1.13$

Figure 6.10.: Supersonic Mach contour around the NACA0012 airfoil, [$T_{01} = 293$ K, $p_{01} = 1$ bar, $c = 100$ mm, $M_\infty = 0.8$, $\alpha = 0°$, $\Delta M_f = 0.015$].

For the case of 70% humidity the main difference is the existence of a weak shock from 3-4 and a slightly stronger shock from 5-6. Also the growth of g_{hom} is much steeper, which is the reason for the weak shock due to heat addition and since it occurs early on the airfoil, the flow has enough time to expand to supersonic for the adiabatic shock (5-6). Again it is this adiabatic shock (5-6) that cuts off the growth of g_{hom}

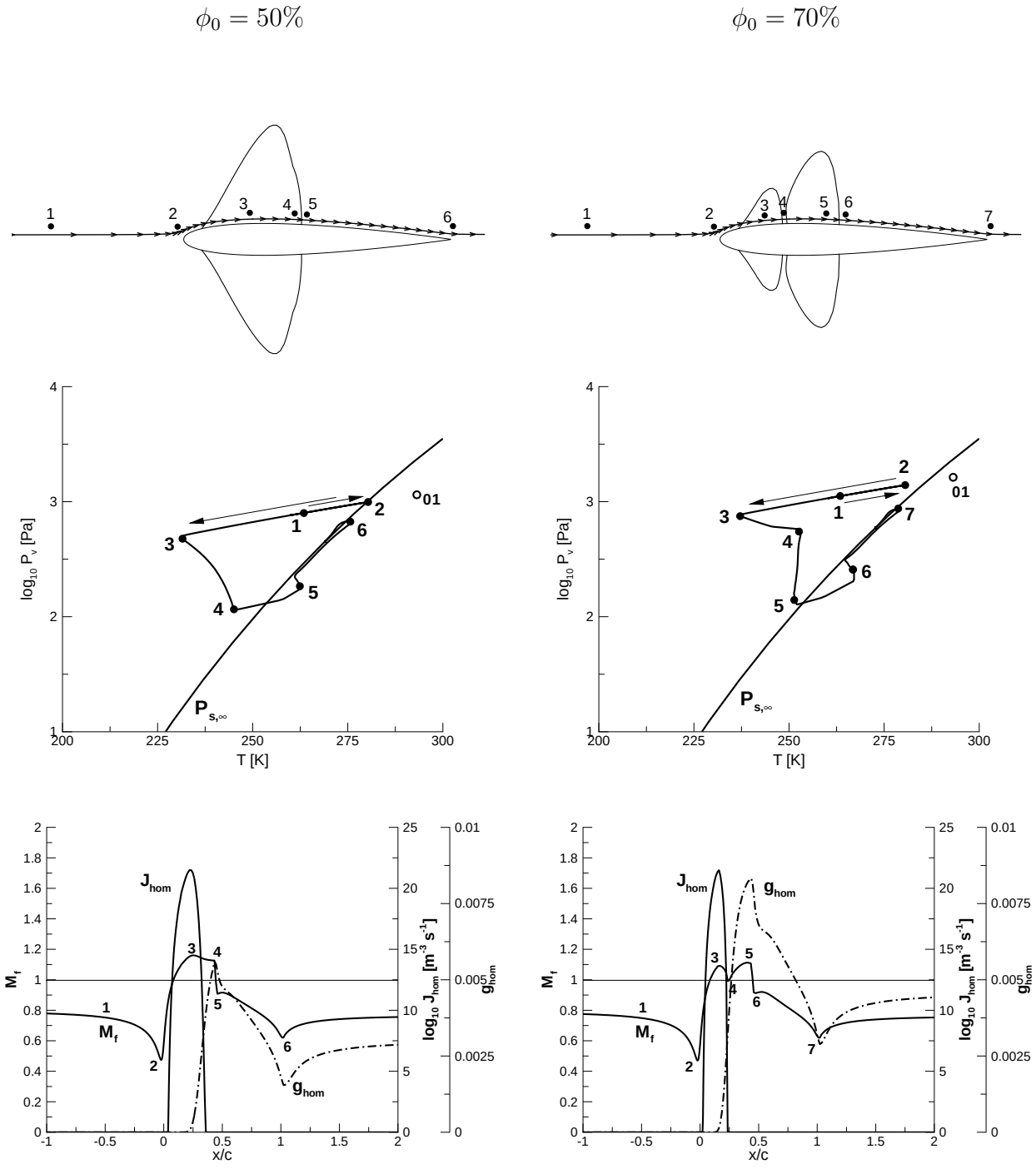

Figure 6.11.: Thermodynamic discussion along a streamline near the airfoil, [$T_{01} = 293$ K, $p_{01} = 1$ bar, $c = 100$ mm, $M_\infty = 0.8$, $\alpha = 0°$]

top	:	Mach l line and streamline near airfoil from which data is extracted
middle	:	p-T diagram with saturation line
bottom	:	Mach, J_{hom}, and g_{hom} distribution along streamline

Figure 6.12 is a comparison to the former work of Dohrmann [85] in regards to the pressure drag coefficient. The main conclusion is that due to homogeneous condensation the pressure drag is increasing for humidities $> 30\%$. The main reason for the increase in drag is due to heat addition (static pressure increase) before the maximum thickness of the airfoil. The second conclusion is that small differences appear in the pressure drag coefficient between the former work of Dohrmann and the current 3-D code. See the end of the previous section for possible reasons for the difference in drag.

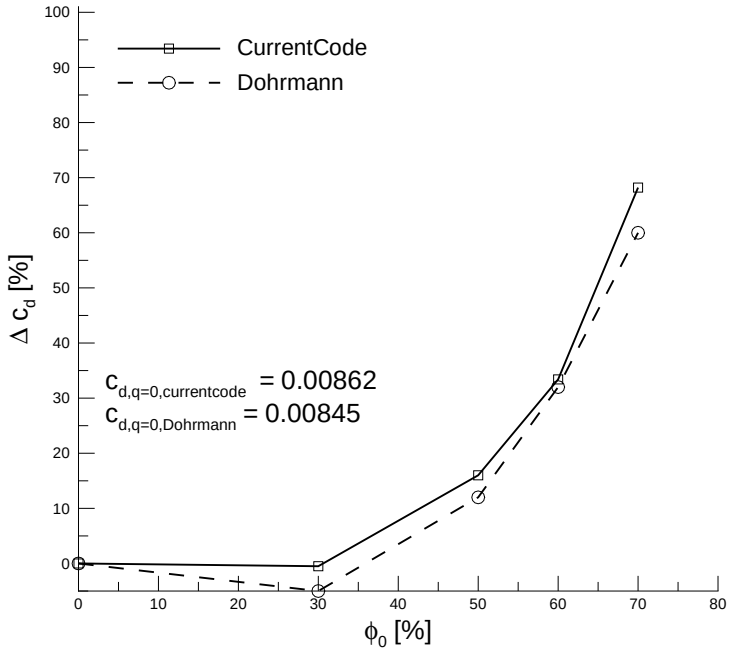

$$\Delta c_d = \frac{c_{d,q>0} - c_{d,q=0}}{c_{d,q=0}}$$

Figure 6.12.: Pressure drag increase due to homogeneous condensation on the NACA0012 airfoil,[$T_{01} = 293$ K, $p_{01} = 1$ bar, $c = 100$ mm, $M_\infty = 0.8$, $\alpha = 0°$].

6.3. RAE2822 - Turbulent

6.3.1. Geometry and Grids

The RAE2822 airfoil was used as a validation test case for turbulence models in subsec. 4.3.2. The same geometry and grid (fig 4.36 and 4.37) are used in this section. The aim of the RAE2822 is to examine the effects of homogeneous condensation on a supercritical airfoil at a small angle of attack with viscous flow. The EASM($k-\omega$) turbulence model is used to model the effects of turbulence which are small for this case at the given angle and Mach number. The main difference here from the NACA0012 is the airfoil is no longer symmetric, viscous effects, and there is now lift involved.

6.3.2. Adiabatic

The adiabatic solution for the RAE2822 at $M_\infty = 0.75$ is also a standard test case for testing CFD models. In subsec. 4.3.2 an angle of 2.31 was used with $M_\infty = 0.75$ and good agreement was obtained between experiment. Here the angle will be rounded up to 3° because the interest lies in the how the adiabatic solution is altered due to heat addition. Figure 6.13 shows the c_p distribution and supersonic contour on the profile. A small compression exists near the nose, followed by a slight expansion to the adiabatic shock.

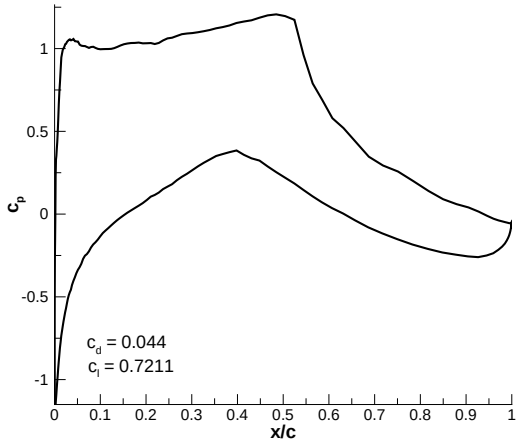

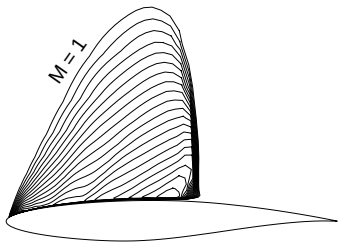

$\Delta M = 0.015$, $M_{max} = 1.30$

Figure 6.13.: c_p distribution and supersonic Mach contour around the RAE2822 airfoil, [$T_{01} = 293$ K, $p_{01} = 1$ bar, $c = 100$ mm, $M_\infty = 0.8$, $\alpha = 0°$]

6.3.3. Diabatic

Moving to flow with heat addition the total conditions are kept constant and the humidity is increased from 30-70%. Figure 6.14 shows the supersonic Mach contour for the different humidities and the maximum Mach number reached. For the supercritical airfoil the supersonic region is only on the top compared with the NACA00012. As the humidity is increased it has the effect of increasing the static pressure which lowers the Mach number. At 50% the supersonic region has been reduced with a lowering of the maximum Mach number, at 60% a second shock region is forming and the compression near the nose is becoming more distinct. At 70% like in the NACA0012 case there are two distinct shocks, where the first shock is due to heat addition and the second is the adiabatic shock.

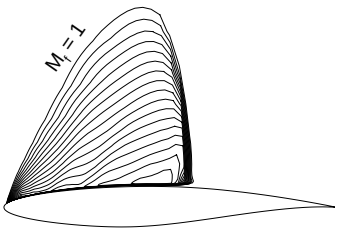

$\phi_0 = 30\%$, $M_{f,max} = 1.25$

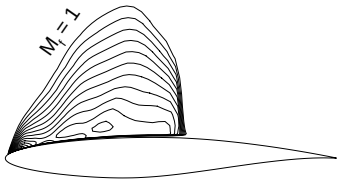

$\phi_0 = 50\%$, $M_{f,max} = 1.21$

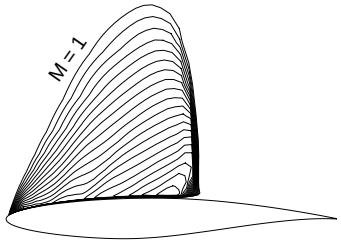

Adiabatic, $M_{max} = 1.30$

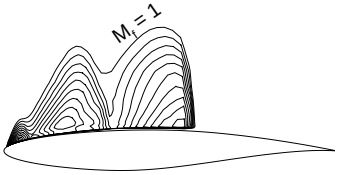

$\phi_0 = 60\%$, $M_{f,max} = 1.20$

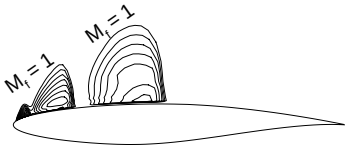

$\phi_0 = 70\%$, $M_{f,max} = 1.18$

Figure 6.14.: Supersonic Mach contour around the RAE2822 airfoil, [$T_{01} = 293$ K, $p_{01} = 1$ bar, $c = 100$ mm, $M_\infty = 0.75$, $\alpha = 3°$, $Re_{\infty,c}$= 1.34 million]

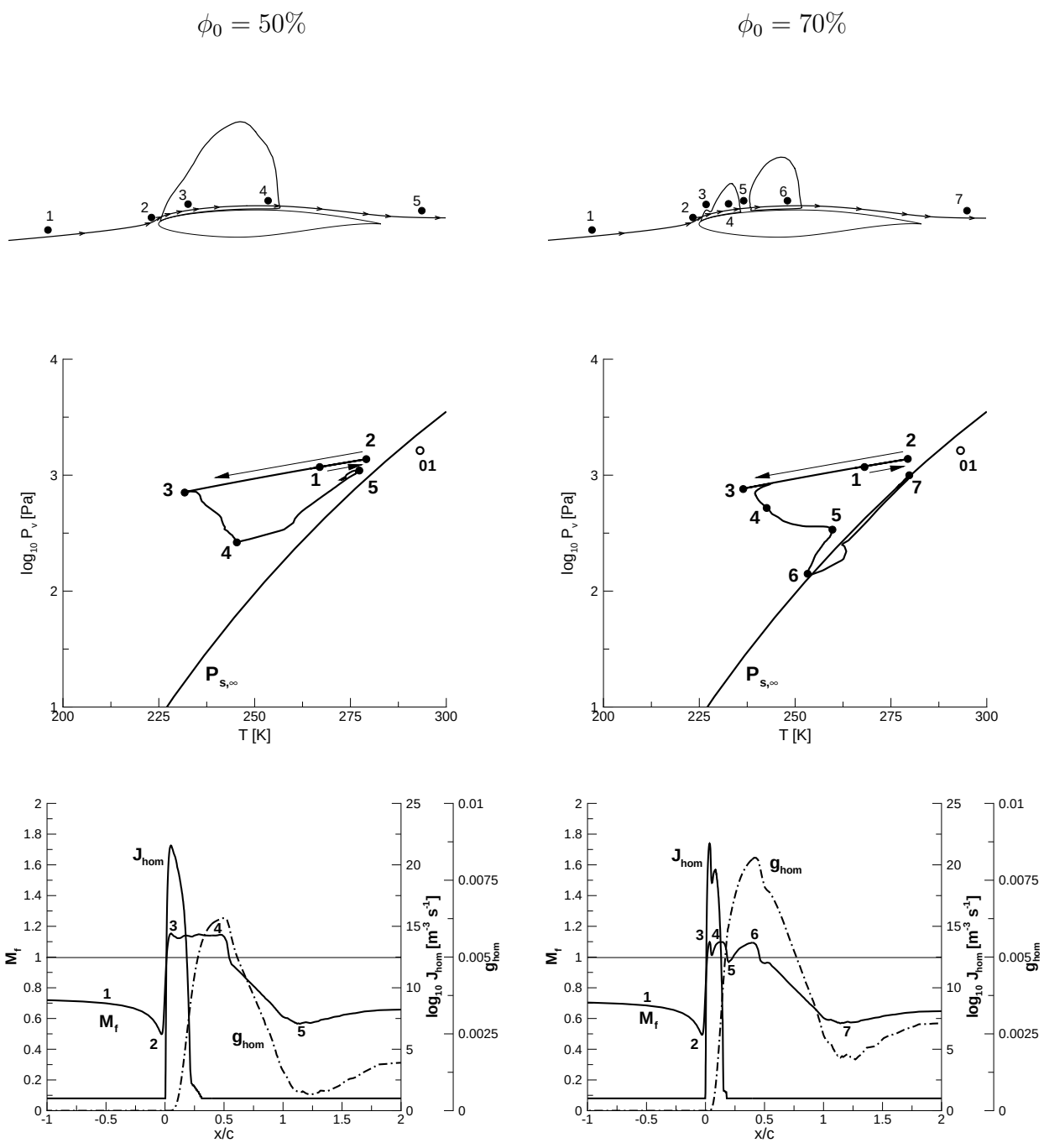

Figure 6.15.: Thermodynamic discussion along a streamline near the airfoil, [T_{01} = 293 K, $p_{01} = 1$ bar, $c = 100$ mm, $M_\infty = 0.75$, $\alpha = 3°$, $Re_{\infty,c}$= 1.34 million]

top	:	Mach l line and streamline near airfoil from which data is extracted
middle	:	p-T diagram with saturation line
bottom	:	Mach, J_{hom}, and g_{hom} distribution along streamline

Figure 6.15 examines a p-T diagram and Mach, J_{hom}, and g_{hom} distribution from a streamline close to the airfoil surface. Two humidities of 50 and 70% are compared. A difference between the RAE2822 airfoil compared to the NACA0012 (fig. 6.11) is at point 3 there is the expansion but then a recompression along the expansion line, where with the growth of g_{hom}, the deviation to point 4 begins. The adiabatic shock 4-5 cuts off the growth of g_{hom}, with the addition of a decrease in g_{hom}. At 70% the same trend as the NACA0012 fig(6.11, right) is present but the compression around the leading edge is much stronger than in the 50% case, also the shock due to heat addition is stronger compared to the NACA0012 at 70%. The nucleation rate is altered by the strong compression, which then begins to rise again until g_{hom} begins to grow. Again the adiabatic shock cuts off and decreases g_{hom}.
With the NACA0012 the drag increased for all cases compared to the adiabatic (fig. 6.12) but for the RAE2822 (fig. 6.16, right) the drag actually decreases and then increases passing through zero somewhere between 60 and 70% humidity. Since lift is present it is also possible to see the effect on lift, which shows a decrease in lift for all humidity cases. This trend also matches that found by Dohrmann[85] for the NACA0012 at $\alpha = 1.25°$. Although with the NACA0012 there was a decrease in lift to a minimum ($\phi_0 = 60\%$) and then it started to increase, whereas for the RAE2822 lift is only decreasing. A possible reason for this difference is the NACA0012 at $\alpha = 1.25°$ still has a supersonic region on the pressure side which starts to decrease at 60%, thus the static pressure increase on the pressure side could take away from the negative effect of static pressure increase on the suction side due to heat addition.

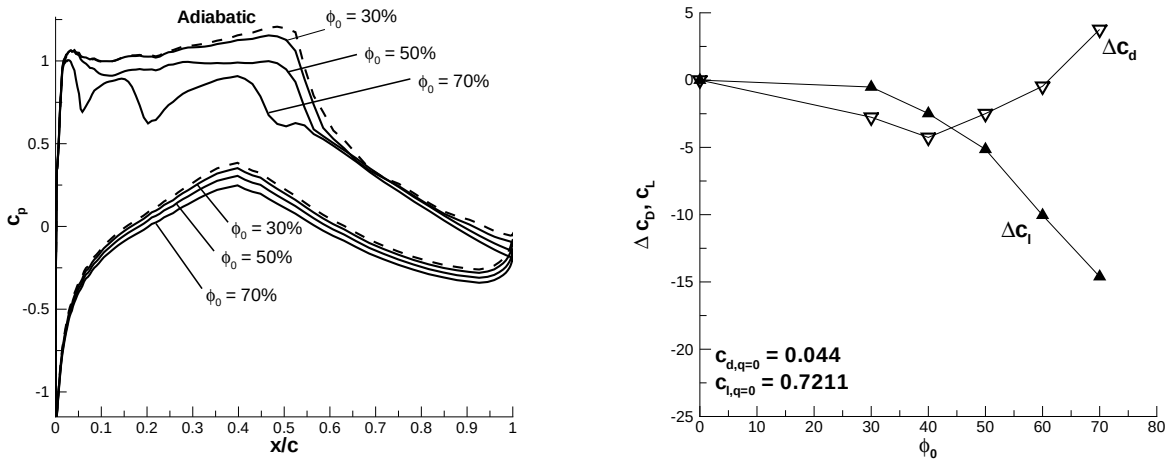

$$\Delta c_d = \frac{c_{d,q>0} - c_{d,q=0}}{c_{d,q=0}}$$

Figure 6.16.: c_p and drag/lift comparison between adiabatic and diabatic flow, [T_{01} = 293 K, p_{01} = 1 bar, c = 100 mm, $M_\infty = 0.75$, $\alpha = 3°$, $Re_{\infty,c}$= 1.34 million]

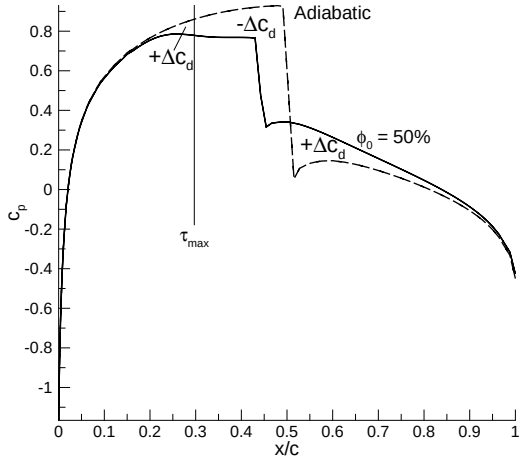

NACA0012, $M_\infty = 0.8$, $\alpha = 0°$, M_{max}=1.17
Euler

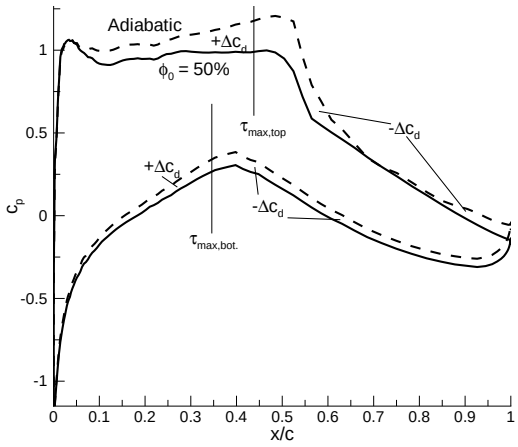

RAE2822, $M_\infty = 0.75$, $\alpha = 3°$, M_{max}=1.21
Turbulent $Re_{\infty,c}$= 1.34 million

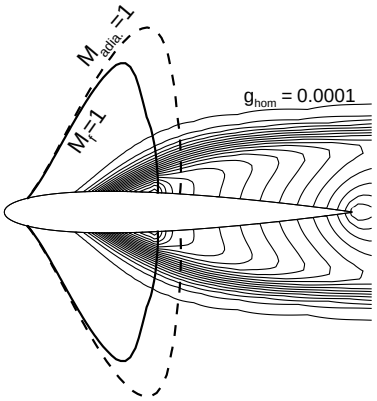

$\Delta g_{hom} = 0.0003$, $g_{hom,max} = 0.0059$

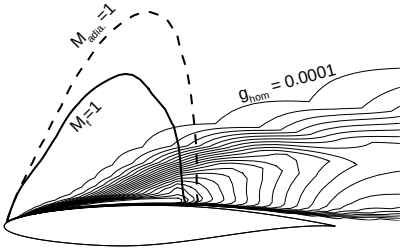

$\Delta g_{hom} = 0.0003$, $g_{hom,max} = 0.0064$

Figure 6.17.: Comparison between NACA0012 and RAE2822 airfoil in regards to drag, [T_{01} = 293 K, $p_{01} = 1$ bar, $c = 100$ mm].

top : c_p distribution for adiabatic and 50% humidity with the x-location of the maximum thickness of the airfoil.

bottom : Mach 1 line and g_{hom} contour to see the effect where heat addition starts on the airfoil.

It is also of interest to examine why there is a decrease in drag for the RAE2822 airfoil at 50%, where there is an increase in the NACA0012 for the same humidity.
From the graphs in fig. 6.17 the following conclusions are drawn. The heat addition before τ_{max} results in a $+\Delta c_d$ for both airfoils. Also the shock occurring earlier or closer to the leading edge due to heat addition results in a $-\Delta c_d$ for both airfoils. In regards to an

Euler simulation the adiabatic shock occurring earlier due to heat addition is much weaker, resulting in a higher c_p compared to with no heat addition, thus increasing drag, noted by the second $+\Delta c_d$ in fig. 6.17 top-left. Whereas, with a viscous simulation the shock is smeared and this difference is not as distinct. It is also not an easy thing to only compare the areas between the adiabatic and diabatic c_p plot because the angle of the surface is very important in saying how much of the pressure is contributed to drag and how much goes to lift. Another important benefit for the supercritical airfoil with heat addition is that the flow is altered in a way to increase the pressure side as humidity is increased, shown in fig. 6.16, left. The change in drag due to heat addition is a complicated phenomena that depends on ϕ_0, shape of the airfoil, α, and M_∞.

7. Wing Condensation

7.1. Infinite Wing

The main idea of the swept wing was developed independently by two people, Adolf Busemann in 1935 and R.T. Jones in 1945 [5]. Figure 7.1 shows the plane view of a straight and swept infinite wing with a corresponding airfoil. If the wing is then swept by 45° the normal Mach number M_n is reduced and in this case it is reduced below the critical Mach number for a NACA0012 airfoil, which is around 0.72. The lower critical Mach number means the wing can undergo a higher free stream Mach number without the huge increase in drag due to compressibility effects (shocks). The above theory is well known and has been in practice since WW II.

Homogeneous-Wind Tunnel Scale
The new point is how condensation effects the lift to drag ratio due to the sweeping of the wing. If the critical Mach number is reduced due to the sweeping effect it is most likely that the condensation onset Mach number is also reduced. In the straight wing case homogeneous condensation would occur near the sonic line, increasing the static pressure which would increase drag. In the case of the swept wing, due to the disappearance of the supersonic region it is reasonable to assume no condensation would occur, thus no increase in drag. In fig. 7.1 the p-T diagram shows the difference in the super-saturation of the air, both cases have the same total, freestream and saturation point, but it is the T_{min} that is different, the less super-saturation the less likely homogeneous condensation can occur. The open circle in the p-T diagram is in regards to that for a swept wing the stagnation line still has a component of velocity that is not zero, so it does not match with the 01 point. For this case the airfoil is symmetric and the angle of attack is zero, thus no lift. For the straight wing, if lift were present homogeneous condensation would decrease the lift due to the static pressure increase on the suction side. In general the swept wing delays or prevents condensation from occurring, which prevents the decrease in the lift to drag ratio.

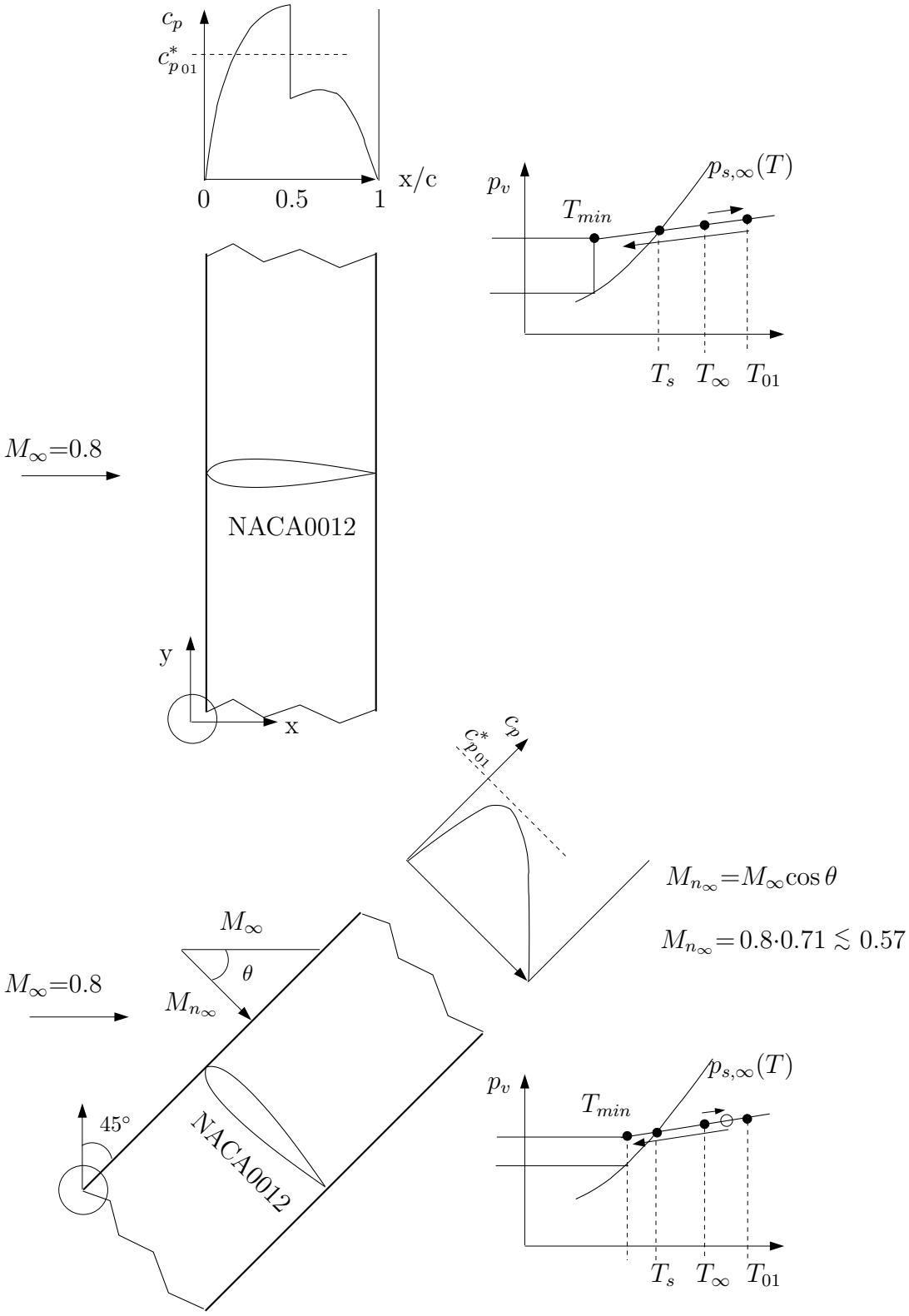

Figure 7.1.: Schematic diagram of a straight and an infinite swept wing with airfoil section.

Heterogeneous-Atmospheric Flight Scale

In fig.7.1 it is shown that the supersonic region is reduced or disappears due to the sweeping effect. In the case of heterogeneous condensation it is possible that if a supersonic region exist, the presence of heterogeneous condensation can enlarge the supersonic region by shifting the shock further to the trailing edge, which increases lift. If the sweeping effect prevents condensation then it prevents this benefit of increased lift. Although heterogeneous condensation requires less of a super-saturation, it is still possible that condensation would occur in the p-T diagram, fig. 7.1 (bottom). With heterogenous condensation there is also a pressure increase which increases drag for this increased lift, so the lift to drag ratio can either be increased or decreased depending on the angle of attack, amount of water vapor, amount of particulates in the air, size of particulates, ..etc. Thus it is necessary to perform numerical simulations of heterogeneous condensation to see the effect on the lift to drag ratio.

7.2. Atmospheric Flight–ONERA M6 Wing - Turbulent

7.2.1. Geometry and Grid

The ONERA M6 [79] is a swept backed wing with zero twist, no body fillets or strakes. The airfoil is symmetric with a 9.7% thickness at the root. Figure 7.2 displays the top view of the wing and root profile. The test case was designed for three dimensional effects from low to transonic speeds at high Reynolds number. The experimental data include pressure measurements at 7 spanwise locations for a range of Mach numbers between 0.7 - 0.93 and angles of attack between 0° and 6°. Figure 7.3 shows the wing in the experimental chamber.

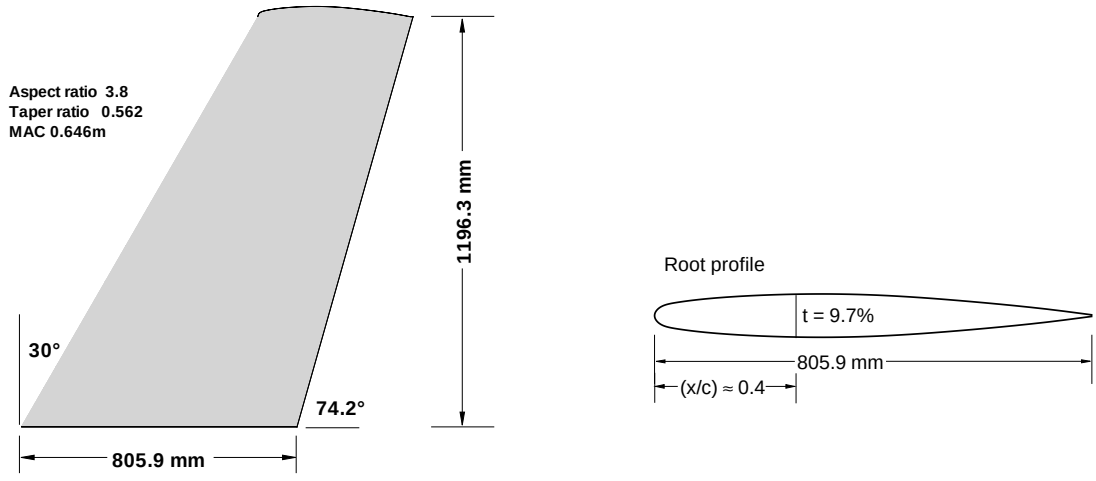

Figure 7.2.: Geometry of the ONERA M6 wing based on experiment.

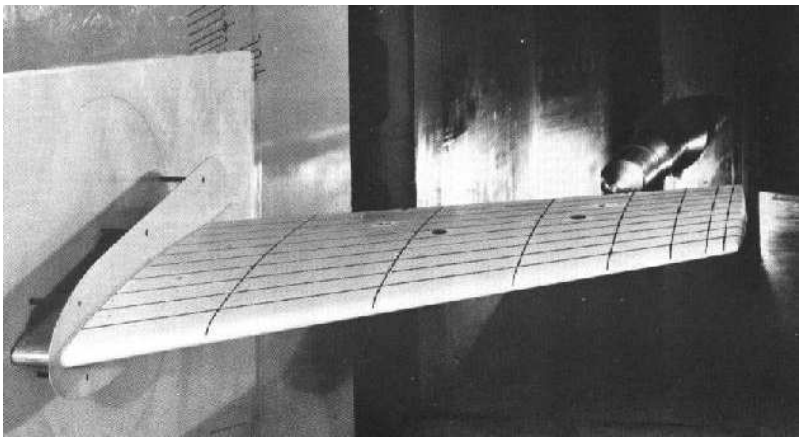

Figure 7.3.: Picture of the experimental setup for the ONERA M6 Wing [79].

Figures 7.4 and 7.5 show different angles of the grid. The cross-section of the wing shows the dense clustering near the airfoil, first grid point 1x10^{-6} m, which is needed for integration to the wall with Reynolds number in the range of 1 to 50 million. In the far field the grid is very coarse since gradients in the primitive variables are nearly zero.

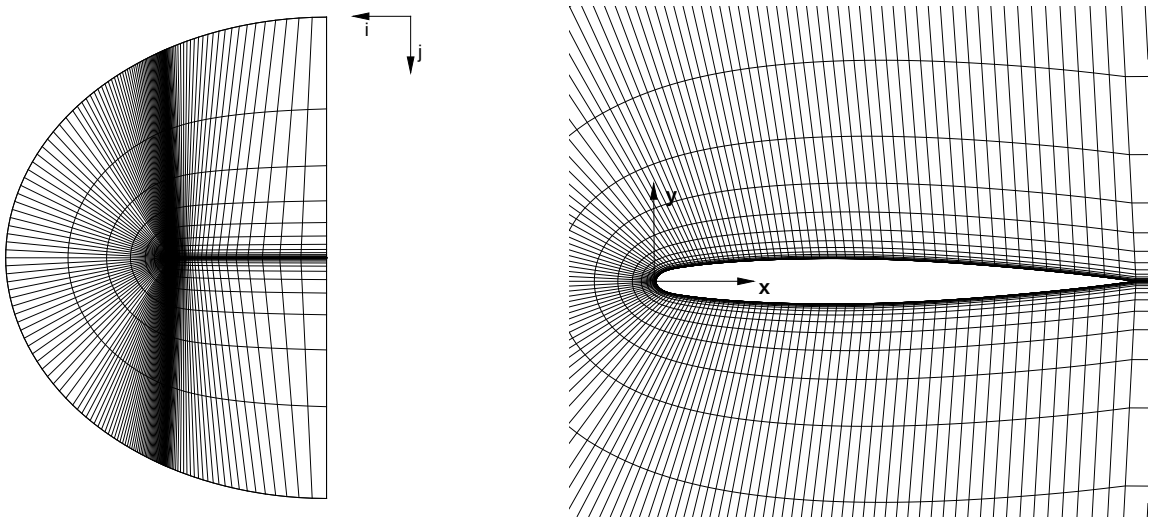

Figure 7.4.: Side view cross-section of wing i=273 and j=40 nodes, [$\Delta y_{wall-1st\,grid\,pt.}$ = 1x10^{-6} m, which is $\approx$ 12-15 grid points in the boundary layer], Left: entire cross-section, Right: closeup view around the airfoil.

The top view of the wing (fig.7.5, right) shows clustering of cells near the root and tip. The grid in (fig.7.5, left) was left out before and after the wing, so the wing can be distinguished, thus showing the beginning of the tip to the far field.

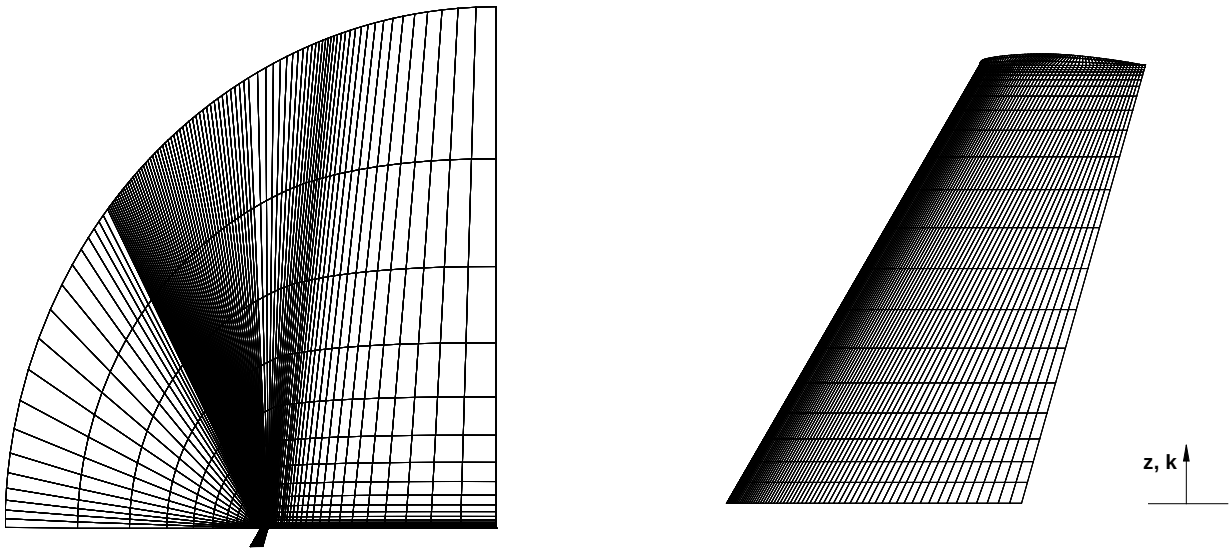

Figure 7.5.: Top view of wing, Left: wing and $k_{maxplane}$, Right: wing top view k=25 nodes.

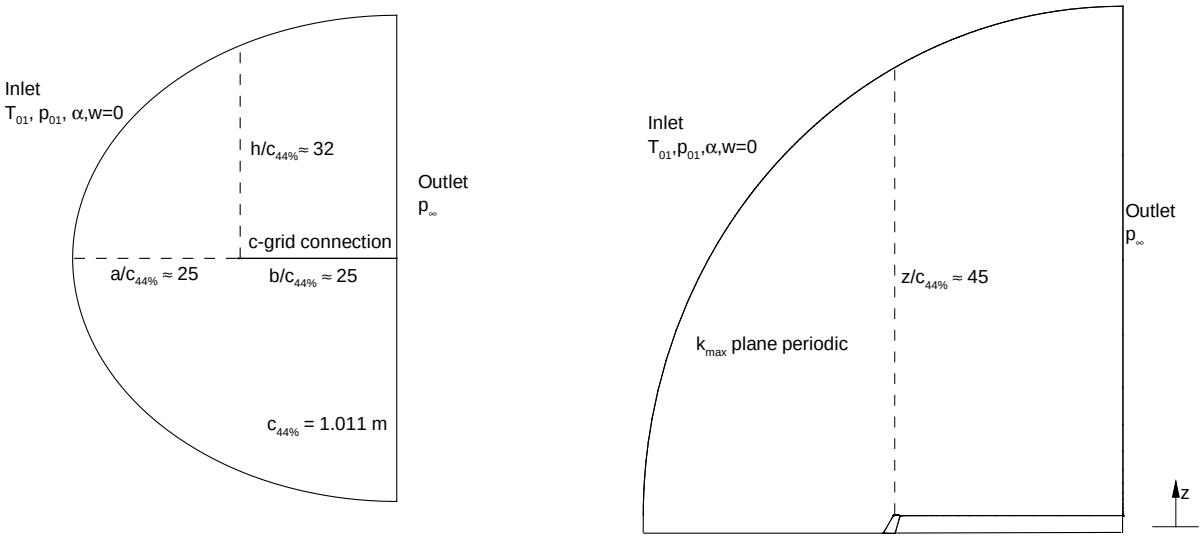

Figure 7.6.: Boundary ratios from wing surface, Left: 2-D cross-section at 44% span, Right: top view.

Figure 7.6 shows the boundary ratio to the wing surface for a 2-D cross-section and top view. The ratios are more than enough for the boundary condition implemented. Also important is the assumption that the w-component of velocity is zero on the inlet, this adds some reflecting characteristics but with the given ratios it is an adequate assumption. Figure 7.7 shows the location of the boundary conditions for the ONERA M6 wing calculation. Due to the C-C-Grid configuration, periodic conditions are needed at k_{max} and j_{max} before and after the profile. The inlet consists of the entire surface around the C-C grid (fig.7.7, right). An Euler wall is assumed for the k=1 surface which is located at the root of the profile. Note there is a gap between the inlet and the leading edge of the wing, this is because there is no boundary, it is the stagnation plane due to the c-grid mapping, thus no boundary condition is required.

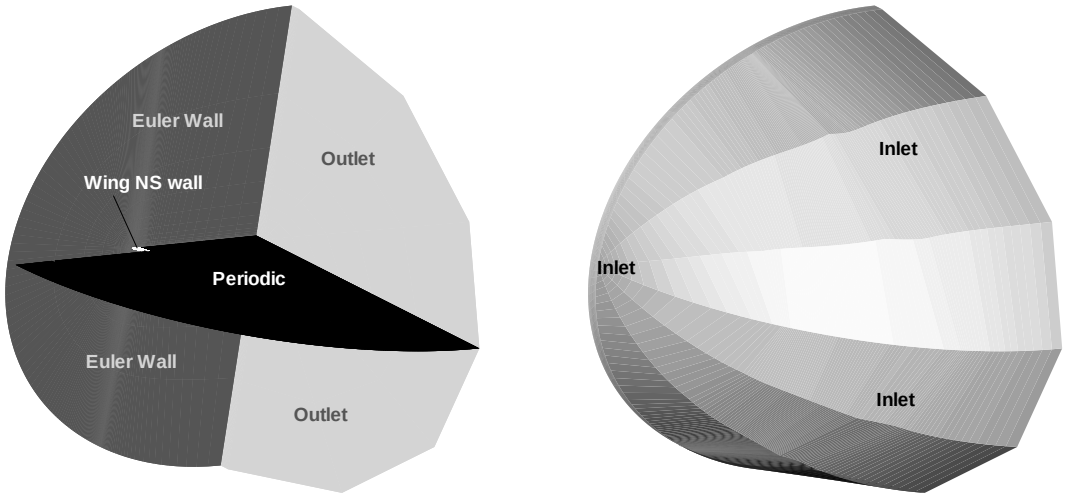

Figure 7.7.: Cross-sections of boundaries.

7.2.2. Adiabatic

For all of the following results the EASM($k-\omega$) turbulence model was chosen based on findings from Chapter 4 section 2 and the following. Since the code requires a single-block, the grid is not optimum in all places especially near tip of the wing. The SST and standard $k-\omega$ turbulence models produced simulations that did not converge for this grid whereas the EASM($k-\omega$) model did. One can conclude from this that the EASM($k-\omega$) model is more robust for non-optimum grids. The robustness might come from the lower and upper bound placed on C_μ. If the solutions did not match so well with the experimental data then a new type of grid would have been developed but with the following results confidence in this single-block grid were obtained.
Before beginning with condensation results a comparison is made between experimental data and two different grid densities. The two grids are A=213i x 35j x 25k and B=213i x 70j x 47k. The i-component was not doubled only the j and k since these components were very coarse. Figure 7.8 compares two different c_p plots at 44 and 80% of the span. There are small differences in the c_p plots but not enough to warrant the extra computational time.

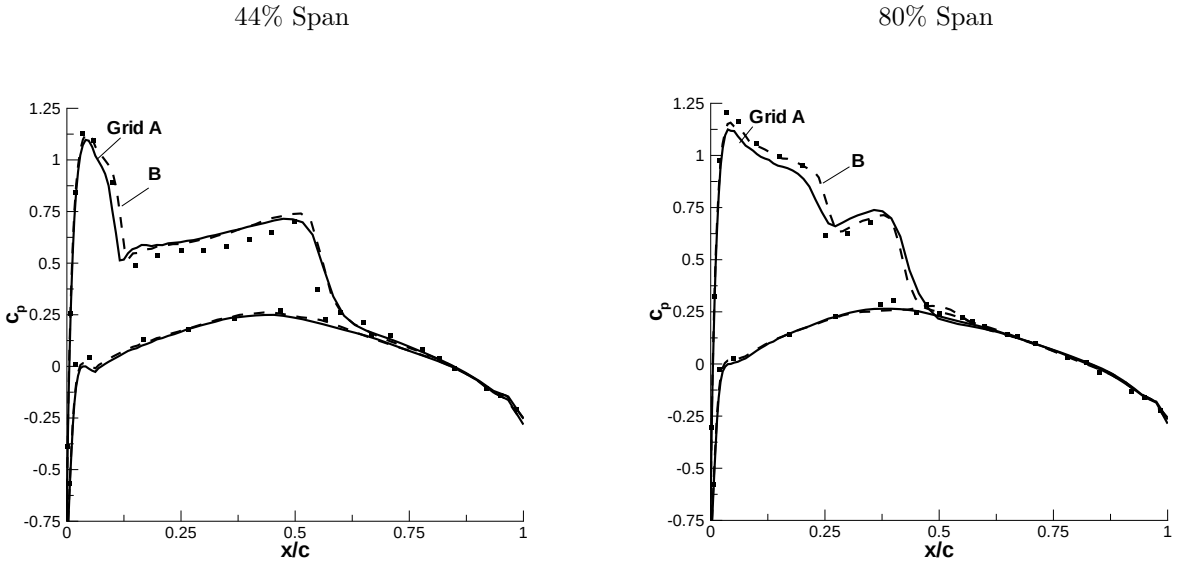

Figure 7.8.: Comparison of pressure coefficient between two different grid densities and compared with experiment [79], [T_∞ = 293.15 K, p_∞ = 1 bar, M_∞ = 0.840, Re_{mac} = 18.92 million, c_{mac} = 1 m, α =3.06°, $\overline{y}^+$ = 0.9 for both grids].
A=213i x 35j x 25k
B=213i x 70j x 47k

It is known that condensation requires denser grids compared to adiabatic calculations, thus for one set of operating conditions condensation was also calculated for both grids. Table 7.1 is a comparison of the drag and lift coefficient for different particle densities between the two grids. The main difference lies in the drag coefficient with a maximum

difference around 7%, whereas the lift coefficients are nearly the same. Also both grids show the same trend, for example at the maximum difference of 7% $N_{het,0}$=1x10^{16}m^{-3}, the relative change between the diabatic and adiabatic case is 8.8% for grid A and 9.2% for grid B, thus the relative change is consistent. Even though there is a slight difference in results between the two grids, the remaining computations will be based on the 213i x 35j x 25k grid. The smaller grid also takes about 30 hours for a solution compared to around 72 hours for the larger grid using a PIV 1.5GHz processor.

Table 7.1.: Grid comparison using the drag, lift, and friction coefficient for different condensing flows, [T_∞ = 293.15 K, p_∞ = 1 bar, M_∞ = 0.840, R_p = 1x10^{-8}m, Re_{mac} = 18.92 million, MAC = 1 m, α =3.06°] A=213i x 35j x 25k; B=213i x 70j x 47k.

Grid	$N_{het,0}$ $[m^{-3}]$	$c_{D,p}$	c_L	c_f
A	0	0.0656	0.290	0.00336
B	0	0.0608	0.292	0.00321
A	1x10^6	0.0663	0.287	0.00328
B	1x10^6	0.0612	0.291	0.00315
A	1x10^{12}	0.0683	0.310	0.00327
B	1x10^{12}	0.0637	0.312	0.00320
A	1x10^{16}	0.0714	0.338	0.00326
B	1x10^{16}	0.0664	0.337	0.00312

Since the angle of attack is also changed a comparison is made with experiment using the smaller grid for α = 1.07° and 6.06° (figs. 7.9 and 7.10). The lower angle of attack has a weaker second shock and the model is able to capture the position and strength, whereas for the larger angle of attack the double shock system is present near the root chord but moving to the tip there is a separation zone which can be seen by the pressure coefficient at 80% span (fig. 7.10, right). The separation point is accurately predicted but the recovery pressure is too high and then too low as it reaches the tip.

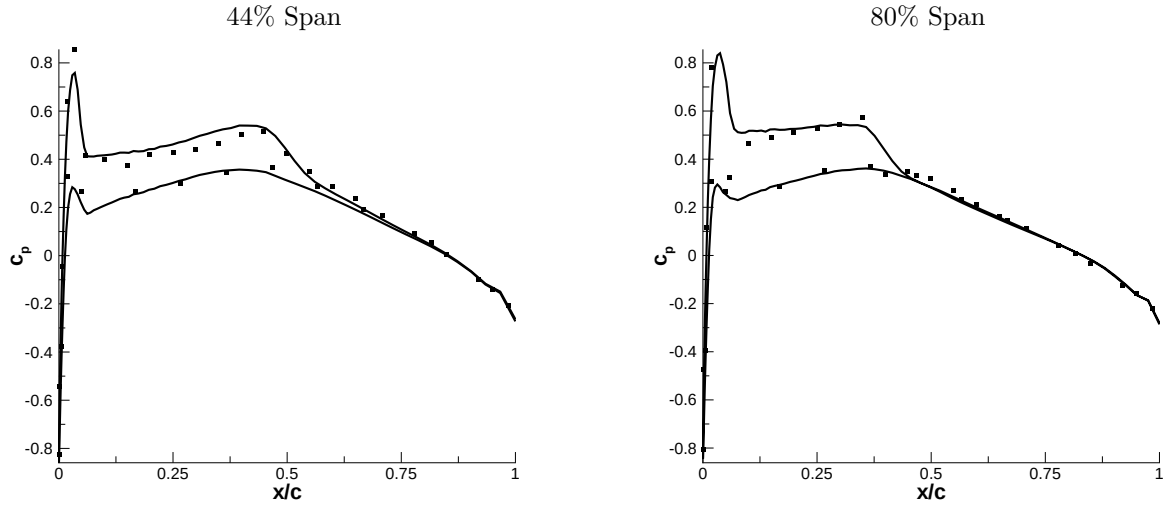

Figure 7.9.: Adiabatic pressure coefficient for an angle of attack of 1.07° compared with experiment [79], [$T_\infty = 293.15$ K, $p_\infty = 1$ bar, $M_\infty \approx 0.84$, $Re_{mac} = 18.96$ million, $MAC = 1$ m, $\overline{y}^+ < 1.0$].

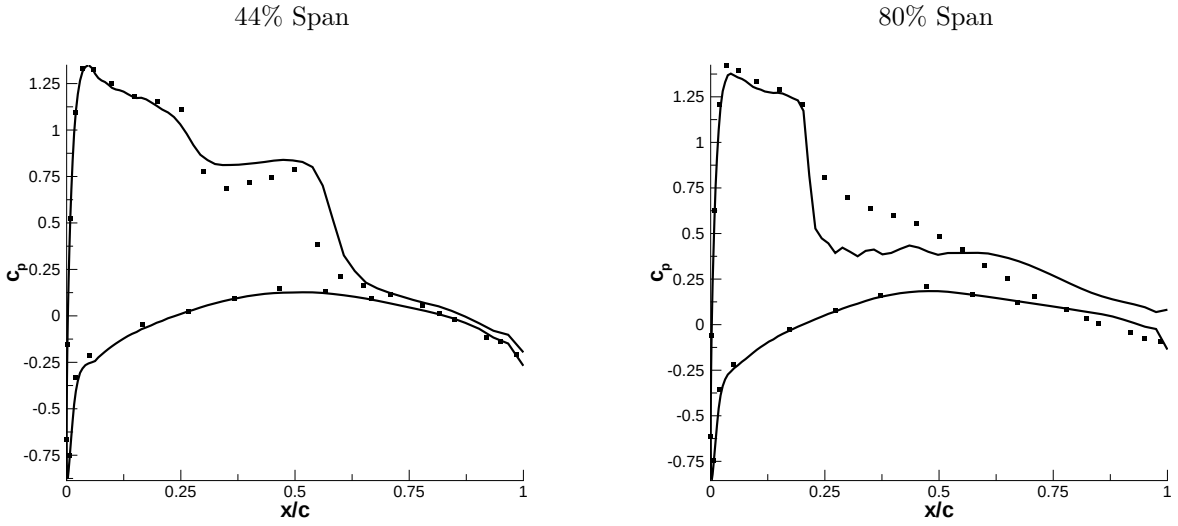

Figure 7.10.: Adiabatic pressure coefficient for an angle of attack of 6.06° compared with experiment [79], [$T_\infty = 293.15$ K, $p_\infty = 1$ bar, $M_\infty \approx 0.84$, $Re_{mac} = 18.79$ million, $MAC = 1$ m, α =6.06°, $\overline{y}^+ < 1.0$].

7.2.3. Range of Particle Density

For all the below test cases the humidity is set equal to $\phi_0 = 16\%$ which corresponds to a free stream humidity of ϕ_∞= 95%. This was chosen to get the maximum effect from condensation. One could lower the humidity to 60 or 70% and then increase the free stream Mach number to 0.9 instead of 0.83 to see similar effects but the lower Mach number was chosen to stay within the framework of the adiabatic experiments.

The first set of results compares the effect of changing the particle density whiling keeping the mean aerodynamic chord constant at 1.0m and the angle of attack at 3.06°. The three particle densities are 1x10^6, 1x10^{12}, 1x10^{16} m^{-3}. The lowest value corresponds to very low concentrations that is used as a lower bound to allow for pure homogeneous to occur if conditions exist. The middle value is typical for atmospheric conditions. The upper value of 1x10^{16} m^{-3} is unrealistic for real flow conditions but is used as an upper bound to reach equilibrium condensation. The physical upper bound on the particulate density using a R_p=1x10^{-8} m assuming spherical particles is 2.4x10^{23} m^{-3}, this would be the situation where no gas is possibly only particles flowing, thus 1x10^{16} m^{-3} is still way below this physical limit. One other interesting point is to examine what the typical range of heterogeneous nucleation rates are based on the particle densities and flows encountered. Using an adiabatic result based on a MAC=1.0m, angle of attack $\alpha = 3.06°$ and the projected streamline from fig. 7.18 (top-center) two heterogeneous nucleation rates along the streamline are generated. The nucleation rates are approximated by the following equation

$$J_{het} = \frac{d\mathbf{u}}{ds}\frac{\rho_\infty}{\rho_{01}} N_{het,0} \tag{7.1}$$

where $d\mathbf{u}$ is the total velocity and ds is a length scale along the streamline path.

Figure 7.11 shows a typical range for the heterogeneous nucleation rate outside the boundary layer along the wing top surface, At 10^{16} m^{-3} a range of 18-21 $m^{-3}s^{-1}$ is achieved and at 10^{12} m^{-3} this value is decreased to a range of 14-17 $m^{-3}s^{-1}$ which matches the decrease from 10^{16} m^{-3} to 10^{12} m^{-3}. The lower value at 10^{12} m^{-3} explains why there is a combination of homogeneous and heterogeneous condensation present because the homogeneous nucleation rates will dominate at large expansions near the leading edge.

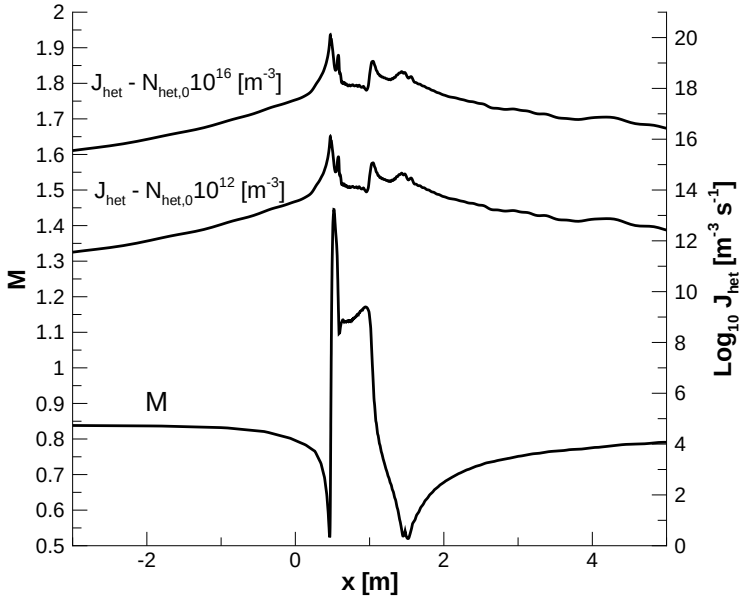

Figure 7.11.: Mach and J_{het} along streamline from fig. 7.18 (top-center), [T_∞ = 293.15 K, p_∞ = 1 bar, $M_\infty \approx 0.84$, R_p = 1x10^{-8}m, Re_{mac} = 18.92 million, MAC = 1 m, α =3.06°].

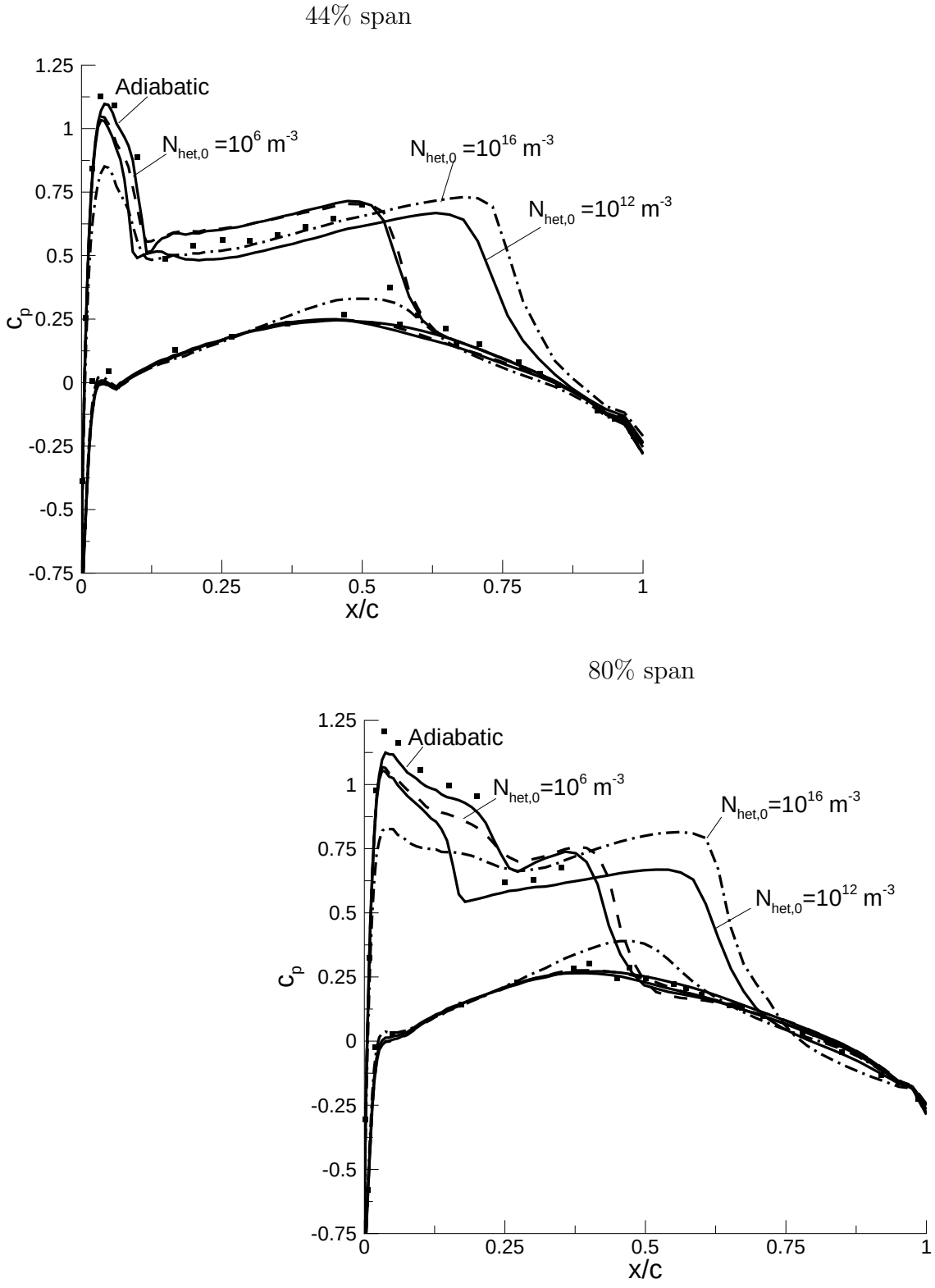

Figure 7.12.: Pressure coefficient for different particle densities, [$T_\infty = 293.15$ K, $p_\infty = 1$ bar, $M_\infty \approx 0.84$, $Re_{mac} = 18.92$ million, $R_p = 1\text{x}10^{-8}$m, $MAC = 1$ m, α =3.06°, $\overline{y}^+ < 1$ for all].

Going back to tab. 7.1, besides the grid comparison it is also shows that the lift and drag increases with particle density. By examining c_p plots one can see where this increase comes from. Figure 7.12 compares the change in c_p due to different particle densities at 44 and 80% span.
At a particle density of 10^6 m^{-3} (dashed line) there is a small decrease in c_p at the leading edge but the position of the second shock is unchanged. The reason for this is that the flow is dominated by homogeneous condensation and the large acceleration at the leading edge causes a small amount of homogeneous condensation (subcritical heat addition $M > 1$).
At a particle density of 10^{12} m^{-3} the flow field is a combination of homogeneous / heterogeneous where homogenous condensation dominates at the leading edge and heterogeneous condensation dominates before the second shock on the suction side. The heterogeneous condensation pushes the second shock closer to the trailing edge and thus increases lift by delaying the increase in pressure due to the shock. Note that the pressure is higher before the second shock (fig.7.12) which decreases lift but since the supersonic region is increased, the overall change is an increase in lift. The drag is increased because of the condensation occurring on the leading edge, which increases the static pressure (sub-critical heat addition $M > 1$) and also the increased supersonic region after the maximum thickness on the suction side.
At a particle density of 10^{16} m^{-3} the flow field is dominated by heterogeneous condensation at the leading edge, before the second shock, and a small amount is forming on the pressure side. Here the supersonic region is extended more than the 10^{12} m^{-3} case. The small bump on the pressure side has two negative effects; it increases drag and decreases lift. The drag is increased because of subsonic heat addition $M < 1$, where the pressure decrease occurs mostly after the maximum thickness. The maximum thickness is around x/c = 0.4. Drag is also greatly increased on the leading edge by the sub-critical heat addition $M > 1$.
Figure 7.13 shows the condensate mass fraction for g_{hom} or g_{het} and the Mach 1 line at 44% chord. These plots give an idea of how much condensation is occurring and what type. There is no figure for g_{het} at 10^6 and g_{hom} at 10^{16} m^{-3} because this type of condensation does not occur. The key elements of fig. 7.13 is the increase in the sonic region with particle density and the different types of condensation. The wavy structure at low values of g_{het} is purely numerical due to the coarsening of the grid away from the profile.

$N_{het,0} = 1\text{x}10^{12}\ m^{-3}$ $N_{het,0} = 1\text{x}10^{12}\ m^{-3}$

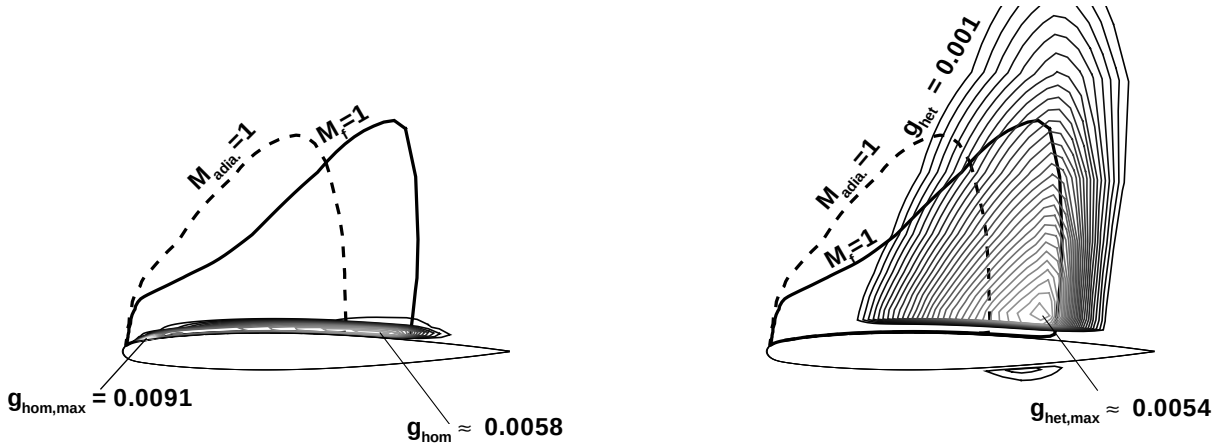

$N_{het,0} = 1\text{x}10^{6}\ m^{-3}$ $N_{het,0} = 1\text{x}10^{16}\ m^{-3}$

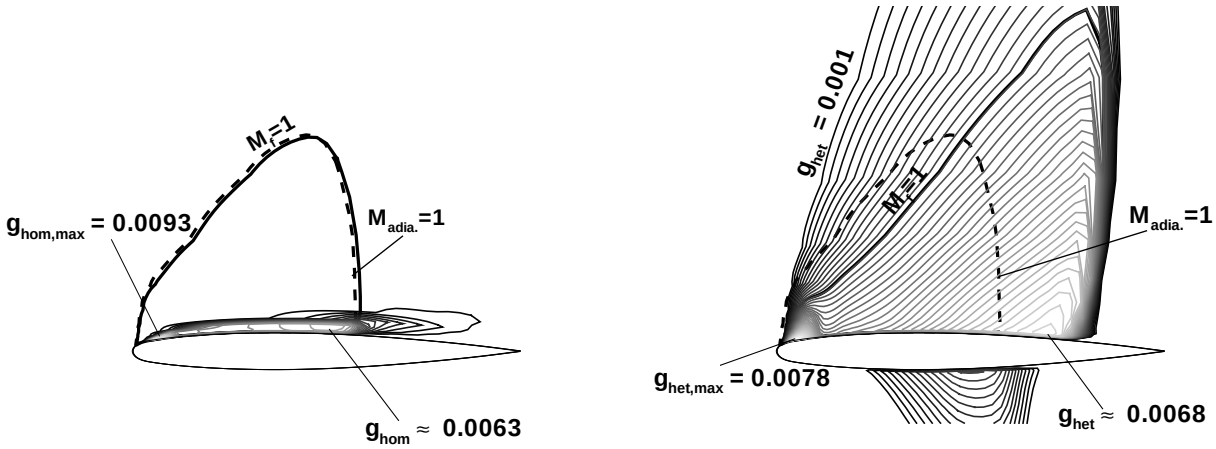

$\Delta g_{hom} = 0.004$ $\Delta g_{het} = 0.002$

$g_{max} = 0.134$

Figure 7.13.: Homogeneous (left) and heterogeneous (right) condensate mass fraction and Mach 1 line at 44% span, [$T_\infty = 293.15$ K, $p_\infty = 1$ bar, $M_\infty \approx 0.84$, $Re_{mac} = 18.92$ million, $R_p = 1\text{x}10^{-8}$m, $MAC = 1$ m, α =3.06°].

7.2.4. Mean Aerodynamic Chord Influence

At 10^6 m^{-3} the effect of homogeneous condensation is very small for different MACs. The maximum value of log_{10} J_{hom} at 44% span for a MAC of 0.5m, 1.0m, 2.0m, and 4.0m is 22.4, 19.8, 21.1, and 18.5 $[m^{-3}s^{-1}]$. A MAC of 0.5 is not a realistic wing size but it is used to see how trends are developing and perhaps there are some components of a plane with this type of size. The smallest MAC of course has the largest J_{hom} because the smaller length scale has the largest cooling rate, but with this difference there is no noticeable difference in c_p.
For $10^{12}m^{-3}$ there are large differences in c_p for the range of MACs, which translate to differences in drag and lift. Table 7.2 is a summary of the change in the drag, lift, and friction coefficient for different MACs. The drag and lift are both increasing with an increase in MAC. The c_f coefficient decreases which corresponds to the increase in Reynolds number.

Table 7.2.: MAC comparison on condensation using the drag, lift and friction coefficient, [T_∞ = 293.15 K, p_∞ = 1 bar, $M_\infty \approx 0.84$, α =3.06°, $N_{het,0}$ = 1x$10^{12}m^{-3}$].

MAC [m]	$Re_{mac} \times 10^6$	$c_{D,p}$	c_L	c_f
0.5	9.46	0.0668	0.294	0.00361
1.0	18.92	0.0683	0.310	0.00327
2.0	37.84	0.0697	0.326	0.00305
4.0	75.68	0.0705	0.323	0.00278

Figure 7.14 demonstrates the trend of increasing lift and drag found in tab.7.2, but the difference in lift between 2 and 4m begins to plateau. In the c_p plots, 4m was not graphed because it follows the same trend as 2m and thus it avoids a crowded graph. At a MAC of 2.0 or 4.0m the supersonic region is the largest and the leading edge is experiencing the greatest static pressure increase, which increases the drag. The fig. 7.14 caption also shows the difference in $\overline{y}^+$ for the different MACs, which means the grid was rescaled and thus the distance of the first grid point also increases, but the values are still below 2.5.

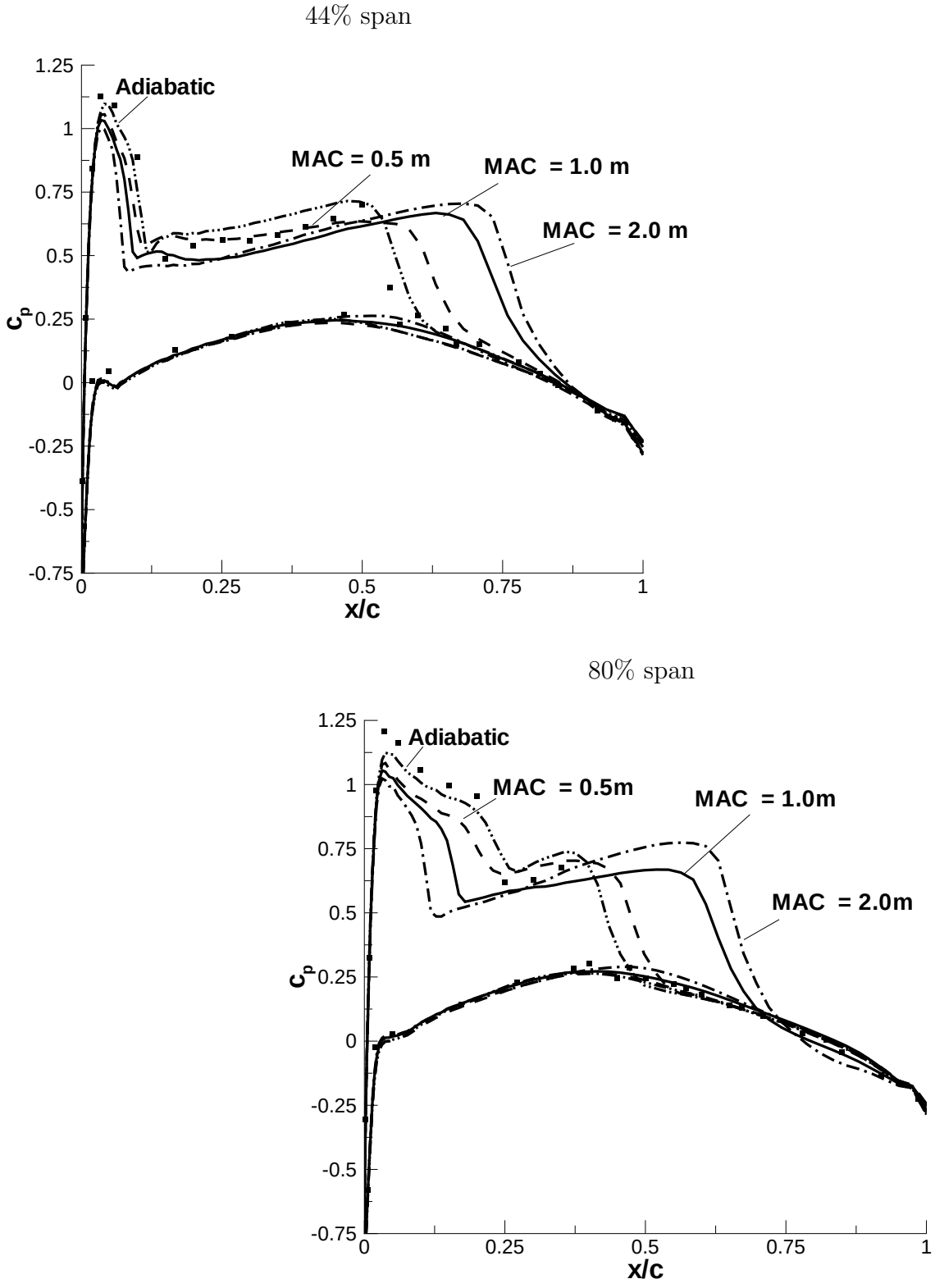

Figure 7.14.: Pressure coefficient for different MACs, [$T_\infty = 293.15$ K, $p_\infty = 1$ bar, $M_\infty \approx 0.84$, α =3.06°, $N_{het,0} = 1\text{x}10^{12}\text{m}^{-3}$, $R_p = 1\text{x}10^{-8}$m, $\overline{y}^+ = 0.5$–MAC=0.5, $\overline{y}^+ = 0.9$–MAC=1.0, $\overline{y}^+ = 1.6$–MAC=2.0].

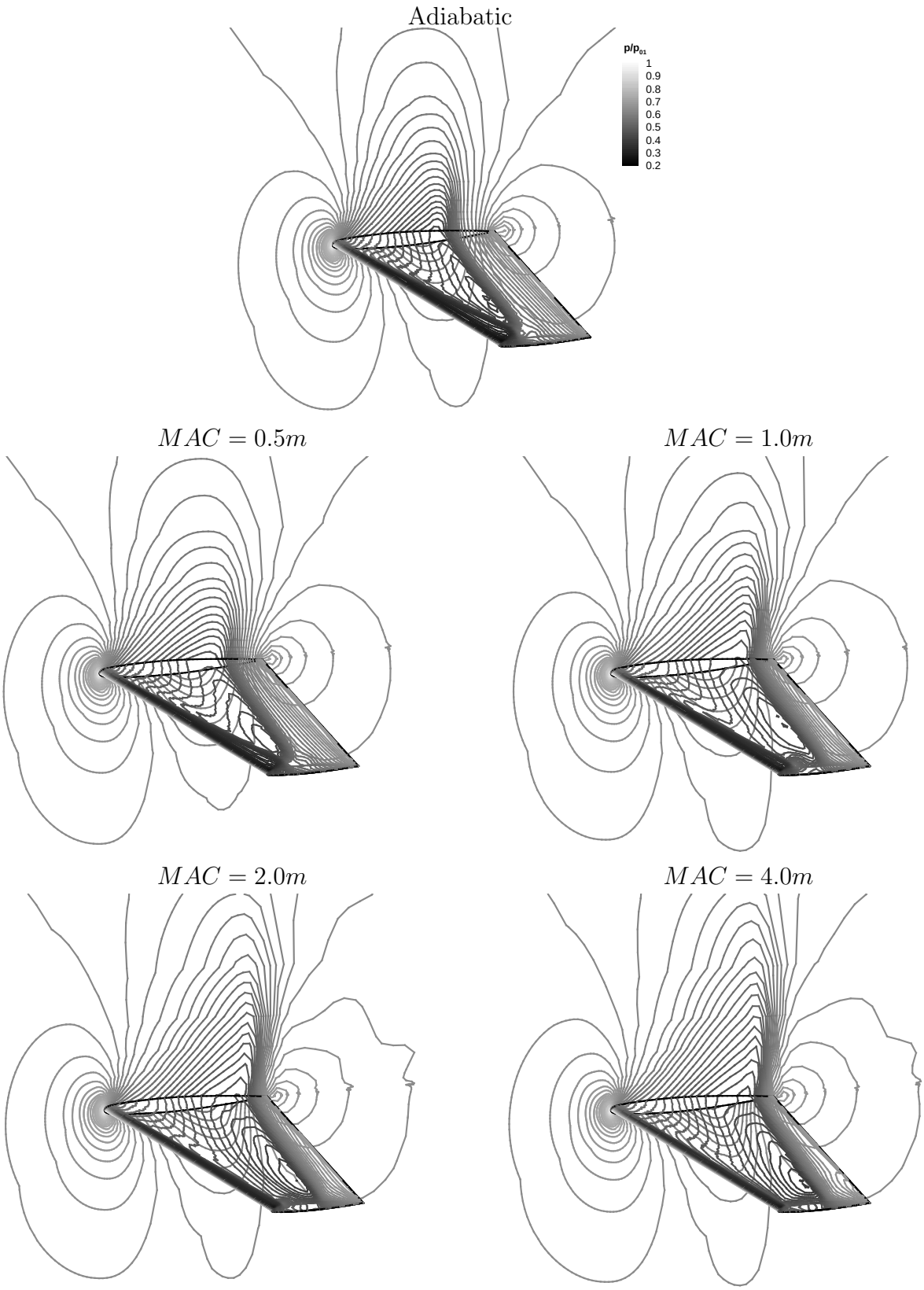

Figure 7.15.: Wind top and side wall pressure distribution, [T_∞ = 293.15 K, p_∞ = 1 bar, $M_\infty \approx 0.84$, $\alpha = 3.06°$,$N_{het,0} = 1\text{x}10^{12}$ m^{-3}, $R_p = 1\text{x}10^{-8}$m].

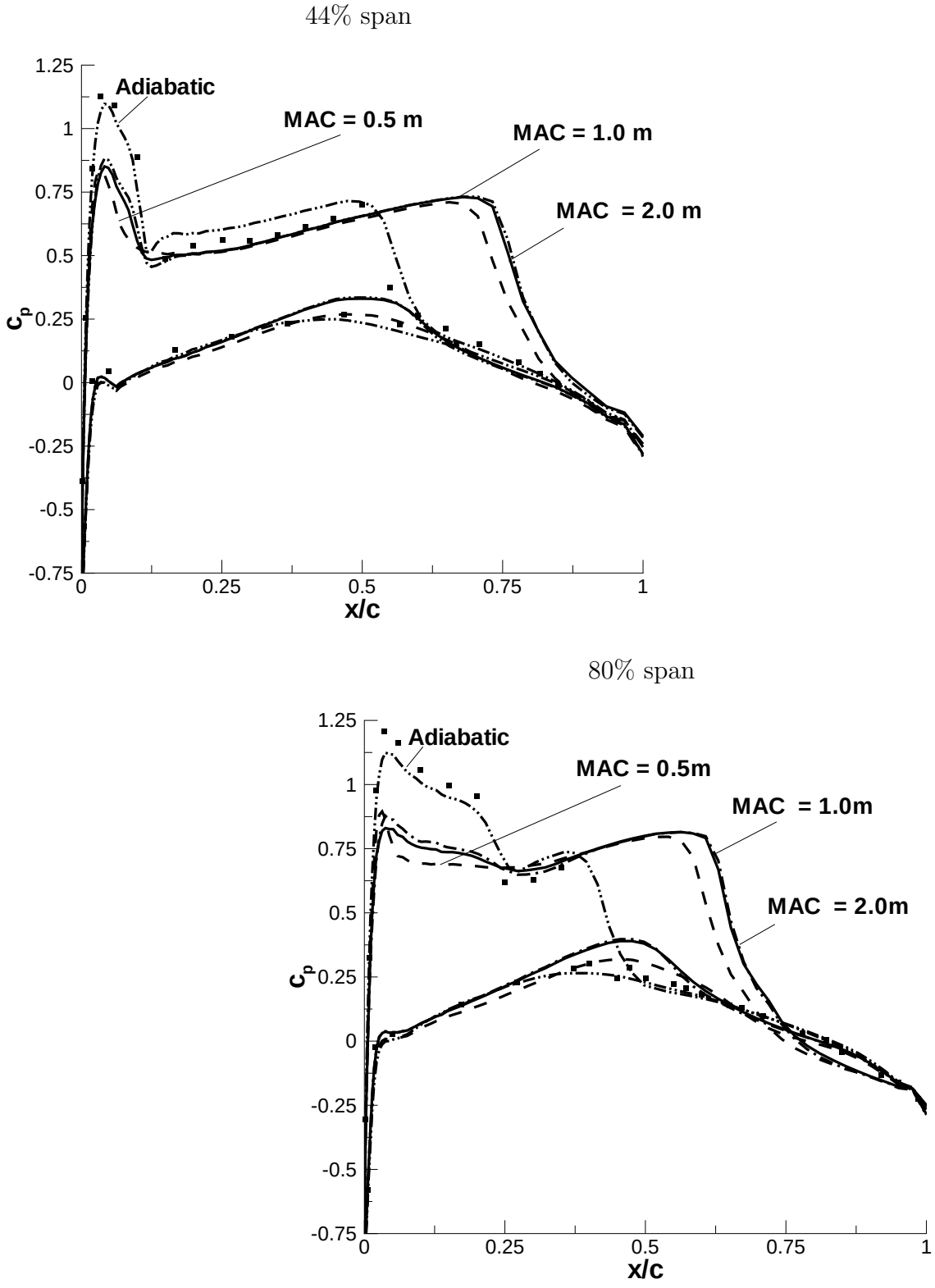

Figure 7.16.: Pressure coefficient for different MACs, [$T_\infty = 293.15$ K, $p_\infty = 1$ bar, $M_\infty \approx 0.84$, α =3.06°, $N_{het,0} = 1\text{x}10^{12}\text{m}^{-3}$, $R_p = 1\text{x}10^{-8}$m, $\overline{y}^+ = 0.5$–MAC=0.5, $\overline{y}^+ = 0.9$–MAC=1.0, $\overline{y}^+ = 1.6$–MAC=2.0].

Figure 7.15 shows the wing top and root profile pressure distribution for different MACs. Compared to the adiabatic case (center-top), for the same particle density ($N_{het,0}$ = 1x10^{12}m^{-3}) and with an increase in the MAC, the supersonic region increases by moving the second shock further to the trailing edge and the leading edge static pressure slightly increases.
At 10^{16} m^{-3} there is somewhat the same trend as 10^{12} m^{-3} but it is on a smaller scale. There are large differences between 0.5m, and 1m to 2m but the difference between 1m and 2m is relatively small, which can be seen in fig. 7.16.
The reason behind the change in pressure distribution which translates to a change in drag and lift comes from the heat addition. The following graphs in fig. 7.17 show the location of the heat addition and the mass fraction of available water vapor that condenses. The analysis is based on a cross section at 44% span. At 80% span the same trends exist but slightly different amounts of heat addition. The first set of graphs fig.7.17 (top 2-rows) shows the mass fraction of homogeneous condensation at different MAC lengths. As the MAC is increased the mass fraction slightly decreases for the 10^{6} m^{-3} case because of the decrease in cooling rate but the position is nearly the same. As for the 10^{12} m^{-3} case there is a decrease in the amount of g_{hom} because of the g_{het} present and again the same trend of a decrease in g_{hom} with an increase in the length scale. Note for 10^{16} m^{-3} there is no g_{hom} present because of the dominance of the particles (equilibrium condensation).

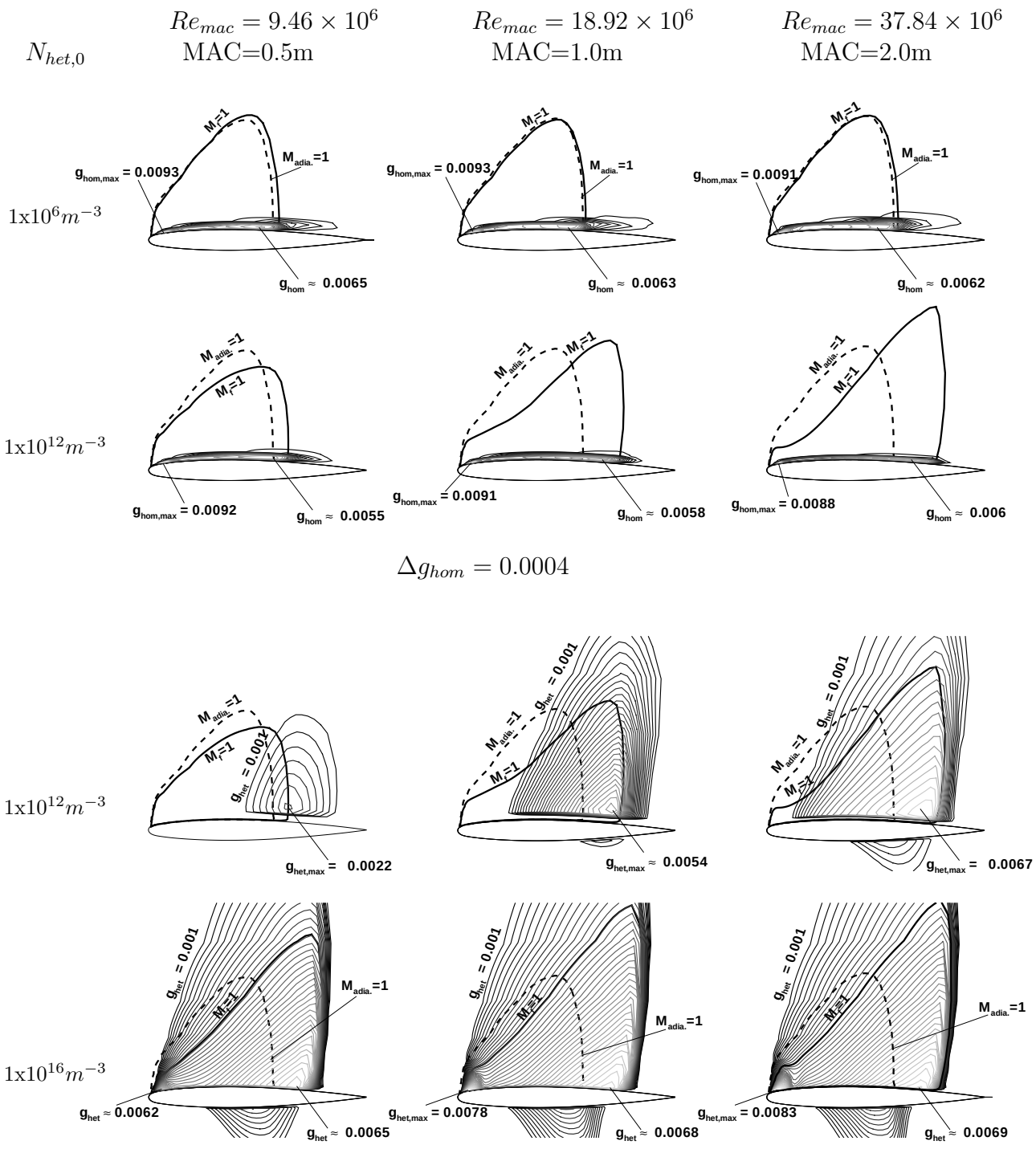

Figure 7.17.: Homogeneous and heterogeneous condensate mass fraction with Mach l lines, [T_∞ = 293.15 K, p_∞ = 1 bar, $M_\infty \approx 0.84$, $\alpha = 3.06°$, R_p = 1x10^{-8}m, cross-section is at 44% span, $g_{max} = 0.0134$].

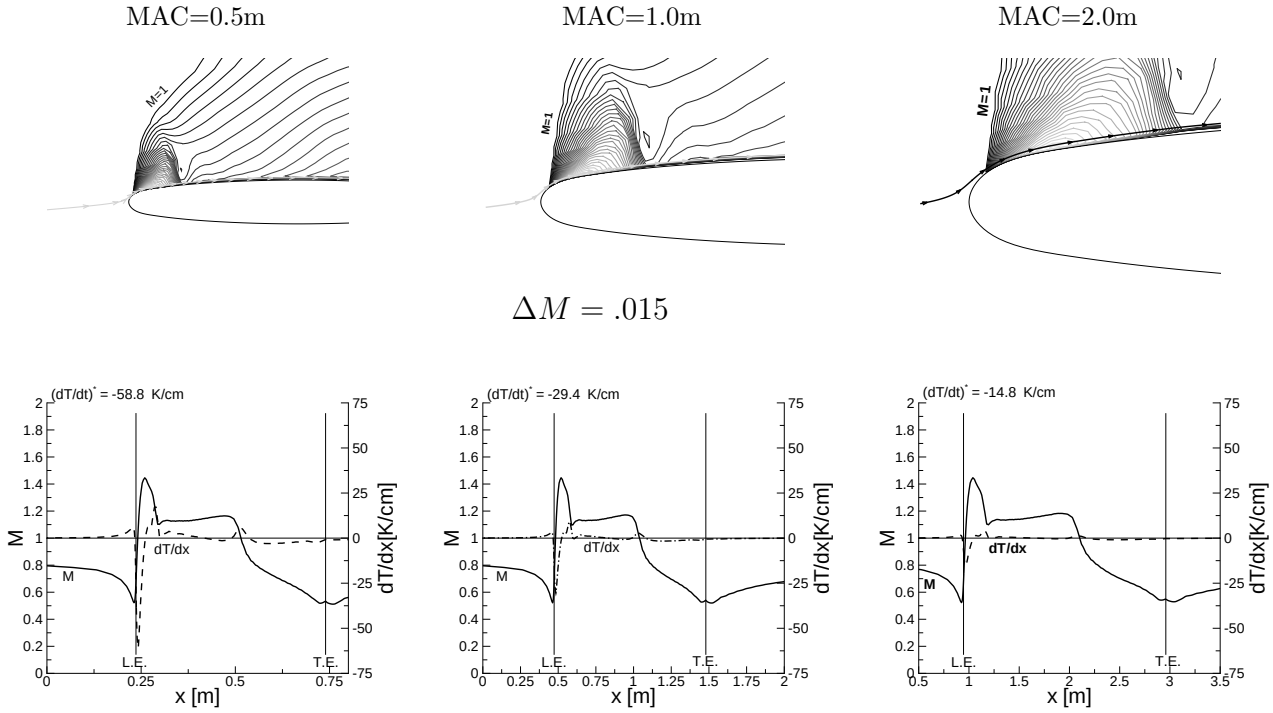

Figure 7.18.: Supersonic Mach contour and temperature gradient values extracted from projected streamline, [$T_\infty = 293.15$ K, $p_\infty = 1$ bar, $M_\infty \approx 0.84$, $\alpha = 3.06°$, $R_p = 1\text{x}10^{-8}$m, cross-section is at 44% span].

The increase in the supersonic region fig. 7.17 (bottom 2-rows) is due to heterogeneous condensation. For the heterogenous mass fraction, there is none present at 10^6 m^{-3} but for 10^{12} m^{-3} (fig. 7.17 3rd row) there is a large increase in g_{het} as the length scale is increased. It is speculated that the larger chord length increases the time for heterogenous condensation to occur. Also notice in fig. 7.17 (row 2-4) the supersonic region increases as the MAC in increased. For fig. 7.17 (row-4) the flow is dominated by heterogeneous condensation and the effect of increasing the MAC is not as pronounced but the same trend is present.

Figure 7.18 (top) shows too scale at 44% span the three different MACs with a projected streamlines close to the boundary layer edge. Figure 7.18 (bottom)shows the adiabatic Mach number and temperature gradient along each streamline. Homogeneous condensation as seen by fig. 7.17 (top 2-rows), shows that the condensation starts near the leading edge, which is donated by L.E. in fig. 7.18. Here the temperature gradient is largest for the smaller of the MACs and decreases by approximately half as the chord is doubled. Thus the smaller MAC has the largest homogeneous condensation and the smallest heterogeneous compared to the opposite trend for the larger MAC, this trend is related to what is shown in fig. 7.18. Note this trend is in regards to particle densities $\leq 10^{12}\text{m}^{-3}$ After the first shock, where heterogeneous condensation begins the temperature gradient is nearly constant. At the trailing edge there is another small peak due to the small compression at the trailing edge.

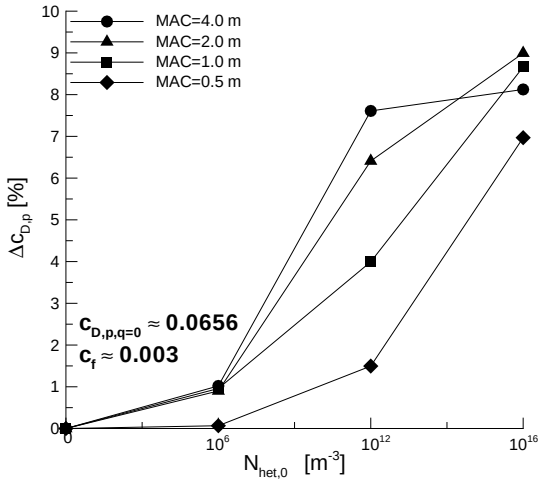

$$\Delta c_{D,p} = \frac{c_{D,p,q>0} - c_{D,p,q=0}}{c_{D,p,q=0}}$$

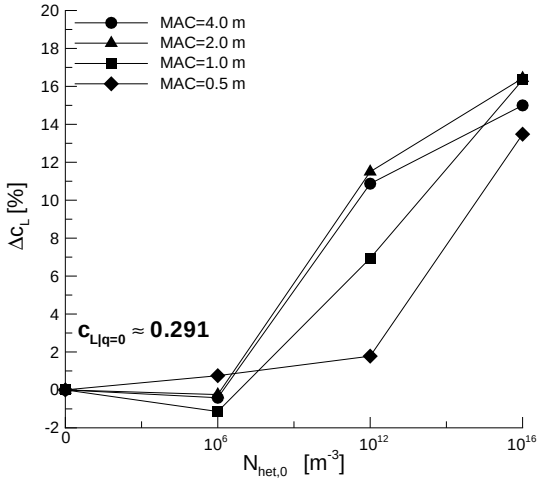

$$\Delta c_L = \frac{c_{L,q>0} - c_{L,q=0}}{c_{L,q=0}}$$

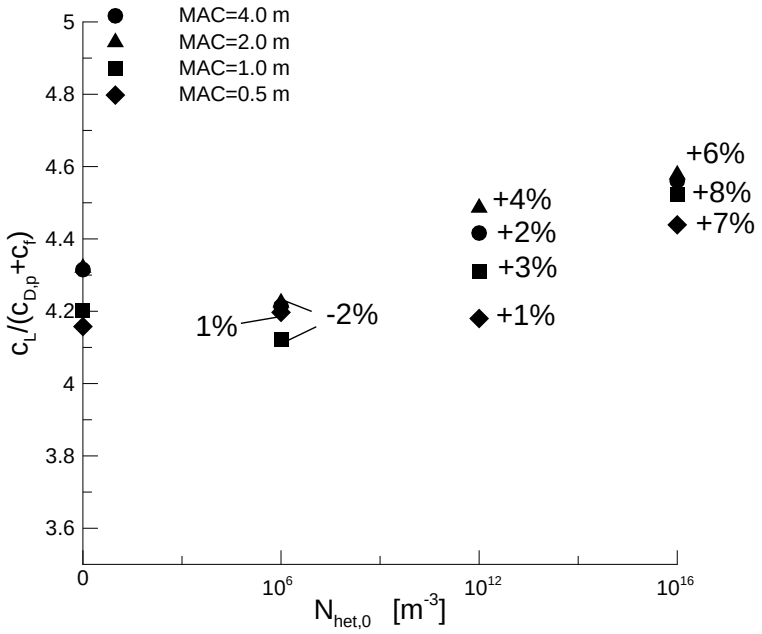

±% represents the increase or decrease in the lift to drag ratio compared to the adiabatic case.

Figure 7.19.: Effect on drag, lift and the lift to drag ratio for the different MACs and particle densities, [$T_\infty = 293.15$ K, $p_\infty = 1$ bar, $M_\infty \approx 0.84$, α =3.06°, $R_p = 1\text{x}10^{-8}$m].

The lift to drag ratio is used as a final analysis to compare the effects of particle concentration on MAC length. Again at $10^{12}m^{-3}$ the largest difference is present with a trend of a small increase in the ratio as particle density increases. To be numerically honest fig.7.19 is an expanded scale with a maximum difference between adiabatic and condensing flow of $\approx 5\%$, thus care must be taken in determining how much condensation is effecting the flow under these conditions.

7.2.5. Angle of Attack

Table 7.3.: Angle of attack comparison on condensation using the drag, lift, and friction coefficient, [$T_\infty = 293.15$ K, $p_\infty = 1$ bar, $M_\infty \approx 0.84$, $R_p = 1\text{x}10^{-8}$m, $MAC = 1.0$m].

α	$N_{het,0}$ $[m^{-3}]$	$c_{D,p}$	c_L	c_f
1.07°	0	0.0272	0.099	0.00336
3.06°	0	0.0656	0.290	0.00336
6.06°	0	0.1277	0.547	0.00297
1.07°	$1\text{x}10^6$	0.0272	0.099	0.00336
3.06°	$1\text{x}10^6$	0.0663	0.287	0.00327
6.06°	$1\text{x}10^6$	0.1273	0.534	0.00295
1.07°	$1\text{x}10^{12}$	0.0306	0.108	0.00333
3.06°	$1\text{x}10^{12}$	0.0683	0.310	0.00327
6.06°	$1\text{x}10^{12}$	0.1258	0.587	0.00315
1.07°	$1\text{x}10^{16}$	0.0348	0.122	0.00328
3.06°	$1\text{x}10^{16}$	0.0714	0.338	0.00326
6.06°	$1\text{x}10^{16}$	0.1273	0.584	0.00311

Table 7.3 compares condensation effects with three different angles of attack for a MAC of 1m. At the lower angle of attack there is an absence of homogeneous condensation on the leading edge because of the decrease in acceleration around the leading edge, thus the drag and lift is unchanged from the adiabatic case. Like in the different MAC lengths subsection 7.2.4, the same plots of g_{hom} and g_{het} with Mach 1 lines are plotted (figs 7.20 and 7.21). At 1.07° $10^6 m^{-3}$ there is no homogeneous condensation present which was noted from table 7.3 but as the angle of attack is increased for the same particle density the fraction of homogeneous condensation increases (fig. 7.20), which is due to the larger acceleration around the leading edge. The most interesting result comes from looking at g_{hom} at 80% span for an angle of 6.06°. At this point there is separation on the wing and thus one can see the condensate de-attach and break up. This occurs only for the case of 10^6 m^{-3} because at 10^{12} m^{-3} the higher particle density suppresses the separation zone at the tip but the shift in shock on the curved surface begins a new separation zone near the trailing edge, this will also be clarified further with (fig. 7.22).

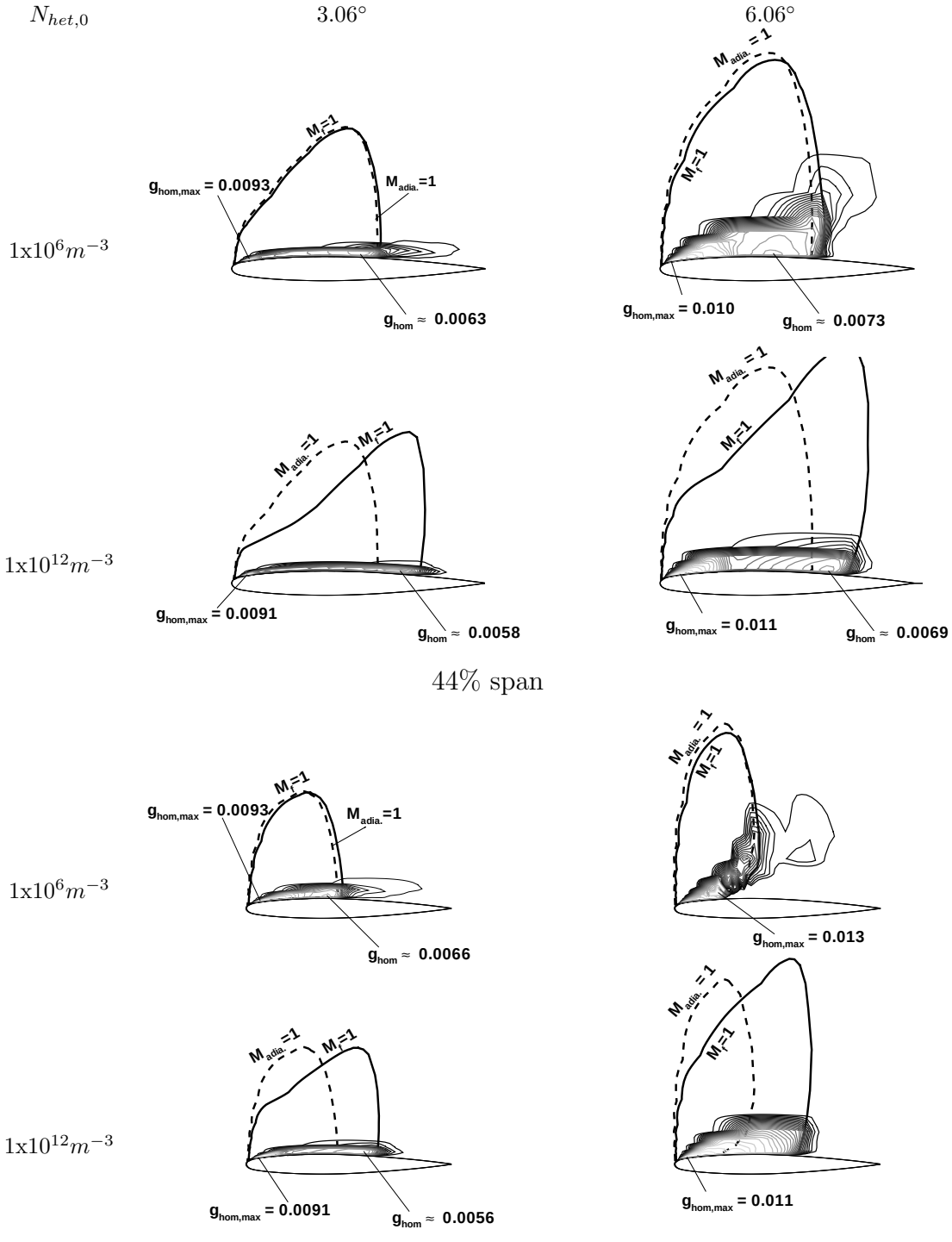

Figure 7.20.: Homogeneous condensate mass fraction and Mach l lines, [$T_\infty = 293.15$ K, $p_\infty = 1$ bar, $M_\infty \approx 0.84$, $R_p = 1x10^{-8}$m, $MAC = 1.0$m].

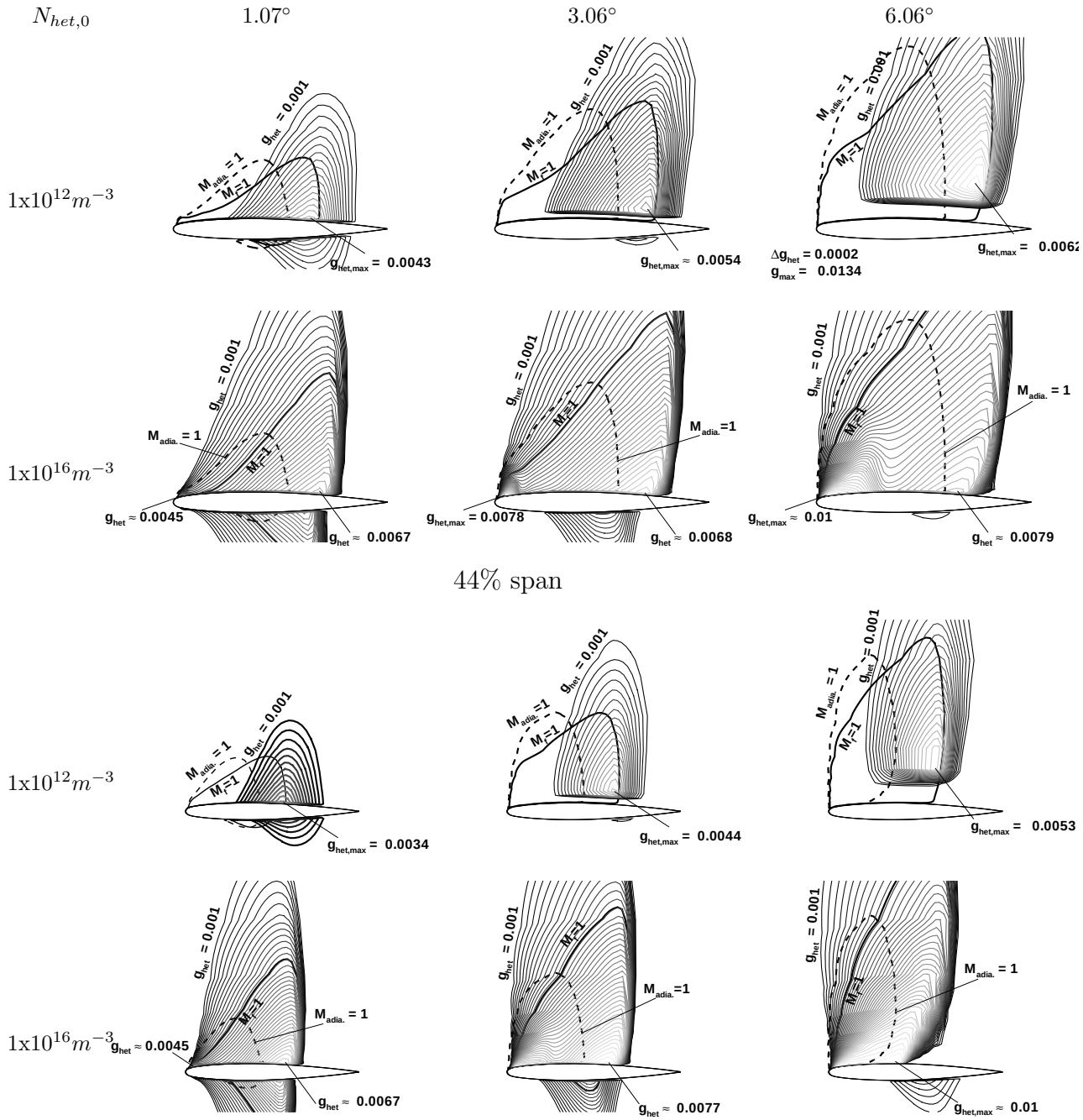

$$\Delta g_{hom} = 0.0002, \quad g_{max} = 0.0134$$

Figure 7.21.: Heterogenous condensate mass fraction and Mach l line, [$T_\infty = 293.15$ K, $p_\infty = 1$ bar, $M_\infty \approx 0.84$, $R_p = 1x10^{-8}$m, $MAC = 1.0$m].

For heterogeneous condensation with the variation in angle of attack the condensation fraction increases which is due to the larger supersonic region caused by increasing the angle of attack (fig. 7.21). At a low angle there is condensation present on the top and bottom part of the wing. For 10^{12} m^{-3} note that near the surface of the airfoil there is a gap between the surface and the beginning of the heterogeneous mass fraction which corresponds to the presence of the homogeneous condensation that is convected from the production at the leading edge. At 10^{16} m^{-3} a new separation line is reemerging which can be seen by the wedge shaped cut off of heterogeneous condensate (fig. 7.21, bottom right). Even the though pre-shock Mach number is less than the adiabatic case around 1.35 (adiabatic) compared to 1.2 (diabatic-10^{16} m^{-3}) the shock is occurring at a higher slope of the airfoil which is causing the separation to occur.

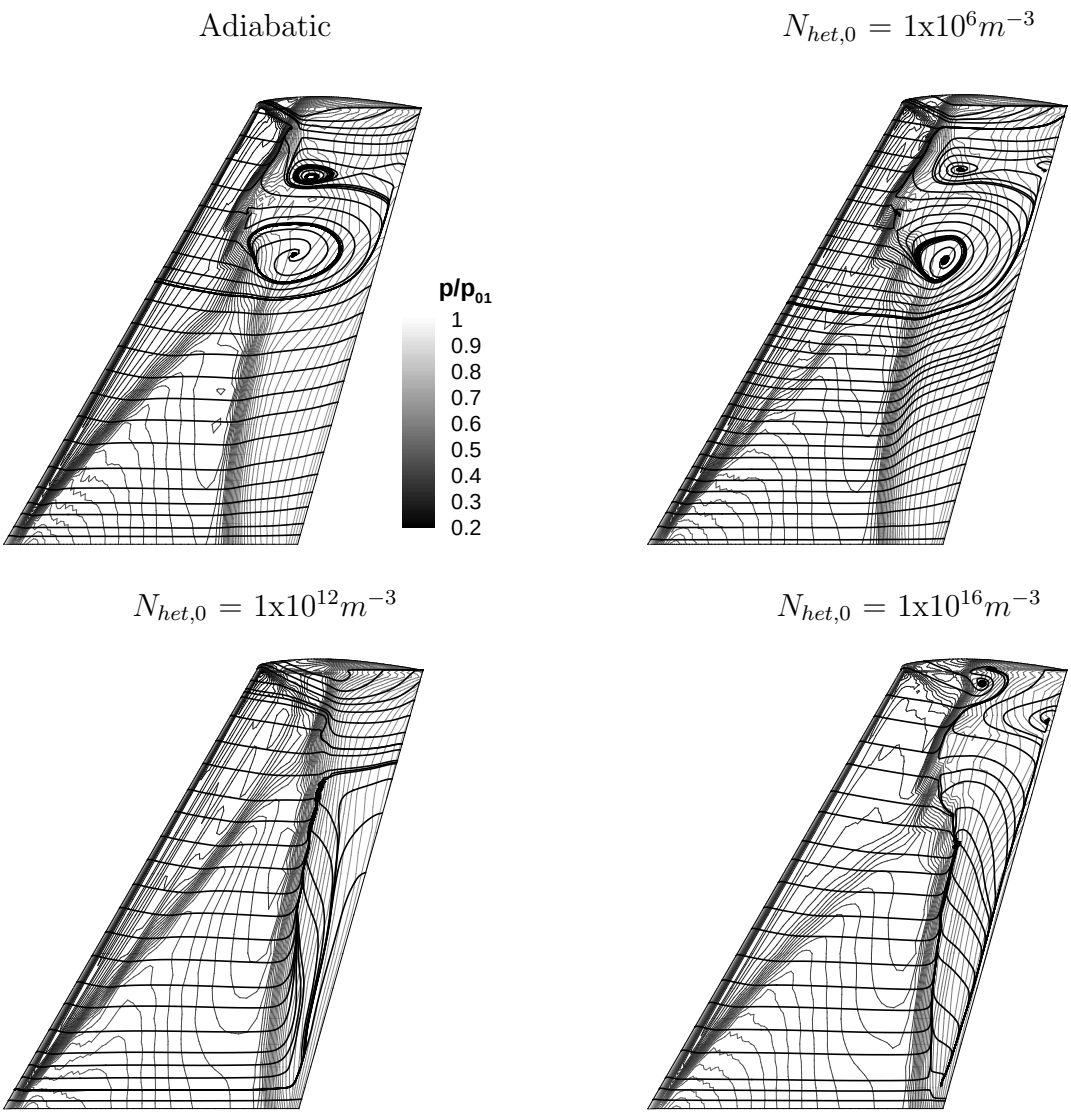

The computed skin friction lines are calculated based on the wall shear stress eqs. 2.35-2.37, which are then cast into the three vector components where streamlines are drawn from.

Figure 7.22.: Wing top computed skin friction lines (bold lines) overlaid on a contour plot of the pressure ratio, [T_∞ = 293.15 K, p_∞ = 1 bar, $M_\infty = 0.84$, $\alpha = 6.06°$, $R_p = 1\text{x}10^{-8}$m, MAC = 1.0m].

An interesting result with the higher angle of attack (6.06°) is that the drag is relatively constant except for the 10^{12} m^{-3} case and again the same trend for lift increasing as $N_{het,0}$ increases. The drag for the higher angle of attack is partially dominated by the separation occurring near the tip. Figure 7.22 shows the pressure distribution and computed skin friction lines for the adiabatic case, notice the large separation region near the tip, which is also present in the experiment. Unfortunately no oil flow pattern pictures were in the

report, thus the separation zone is inferred from the c_p data. As condensation is increased fig. 7.22 from top to bottom, it has the effect of decreasing the separation region which decreases drag but due to the heat addition at the leading edge, drag is increased, so this balance is observed. It seems at $10^{12}m^{-3}$ this is optimum for drag because the separation region is decreased at the tip but it does not shift the shock too far on the curved surface, which is developing a second separation region ($10^{16}m^{-3}$ case.

The skin friction lines for the angle of attack of 3.06° is very different from 6.06°. In the adiabatic flow there is no separation region and for particle densities of 10^6 and 10^{12} m^{-3} there is no noticeable difference from the adiabatic flow. Figure 7.23 compares the adiabatic and 10^{16} m^{-3} skin friction lines for an angle of attack of 3.06°.

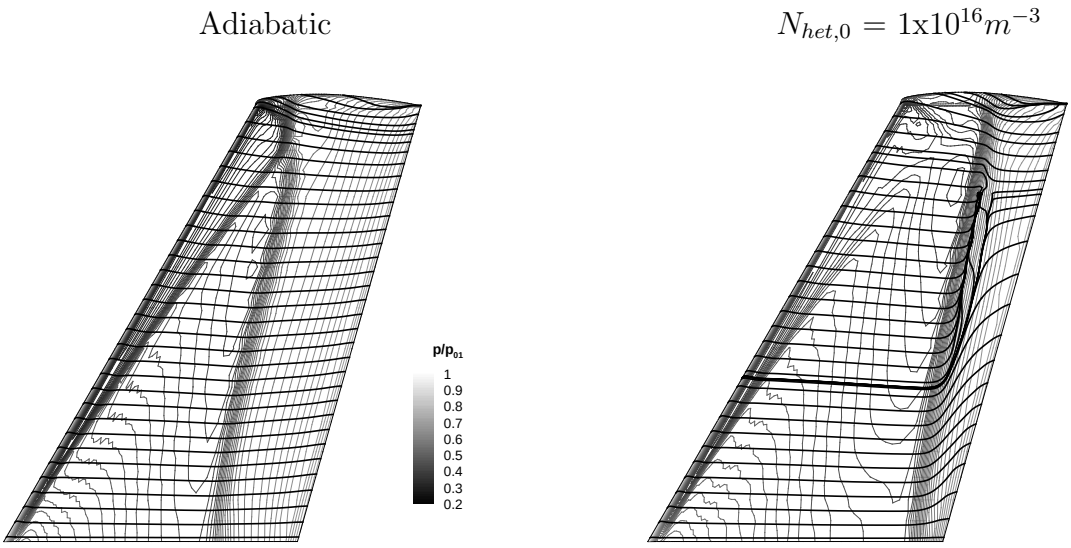

Figure 7.23.: Wing top computed skin friction lines (bold lines) overlaid on a contour plot of the pressure ratio, [T_∞ = 293.15 K, p_∞ = 1 bar, M_∞ = 0.84, α = 3.06°, R_p = 1x10^{-8}m, MAC = 1.0m].

For the final analysis the drag to lift ratio is computed and compared between angle of attack and particle densities. In fig. 7.24 the low angle of attack 1.07° shows a constant are slightly decreasing function for the lift to drag ratio, whereas for 3.06° and 6.06° there is an increase. Also the contribution of friction is more for the low angle of attack, accounting for about 10% of the total, compared to 5% and 2.5% for 3.06° and 6.06°. Again an expanded scale is used for fig. 7.24 like fig.7.19, but with α = 6.06° there is a maximum change in the ratio of about $\approx$ 10%, where one can argue that there is definitely an effect on wing performance with condensation.

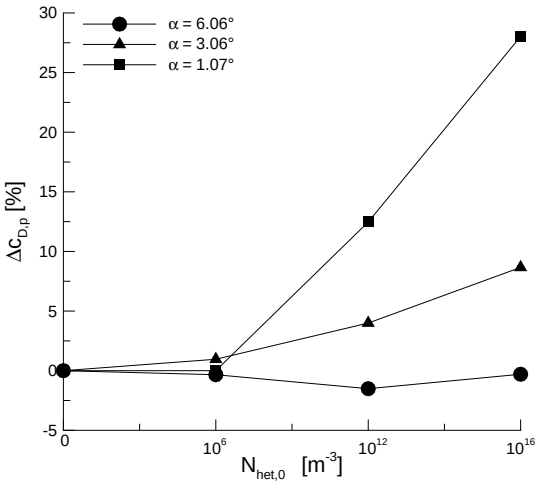

$$\Delta c_{D,p} = \frac{c_{D,p,q>0} - c_{D,p,q=0}}{c_{D,p,q=0}}$$

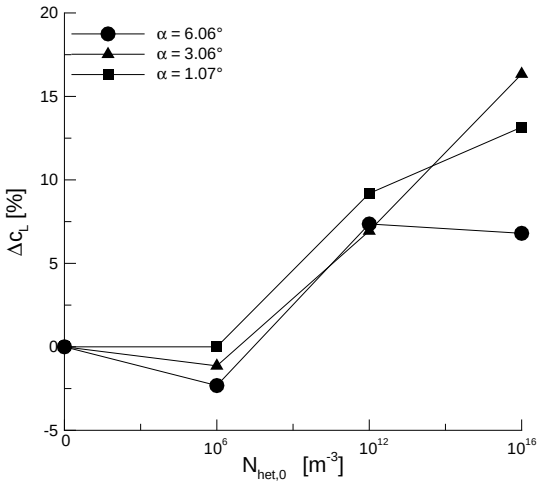

$$\Delta c_L = \frac{c_{L,q>0} - c_{L,q=0}}{c_{L,q=0}}$$

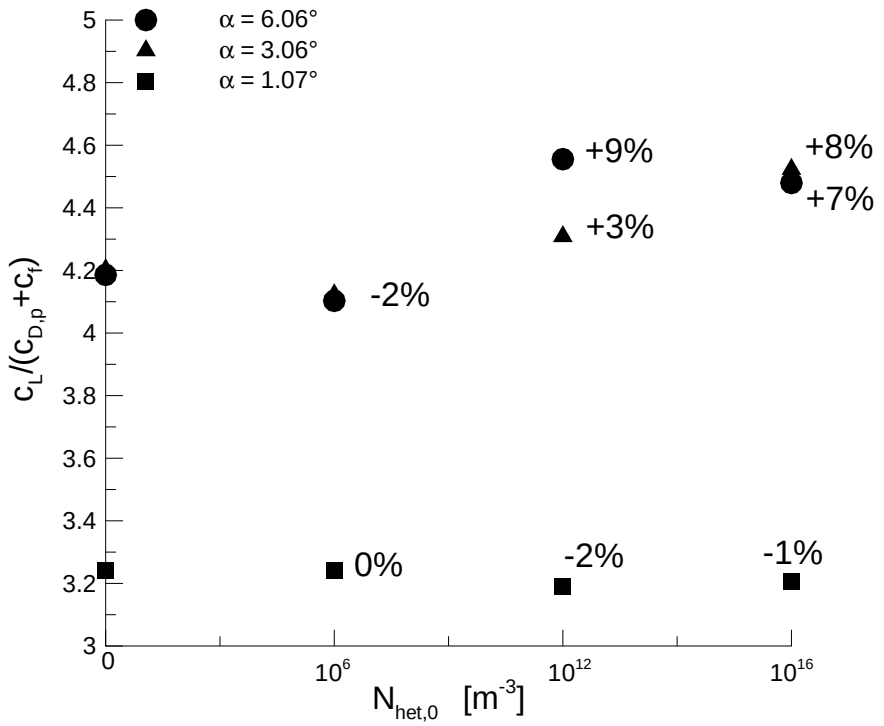

±% represents the increase or decrease in the lift to drag ratio compared to the adiabatic case.

Figure 7.24.: Effect on drag, lift and the lift to drag ratio as a function of particle density for different angles of attack, [$T_\infty = 293.15$ K, $p_\infty = 1$ bar, $M_\infty \approx 0.84$, $R_p = 1\text{x}10^{-8}$m, $MAC = 1.0$m].

7.3. In-Draft Wind Tunnel Scale-ONERA M6 Wing - Turbulent

7.3.1. Moist Air

$\alpha = 3.06°$

For the in-draft wind tunnel, the free stream conditions for the atmospheric flight become the stagnation conditions (T_{01} = 293.15 K, p_{01} = 1 bar). The wing is then scaled down to model size with a MAC of 0.1m and a span of 0.185m. The effect of condensation is pure homogeneous, even with foreign nuclei present they do not cause an effect because the time scale of cooling is equal to the time scale of the agglomeration of the vapor molecules. The range of humidities used is 30-99%. The high humidities are not realistic for operating wind tunnels which conduct experiments on external bodies but it is calculated for a purely scientific reason to see the effect of heat addition on this scale. To avoid condensation in an in-draft wind tunnel, the air is usually dried before entering the experimental chamber. Even with 30% relative humidity an effect can be seen compared to the adiabatic case. Figure 7.25 shows the pressure coefficient at 44 and 80% of the span. In this case compared to fig.7.12 the heat addition increases the static pressure at the leading edge, which moves the second shock position toward the leading edge, compared with heterogenous condensation which increases the supersonic region by moving the second shock closer to the trailing edge. Also in fig. 7.25, as the humidity is increased to 70% the second shock is smeared and as humidity is increased further, the second shock reappears. For example a ϕ_0 of 50 and 90% are nearly identical.

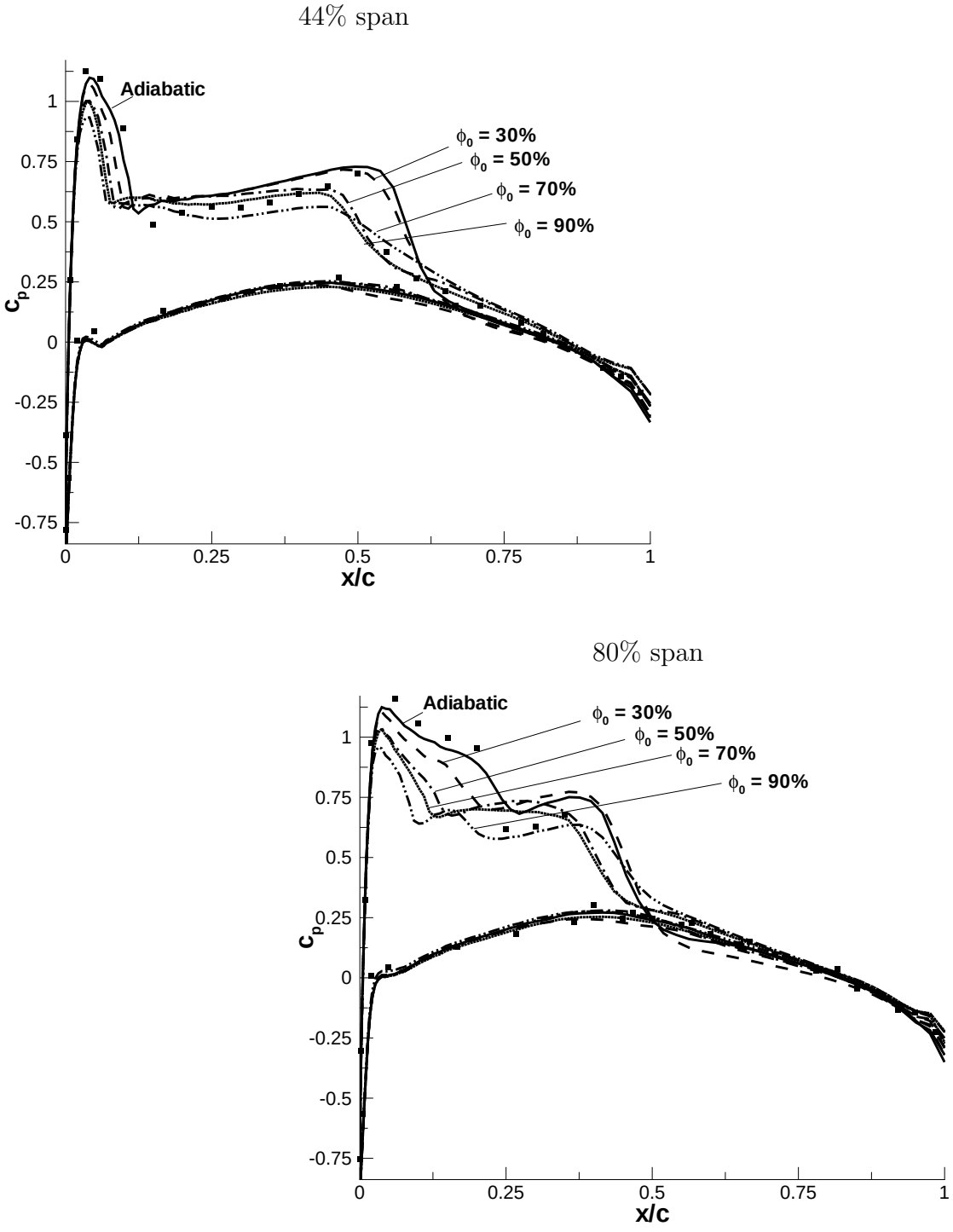

Figure 7.25.: Pressure coefficient for adiabatic flow and for different relative humidities. [T_{01} = 293.15 K, $p_{01} = 1$ bar, $M_\infty \approx 0.840$, $Re_{mac,\infty} = 1.41$ million, $\alpha = 3.06°$, $MAC = 0.1$m].

When the pressure drag and lift coefficient ratio differences are plotted versus humidity, there is minimum in lift near 75% and a maximum in drag (fig.7.26 left). In large scale wings, the friction coefficient (c_f) was on the order of 5% the total drag but in fig.7.26 the friction drag is around 1/3 the total, which decreases as humidity is increased thereby decreasing the total drag as humidity in increased. The percent difference between the adiabatic and ϕ_0 of 70% is c_L = -22% and c_D = -4.1%. Examining the lift to drag ratio with and without friction (fig. 7.26 bottom) the trend follows that of the lift coefficient and the decrease in friction drag with humidity causes the difference between the min and max to decrease.

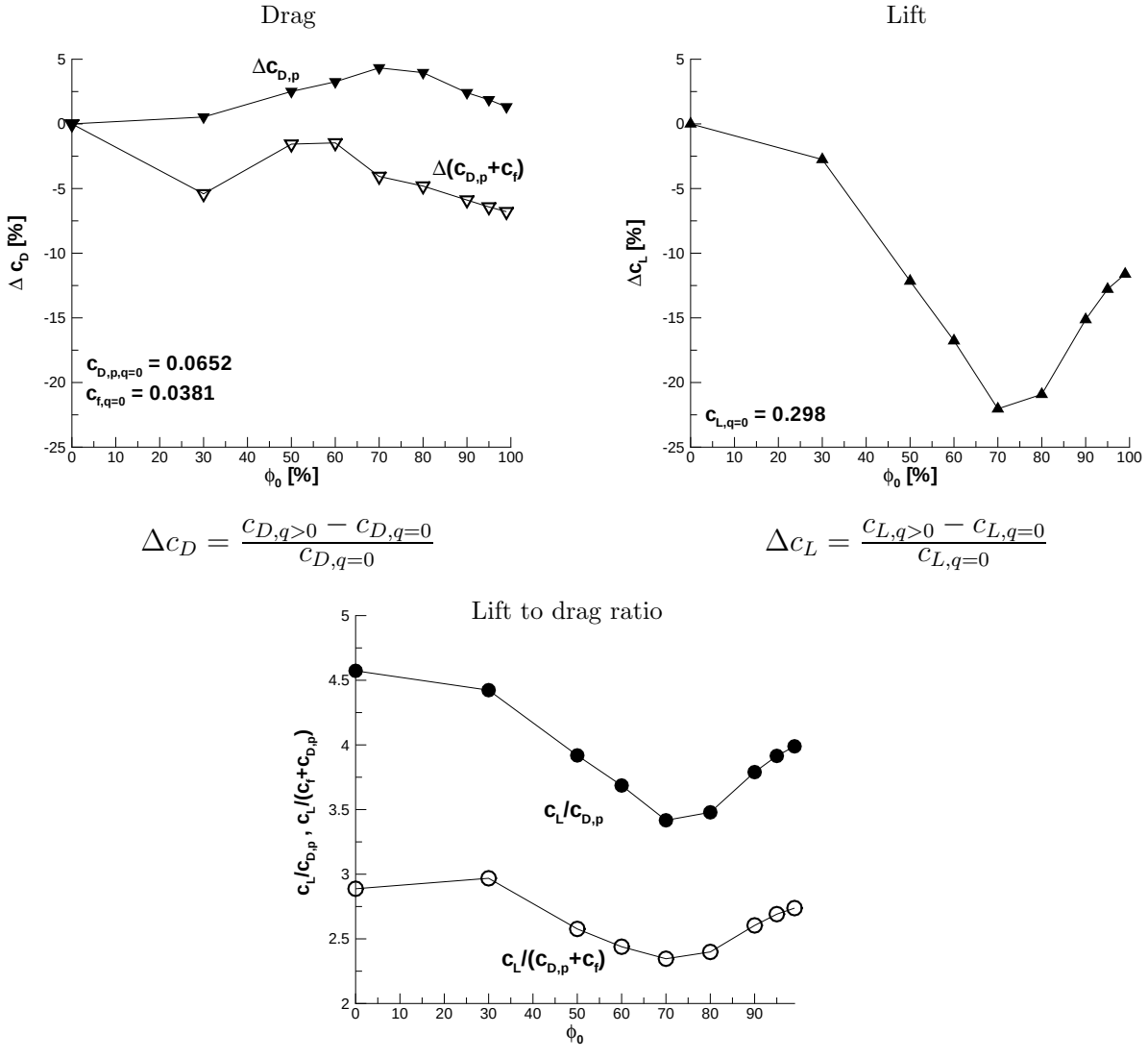

$$\Delta c_D = \frac{c_{D,q>0} - c_{D,q=0}}{c_{D,q=0}} \qquad \Delta c_L = \frac{c_{L,q>0} - c_{L,q=0}}{c_{L,q=0}}$$

Figure 7.26.: Effect on lift and drag, [3.06°].

Figure 7.27 shows the nucleation rate and condensate mass fraction with Mach 1 lines. One major difference between the scale model condensate fraction and that of large scale wing (MAC=1m) in atmospheric flight is the condensate remains after the second shock compared to fig. 7.13 (left). Also as the humidity is increased from top left to bottom right the supersonic region is decreasing and at 90% humidity there is condensate in the freestream before reaching the airfoil. A similarity between the model wing and atmospheric wing geometry is the large angle of 3.06° is responsible for the large nucleation rates near the leading edge causing most of the condensate. A second nucleation region does occur before being terminated by the second shock, where this region is not present in the large scale wings at low particle densities of $10^6 m^{-3}$. At 70% fig. 7.27 the nucleation region around the airfoil is larger compared to the 90% case, this is because there was already nucleation at the inlet, responsible for condensate forming fig. 7.28. The formation of condensate before the airfoil results in a slightly lower free stream Mach number, which is why the 70% - 75% percent has the largest effect, it results in the most sub-critical heat addition, thus having a minimum in the lift to drag ratio.

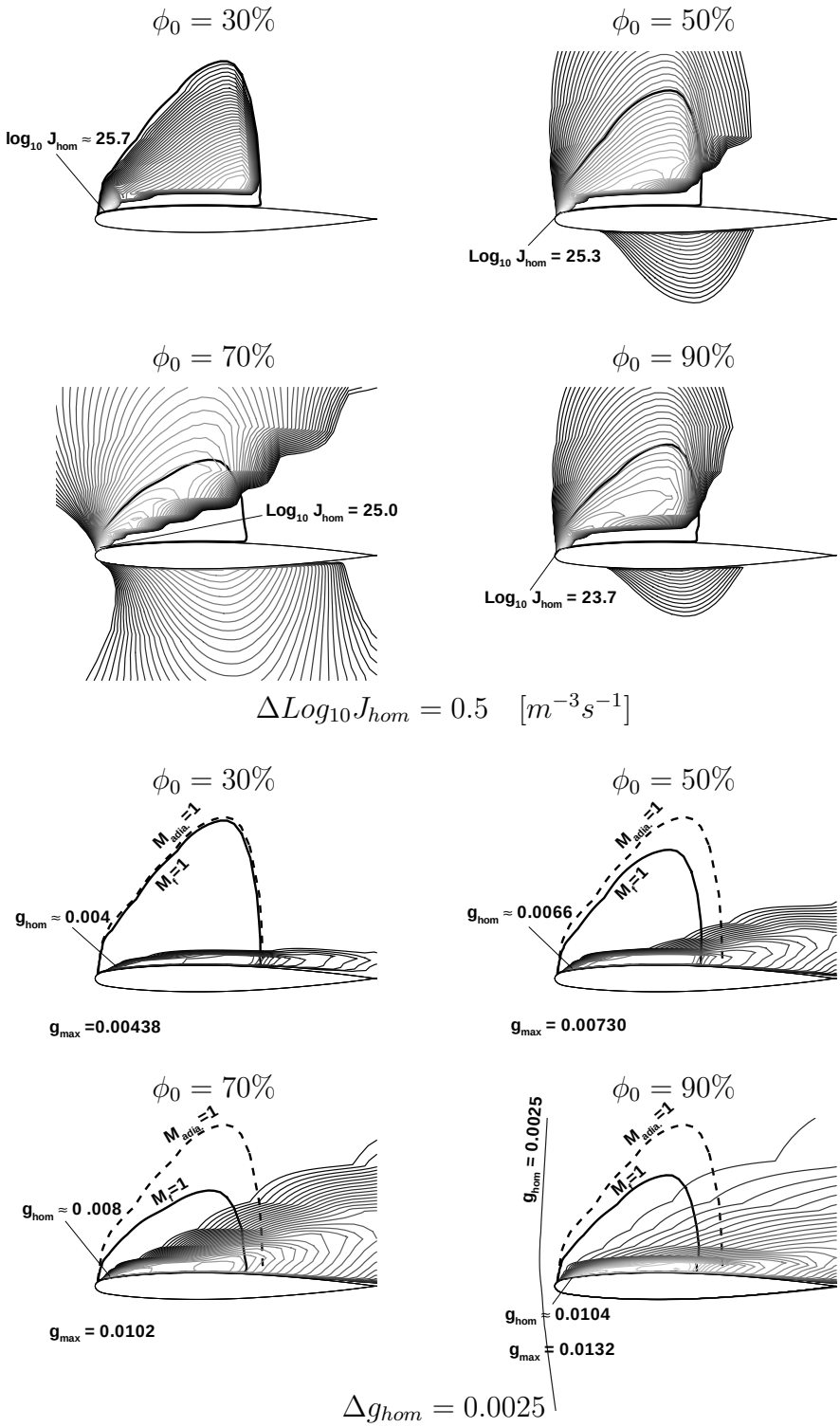

Figure 7.27.: Nucleation rate (top 4) and Homogeneous condensate mass fraction (bottom 4) with Mach 1 lines. [$T_{01} = 293.15$ K, $p_{01} = 1$ bar, $M_\infty \approx 0.840$, $Re_{mac,\infty} = 1.41$ million, $\alpha = 3.06°$, $MAC = 0.1$m, $c_{44\%} = 0.1m$].

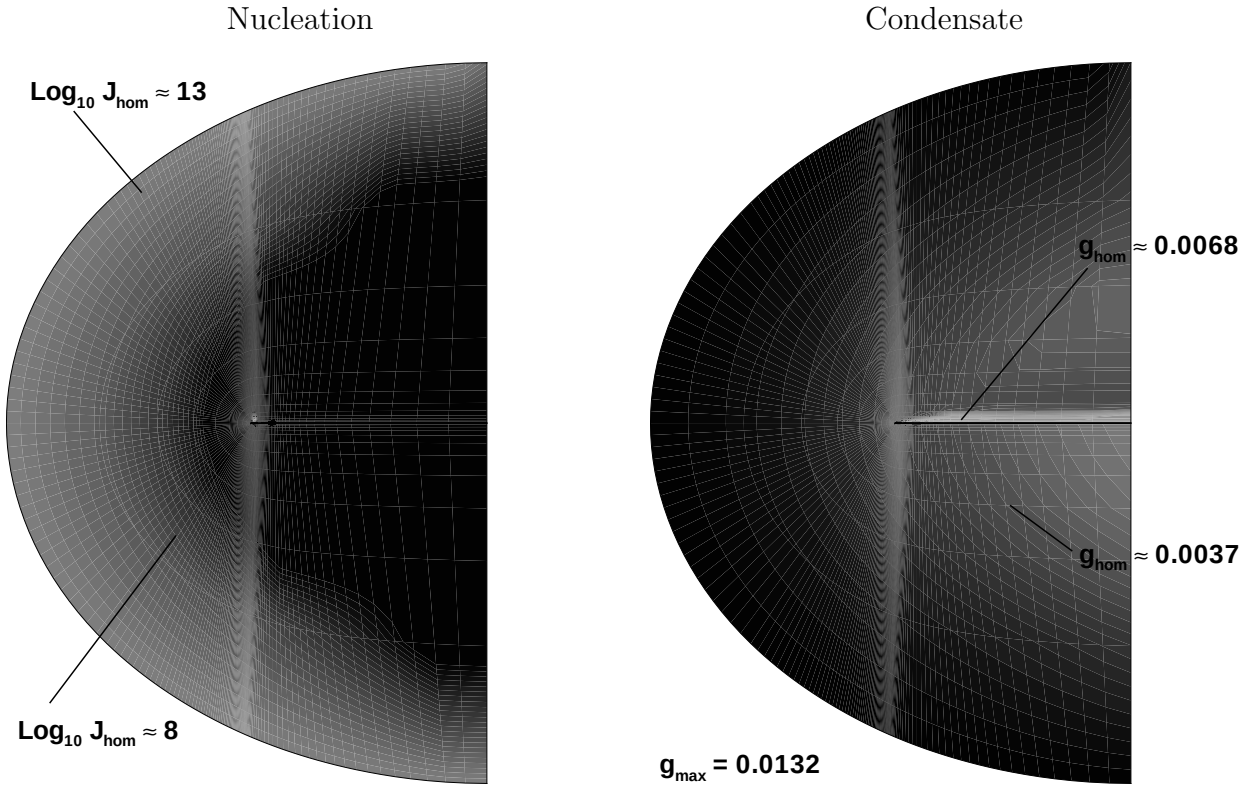

Figure 7.28.: Nucleation rate and homogeneous condensate mass fraction in the far field. [$T_{01} = 293.15$ K, $p_{01} = 1$ bar, $M_\infty \approx 0.840$, $Re_{mac,\infty} = 1.41$ million, $\alpha = 3.06°$, $MAC = 0.1$m, $\phi_0 = 90\%$].

An important numerical point about fig. 7.28 is that the inlet boundary condition is based on the 1-D adiabatic compressible relations, thus having large amounts of condensate on the inlet would not cause the program to necessarily crash but the correct boundary conditions are not being applied because they are based on adiabatic conditions. Fig. 7.28 (right) shows that the condensate on the inlet is around 0.00035 ($g/g_{max} \approx 3\%$) which is not zero, but very small.
The contour plots give much information but it is also interesting to examine some thermodynamic variables along a streamline. Figure 7.29 (top) shows a projected streamline for the adiabatic case, on the left is 44% span and the right is 80% span, note beside the chord length being slightly smaller, the nose radius and thickness is reduced. The streamline is started near the nose at the boundary layer edge. The adiabatic Mach number and temperature gradient is plotted in fig. 7.29 (bottom) from the above projected streamline. At the freestream the temperature gradient is zero and then a large negative peak for the expansion around the nose, followed by two positive peaks which coincides with the double shock system. Interesting is that at Mach 1 the temperature gradient is nearly the same for the two chord lengths, with the smaller chord having a slightly larger peak value at the expansion. The four set of figures (figs. 7.30 - 7.33) include a streamline plot of Mach

contour ($M > 1$), p-T diagram, Mach (M), nucleation (J), and condensate mass fraction (g) for humidities of 30-90% for two spanwise locations (44% and 80%). As the humidity is increased the p-T diagram shifts higher on the $log_{10}\ p_v$ axis. The 30% case is very similar to the adiabatic with the distinct double shock system. As the humidity is increased this double shock system weakens which was also shown in the c_p plots (fig. 7.25). For all cases the flow is super-saturated in the freestream, after the first shock the states return to the saturation line or even past, but not enough to evaporate the entire condensate which was seen in the contour plots of g_{hom} (fig.7.27). The differences between J_{hom} and g_{hom} in the two spans are minor, with major differences in the Mach number. The small difference is mainly based on the way the streamlines were created because they do not necessarily pass through the maximum of J_{hom} and g_{hom}, at each span.

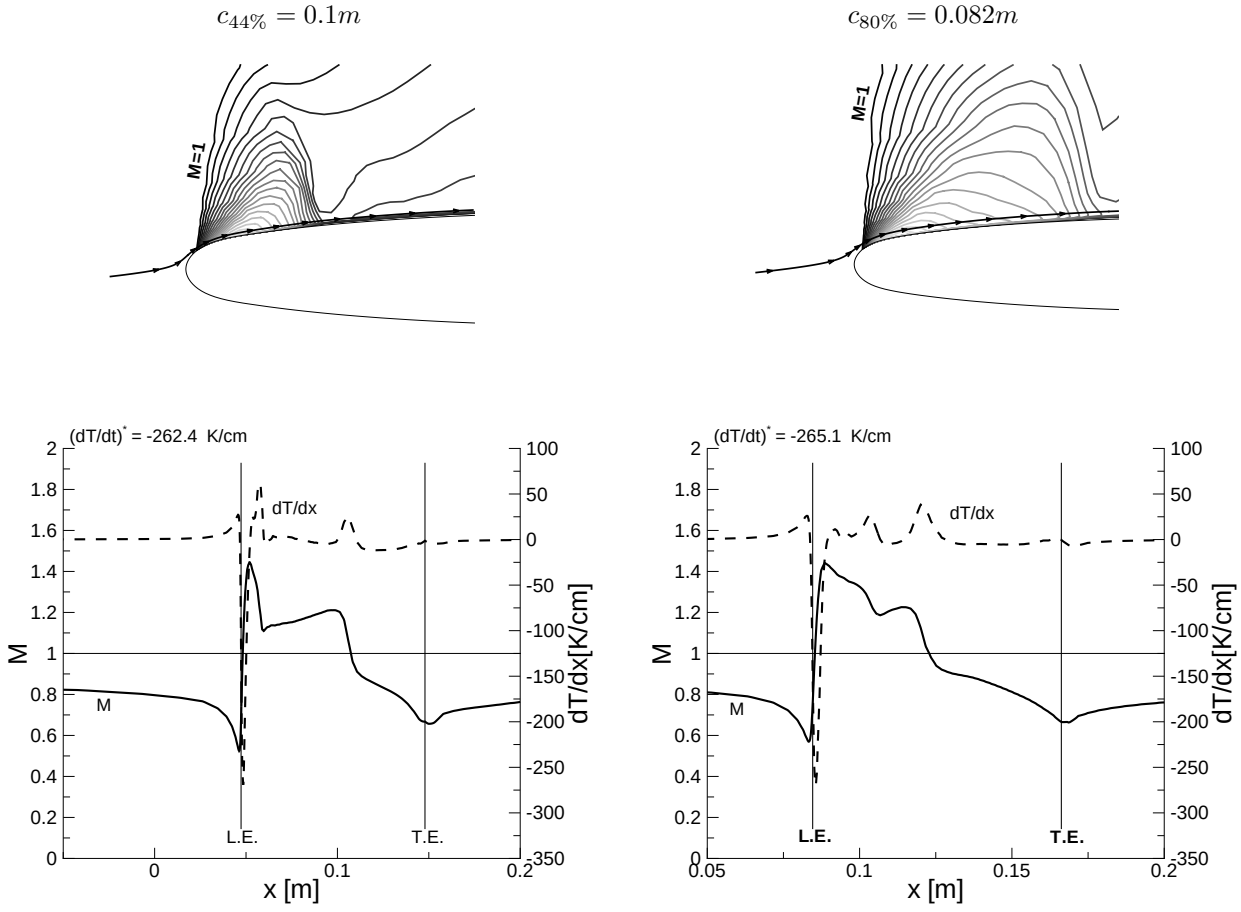

Figure 7.29.: Adiabatic Mach and temperature gradient streamline values [$T_{01} = 293.15$ K, $p_{01} = 1$ bar, $M_\infty \approx 0.840$, $Re_{mac,\infty} = 1.41$ million, $\alpha = 3.06°$, $MAC = 0.1$m].

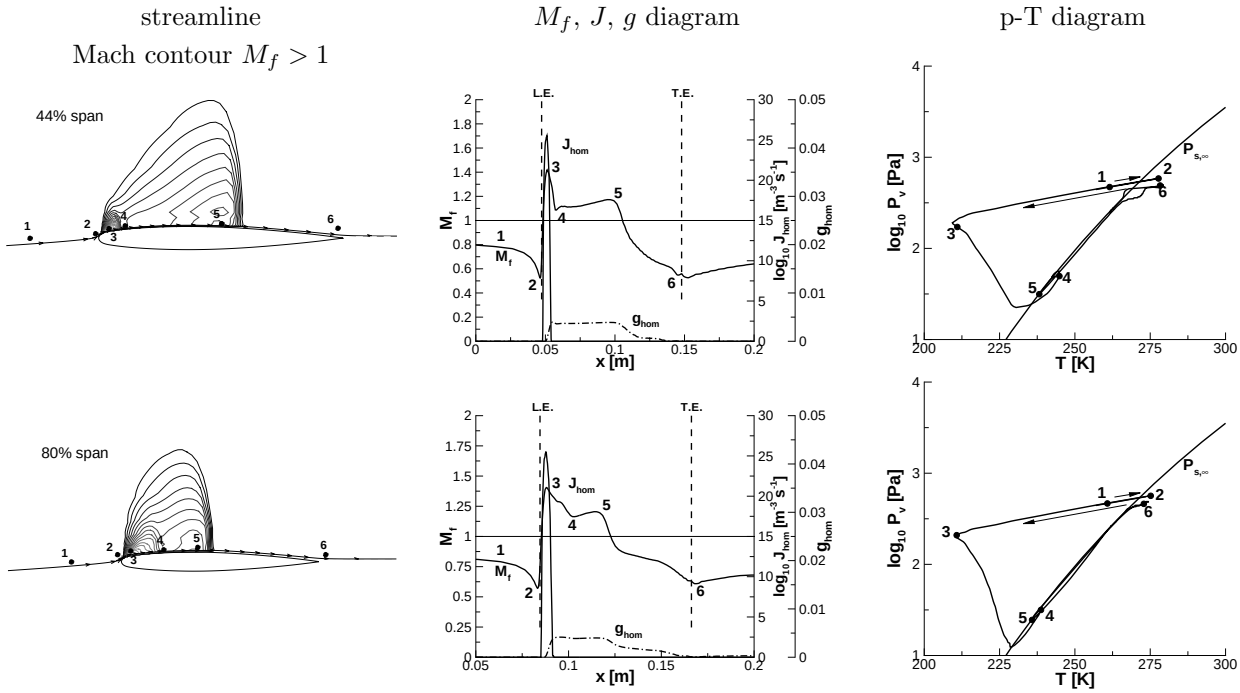

Figure 7.30.: Thermodynamic discussion of properties along a streamline at 44% and 80% span, [$\boldsymbol{\phi_0 = 30\%}$, $T_{01} = 293.15$ K, $p_{01} = 1$ bar, $M_\infty \approx 0.840$, $Re_{mac,\infty} = 1.41$ million, $\alpha = 3.06°$, $MAC = 0.1$m].

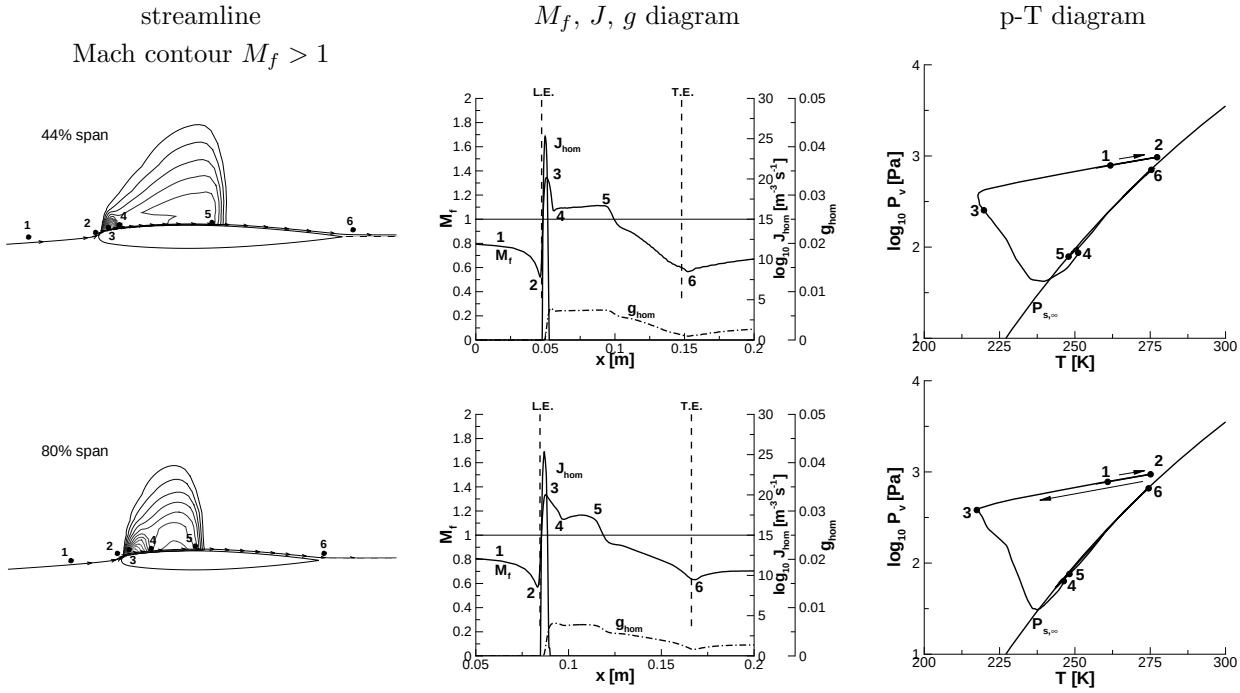

Figure 7.31.: Thermodynamic discussion of properties along a streamline at 44% and 80% span, [$\boldsymbol{\phi_0 = 50\%}$, $T_{01} = 293.15$ K, $p_{01} = 1$ bar, $M_\infty \approx 0.840$, $Re_{mac,\infty} = 1.41$ million, $\alpha = 3.06°$, $MAC = 0.1$m].

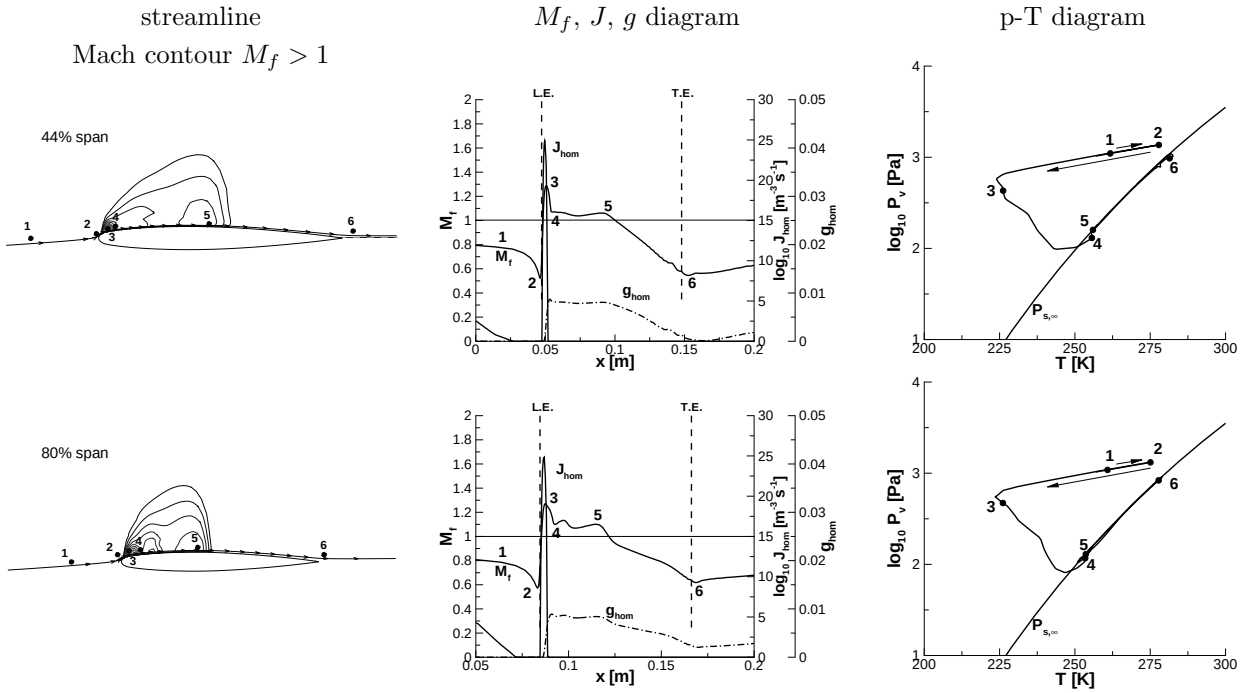

Figure 7.32.: Thermodynamic discussion of properties along a streamline at 44% and 80% span, [$\boldsymbol{\phi_0 = 70\%}$, $T_{01} = 293.15$ K, $p_{01} = 1$ bar, $M_\infty \approx 0.840$, $Re_{mac,\infty} = 1.41$ million, $\alpha = 3.06°$, $MAC = 0.1$m].

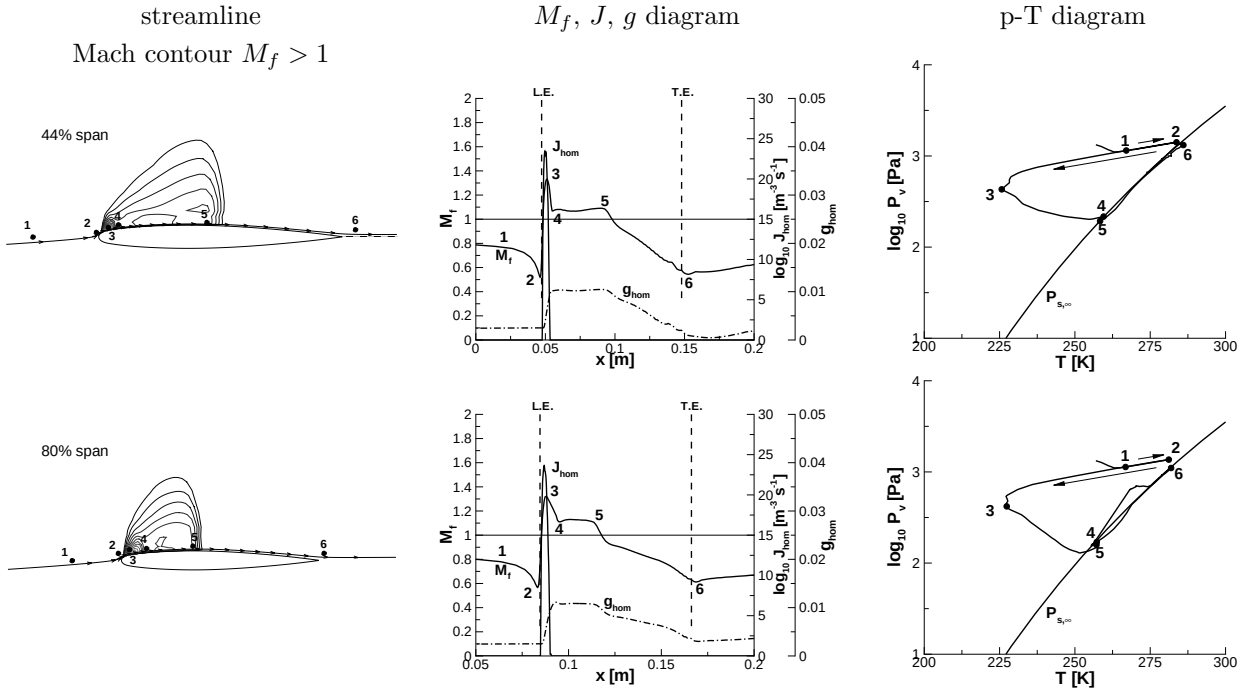

Figure 7.33.: Thermodynamic discussion of properties along a streamline at 44% and 80% span, [$\boldsymbol{\phi_0 = 90\%}$, $T_{01} = 293.15$ K, $p_{01} = 1$ bar, $M_\infty \approx 0.840$, $Re_{mac,\infty} = 1.41$ million, $\alpha = 3.06°$, $MAC = 0.1$m].

$\alpha = 6.06^{\circ}$

The same trends as for the $\alpha = 3.06^{\circ}$ are present in 6.06°, with the supersonic region shrinking on the suction side as humidity is increased but after 70% it stabilizes are slightly increases, fig. 7.34. This should not be a surprise since the saturation point is the same, only the angle of attack has been changed. The only difference with the higher angle of attack is that it produces larger nucleation rates and more condensate. Like in fig. 7.26, fig. 7.35 shows the same trend of decreasing lift with humidity, reaching a minimum around 70-75% and slowly increasing. For the larger angle of attack the adiabatic friction drag is only 20% of the total drag compared to 37% for 3.06°. At 6.06° the pressure drag dominates the total drag and thus a trend of slight increasing to a maximum around 70-75% like in the c_{D_p} of fig. 7.26 (left). The lift to drag ratio fig.7.35(bottom) again follows the same trend as the lift.

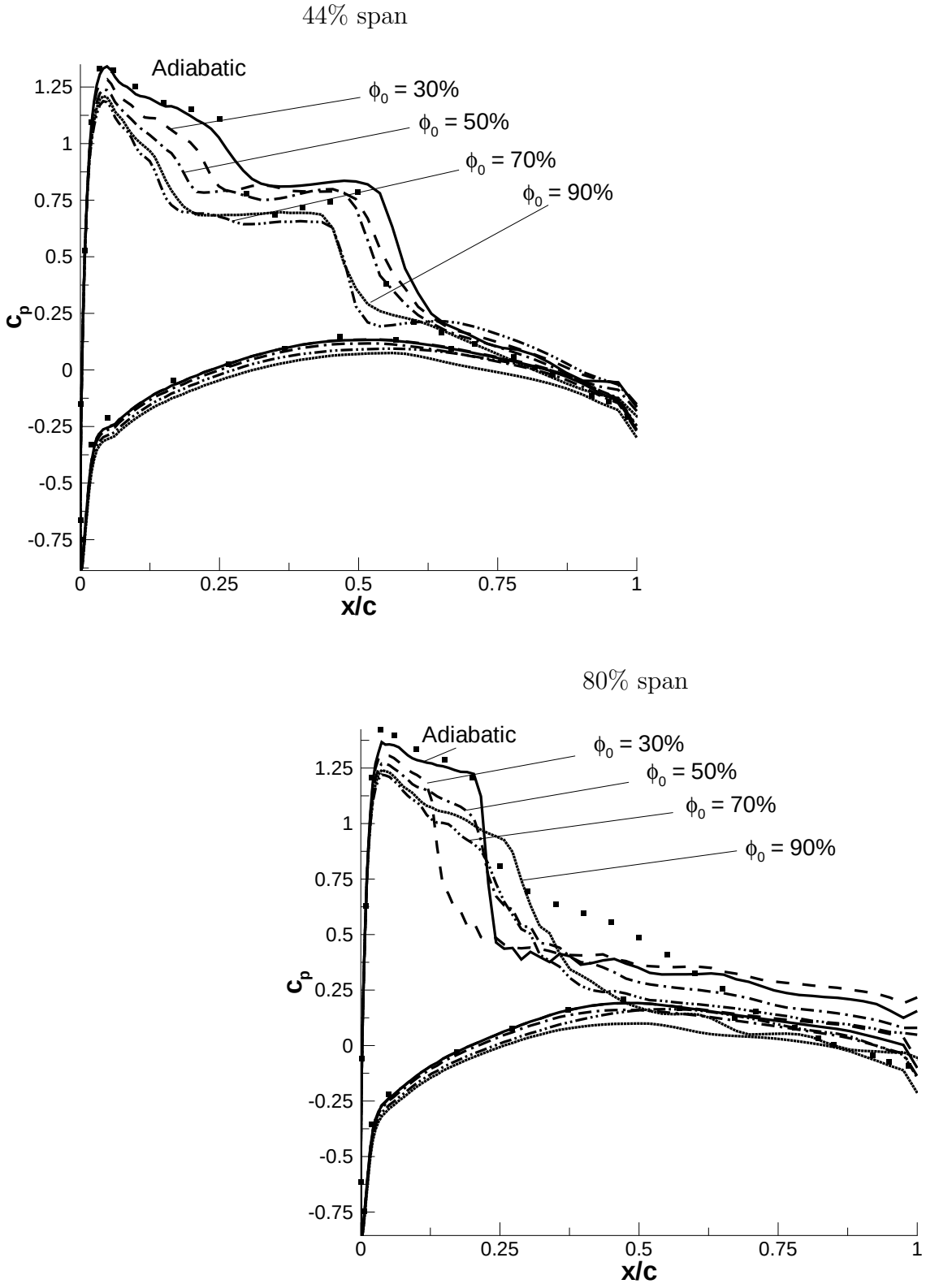

Figure 7.34.: Pressure coefficient for adiabatic and different relative humidities. [$T_{01} = 293.15$ K, $p_{01} = 1$ bar, $M_\infty \approx 0.840$, $Re_{mac,\infty} = 1.41$ million, $\alpha = 6.06°$, $MAC = 0.1$m].

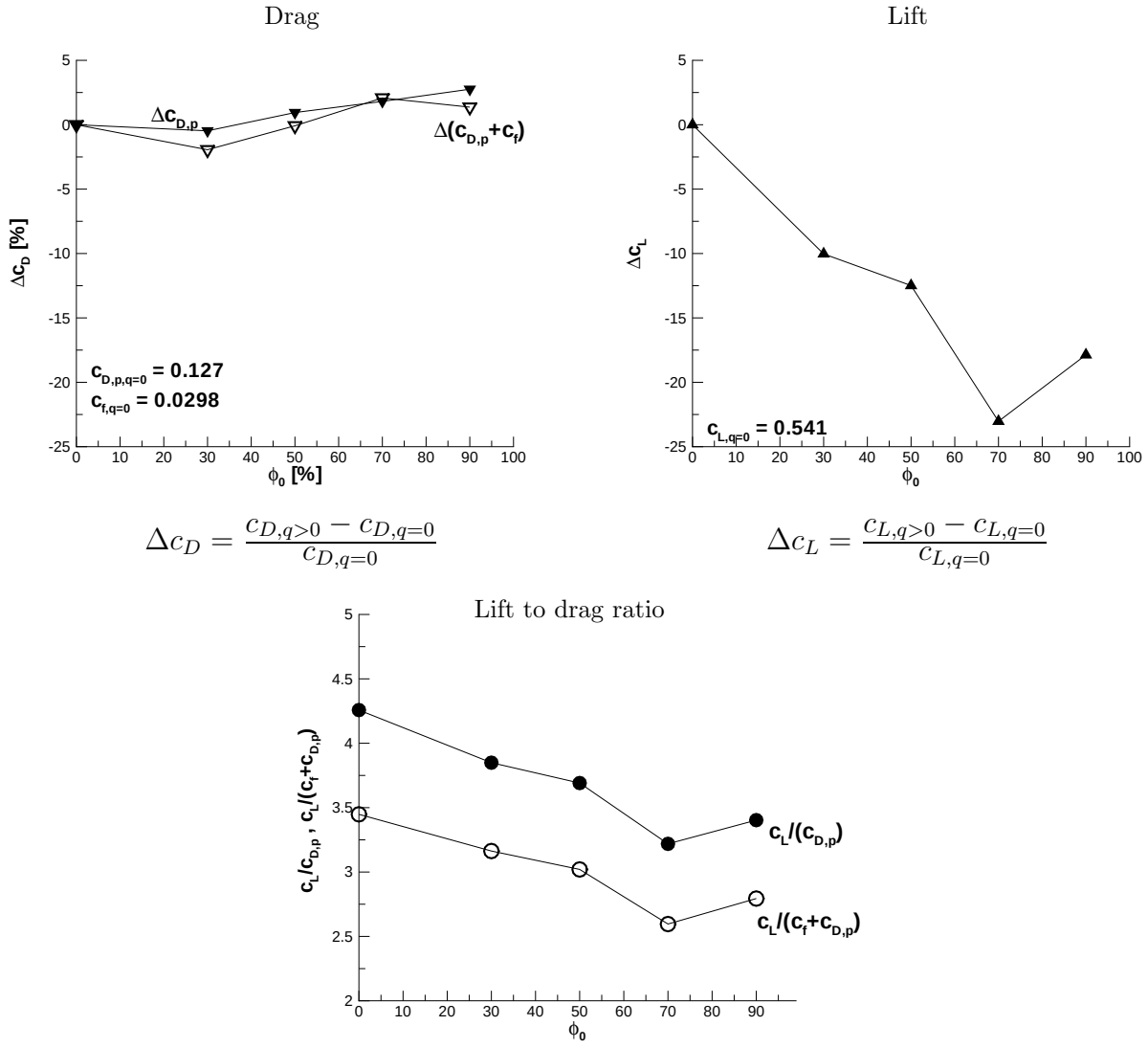

Figure 7.35.: Effect on lift and drag, [6.06°].

Figure 7.36 shows the condensate mass fraction at 44 and 80% of the wing span, at 44% (top 4) a much larger condensate zone is present compared to fig. 7.27 and at 80% (bottom 4) the separation region is decreased with an increase in humidity, which is visualized by the condensate remaining more attached to the profile as the humidity is increased (top left to bottom right). The same trend was present for atmospheric flight with an increase from 10^6 to $10^{12}m^{-3}$ particle density, fig. 7.20

The computed skin friction lines and pressure distribution are shown in fig. 7.37 which can be compared with fig. 7.22 in the atmospheric flight section. In the adiabatic flow (top center) a large separation region is present from about 60% span to the tip. The increase in humidity does not remove the separation entirely but decreases its strength and shifts it slightly closer to the tip.

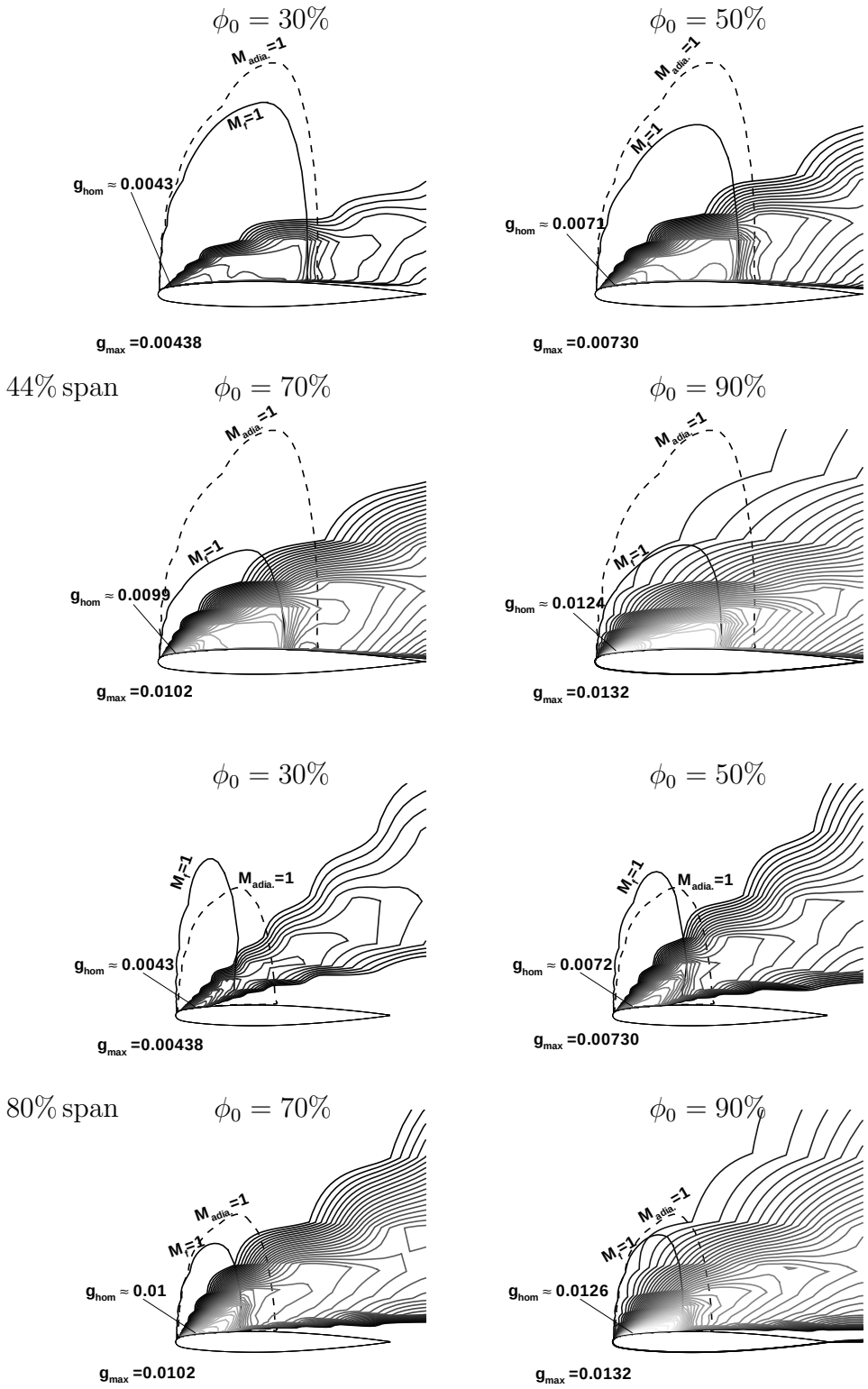

Figure 7.36.: Homogeneous condensate mass fraction and Mach 1 line. [$T_{01} = 293.15$ K, $p_{01} = 1$ bar, $M_\infty \approx 0.840$, $Re_{mac,\infty} = 1.41$ million, $\alpha = 6.06°$, $MAC = 0.1$m, $c_{44\%} = 0.1$m, $c_{80\%} = 0.082$m].

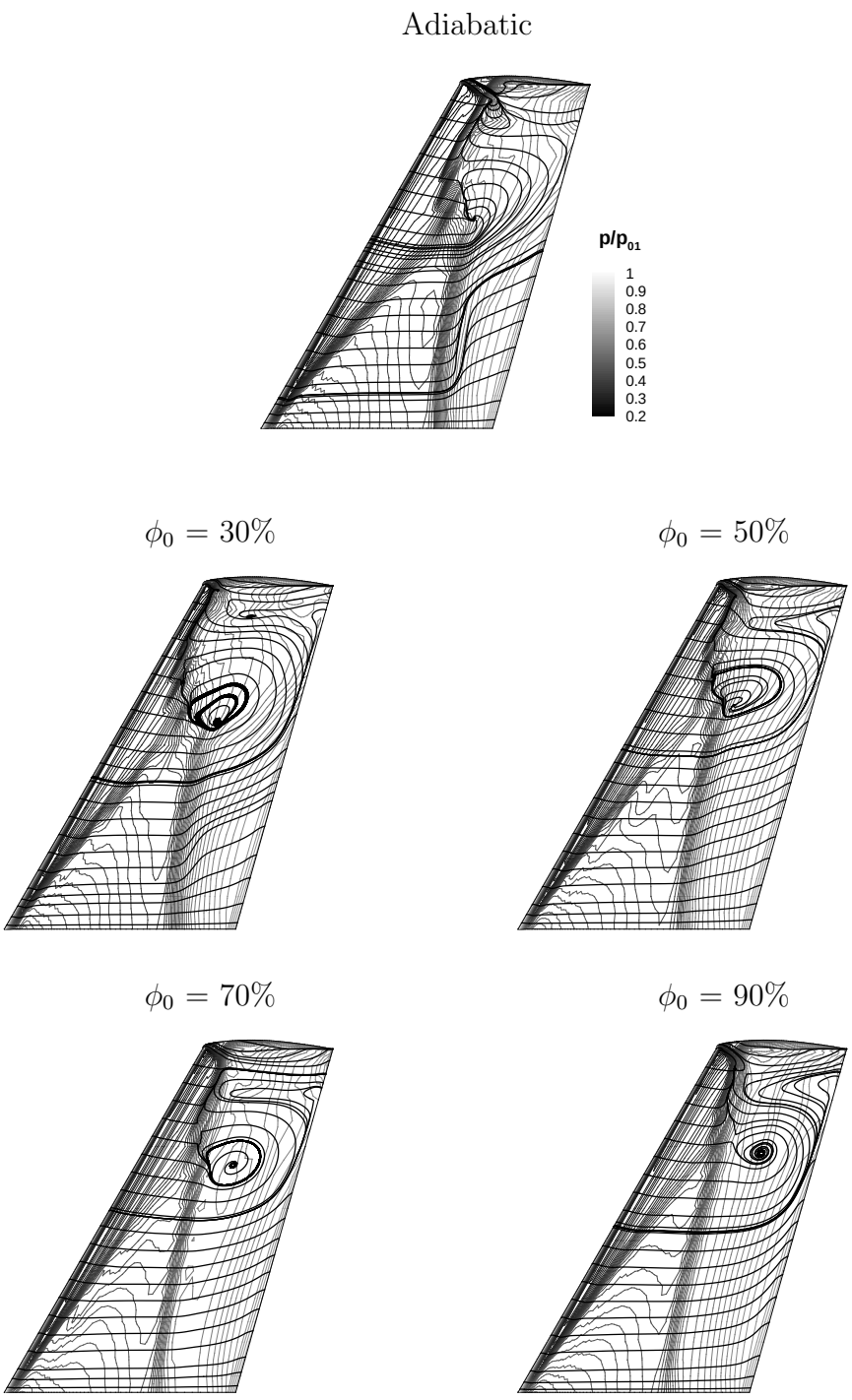

The computed skin friction lines are calculated based on the wall shear stress eqs. 2.35-2.37, which are then cast into the three vector components where streamlines are drawn from.

Figure 7.37.: Wing top computed skin friction lines (bold lines) overlaid on a contour plot of the pressure ratio, [$T_{01} = 293.15$ K, $p_{01} = 1$ bar, $M_\infty \approx 0.840$, $Re_{mac,\infty} = 1.41$ million, $\alpha = 6.06°$, $MAC = 0.1$m].

$\alpha = 1.07°$

At a low angle of attack the effect of condensation is delayed until around 50% humidity (fig. 7.38) compared to the above cases (figs. 7.25 and 7.34), which is reasonable for lower expansions around the leading edge. At higher humidities $> 70\%$ the second shock is smeared, which actually caused longer iterations for a converged solution. At first is was thought the flow became unsteady but looking at a time series of c_p it reached a steady solution.

Figure 7.39 shows the nucleation rate and condensate at 44% span for humidities 30-90%. At 30% the expansion is too weak and no condensate is present, likewise at 50% the effects are very weak. At 70 and 90% humidity, condensate is visible on the pressure side, which reduces the lift. Nucleation rates (fig. 7.39) are similar to that found at 3.06° (fig. 7.27), thus even though nucleation rates are similar, the expansion is not supercooled enough to allow for large amounts of condensate to form.

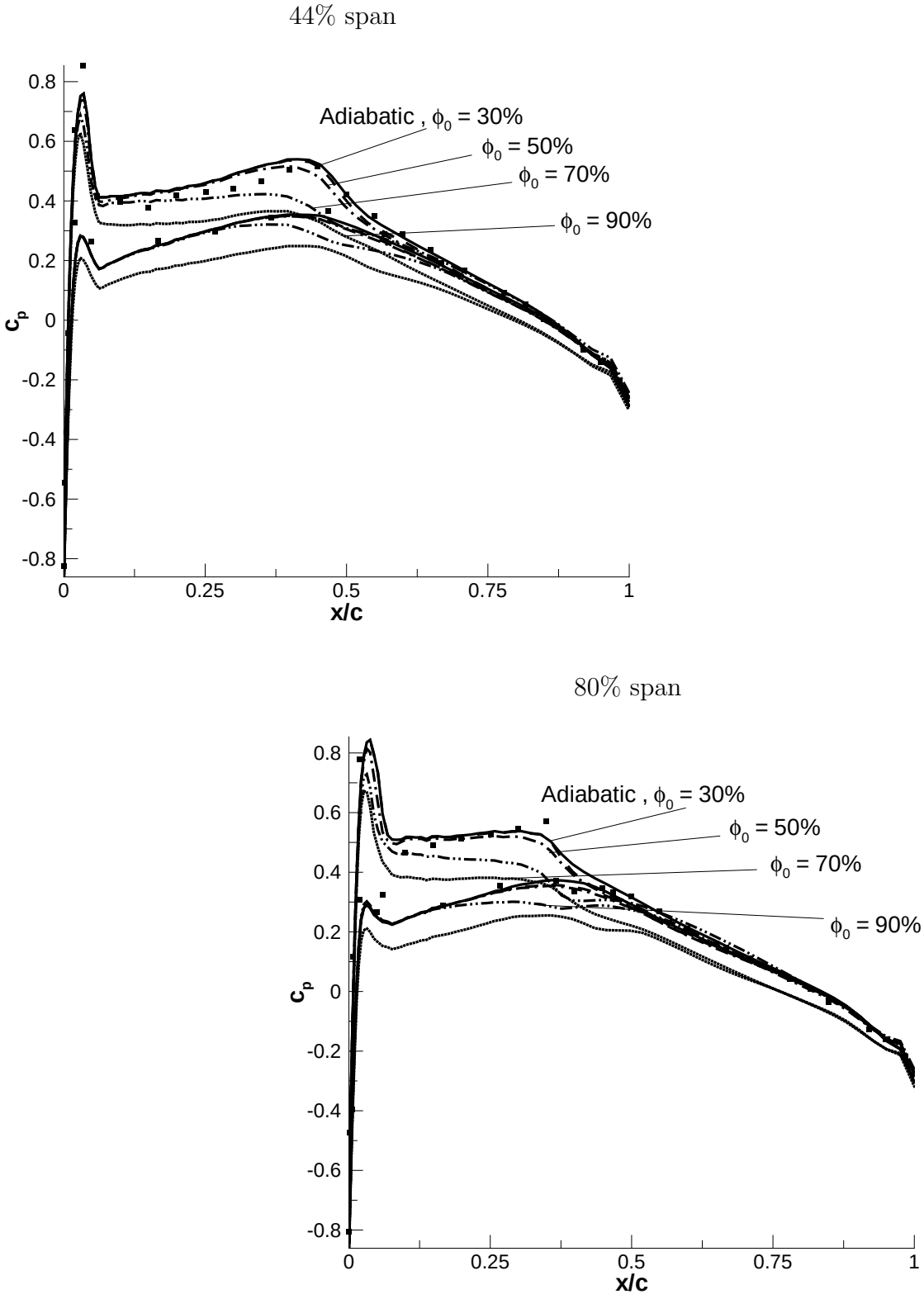

Figure 7.38.: Pressure coefficient for adiabatic and different relative humidities. [$T_{01} = 293.15$ K, $p_{01} = 1$ bar, $M_\infty \approx 0.840$, $Re_{mac,\infty} = 1.41$ million, $\alpha = 1.07°$, $MAC = 0.1$m].

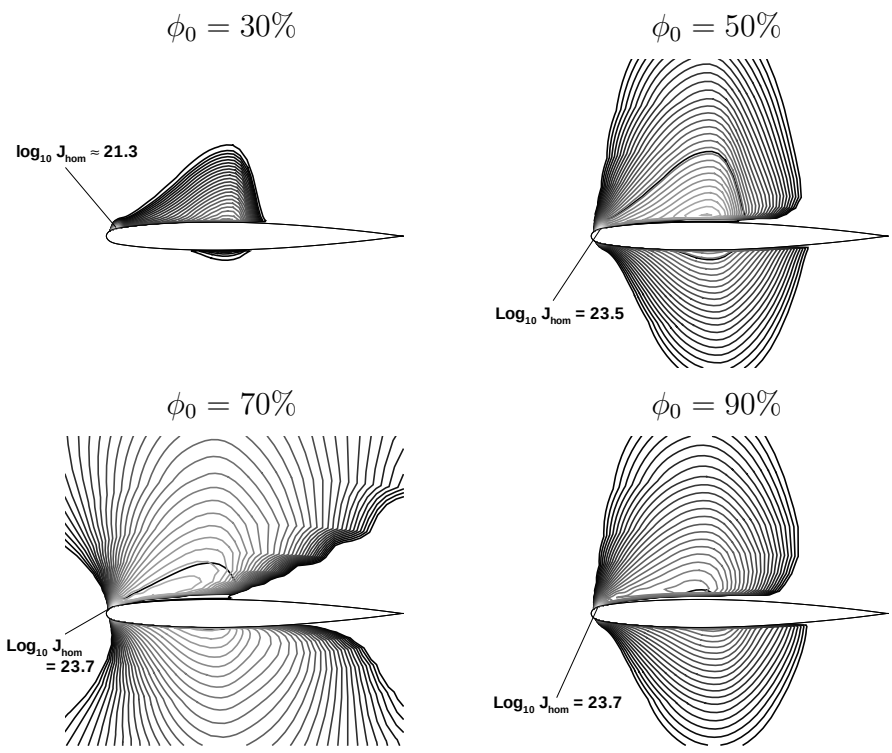

$$\Delta Log_{10} J_{hom} = 0.5 \quad [m^{-3} s^{-1}]$$

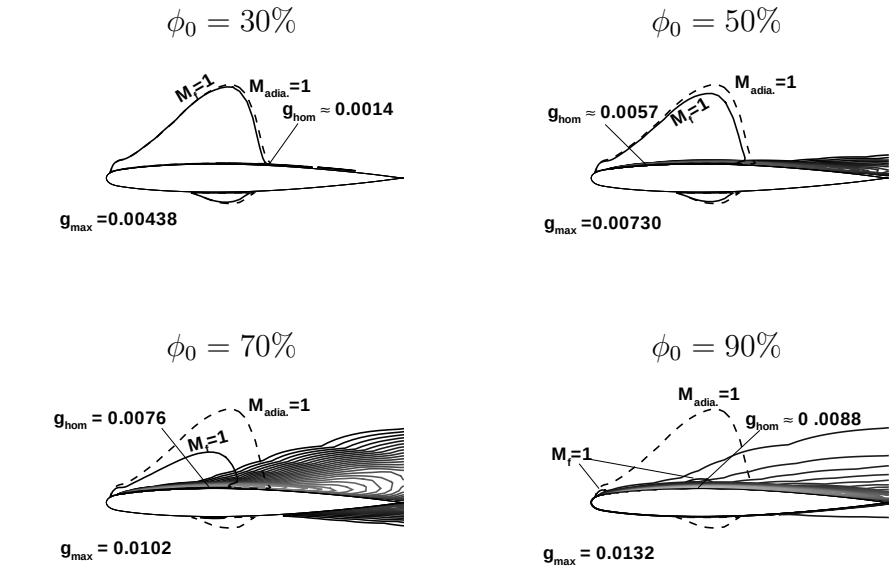

$$\Delta g_{hom} = 0.0025$$

Figure 7.39.: Nucleation rate and homogeneous condensate mass fraction with Mach 1 lines. [$T_{01} = 293.15$ K, $p_{01} = 1$ bar, $M_\infty \approx 0.840$, $Re_{mac,\infty} = 1.41$ million, $\alpha = 1.07°$, $MAC = 0.1$m, $c_{44\%} = 0.1m$].

The pressure drag and lift (fig. 7.40, left) exhibit the same behavior of a local minimum around 70% humidity as (figs. 7.26 and 7.35), except here the friction coefficient is greater than the pressure drag coefficient. Since the friction drag is decreasing the total drag decreases with an increase in humidity, like the 3.06° case fig.7.26 (left). Figure 7.40 (bottom) shows the lift to drag ratio with and without friction, the curve maintains the behavior of lift but the difference between the min and max is altered between the two curves because of the positive benefit with the friction drag. Without taking into account friction the maximum deviation from adiabatic is 32% compared to 24% with friction.

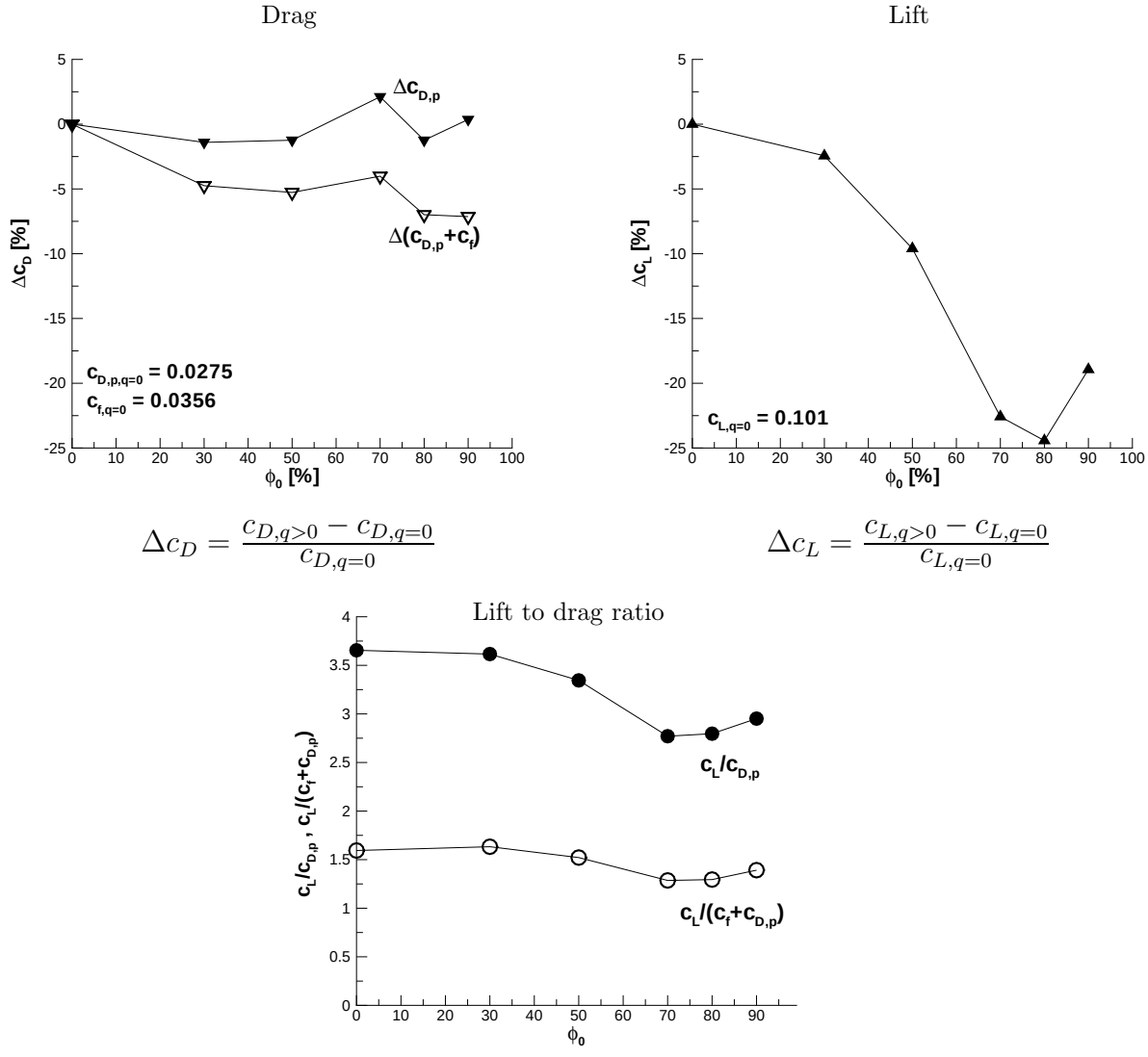

Figure 7.40.: Effect on lift and drag, [1.07°].

Summary

Schnerr and Dohrmann [85] have computed simulations for a NACA0012 airfoil in an in-draft wind tunnel environment. The chord length was 100mm, with a $M_\infty = 0.8$ and an angle of attack $\alpha = 1.25°$. Even if the flow is mostly 2-D for the 3-D wing at low angles of attack the time scale is different for each span segment because the chord length is changing throughout the span, thus the MAC is 100mm, but the root chord is 124mm and the tip chord is 70mm. Therefore, it is not possible to conclude the 3-D wing should have the same effects as a 2-D case. From [85] the lift coefficient decreased by around 35% and reached a minimum at 60% relative humidity and then began to increase which is the same trend for the 3-D wing with all angles of attack. The decrease in lift for the 3-D wing is around 32%, 28%, and 30% for α 1.07°, 3.06°, and 6.06°. In regards to the drag, [85] reports a decrease in drag of about 25% until 60% relative humidity and then begins to increase. For the 3-D wing the drag remained relatively constant for all angles of attack with a slight increase for 3.06° and 6.06°.

7.4. Cryogenic Wind Tunnel - Turbulent

7.4.1. Nitrogen

The main reason for using a pure N_2 wind tunnel is to achieve a flight Reynolds number based on a small scale geometry. The advantage here is that mass flow is kept small because of the model geometry and the Reynolds number is increased by using the dependence of gas viscosity. Gases becomes less viscous if the temperature is reduced, therefore higher Reynolds numbers are reached when working under cryogenic conditions compared to gas at room temperature. The optimum design is to have the lowest temperature possible to reduce tunnel size but then the question arises, if there will be condensation onset at this low temperature near saturation?

The following results for the ONERA M6 wing are based on the model validated in subsec. 4.2.1. The main points of the model are, the modified Gyaramthy droplet growth law, the ASHRAE function for σ, and the Tolman correction factor δ of 0.5^{-10} are used.

7.4.2. ONERA M6 Wing

$\alpha = 3.06°$

Figure 7.41 shows the pressure coefficient at 44 and 80% of the span. The adiabatic line matches that of the experiment even for the slightly altered Reynolds number and physical constants. Under the given operating conditions, condensation of N_2 is slightly present, which is seen by the deviation of the pressure from the adiabatic case near the leading edge.

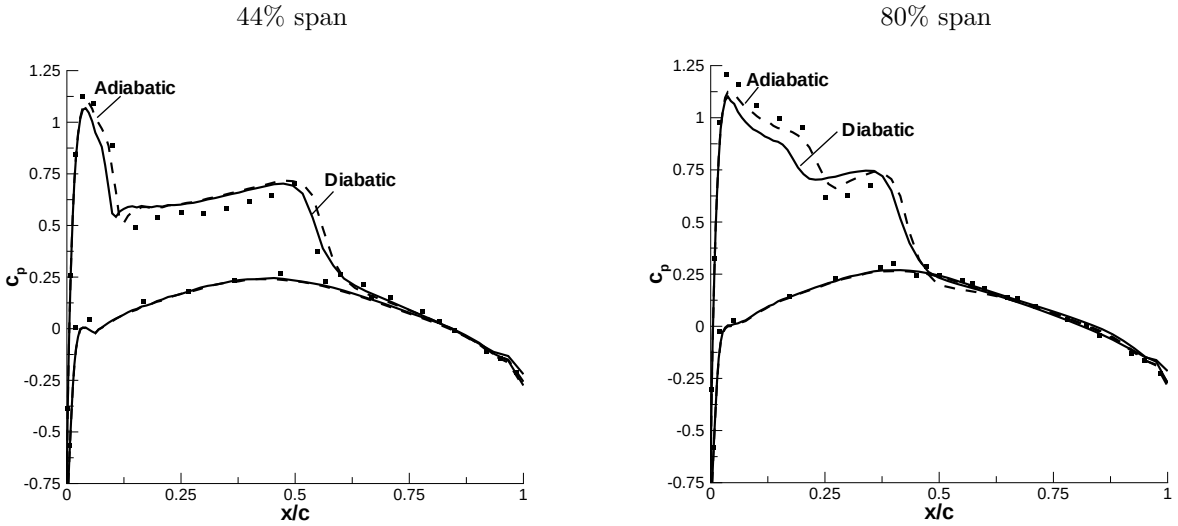

Figure 7.41.: Pressure coefficient for adiabatic and diabatic case, [$T_{01} = 99.0$ K, $p_{01} = 5.07$ bar, s_0=0.70, $M_\infty \approx 0.840$, $\alpha = 3.06°$, $MAC = 0.1$m, $Re_{MAC,\infty} = 31.4$ million].

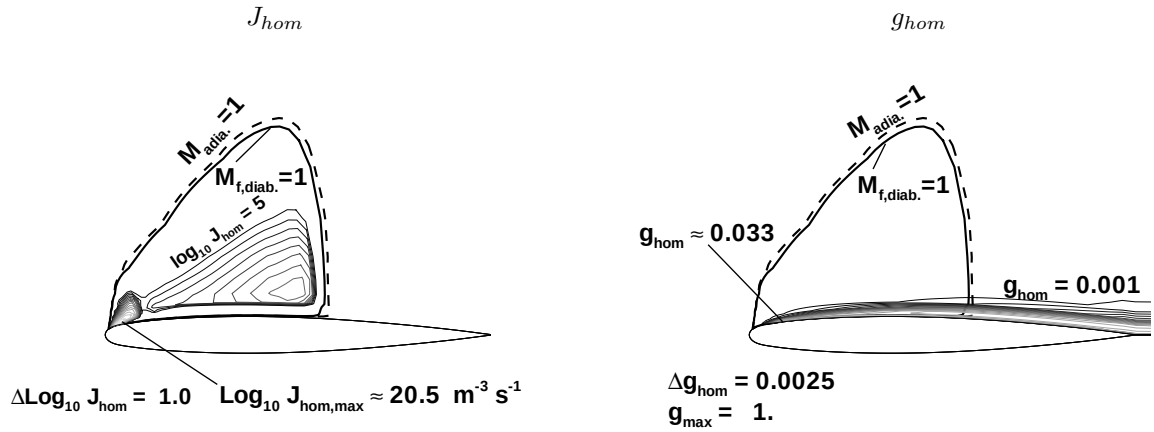

Figure 7.42.: Nucleation rate and homogeneous condensate mass fraction with Mach 1 line at 44% span, [T_{01} = 99.0 K, p_{01} = 5.07 bar, s_0=0.70, $M_\infty \approx 0.840$, $\alpha = 3.06°$, MAC = 0.1m, $Re_{MAC,\infty}$ = 31.4 million].

Figure 7.42 compares the nucleation rate and homogeneous mass fraction at 44% span. A streamline starting just outside the boundary layer edge near the nose is projected in the 2-D cross-section (44% span), fig. 7.43 (top) with the supersonic Mach contour as the background. The streamline values of Mach, J_{hom}, g_{hom} are plotted in fig. 7.43 (bottom left) and as well as a p-T diagram (bottom right) with the related state points. In the CAST-10 simulation for these conditions the free stream was not saturated but due to the higher Mach number of 0.84 compared to 0.65 the flow at 1 is already saturated. From 1 to 2 is a small compression upon reaching the airfoil but remaining super-saturated. There is an expansion around the airfoil from 2 to 3 but then the growth of condensate begins at point 3. From 3 the growth of g_{hom} begins to reduce J and the shock from 3-4 cuts off the growth of g_{hom} which then remains constant. A small expansion from 4 to 5 and then the state passes the saturation line at the trailing edge. Although the compression beyond the saturation line is not enough to completely evaporate the condensate. After the compression the state returns closely to state point 1, which is super-saturated.

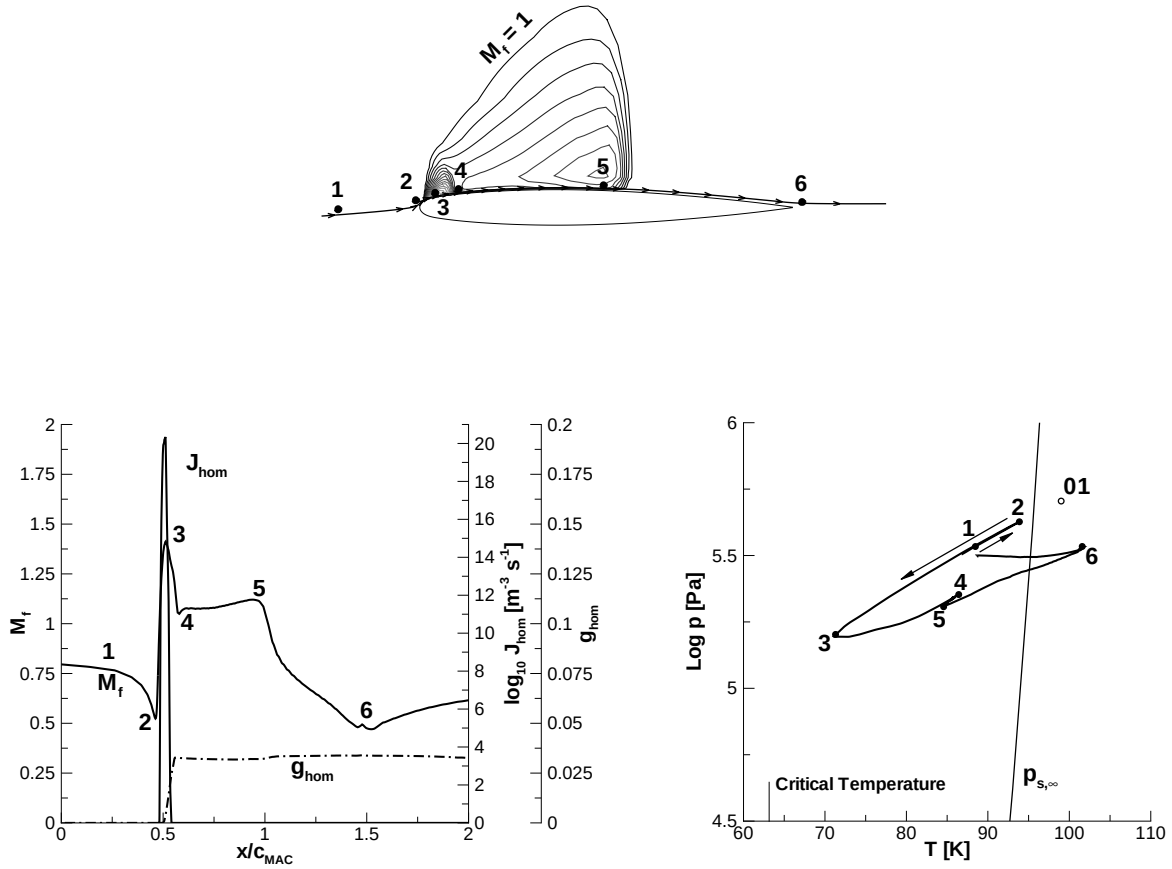

Figure 7.43.: Thermodynamic discussion of properties along a streamline at 44% span,[T_{01} = 99.0 K, p_{01} = 5.07 bar, s_0=0.70, $M_\infty \approx 0.840$, $\alpha = 3.06°$, MAC = 0.1m, $Re_{MAC,\infty}$ = 31.4 million].

top	:	Mach contour and projected streamline near the boundary layer edge.
bottom left	:	Mach, J_{hom}, and g_{hom} values extracted from streamline.
bottom right	:	p-T diagram based on streamline.

At 80% span the same trends are visible except for the small expansion from 4-5 is not as distinct, of course there are small differences in the state points but the overall shape is the same.

$\alpha = 6.06°$

At a higher angle of attack 6.06°, condensation of N_2 is also present which is expected due to the higher expansion compared to 3.06°. The deviation from adiabatic is seen in the c_p plots at 44 and 80% span (7.44).
Figure 7.45 compares the nucleation rate and condensate fraction at 44 and 88% span. At 80% span there is separation, which also occurred for the atmospheric and model test case. In the atmospheric flight condition for low particle density fig. 7.20 and the wind tunnel fig. 7.36 the condensate broke off with the separation zone but here the condensate remains attached to the trailing edge. Also under higher humidities and particle concentration the separation zone was reduced or moved but here the effect is very small. The reason for this is most likely due to the fact that N_2 condensation is much smaller due to the latent heat of vaporization is $\approx$ 10 times smaller compared with water.
Figure 7.46 shows the pressure distribution and computed skin friction lines for the suction side of the wing surface, similar plots were made for moist air in atmospheric flight fig. 7.22.
Figure 7.47 examines the thermodynamic properties along a projected streamline near the boundary layer edge at two spanwise locations. In fig.7.47 (top left) the streamline abruptly changes upward after the shock which indicates the separation region at 80% span. As g_{hom} begins and increases, J_{hom} is cut off and thus a very narrow peak for the nucleation rate exists. In the p-T diagram fig. 7.47 (bottom) the state is super-saturated like in fig. 7.43 crossing the saturation line after the second shock and returning to the super-saturated state in the freestream.

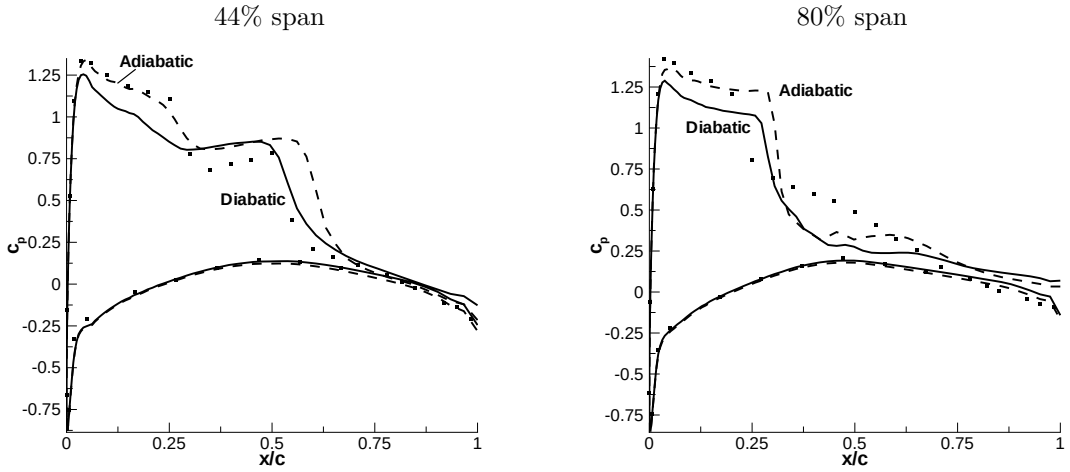

Figure 7.44.: Pressure coefficient for adiabatic and diabatic case, [$T_{01} = 99.0$ K, $p_{01} = 5.07$ bar, s_0=0.70, $M_\infty \approx 0.840$, $\alpha = 6.06°$,$MAC = 0.1$m, $Re_{MAC,\infty} = 31.4$ million].

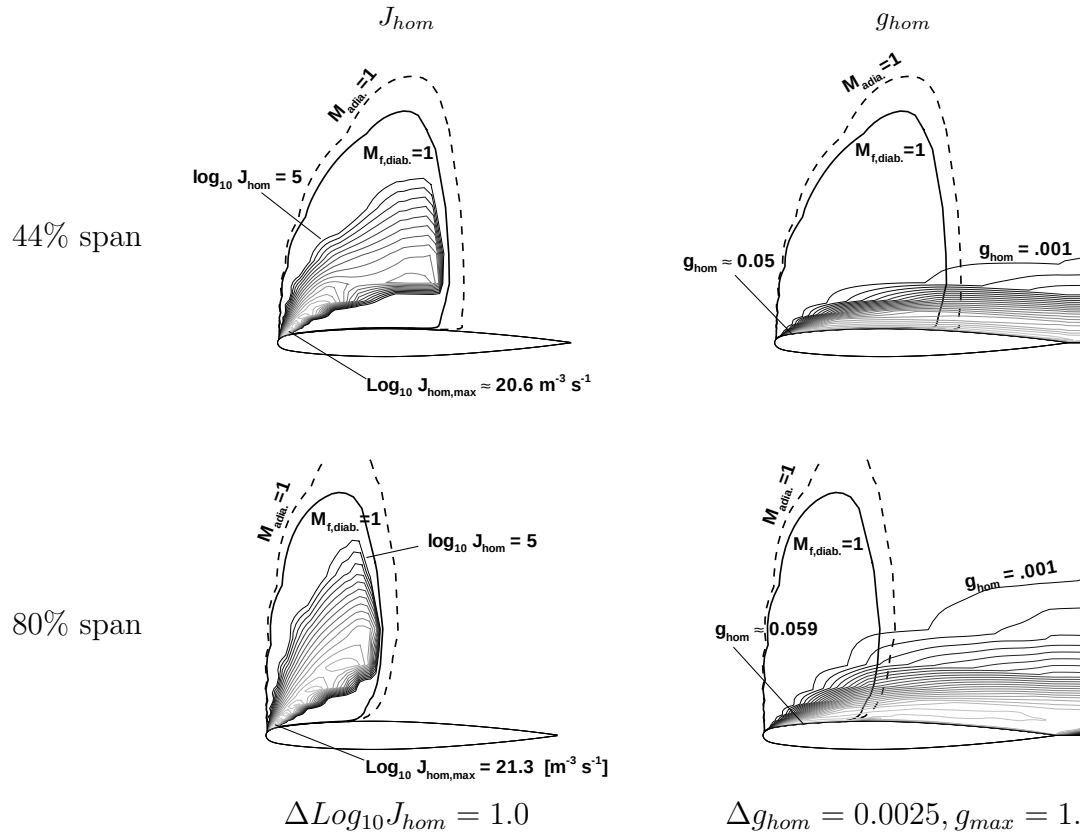

Figure 7.45.: Nucleation rate and homogeneous condensate mass fraction with Mach 1 line, [T_{01} = 99.0 K, p_{01} = 5.07 bar, s_0=0.70, $M_\infty \approx 0.840$, $\alpha = 6.06°$, MAC = 0.1m, $Re_{MAC,\infty}$ = 31.4 million].

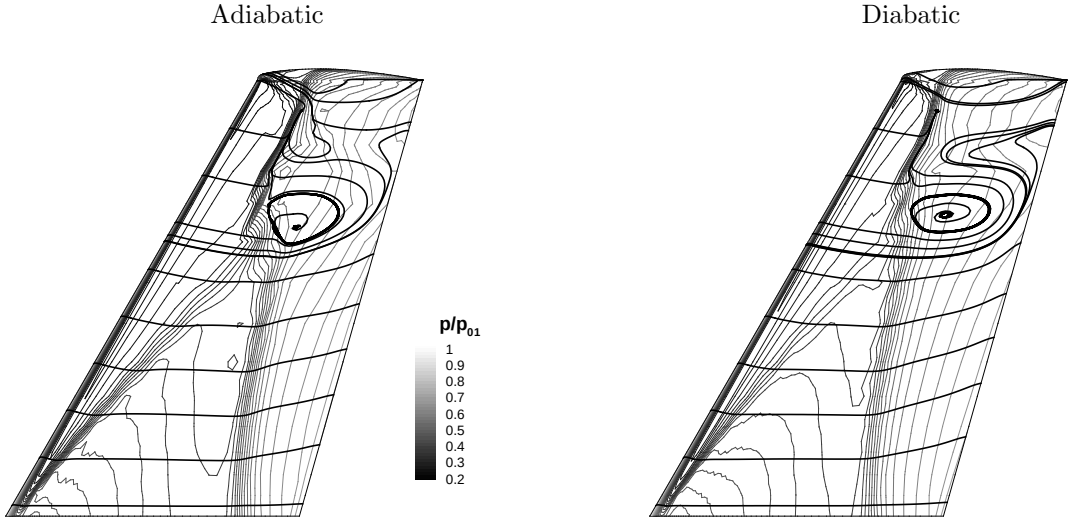

Figure 7.46.: Wing top computed skin friction lines (bold lines) overlaid on a contour plot of the pressure ratio,[T_{01} = 99.0 K, p_{01} = 5.07 bar, s_0=0.70, $M_\infty \approx 0.840$, $\alpha = 6.06°$, MAC = 0.1m, $Re_{MAC,\infty}$ = 31.4 million]

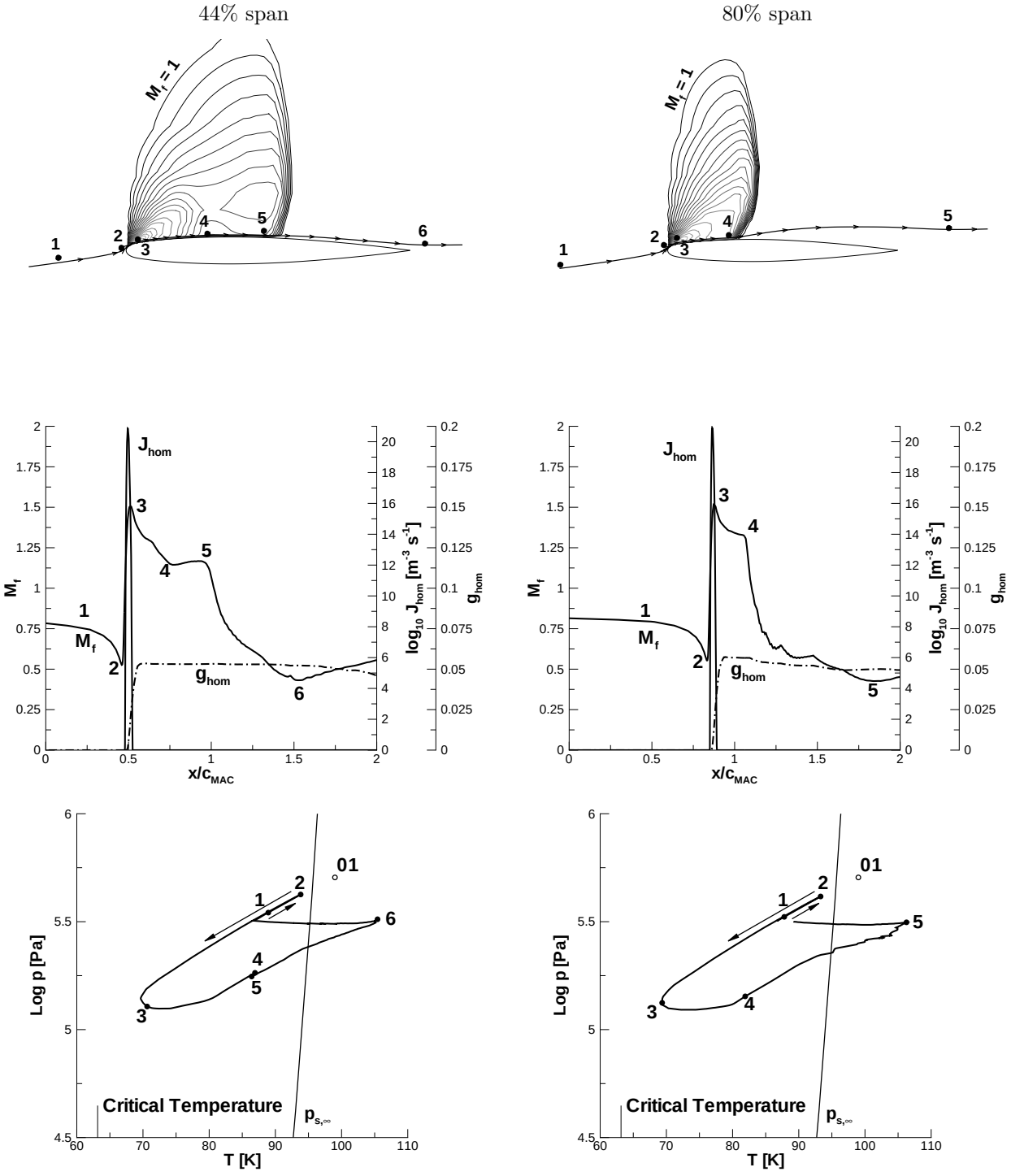

Figure 7.47.: Thermodynamic discussion of properties along a streamline,[T_{01} = 99.0 K, p_{01} = 5.07 bar, s_0=0.70, $M_\infty \approx 0.840$, $\alpha = 6.06°$, MAC = 0.1m, $Re_{MAC,\infty}$ = 31.4 million].

top : Mach contour and projected streamline near the boundary layer edge.
middle : Mach, J_{hom}, and g_{hom} values extracted from streamline.
bottom : p-T diagram based on streamline.

$\alpha = 1.07°$

At $\alpha = 1.07°$ the angle of attack is too small which means the expansion around the airfoil is too low to produce the growth of condensate. Nucleation is present, but only at about Log_{10} J of 17 $[m^{-3}s^{-1}]$, which is not enough for N_2 to condense.

Summary

As a summary the drag, lift, and lift to drag ratio for all cases are compared. Figure 7.48 (left) shows a steep decrease in the lift due to condensation as the angle of attack is increased, whereas drag is nearly constant. Figure 7.48 (right) shows the difference in the lift to drag ratio due to condensation. Here the effect of condensation is always negative mainly due to the decrease in lift on the suction side. The normal trend for this type of plot is an increase in the lift to drag ratio as α increases, but due to the adiabatic separation at 6° the data points decrease after 3°, which shows the maximum operating angle for the Mach number is somewhere between $3° - 6°$.

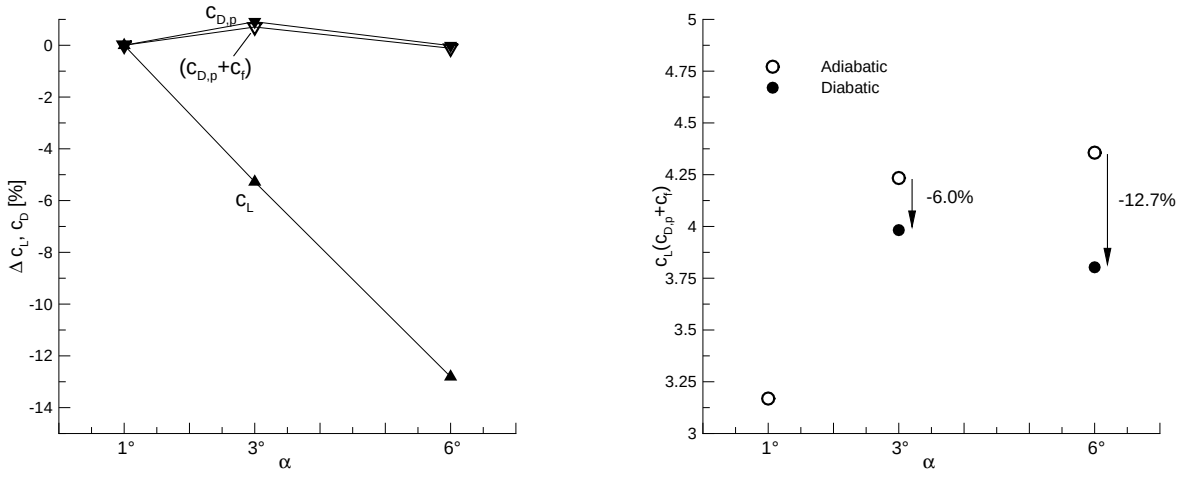

$$\Delta c_D = \frac{c_{D,q>0} - c_{D,q=0}}{c_{D,q=0}}$$

Figure 7.48.: Effect on lift and drag,[$T_{01} = 99.0$ K, $p_{01} = 5.07$ bar, $M_\infty \approx 0.840$, $c_{mac} = 0.1$m, $Re_{MAC,\infty} = 31.4$ million].

left : percent change in the pressure drag, lift, and total drag.
right : difference between the adiabatic and diabatic lift to drag ratio.

In the beginning of this section it was stated that the advantage of a cryogenic N_2 wind tunnel is to achieve flight Reynolds numbers for a small chord length. The reason for this can been seen in examining the lift to drag ratio. Table7.4 shows the difference in the lift to drag ratio for the corresponding Reynolds number. The large difference is between the

model size wing using an in-draft wind tunnel with air as the medium, compared to the cryogenic and atmospheric flight condition. The smaller Reynolds number of 1.41 million increases the friction drag by a factor of 10, which lowers the lift to drag ratio.

Table 7.4.: Comparison of the adiabatic lift to drag ratio for different operating conditions, $[M_\infty \approx 0.840, \alpha = 3.06°]$.

	Atmospheric Air MAC = 1.0 m T_∞=293 K	In-Draft Wind Tunnel Air MAC = 0.1 m T_∞=293 K	Cryogenic Wind Tunnel N_2 MAC = 0.1 m T_{01}=99 K
$\frac{c_L}{c_D}$	4.20	2.89	4.23
$Re_{MAC,\infty}$x10^6	18.92	1.41	31.4

7.5. Atmospheric Flight–F16 Wing - Turbulent

7.5.1. Geometry and Grid

The F16 Falcon wing consist of a NACA64A204 airfoil at the root and tip. The airfoil has a thickness of 4% with a sharp leading edge. The airfoil is a supercritical type and the main reason for the NACA64A204 instead of the designed NACA64204 is because due to manufacturing limitations the designed version could not be made, so the A stands for the modification. The wing has a leading edge sweep angle of 40° with a straight trailing edge. Figure 7.49 displays the wing planform geometry and airfoil shape at the root and tip. A very important point must be clarified as to what is modeled at the root profile. As seen from fig. 7.50 top and middle the beginning and end of the root profile is not so clear due to the wing body junction. Thus for the below computations a wing-body junction is NOT modeled, for the time being an Euler wall is assumed at the root profile.

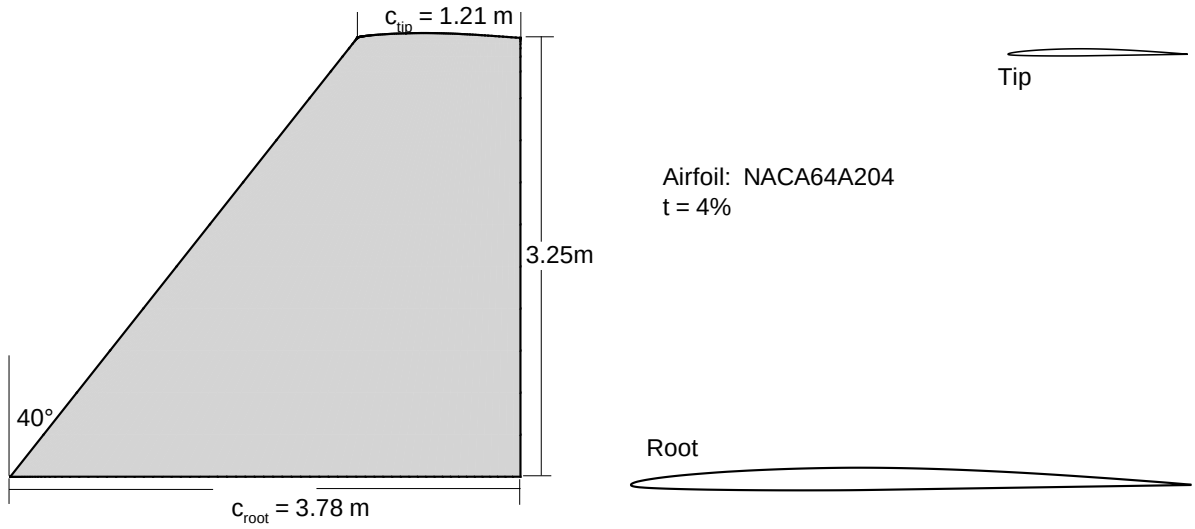

Figure 7.49.: Geometry of the F16 wing.

The only data that could be found for the geometry of the wing was luckily the airfoil shape, wing span and leading edge sweep. The root and tip lengths were derived from the middle picture in fig.7.50. Figure 7.51 shows the graphical procedure for determining the neutral point on the wing planform for which the MAC passes through. The MAC from the graphical procedure is 2.72m, which is 1.35m from the root profile.

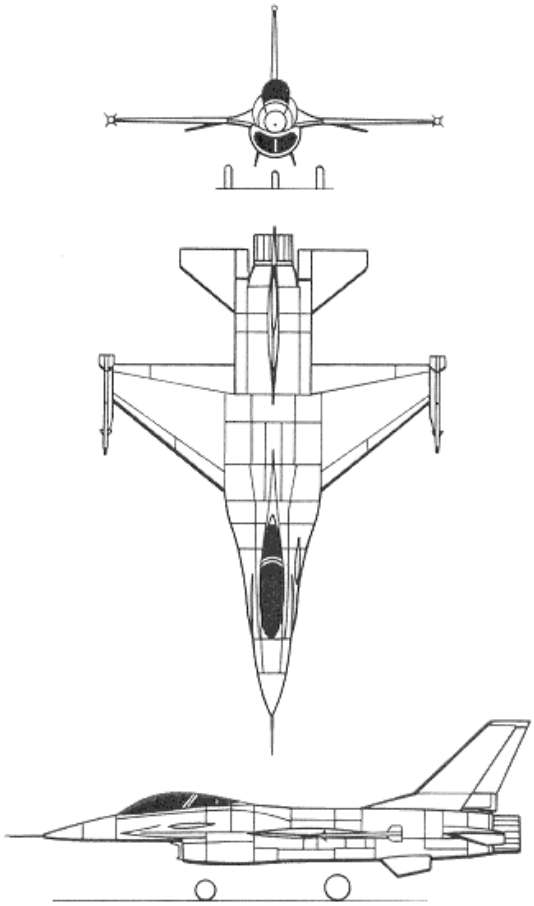

Figure 7.50.: F16 schematic. [3]

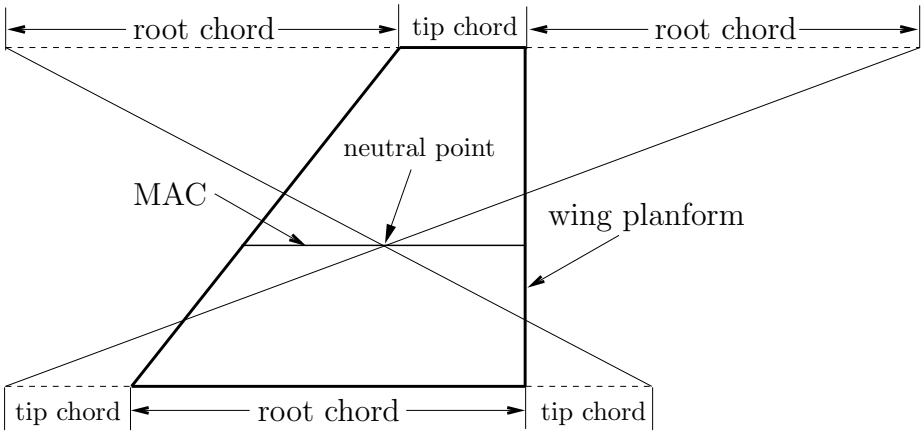

Figure 7.51.: Diagram depicting how the MAC chord is determined from the wing planform, [$MAC = 2.72$ m].

The grid for the F16 wing consist of 233i x 40j x 26k, which is very similar to the ONERA M6 wing grid, but with more points at the tip of the wing, 10 instead of 6. Figures 7.52 and 7.53 show different perspectives of the F16 wing grid. The wing top surface is coarse for most of the span but strong w-components of velocity are not expected in this region and thus more points were clustered at the tip. For the primitive single block code that is used and solving a system of 10 equations, the grid is an optimization of both CPU time and quality of results. From the experience with the ONERA M6 wing grid and comparisons to experimental data sec. 7.2 there is confidence that the grid is able to obtain reliable results.

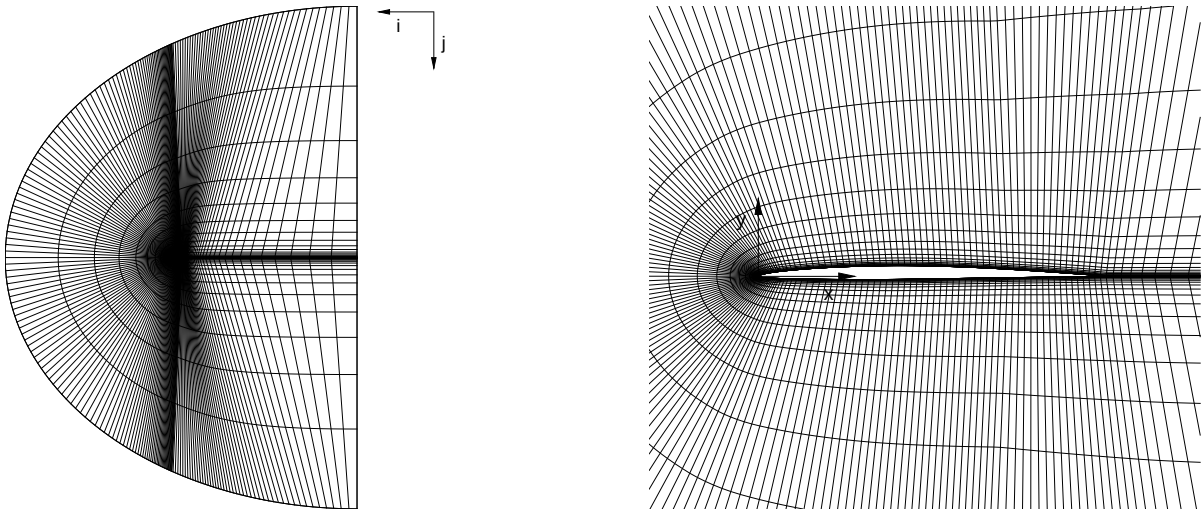

Figure 7.52.: Grid of the F16 wing, Left: Cross-section at 38% span, Right: closeup view.

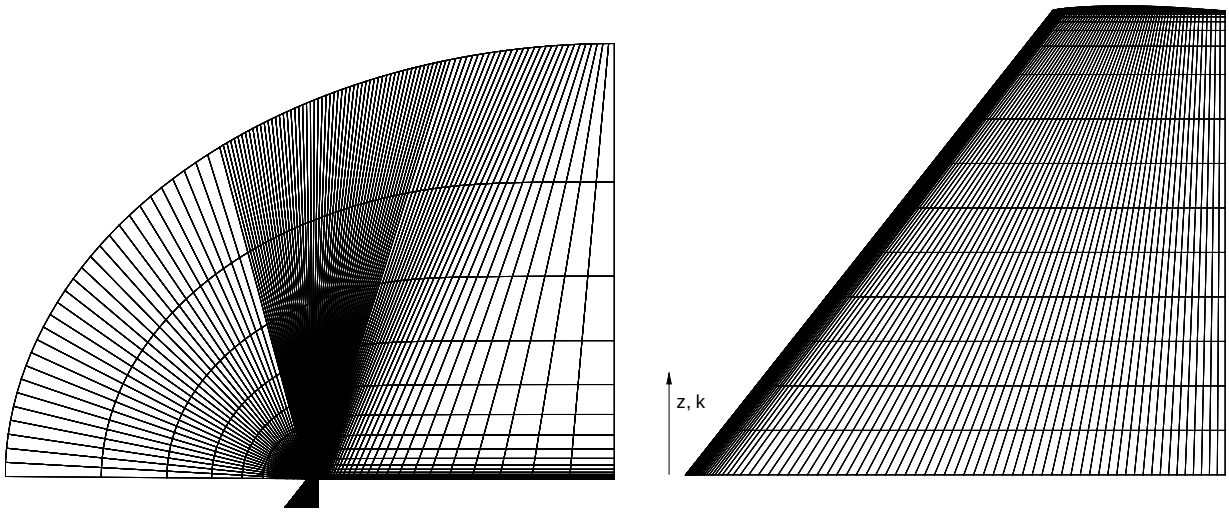

Figure 7.53.: Grid of the F16 wing, Left: k_{max} plane, Right: wing top grid.

The boundary conditions are the same as in the ONERA M6 wing case sec.7.2.1 but to be complete fig. 7.54 shows the F16 ratios from the wing to the boundaries. The ratios are much shorter than the ONERA M6 case because the F16 wing grid was made after the "non-reflecting" free stream boundary condition was developed.

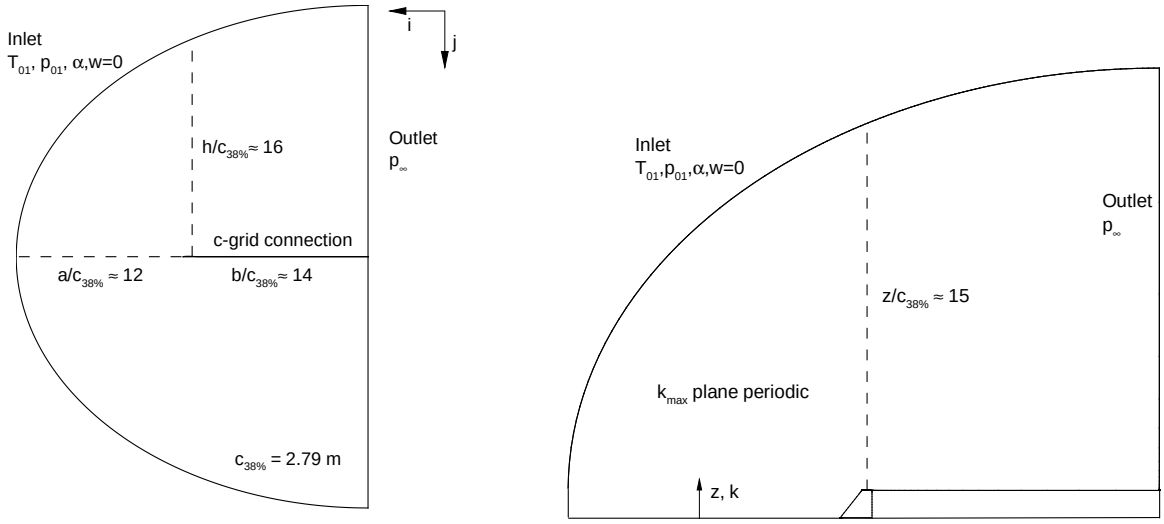

Figure 7.54.: Boundary ratios from wing surface, Left: 2-D cross-section at 38% span, Right: top view.

7.5.2. Mach = 0.9

Since the F16 wing airfoil thickness is so small, a free stream Mach number of 0.9 was used as the starting point to achieve a large enough supersonic region, which is needed to see the effect of condensation. For this wing only atmospheric flight conditions will be analyzed, since the interest lies in the effect of how lift and drag are effected due to condensation on the real wing geometry of the plane. Most of the analysis will consist of 2-D plots at various cross-sections (38, 77, and 99%). The chord length associated are 2.79, 1.81, and 1.22m. The diabatic parameters are a particle concentration of $10^{12}m^{-3}$, radius $R_p = 1\text{x}10^{-8}m$, and a free stream humidity of ϕ_∞ =90%. Figure 7.55 shows the pressure coefficient at 38, 77, and 99% span for the adiabatic and diabatic case with varying angle of attack.
For $\alpha = 0°$ and 3° the supersonic region is extended due to heterogenous condensation occurring in this region, also there is a pressure decrease after the leading edge for $\alpha = 3°$, near the tip a double shock system is forming on the wing. At a higher angle of attack the shock position is unchanged due to condensation being produced only at the leading edge, which is why there is a much larger pressure increase at the leading edge compared to the previous two angles. An important point here is that at this high angle of attack there is an absence of heterogeneous condensation, thus the flow becomes pure homogeneous. To understand these c_p plots further it is necessary to examine contour plots of g_{het} and g_{hom} at these cross sections.

For $\alpha = 0°$ (fig. 7.56) the flow is pure heterogenous condensation because there is not a strong enough acceleration (supercooling) around the nose, thus with heterogeneous the shock is moved further to the trailing edge. At an angle of 3° (figs. 7.58 and 7.57) the flow is a mixture of homogeneous and heterogeneous but only near the nose is homogeneous condensation present. The heterogeneous condensation is present on the upper surface near the second shock. The largest amount of heterogeneous condensate is occurring at 77% because there is a stronger acceleration compared to 38% but not strong enough to cause homogeneous condensation which would reduce the amount of heterogeneous condensate. At $\alpha = 6°$ (figs. 7.60 and 7.59) the wing system has moved to complete homogeneous condensation because of the large acceleration. Also important is the larger nucleation rates near the nose and thus higher condensate concentrations, which is the reason for the large static pressure increase.

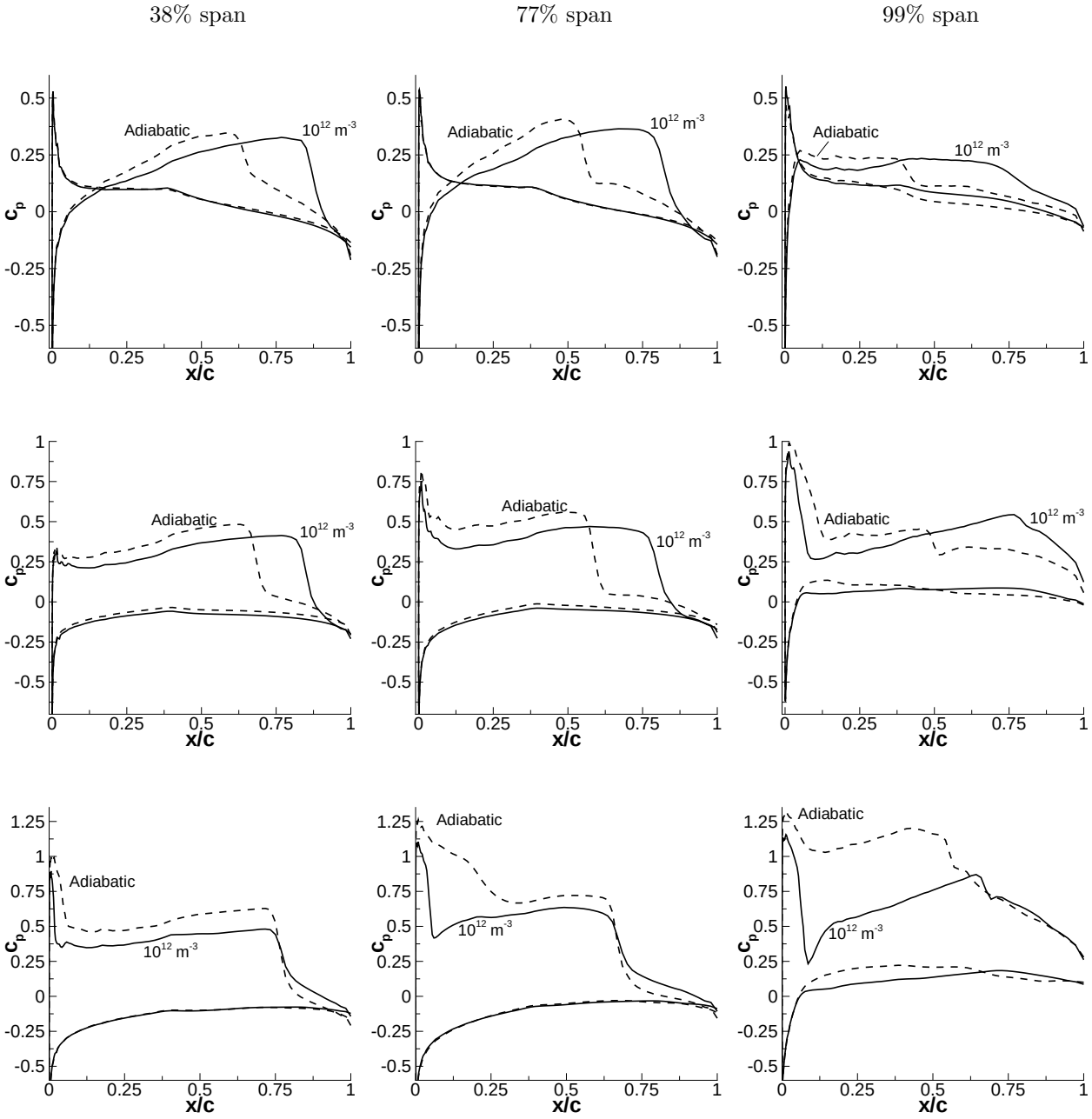

Figure 7.55.: Pressure coefficient, [$T_\infty = 295$ K, $p_\infty = 1$ bar, $M_\infty = 0.9$, $\phi_\infty = 90\%$, $N_{het,0} = 1\text{x}10^{12}$ m^{-3}, $R_p = 1\text{x}10^{-8}$m, $MAC = 2.72$ m, $Re_{MAC,\infty}$=54.8 million].

top : $\boldsymbol{\alpha = 0.0^\circ}$
middle : $\boldsymbol{\alpha = 3.0^\circ}$
bottom : $\boldsymbol{\alpha = 6.0^\circ}$

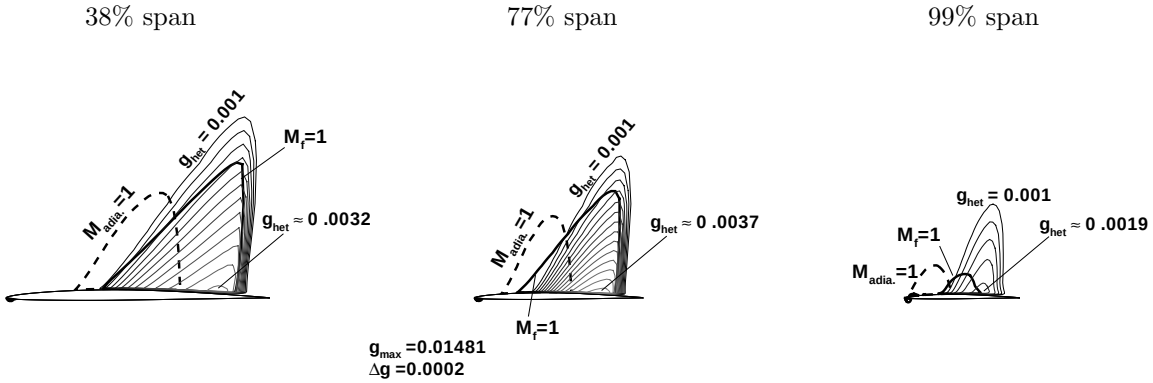

Figure 7.56.: Heterogeneous condensate mass fraction and Mach 1 lines, [$T_\infty = 295$ K, $p_\infty = 1$ bar, $M_\infty = 0.9$, $\phi_\infty = 90\%$, $N_{het,0} = 1\text{x}10^{12}$ m^{-3}, $R_p = 1\text{x}10^{-8}$m, $\alpha = \mathbf{0}°$].

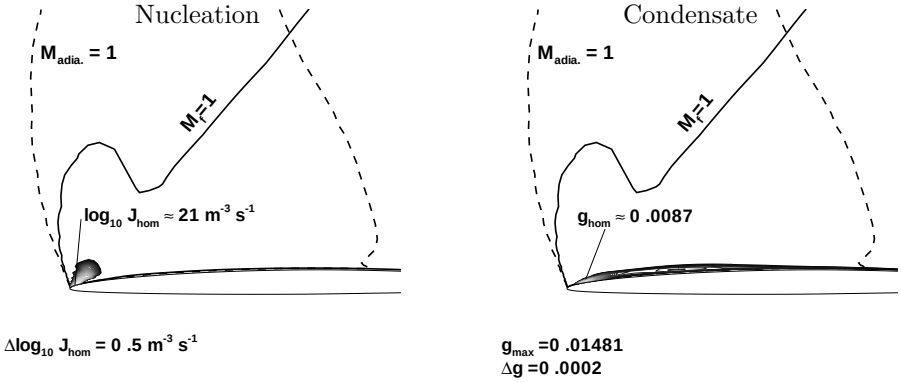

Figure 7.57.: Nucleation rate and homogeneous condensate mass fraction with Mach 1 line, [$T_\infty = 295$ K, $p_\infty = 1$ bar, $M_\infty = 0.9$, $\phi_\infty = 90\%$, $N_{het,0} = 1\text{x}10^{12}$ m^{-3}, $R_p = 1\text{x}10^{-8}$m, $\alpha = \mathbf{3}°$, 99% span].

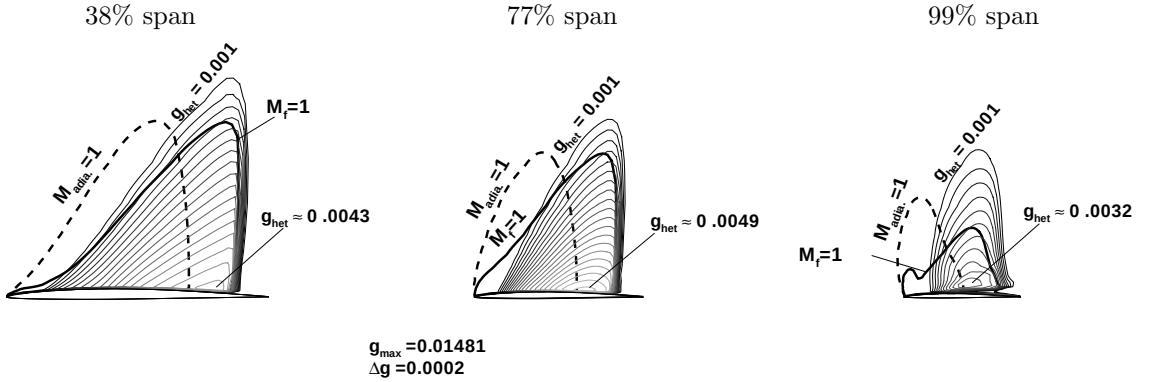

Figure 7.58.: Heterogeneous condensate mass fraction and Mach 1 lines, [$T_\infty = 295$ K, $p_\infty = 1$ bar, $M_\infty = 0.9$, $\phi_\infty = 90\%$, $N_{het,0} = 1\text{x}10^{12}$ m^{-3}, $R_p = 1\text{x}10^{-8}$m, $\alpha = \mathbf{3}°$].

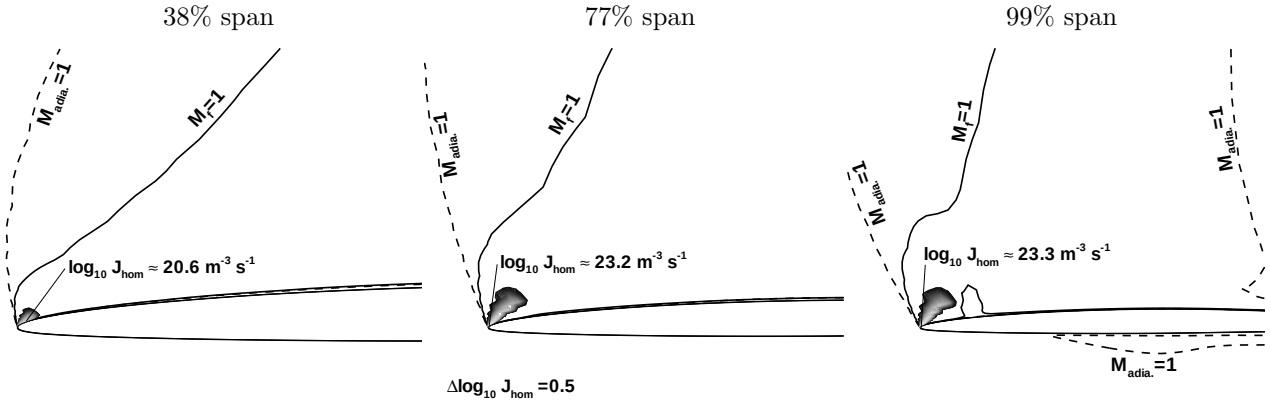

Figure 7.59.: Nucleation rate and Mach 1 lines, [$T_\infty = 295$ K, $p_\infty = 1$ bar, $M_\infty = 0.9$, $\phi_\infty = 90\%$, $N_{het,0} = 1\text{x}10^{12}$ m^{-3}, $R_p = 1\text{x}10^{-8}$m, $\alpha = \mathbf{6}°$].

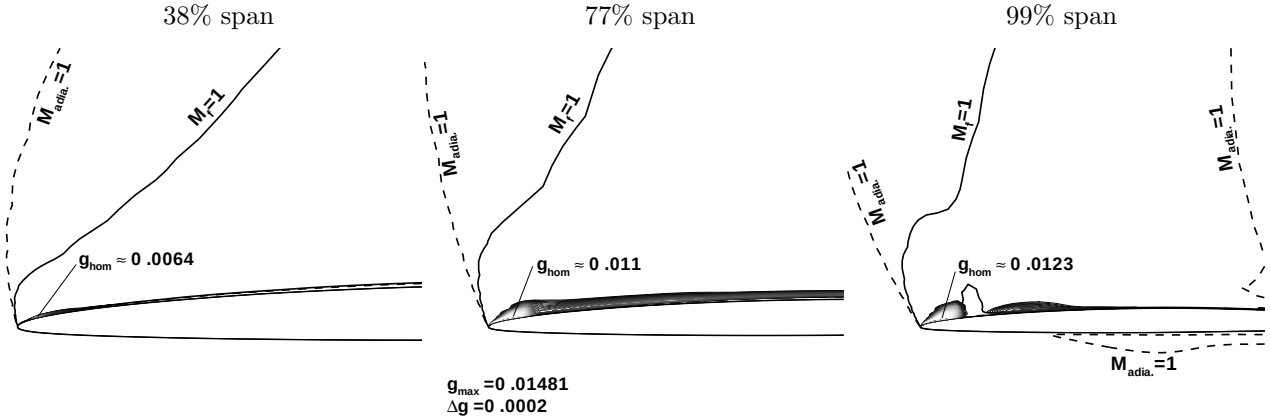

Figure 7.60.: Homogeneous condensate mass fraction and Mach 1 lines, [$T_\infty = 295$ K, $p_\infty = 1$ bar, $M_\infty = 0.9$, $\phi_\infty = 90\%$, $N_{het,0} = 1\text{x}10^{12}$ m^{-3}, $R_p = 1\text{x}10^{-8}$m, $\alpha = \mathbf{6}°$].

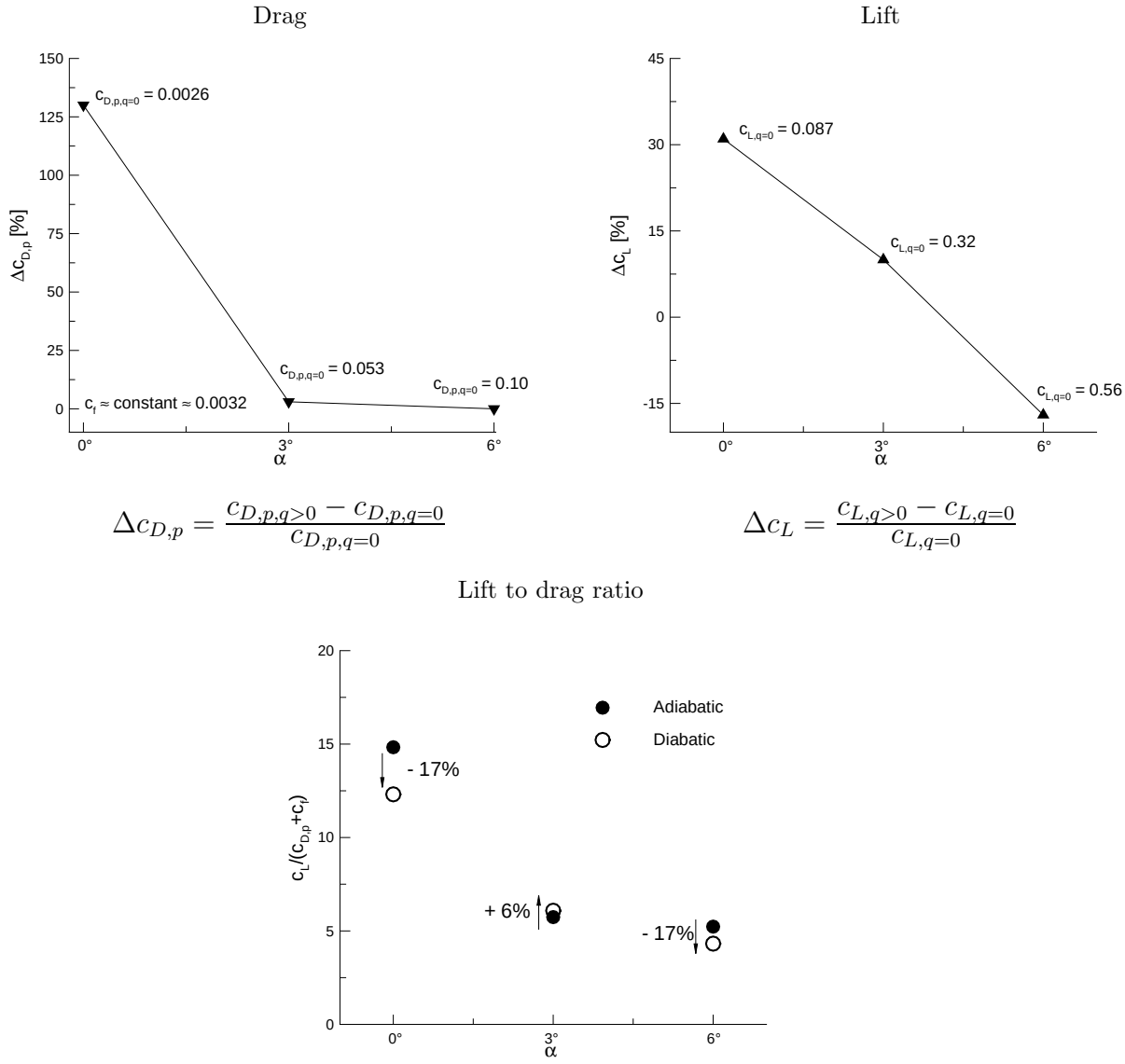

% difference represents the increase or decrease in the lift to drag ratio from the adiabatic case.

Figure 7.61.: Lift to drag ratio, [T_∞ = 295 K, p_∞ = 1 bar, M_∞ = 0.9, ϕ_∞ = 90%, $N_{het,0}$ = 1x10^{12} m^{-3}, R_p = 1x10^{-8}m, MAC = 2.72 m, $Re_{MAC,\infty}$=54.8 million].

The c_p plots already give an idea to what drag and lift are doing but by calculating the drag and lift, the entire wing surface can be analyzed. Figure 7.61 (top) displays the drag and lift for the 3 angles of attack. For example, in the lift graph +10% at $\alpha = 3°$ means the lift has increased by 10% due to the effects of condensation. At $\alpha = 0°$ the drag experiences the greatest change due to condensation and the friction coefficient makes up about 1/3 of the total drag. As the angle of attack is increased the effect of condensation becomes less. At $\alpha = 6°$ the static pressure increase at the leading edge is balanced by the static

pressure increase after the maximum thickness of the airfoil thus there is no net change in drag. Also for all angles the friction drag is relatively constant. In regards to lift there is an increase in lift due to the supersonic region increasing, but then at $\alpha = 6^\circ$ the lift is decreased because of the static pressure increase at the leading edge and no heterogeneous condensation occurred, which usually moves the shock to the trailing edge increasing the supersonic region. Looking at each component is not enough, what is most important is the lift to drag ratio (fig. 7.61, bottom). Due to the high increase in drag at $\alpha = 0^\circ$ the ratio decreases compared to the adiabatic case. Only at $\alpha = 3^\circ$ is there a benefit with condensation.

To visualize the change in Mach contour (supersonic region) due to condensation, the entire 3-D surface on the suction side of the F16 wing under Mach 0.9 conditions is plotted ($M > 1$, fig. 7.62). For $\alpha = 0^\circ$ and 3° the supersonic region is shifted to the trailing edge and is enlarged. For $\alpha = 6^\circ$ (bottom) there is no shift to the trailing edge and the supersonic region is decreased because of the homogeneous condensation occurring at the leading edge. In chap. 1 sec. 1.2, the discussion condensation on airfoil/wings, pictures are presented which show the different types of condensation during different flight conditions. At low angles there were large envelopes of condensation whereas for smaller angles the condensation is refined to a thin layer. Figure 7.63 is an attempt to show numerically what is presented in the flight pictures. One contour level (0.001) of the homogeneous or heterogeneous mass fraction is chosen for the different flight angles, fig.7.63. At $\alpha = 0^\circ$ only heterogenous condensate is present, showing the distinct diamond shape found in figs. 1.2(left) and 1.7. At $\alpha = 3^\circ$ the heterogeneous condensate is larger compared to 0° by starting earlier and having a larger envelope, also present is homogeneous condensate near the tip. Going to $\alpha = 6^\circ$ heterogenous condensate is no longer present with homogenous starting at the leading edge and then evaporating through the shock, this situation is very similar to the flight picture 1.4(left).

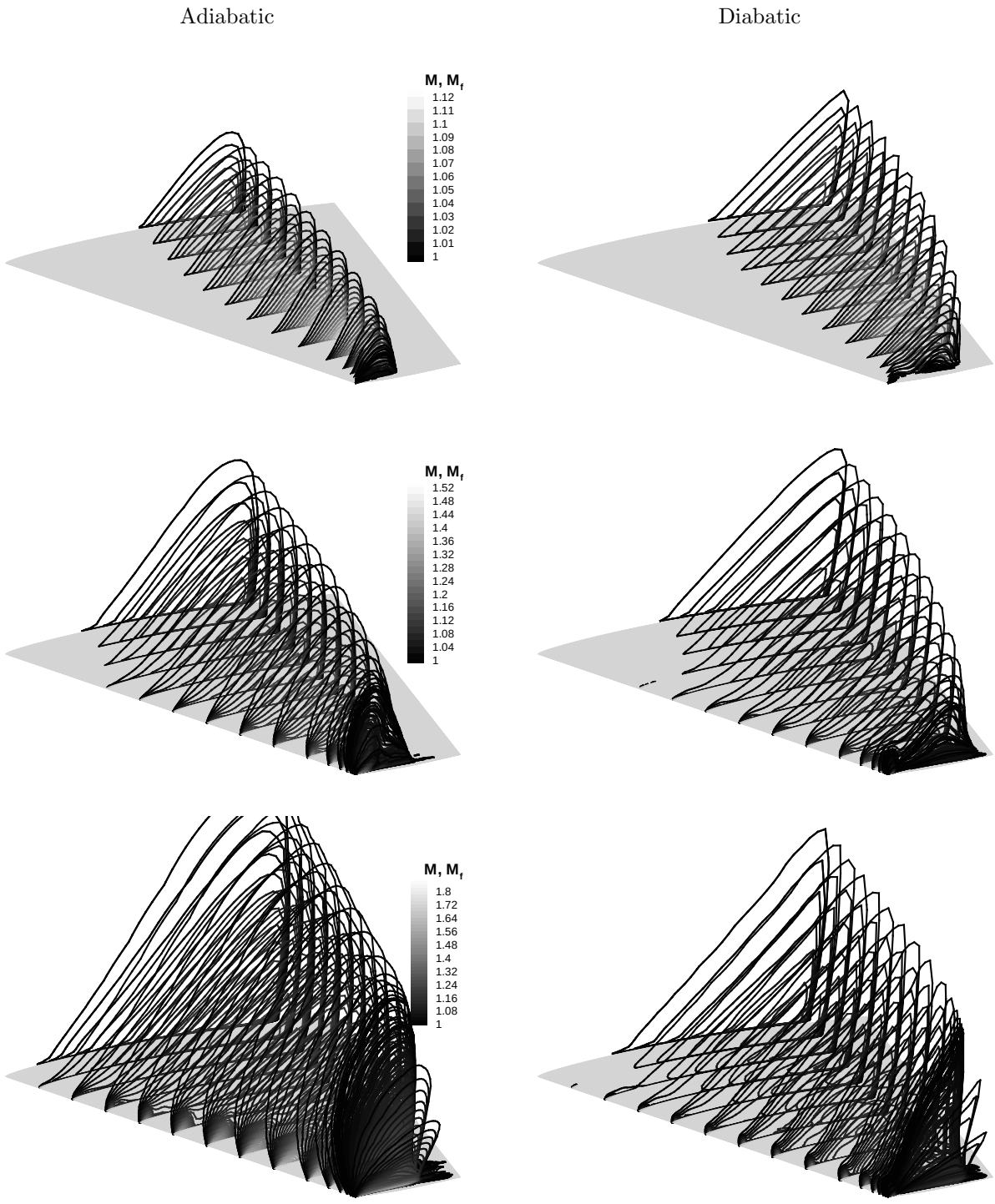

Figure 7.62.: Supersonic region on the upper surface of the F-16 Falcon wing, [T_∞ = 295 K, p_∞ = 1 bar, M_∞ = 0.9, ϕ_∞ = 90%, $N_{het,0}$ = 1x10^{12} m^{-3}, R_p = 1x10^{-8}m, MAC = 2.72 m, $Re_{MAC,\infty}$=54.8 million].

top	:	$\boldsymbol{\alpha = 0.0^\circ}$
middle	:	$\boldsymbol{\alpha = 3.0^\circ}$
bottom	:	$\boldsymbol{\alpha = 6.0^\circ}$

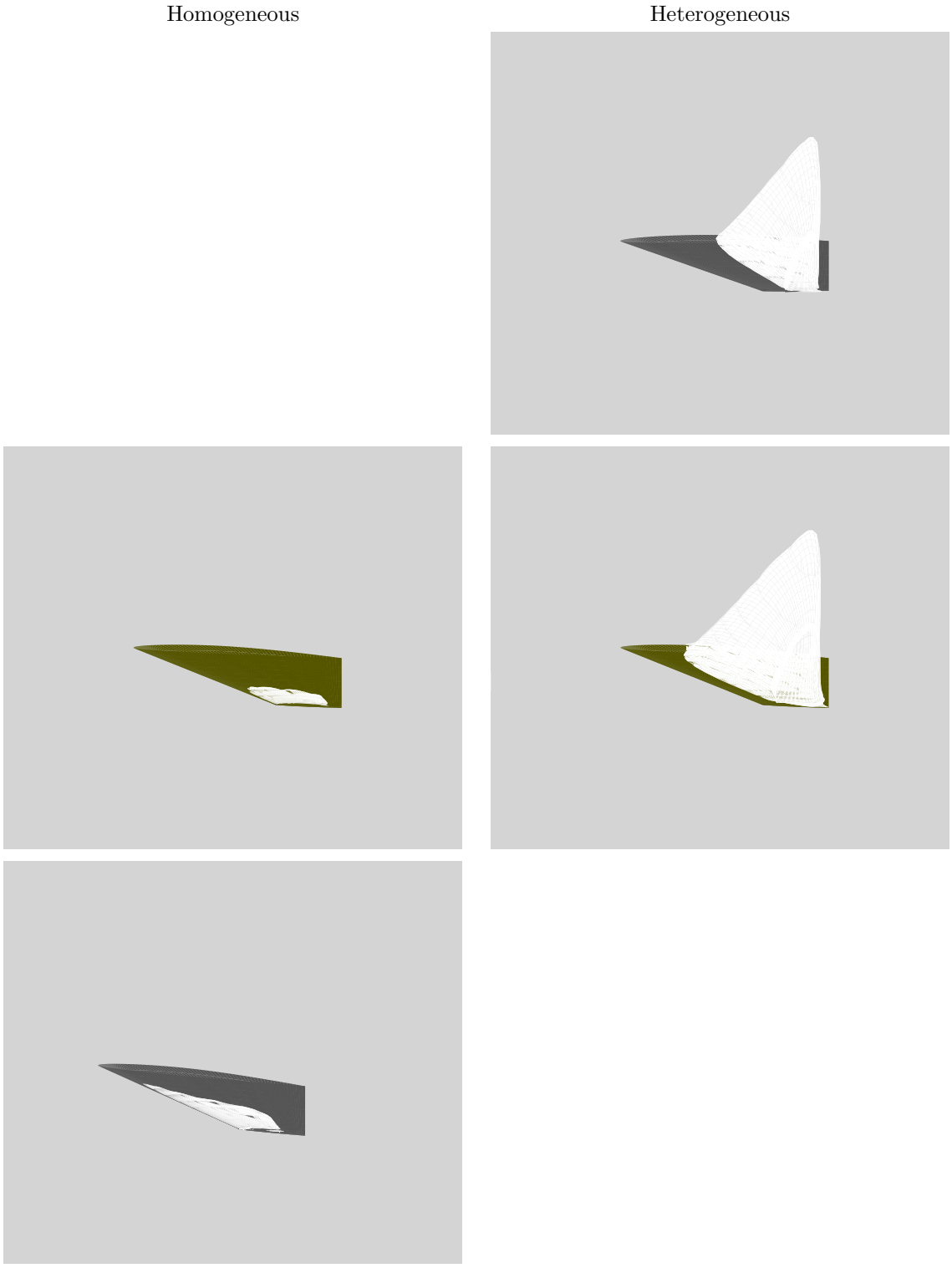

Figure 7.63.: Homogeneous/Heterogeneous condensate mass fraction on the upper surface of the F-16 Falcon wing, [T_∞ = 295 K, p_∞ = 1 bar, M_∞ = 0.9, ϕ_∞ = 90%, $N_{het,0}$ = 1x10^{12} m^{-3}, R_p = 1x10^{-8}m, MAC = 2.72 m, $Re_{MAC,\infty}$=54.8 million].

top	:	$\boldsymbol{\alpha = 0.0^\circ}$
middle	:	$\boldsymbol{\alpha = 3.0^\circ}$
bottom	:	$\boldsymbol{\alpha = 6.0^\circ}$

7.5.3. Mach = 1.1

So far only subsonic free stream conditions have been analyzed, consisting of a local supersonic pocket on the wing. The next set of results examines a free stream Mach number of $M = 1.1$. $M = 1.1$ was chosen to ensure a complete supersonic free stream and wake leaving the domain but not high enough to get into real gas effects.

because calculating at exactly $M = 1$ is numerically impossible for this code and if $M = 1.01$ is used, the program is able to run but then the outflow boundary is a mixture of subsonic and supersonic. Since the problem of interest is not to handle difficult boundary conditions, the Mach number was chosen at 1.1
Figure 7.64 compares the c_p distribution at the same 3 span stations as in the $M = 0.9$ case for $\alpha = 0 - 6°$. Since the free stream is supersonic it is not possible for heterogeneous condensation to extend the supersonic region on the wing because the shock is at the trailing edge. As α is increased the same trend of a larger distance between the pressure on the lower and upper side is present, but with condensation the c_p on the suction side is always lower than the adiabatic case. Also as α is increased the deviation from the adiabatic c_p line occurs closer to the leading edge, thus condensation is occurring earlier on the profile as α is increased. To see where the increase in pressure on the suction side comes from, fig. 7.65 shows at 3 span wise locations the heterogeneous portion of condensation and $M = 1$ line. As the angle of attack is increased the subsonic pocket at the leading edge increases but these is purely an adiabatic trend, in fact the $M = 1$ line between adiabatic and diabatic is indistinguishable. Again as α is increased the amount of heterogeneous condensate increases, but instead of shifting the shock like in the $M = 0.9$ case it just lowers the shock strength at the trailing edge.

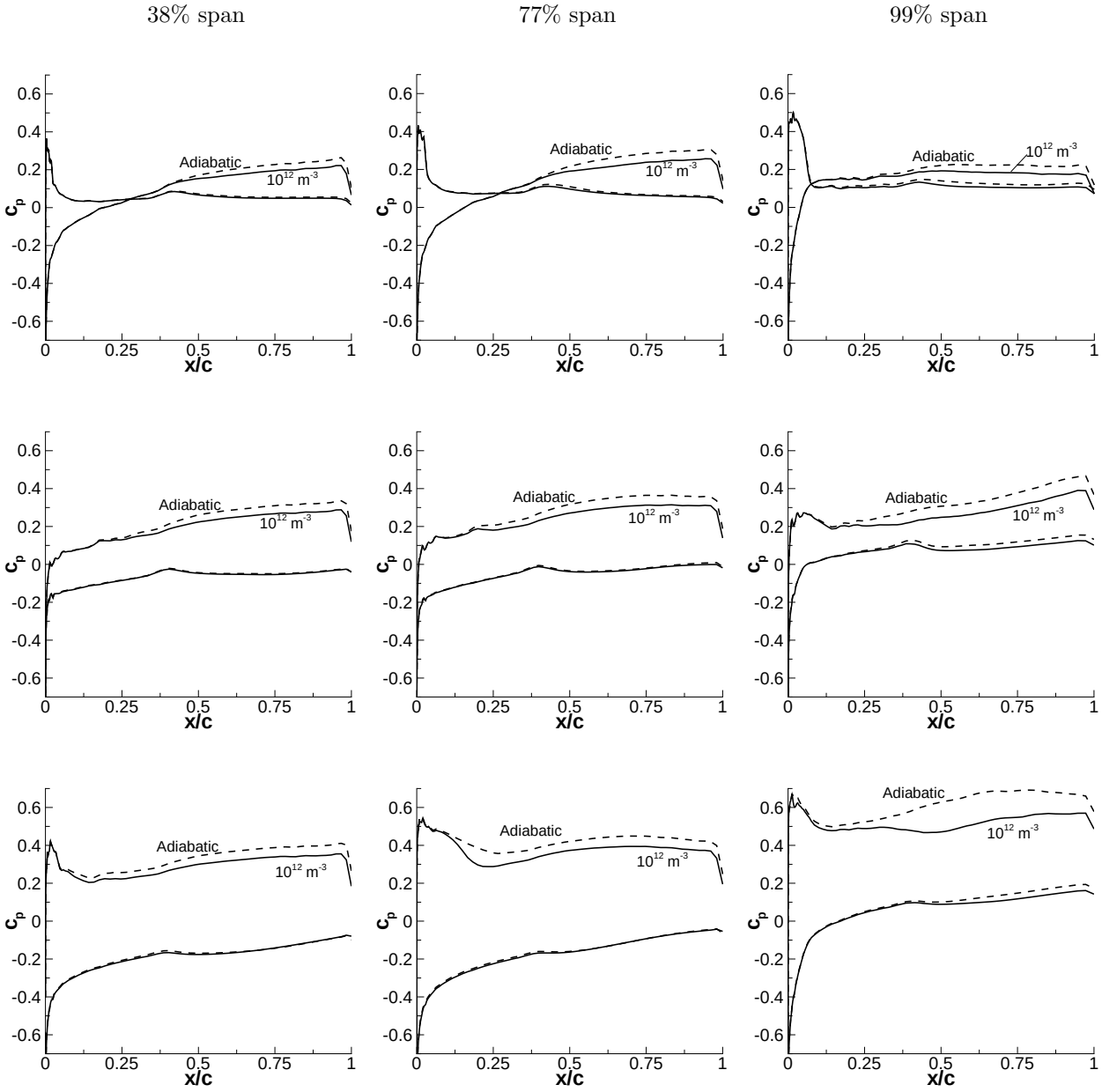

Figure 7.64.: Pressure coefficient, [$T_\infty = 295$ K, $p_\infty = 1$ bar, $M_\infty = 1.1$, $\phi_\infty = 90\%$, $N_{het,0} = 1\text{x}10^{12}$ m^{-3}, $R_p = 1\text{x}10^{-8}$m, $MAC = 2.72$ m, $Re_{MAC,\infty}$=67.0 million].

top	:	$\boldsymbol{\alpha = 0.0^\circ}$
middle	:	$\boldsymbol{\alpha = 3.0^\circ}$
bottom	:	$\boldsymbol{\alpha = 6.0^\circ}$

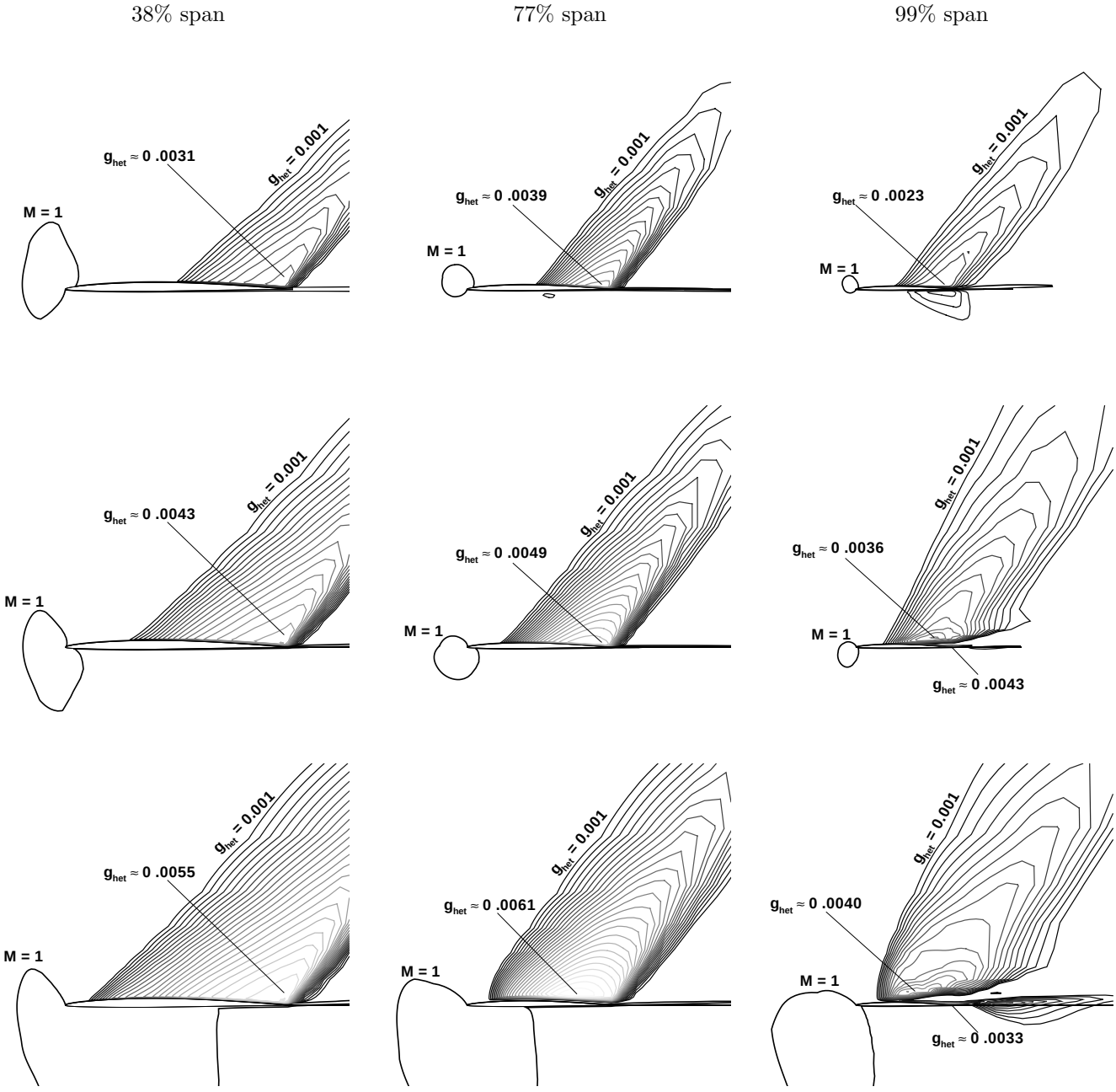

$$g_{max} = 0.01481, \quad \Delta g_{het} = 0.0002$$

Figure 7.65.: Heterogeneous condensate mass fraction and Mach 1 line, [$T_\infty = 295$ K, $p_\infty = 1$ bar, $M_\infty = 1.1$, $\phi_\infty = 90\%$, $N_{het,0} = 1\text{x}10^{12}$ m^{-3}, $R_p = 1\text{x}10^{-8}$m, $MAC = 2.72$ m, $Re_{MAC,\infty}$=67.0 million].

top : $\boldsymbol{\alpha = 0.0^\circ}$
middle : $\boldsymbol{\alpha = 3.0^\circ}$
bottom : $\boldsymbol{\alpha = 6.0^\circ}$

In regards to the drag and lift coefficient fig. 7.66 (top) there is a decrease in drag for 0° but for 3° and 6° there is relatively no change. The big difference comes in the decrease of the lift coefficient, which can be informed in the c_p plots. Since the drag is not changing that much the lift drag ratio (fig. 7.66, bottom) is dominated by the lift coefficient, which also exhibits a decrease. Thus for supersonic flight on the F16 Wing under the range of angles of attack applied, condensation has a negative impact on flight.

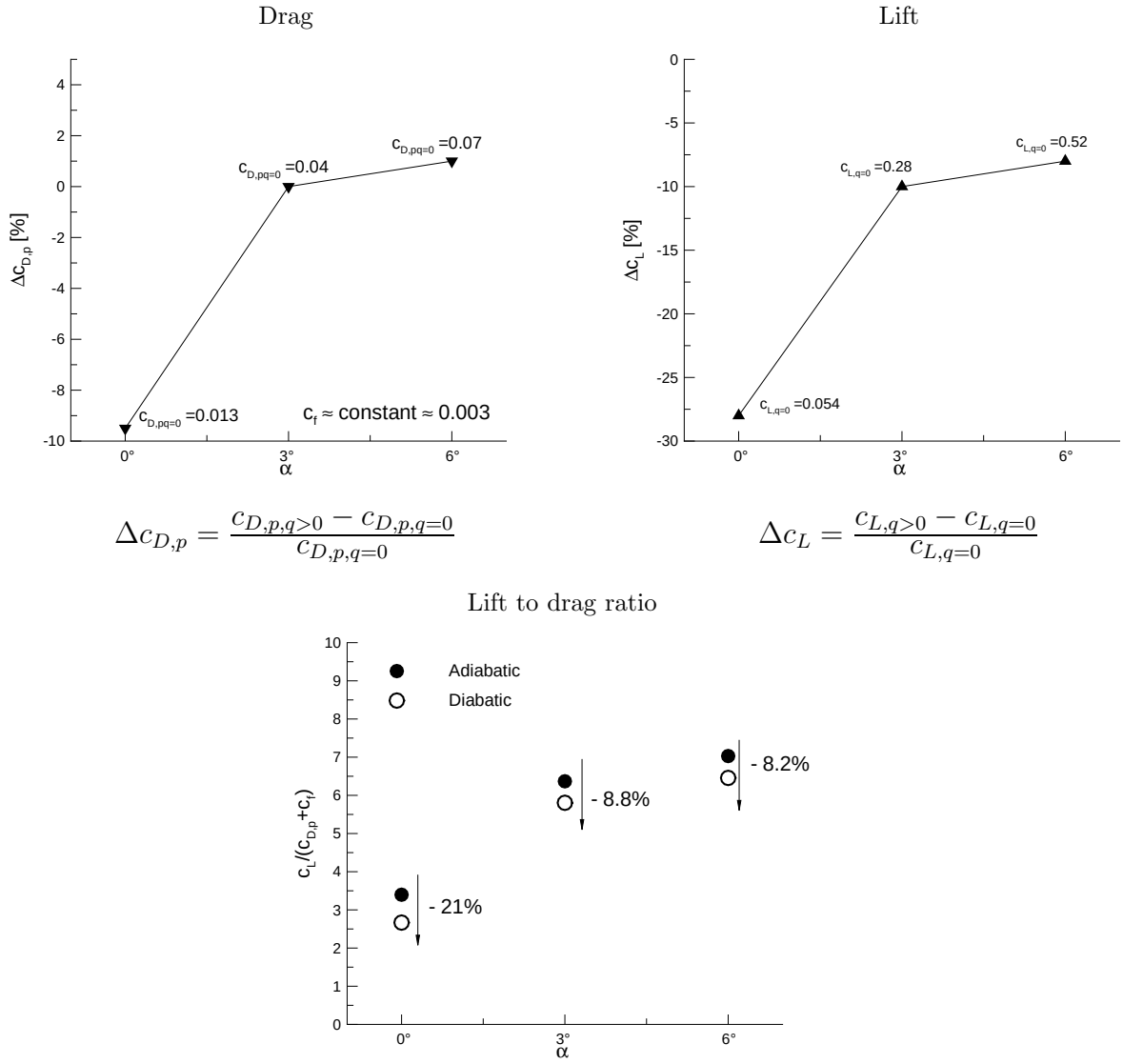

$$\Delta c_{D,p} = \frac{c_{D,p,q>0} - c_{D,p,q=0}}{c_{D,p,q=0}} \qquad \Delta c_L = \frac{c_{L,q>0} - c_{L,q=0}}{c_{L,q=0}}$$

% difference represents the decrease in the lift to drag from the adiabatic case.

Figure 7.66.: Lift to drag ratio, [T_∞ = 295 K, p_∞ = 1 bar, M_∞ = 1.1, ϕ_∞ = 90%, $N_{het,0}$ = 1x10^{12} m^{-3}, R_p = 1x10^{-8}m, MAC = 2.72 m, $Re_{MAC,\infty}$=67.0 million].

8. Summary

Homogeneous condensation of moist air is produced if the timescale of cooling is equal to the timescale of the agglomeration of the vapor molecules ($\sim 1\mu s$), whereas if foreign nuclei are present, they can prevent the process of the meta-stable state or result in condensate for smaller expansion rates. A wide range of flows have been calculated, ranging from 2-D Euler to 3-D turbulent separation. In regards to unsteady internal flow with heat addition it has been shown that disturbances in an axisymmetric nozzle can change the flow from an oscillating symmetric shock system to an unsymmetric shock surface that spirals through the nozzle. For low-altitude transonic flight on the ONERA M6 and F-16 Falcon wing with heterogeneous condensation, the lift to drag ratio can be influenced by as much as 20%. If the wing is experiencing separation, condensation can improve the lift to drag ratio, whereas for attached flow with small flight angles, condensation reduces the lift to drag ratio.
From this study no new general law has been established which says, if given these parameters this will happen. Thus instead of putting all the different characteristics of how condensation effects the flow into one box, they will be kept separate and looked upon as individual events that may have some relationship.

8.1. Internal Flow

In the 3-D A1 nozzle the same trend as in the 2-D plane nozzle was present with the symmetric shock due to heat addition moving toward the throat and then disappearing to re-establish itself downstream, thus starting the process again. With the addition of a disturbance the symmetric shock system became unsymmetric for the 2-D case and with the right disturbance rotated for the 3-D A1 axisymmetric nozzle. Adding a third dimension to the system enabled the shock to spiral.
The 3-D skewed bump test case showed that on the flat surface (top wall) condensation reduced the separation region but on the swept bump it moved the shock closer to the throat increasing the separation region. It can not be concluded though, that condensation on a curved surface in a nozzle increases the separation region because in regards to the 2-D test case of the transonic nozzle, condensation reduced the separation zone. This finding is based on side calculations, which are not included in the thesis. The curvature of the bump in the transonic diffusor is very different and the separation bubble is along the entire span but for the swept bump, it is only on half the bump surface. In conclusion it is safe to say on a flat or smooth curved surface, condensation will reduce the separation bubble, but for a bump or nozzle with high curvature the separation bubble can be increased.

8.2. External Flow

For external atmospheric flight conditions a wide variety of simulations were performed. In regards to the ONERA M6 test case wing, the chord, angle of attack, and particle concentration were changed to see their effect. By increasing the mean aerodynamic chord length from 0.5m to 2m, the effect of heterogeneous condensation was increased. At higher angles of attack 3° and 6° a mixture of homogeneous and heterogenous condensate are present. Also by having a low concentration of particles, homogeneous is more dominate where for higher concentrations heterogeneous dominates. Moving to the F-16 wing only the angle of attack and free stream Mach number were changed to see the effects of condensation at different flight conditions. More emphasis should be placed on the F-16 wing because the airfoil cross-section is more realistic than the ONERA M6, but each one serves its purpose because the ONERA M6 is a well establish test wing with available pressure data. Table 8.1 highlights the percent change in the lift to drag ratio of the two wings at different angles of attack.

Table 8.1.: Lift to drag ratio change due to condensation, [T_∞=295 K, p_∞ = 1 bar, ϕ_∞ = 90%, $N_{het,0}$ = 1x10^{12} m^{-3}, R_p = 1x10^{-8} m].

Wing	0°	1°	3°	6°
F-16 [M=0.9]	-17.0%		+6.0%	-17.0%
F-16 [M=1.1]	-21.0%		-8.8%	-8.2%
ONERA M6 [c_{MAC}=1m]		-1.6%	+3.0%	+9.0%
ONERA M6 [c_{MAC}=2m]			+4.0%	

For supersonic flight on the F16 wing, condensation has a negative impact for any angle, whereas at a subsonic freestream for $\alpha = 3°$ there is slight increase in the lift to drag ratio.

8.3. Relationship

Is there a relationship between the physics of unsteady homogeneous condensation and steady heterogeneous condensation? The main points of homogeneous condensation are a non-equilibrium process, temperature gradient, time scale of cooling, and a fast expansion. For heterogeneous it is an equilibrium process that strongly depends on particle concentration and particle size distribution.
One natural phenomena that comes to mind, outside the lab, not on a wing surface, but simply the formation, the life span, and decay of a tornado. What are the processes involved in tornado formation? Is there a bifurcation point? With the rotational wind speeds, what Mach numbers are reached? What does temperature gradient and time scale of cooling/heating attribute? For sure particle size and concentration play an important role in the visualization of a tornado but is there more. A summary of Rasmussen and

Markowski [73] is given below

> For a tornado to form it is postulated that two main ingredients must be present; strong rotating updrafts and nearby downdrafts to bring the rotation to the ground. One main reason for a rotating updraft near the ground is because of a contrast in temperature over a short distance (sounds familiar, one of the factors of homogeneous condensation is temperature gradient). To bring the rotation to the ground there must be a sinking current of air, but it is not entirely known why this occurs. One idea is that it is related to the presence of a thin curtain of rain. Even with the rotation and downdraft a tornado can not form, the downdraft must be special, it must be a warm downdraft compared to a thunderstorm downdraft caused by the evaporation of rain (heat must be absorbed to evaporate the rain to vapor), which produces a cool wind that flows out away from the rainy area. It is postulated that these "uncool" downdrafts happen when the air near the ground is very humid, thus the water can not evaporate as much into warm, humid air (again familiar, condensation and bifurcation is strongly dependent on humidity).

From the above paragraph there are some strong connections between heat addition due to condensation and the event of tornado formation. The purpose here is not to say with the current code presented in this thesis one can begin tornado modeling but rather trying to show a relationship between homogeneous and heterogeneous condensation outside the context of a controled experiment.

8.4. Further Study

From a numerical point of view, the first step for further advancement is to catch up to current numerical techniques by developing a multi-block scheme to handle complex geometries. From the step of multi block, parallelization should be performed to lower computational time. In regards to external flow, advances in numerics to handle an airfoil or wing with flap to see how the condensate convected from the airfoil or wing interacts with the use of a flap, this is especially important at high angles of attack at low altitudes (landing configuration).
In regards to the physical modeling, not much can be done to improve the classical theory of nucleation for homogeneous condensation beyond what van Dongens group has done but with heterogeneous condensation there is room for improvement and understanding. One step is to implement a model which takes into account a particle size and concentration distribution. For a 2-D nozzle or airfoil, what happens if the size and concentration distribution change with time? Another scope would be to cooperate with an agency that conducts experiments with particles in transonic flow, where the goal of the experiment is to better understand droplet growth on particles and set up a numerical test case for heterogeneous condensation models.

Bibliography

[1] S. Adam, *Numerische und experimentelle Untersuchung instationärer Düsenströmungen mit Energiezufuhr durch homogene Kondensation*, Dissertation, Fakultät für Maschinenbau, Universität Karlsruhe (TH), 1996.

[2] S. Adam and G.H. Schnerr, *Instabilities and Bifurcation of Nonequilibrium Two-Phase Flows*, J. Fluid Mechanics, Vol. 348, pp. 1–28, 1997.

[3] Aerospaceweb.org, *Fighter Gallery*, The Aircraft Musuem, 2003, <www.aerospaceweb.org/aircraft/fighter/>

[4] W.K. Anderson, J.L. Thomas, and B. van Leer, *Comparison of Finite Volume Flux Vector Splittings for the Euler Equations*, AIAA-Journal, Vol. 24, pp. 1453–1460, 1986.

[5] J.D. Anderson Jr., *Fundamentals of Aerodynamics*, Mc Graw Hill, 3rd ed., 2001.

[6] D. Barschdorff, *Kurzzeitfeuchtemessung und ihre Anwendung bei Kondenstionserscheinungen in Lavaldüsen*, Strömungsmechanik und Strömungsmaschinen, G. Braun-Verlag, Karlsruhe, Vol. 6, pp. 18–39,1967.

[7] D. Barschdorff, *Verlauf der Zustandsgrössen und gasdynamische Zusammenhaenge der spontanen Kondensation reinen Wasserdampfes in Lavaldüsen*, Forsch. Ing.-Wes., Vol. 37, No. 5, 1971.

[8] H. Benetschik, *Berechnung der sub-und transsonischen dreidimensionalen Strömung in Verdichtern mit einem impliziten Relaxationsverfahren*, Fakultät für Maschinenwesen Rheinisch-Westfälischen Technischen Hochschule Aachen, Habilitationsschrift, 1997.

[9] D. Biswas and Y. Fukuyama, *Calculation of Transitional Boundary Layers with an Improved Low-Reynolds-Number Version of the $k-\epsilon$ Turbulence Model*, ASME paper 93-GT-73.

[10] T.J. Bogar, M. Sajben, and J.C.Kroutil, *Characteristic Frequencies of Transonic Diffuser Flow Oscillations*, AIAA Journal, Vol.21, No.9, pp. 1232-1240, Sep.1983.

[11] M. Bratos and G.E.A. Meier, *Two-Dimensional Two-Phase Flows in a Laval Nozzle with Nonequilibrium Phase Transition*, Arch. Mech., pp. 1025–1037, 1976.

[12] B. Carnahan, H.A. Luther, and J.O. Wilkes, *Applied Numerical Methods*, John Wiley, New York, 1969.

[13] J.F. Campbell, J.R. Chambers, and C.L. Rumsey, *Observation of Airplane Flowfields by Natural Condensation Effects*, Journal of Aircraft, Vol. 26, no.7 pp. 593–604, 1989.

[14] K.Y. Chien, *Predictions of Channel and Boundary-Layer Flows with a Low-Reynolds-Number Turbulence Model*, AIAA Journal, Vol. 23, no. 9 pp. 1308–1319, 1985.

[15] A.V. Chirikin, *Numerical Study of Nonequilibrium Heterogeneous – Homogeneous Condensation of Steam in Supersonic Nozzles*, Fluid Dynamics, Vol. 12, No. 1, pp. 114–120, 1977.

[16] A.V. Chirikin and G.A. Saltanov, *Heterogeneous Condensation in High Speed Two-Phase Streams*, Fluid Dynamics, pp. 580–585, 1977.

[17] W.J. Coirier and B. van Leer, *Numerical Flux Formulas for the Euler and Navier-Stokes Equations: II. Progress in Flux-Vector Splitting*, AIAA-Paper 91-1566, 1991.

[18] P.H. Cook, McDonald, M.A., and Firmin, M.C.P., *"Airfoil RAE 2822 - Pressure Distributions, and Boundary Layer and Wake Measurements,"* AGARD-AR-138, 1979.

[19] M.S. Cramer, *Gallery of Fluid Dynamics*, Virginia Tech, 2003, <www.eng.vt.edu/fluids/msc/gallery/gall.htm>

[20] F.L. Daum and G. Gyarmathy, *Condensation of Air and Nitrogen in Hypersonic Wind Tunnels*, AIAA-Journal, Vol. 6, No. 3, 1968.

[21] H. Deconinck and R. Struys, *Consistent Boundary Conditions for Cell Centered Upwind Finite Volume Euler Solvers*, Numerical Methods for Fluid Dynamics III (Eds. K. W. Morton and M. J. Baines), Clarendon Press, Oxford, 1988.

[22] C.F. Delale, G.H. Schnerr and J. Zierep, *Asymptotic Solution of Transonic Nozzle Flows with Homogeneous Condensation. Part I. Subcritical flows., Part II. Supercritical flows*, Physics of Fluids A, Vol. 5, S. 2969–2995, 1993.

[23] U. Dohrmann, *Ein numerisches Verfahren zur Berechnung stationärer transsonischer Strömungen mit Energiezufuhr durch homogene Kondensation*, Dissertation, Fakultät für Maschinenbau, Universität Karlsruhe (TH), 1989.

[24] E.H. Dotson, *Homogeneous Nucleation and Droplet Growth in Nitrogen*, (Joint Inst. for Advancement of Flight Sciences, Hampton, VA, United States) NASA Center for AeroSpace Information (CASI) NASA-CR-172206 , 1983.

[25] M. Düker, *Nitrogen Condensation in Stream Tubes Duplicating the Airfoil flow in a Cryogenic Transonic Wind Tunnel*, DFVLR-AVA-Report / IB 222-83 A 08, Göttingen, 1983.

[26] M. Düker and G. Koppenwallner, *Comparisons between Experimental Observations and Predictions Obtained with Classical Homogeneous Nucleation Theory for Nitrogen Condensation in Large Freejet Experiments*, 12th International Symposium on Rarefied Gas Dynamics, Charlottesville, Va., Paper 172, July 7-11, 1980.

[27] A. Eberle, *A New Flux Extrapolation Scheme Solving the Euler Equations for Arbitrary 3-D Geometry and Speed*, Messerschmitt-Boelkow-Blohm, Munich, FRG, 1984.

[28] J. Frenkel, *Kinetic Theory of Liquids*, Oxford University Press, New York, 1946. Nachgedruckt durch Dover, New York, 1955.

[29] M. Furukawa, M. Yamaski and M. Inoue, *A Zonal Approach for Solving the Compressible Navier-Stokes Equations Using a TVD Finite Volume Method*, JSME International Journal, Series II, Vol. 33, No. 4, 1990.

[30] J.W. Gibbs, *The Collected Works of J. Willard Gibbs*, Vol. I, Longmans and Green and Co., New York, 1928.

[31] U.C. Goldberg, *Towards a Pointwise Turbulence Model for Wall-Bounded and Free Shear Flows*, J. Fluids Engineering, Vol. 116, pp. 72–76, 1994.

[32] U.C. Goldberg, *Exploring a Three-Equation R-k-ϵ Turbulence Model*, J. Fluids Engineering, Vol. 118, pp. 795–799, 1996.

[33] s.K. Godunov, *A finite difference method for the numerical computation of discontinuous solutions of the equations of fluid dynamics*, Mat. Sb., Vol. 47 pp. 357–393, 1959.

[34] A. Guha and J.B. Young, *Time-Marching Prediction of Unsteady Condensation Phenomena Due to Supercritical Heat Addition*, IMechE C423/057, pp. 167–177, 1991.

[35] G. Gyarmathy, *Zur Wachstumsgeschwindigkeit kleiner Flüssigkeitstropfen in einer uebersättigten Atmosphäre*, Z. fuer angew. Math. Physik, Vol. 14, No. 3, pp. 280–293, 1963.

[36] R.M. Hall, *Onset of Condensation Effects with an NACA 0012-64 Airfoil Tested in the Langley 0.3-Meter Transonic Cryogenic Tunnel*, NASA Langley Research Center, Hampton, VA, United States, NASA Center for AeroSpace Information (CASI) NASA-TP-1385, 1979.

[37] K. Hanjalic, I. Hadzic, and S. Jakirlic, *Modeling Turbulent Wall Flows Subjected to Strong Pressure Variations*, Transactions - American Society of Mechanical Engineers Journal of Fluids Engineering, Vol. 121, No.1 pp. 57–64, 1999.

[38] A. Harten, P.D. Lax, and B. Van Leer, *On upstream differencing and Godunov-type schemes for hyperbolic conservation laws*, SIAM Rev., Vol. 25, pp. 35–61, 1983.

[39] M. Heiler, *Instationäre Phänomene in homogen/heterogen kondensierenden Düsen- und Turbinenströmungen* , Dissertation, Fakultät für Maschinenbau, Universität Karlsruhe (TH), 1999.

[40] P.G. Hill, *Condensation of Water Vapor during Supersonic Expansion in Nozzles*, J. Fluid Mech, Vol. 25, pp. 593–620, 1966.

[41] ICEM CFD, CFD & Structural Engineering GmbH, Hannover.

[42] A. Jameson, and S. Yoon, *Multigrid Solution of the Euler Equations Using IMplicit Schemes*, AIAA Journal, Vol. 24, no. 11, pp. 1737–1743, 1986.

[43] S. Kotake and I.I. Glass, *Condensation of Water Vapor on Heterogeneous Nuclei in a Shock Tube*, UTIAS Report No. 207, University of Toronto, Institute for Aerospace Studies, 1977.

[44] S. Kotake and I.I. Glass, *Condensation of Water Vapor in Rarefraction Waves: II. Heterogeneous Nucleation*, AIAA-Journal, Vol. 15, pp. 215–221, 1977.

[45] S. Kotake and I.I. Glass, *Flows with Nucleation and Condensation*, Prog. Aerospace Sc., Vol. 19, pp. 129–196, 1981.

[46] G. Lamanna, B. Prast and M.E.H. van Dongen, *Experimental and Numerical Study of Supersonic Expansion Flow with Condensation*, Paper 220, CD Rom Proceedings of the 8th International Symposium on Flow Visualization (ISBN 0 9533991 0 9), Sorrento, 1.–4. Sept. 1998.

[47] J.C. Lee and Z. Rusak, *Transonic Flow of Moist Air Around a Thin Airfoil with Equilibrium Condensation*, Journal of Aircraft, Vol.38, No.4, 2001, pp. 693–702.

[48] M.A. Leschziner and H. Loyau, *Numerical investigation of three-dimensional transonic flow with large separation, ICAS 2000 Congress.*

[49] M.A. Leschziner, P. Batten, and H. Loyau, *Modeling shock-affected near-wall flows with anisotropy-resolving turbulence closures*, Int. Journal of Heat and Fluid Flow, Vol. 21, pp. 239–251, 2000.

[50] P.E. Liley and P.D. Desai,*Thermodynamic Properties of Refrigerants*, ASHRAE, ISBN 1-883413-10-9, 1993.

[51] M.S. Liou and C. Steffen, *A New Flux Splitting Scheme*, J. of Comp. Physics, Vol. 107, No. 1, pp. 23–29, 1993.

[52] C.C.M. Luijten and M.E.H. van Dongen, *Nucleation at high pressure. I. Theoretical considerations*, J. Chem. Phys., Vol. 111, No. 1, pp. 8524–8534, 1999.

[53] C.C.M. Luijten, P. Peeters, and M.E.H. van Dongen, *Nucleation at high pressure. II. Wave tube data and analysis*, J. Chem. Phys., Vol. 111, No. 1, pp. 8535–8548, 1999.

[54] F. Menter, *Personnel Communication*,2002.

[55] F.R. Menter, *Two-Equation Eddy-Viscosity Turbulence Models for Engineering Applications*, AIAA Journal, Vol. 32, No.8, 1994.

[56] F.R. Menter, *A Comparison of Some Recent Eddy-Viscosity Turbulence Models*, Transactions - American Society of Mechanical Engineers Journal of Fluids Engineering, Vol. 118, No.3, pp. 514–519, 1994.

[57] R. Merz, *Entwicklung eines Mehrgitterverfahrens zur numerischen Losung der dreidimensionalen kompressiblen Navier-Stokes-Gleichungen für mehrstufige Turbomaschinen*,VDI Verlag, Dusseldorf 1998.

[58] V. Michellasi, *Shock-boundary layer interaction and transition modeling in turbomachinery flows*, IMechE, Proc. Instn. Mech. Engers., Vol. 211, Part A., 1997.

[59] G. Mundinger, *Numerische Simulation instationärer Lavaldüsenströmungen mit Energiezufuhr durch homogene Kondensation*, Dissertation, Fakultät für Maschinenbau, Universität Karlsruhe (TH), 1994.

[60] M. B. H. van Noordenburg and H. W. M.Hoeijmakers, *Multiple Inviscid Solutions for the Flow in a Leading-Edge Vortex*, AIAA Journal, Vol. 38, part 5, pp. 812–824, 2000.

[61] E.S. Oran and J.P. Boris, *Numerical Simulation of Reactive Flow*, Elsevier, Amsterdam, 1987.

[62] S. Osher and F. solomon, *Upwind schemes for hyperbolic systems of conservations laws*, Math. Comput., Vol. 38, pp. 339-377, 1981.

[63] V.C. Patel, W. Rodi and G. Scheurer, *Turbulence Models for Near-Wall and Low Reynolds Number Flows : A Review*, AIAA-Journal, Vol. 23, pp. 1308–1319, 1985.

[64] P. Peeters, C.C.M. Luijten, and M.E.H. van Dongen, *Transitional droplet growth and diffusion coefficients*, Int. J. Heat Mass Transfer, Vol. 44, pp. 181–193, 2001.

[65] P. Peeters, J. Hrubý, M.E.H. van Dongen, *High pressure nucleation experiments in binary and ternary mixtures*, J. Phys. Chem. B, Vol. 105, pp. 11763–11771, 2001.

[66] F. Peters and B. Paikert, *Nucleation and Growth Rates of Homogeneously Condensing Water Vapor in Argon from Shock Tube Experiments*, Exp. Fluids, Vol. 7, pp. 521–530, 1989.

[67] V. Petr, *Stability of Transonic Two-Phase Flow with Terminating Shock Wave*, Proc. 2nd Int. Symp. on Exp. and Comp. Aerothermodynamics of Internal Flow (2. ISAIF), Prag, 12.–15. Juli 1993, pp. 441–448, 1993.

[68] T. Pot, J. Delery, and C. Quelin, *Interaction choc-couche limite dans un canal tridimensionnel-nouvelles experiences en vue de la validation du code CANARI,* ONERA TR-92/7078 AY, 1991.

[69] B. Prast, R. A. van Dam, J. F. H. Willems, and M. E. H. Van Dongen *Formation of nano-sized water droplets in a supersonic expansion flow*, Journal of Aerosol Science, Vol. 27, No. 1, pp. 147–148 1996.

[70] H.R. Pruppacher and J.D. Klett, *Microphysics of Clouds and Precipitation*, D. Reidel Publishing Company, 1980.

[71] F. Put, P. H. Kelleners, R. Hagmeijer, and H. W. M. Hoeijmakers, , *Numerical Simulation of Condensing Real Gas Flows*, ASME - Publications - PVP, Vol. 1, pp. 49–56, 2001.

[72] F. Put, *Numerical Simulation of Condensation in Transonic Flows*, Ph.D. Thesis, University of Twente, Enschede, 2003.

[73] E. Rasmussen and P. Markowski, *Severe Storms Research*, National Severe Storms Laboratory, 2003, <www.nssl.noaa.gov/ssr/>

[74] P.L. Roe, *Approximate Riemann solvers, parameter vectors , and difference schemes*, J. Comput. Phys., Vol. 43, pp. 357–372, 1981.

[75] C.L. Rumsey and T.B. Gatski, *Recent Turbulence Model Advances Applied to Multielement Airfoil Computations*, J. of Aircraft, Vol. 38, No. 5, 2001.

[76] M. Sajben and J.C. Kroutil, *Effects of Initial Boundary-Layer Thickness on Transonic Diffusor Flows,*AIAA Journal, Vol.19, No.11, 1991, pp. 1386-1393.

[77] G.A. Saltanov and R.A. Tkalenko, *Investigation of Transonic Unsteady-State Flow in the Presence of Phase Transformations*, Zh. Prikl. Mek. i Tek. Fiz. (UdSSR), Vol. 6, pp. 42–48, 1975.

[78] B. Schmidt, *Beobachtungen über das Verhalten der durch Wasserdampf-Kondensation ausgeloesten Störungen in einer Überschall-Windkanaldüse*, Dissertation, Fakultät für Maschinenbau, Universität Karlsruhe (TH), 1962.

[79] V. Schmitt and F. Charpin, *Presssure Distributions on the ONERA-M6-Wing at Transonic Mach Numbers*, Experimental Data Base for Computer Program Assessment. Report of the Fluid Dynamics Panel Working Group 04, AGARD AR 138, May 1979.

[80] G.H. Schnerr and G. Mundinger, *Numerical Visualization of Self-Excited Shock Oscillations in Two-Phase Flows*, Proc. of the 5th Int. Symp. on Comp. Fluid Dynamics (Ed.: H. Daiguji), Japan Society of CFD, Sendai, 1993.

[81] G.H. Schnerr, *Homogene Kondensation in stationären transsonischen Strömungen durch Lavaldüsen und um Profile*, Habilitation, Fakultät für Maschinenbau, Universität Karlsruhe (TH), 1986.

[82] G.H. Schnerr and U. Dohrmann, *Transonic Flow Around Airfoils with Relaxation and Energy Supply by Homogeneous Condensation*, AIAA-Journal, Vol. 28, pp. 1187–1193, 1989.

[83] G.H. Schnerr , *2-D transonic flow with energy supply by homogeneous condensation: Onset condition and 2-D structure of steady Laval nozzle flow*, Experiments in Fluids, Vol. 7, pp. 145–156, 1990.

[84] G.H. Schnerr and G. Mundinger, *Similarity, drag, and lift in transonic flow with given internal heat addition*, Euro. J. Mech., B/Fluids, Vol. 12, No.5, pp. 597–611, 1993.

[85] G.H. Schnerr and U. Dohrmann, *Drag and Lift in Nonadiabatic Transonic Flow*, AIAA Journal, Vol. 32, No.1., pp. 101–107, 1994.

[86] G.H. Schnerr and S. Adam, *Visualization of Unsteady Gas/Vapor Expansion Flows*, 3rd International Symposium on Expermental and Computational Aerothermodynamics of Internal Flows, Beijing, China, pp. 1–11, 1996.

[87] G.H. Schnerr and U. Dohrmann, *Numerical Investigation of Nitrogen Condensation in 2-D Transonic Flows in Cryogenic Wind Tunnels*, IUTAM Symposium Göttingen, Germany, 1989.

[88] G.H. Schnerr, *Personnel Communication*, September, 2003.

[89] G.H. Schnerr, *Kompressbile Strömungen mit Phasenwechsel und Energiezufuhr*, Fachgebiet Strömungsmaschinen, Universität Karlsruhe (TH), Lecture notes, 2000.

[90] http://www.sky-flash.com/boom.htm

[91] J.W. Slater, *NPARC Alliance Validation Archive*, NASA Glenn Research Center, 2003, <www.grc.nasa.gov/www/wind/valid/transdif/transdif.html>

[92] D. Sonntag and D. Heinze, *Sättigungsdampfdruck- und Sättigungsdampfdichtetafeln für Wasser und Eis*, VEB Deutscher Verlag für Grundstoffindustrie, 1982.

[93] J.L. Steger and R.F. Warming, *Flux vector splitting of the inviscid gasdynamic equations with application to finite-difference methods*, J. Comput. Phys., Vol. 40, pp. 263-293, 1981.

[94] J. Tannehill, D. Anderson, and R. Pletcher, *Computational Fluid Mechanics and Heat Transfer 2nd. ed.*, Taylor & Francis, 1997.

[95] B. Van Leer, *Flux-vector splitting for the Euler equations*, Lecture Notes in Phys., Vol. 170, pp.507-512 1982.

[96] M. Volmer, *Kinetik der Phasenbildung*, Steinkopff, Leipzig, 1939.

[97] Y. Wada and M. Liou, *Accurate and robust flux splitting scheme for shock and contact discontinuities*, SIAM Journal on Scientific Computing, Vol.18, pp. 633-657, 1997.

[98] B. Wagner, *Estimation of Simulation Errors and Investigations of Operating Range Extensions for the European Transonic Windtunnel ETW*, DORNIER Report FB 81BF/8B, 1981.

[99] P.P. Wegener and L.M. Mack, *Condensation in Supersonic and Hypersonic Wind Tunnels*, Advances in Appl. Mechanics (Eds.: H.L. Dryden and Th. von Kármán), Academic Press Inc., New York, 1958.

[100] P.P. Wegener and A.A. Pouring, *Experiments on Condensation of Water Vapor by Homogeneous Nucleation in Nozzles*, The Physics of Fluids, Vol. 7, No.3, pp. 352–361, 1963.

[101] P.P. Wegener, *Study of Experiments on Condensation of Nitrogen by Homogeneous Nucleation at States Modelling those on the National Transonic Facility*, (Yale Univ., New Haven, CT, United States) NASA Center for AeroSpace Information (CASI) NASA-CR-163217 , 1980

[102] A.J. White and J.B. Young, *A Time-Marching Method for the Prediction of Two-Dimensional Unsteady Flows of Condensing Steam*, J. of Propulsion and Power, Vol. 9, pp. 579–587, 1993.

[103] D.C. Wilcox, *Turbulence Modeling for CFD*, DCW Ind., La Canada, CA, 1998.

[104] D.C. Wilcox, *Simulation of Transition with a two-equation turbulence model*, AIAA Journal, Vol. 32, No.2, 1994.

[105] S. Yamamoto, H. Hagari, and M. Murayama, *Numerical Simulation of Condensation around the 3-D Wing*, Transactions of the Japan Society for Aeronautical and Space Sciences, Vol. 42, No. 138, pp. 182–189, 2000.

[106] D.A. Yoder and N.J. Georgiadis, *Implementation and Validation of the Chien $k-\varepsilon$ Turbulence Model in the Wind Navier-Stokes Code,* NASA/TM-1999-209080, 1999.

[107] J.B. Young, *The Condensation and Evaporation of Liquid Droplets at Arbitrary Knudsen Number in the Presence of an Inert Gas*, Int. J. Heat and Mass Transfer, Vol. 36, pp. 2941–2956, 1993.

[108] J.B. Young, *The Condensation and Evaporation of liquid Droplets in a Pure Vapour at Arbitrary Knudsen Number*, Int. J. Heat and Mass Transfer, Vol. 34, pp. 1649–1661, 1991.

[109] Y.B. Zeldovich, *Theory of the Formation of a new Phase Cavitation*, Zh. Eksp. i. Teor. Fiz. (UdSSR), Vol. 12, pp. 525, 1942.

[110] J. Zierep and S. Lin, *Ein Ähnlichkeitsgesetz für instationäre Kondensationsvorgaenge in Lavaldüsen*, Forschung im Ingenieurwesen, Vol. 34, No.4, pp. 97–132, 1968.

A.

A.1. Binary r Factor

The binary r factor for the ξ diffusive flux terms is given by

$$r_2^{m+} = \frac{1}{2}(1 + SIGN(1, \gamma_2^{\xi m}) \quad r_2^{m-} = \frac{1}{2}(1 - SIGN(1, \gamma_2^{\xi m}) \quad . \tag{A.1}$$

where SIGN is a FORTRAN statement that returns the value of the first argument with the sign of the second argument. The term γ is given by

$$\gamma_{2N}^{\xi m} = \alpha_2^{\xi m}\beta_{2N}^{\xi m} \quad \gamma_{2S}^{\xi m} = \alpha_2^{\xi m}\beta_{2S}^{\xi m} \qquad , \tag{A.2}$$

$$\gamma_{2T}^{\xi m} = \alpha_2^{\xi m}\beta_{2T}^{\xi m} \quad \gamma_{2B}^{\xi m} = \alpha_2^{\xi m}\beta_{2B}^{\xi m} \qquad , \tag{A.3}$$

where

$$\alpha_2^{\xi m} = \frac{1}{2}(\alpha_{2E}^{\xi m} + \alpha_{2W}^{\xi m}) \qquad . \tag{A.4}$$

Thus the binary factor r reduces to a function of metrics, which are defined in sec. 3.8.

A.2. Metric Factors for Diffusive Fluxes

A.2.1. Momentum in the x-direction

The metric coefficients are

$$\beta_{2\,S}^{\xi 2\,N} = \frac{4}{3}(\xi_x)_{i+\frac{1}{2}}(\eta_x)_{i+\frac{1}{2},j\pm\frac{1}{2}} + (\xi_y)_{i+\frac{1}{2}}(\eta_y)_{i+\frac{1}{2},j\pm\frac{1}{2}} + (\xi_z)_{i+\frac{1}{2}}(\eta_z)_{i+\frac{1}{2},j\pm\frac{1}{2}} \qquad , \tag{A.5}$$

$$\beta_{2\,B}^{\xi 2\,T} = \frac{4}{3}(\xi_x)_{i+\frac{1}{2}}(\zeta_x)_{i+\frac{1}{2},k\pm\frac{1}{2}} + (\xi_y)_{i+\frac{1}{2}}(\zeta_y)_{i+\frac{1}{2},k\pm\frac{1}{2}} + (\xi_z)_{i+\frac{1}{2}}(\zeta_z)_{i+\frac{1}{2},k\pm\frac{1}{2}} \qquad , \tag{A.6}$$

$$\beta_{3\,S}^{\xi 2\,N} = -\frac{2}{3}(\xi_x)_{i+\frac{1}{2}}(\eta_y)_{i+\frac{1}{2},j\pm\frac{1}{2}} + (\xi_y)_{i+\frac{1}{2}}(\eta_x)_{i+\frac{1}{2},j\pm\frac{1}{2}} \qquad , \tag{A.7}$$

$$\beta_{3\,B}^{\xi 2\,T} = -\frac{2}{3}(\xi_x)_{i+\frac{1}{2}}(\zeta_y)_{i+\frac{1}{2},k\pm\frac{1}{2}} + (\xi_y)_{i+\frac{1}{2}}(\zeta_x)_{i+\frac{1}{2},k\pm\frac{1}{2}} \qquad , \tag{A.8}$$

$$\beta_{4\,S}^{\xi 2\,N} = -\frac{2}{3}(\xi_x)_{i+\frac{1}{2}}(\eta_z)_{i+\frac{1}{2},j\pm\frac{1}{2}} + (\xi_z)_{i+\frac{1}{2}}(\eta_x)_{i+\frac{1}{2},j\pm\frac{1}{2}} \qquad , \tag{A.9}$$

$$\beta_{4\,B}^{\xi 2\,T} = -\frac{2}{3}(\xi_x)_{i+\frac{1}{2}}(\zeta_z)_{i+\frac{1}{2},k\pm\frac{1}{2}} + (\xi_z)_{i+\frac{1}{2}}(\zeta_x)_{i+\frac{1}{2},k\pm\frac{1}{2}} \qquad , \tag{A.10}$$

$$\alpha_{2\,W}^{\xi 2\,E} = \frac{4}{3}(\xi_x)_{i+\frac{1}{2}}(\xi_x)_{i+\frac{1}{0}} + (\xi_y)_{i+\frac{1}{2}}(\xi_y)_{i+\frac{1}{0}} + (\xi_z)_{i+\frac{1}{2}}(\xi_z)_{i+\frac{1}{0}} \qquad , \tag{A.11}$$

$$\alpha^{\xi 2}_{3\,{}^{E}_{W}} = -\frac{2}{3}(\xi_x)_{i+\frac{1}{2}}(\xi_y)_{i+^{1}_{0}} + (\xi_y)_{i+\frac{1}{2}}(\xi_x)_{i+^{1}_{0}} \quad , \tag{A.12}$$

$$\alpha^{\xi 2}_{4\,{}^{E}_{W}} = -\frac{2}{3}(\xi_x)_{i+\frac{1}{2}}(\xi_z)_{i+^{1}_{0}} + (\xi_z)_{i+\frac{1}{2}}(\xi_x)_{i+^{1}_{0}} \quad . \tag{A.13}$$

A.2.2. Momentum in the y-direction

The metric coefficients are

$$\beta^{\xi 3}_{2\,{}^{N}_{S}} = (\xi_x)_{i+\frac{1}{2}}(\eta_y)_{i+\frac{1}{2},j\pm\frac{1}{2}} - \frac{2}{3}(\xi_y)_{i+\frac{1}{2}}(\eta_x)_{i+\frac{1}{2},j\pm\frac{1}{2}} \quad , \tag{A.14}$$

$$\beta^{\xi 3}_{2\,{}^{T}_{B}} = (\xi_y)_{i+\frac{1}{2}}(\zeta_y)_{i+\frac{1}{2},k\pm\frac{1}{2}} - \frac{2}{3}(\xi_y)_{i+\frac{1}{2}}(\zeta_x)_{i+\frac{1}{2},k\pm\frac{1}{2}} \quad , \tag{A.15}$$

$$\beta^{\xi 3}_{3\,{}^{N}_{S}} = (\xi_x)_{i+\frac{1}{2}}(\eta_x)_{i+\frac{1}{2},j\pm\frac{1}{2}} + \frac{4}{3}(\xi_y)_{i+\frac{1}{2}}(\eta_y)_{i+\frac{1}{2},j\pm\frac{1}{2}} + (\xi_z)_{i+\frac{1}{2}}(\eta_z)_{i+\frac{1}{2},j\pm\frac{1}{2}} \quad , \tag{A.16}$$

$$\beta^{\xi 3}_{3\,{}^{T}_{B}} = (\xi_x)_{i+\frac{1}{2}}(\zeta_x)_{i+\frac{1}{2},k\pm\frac{1}{2}} + \frac{4}{3}(\xi_y)_{i+\frac{1}{2}}(\zeta_y)_{i+\frac{1}{2},k\pm\frac{1}{2}} + (\xi_z)_{i+\frac{1}{2}}(\zeta_z)_{i+\frac{1}{2},k\pm\frac{1}{2}} \quad , \tag{A.17}$$

$$\beta^{\xi 3}_{4\,{}^{N}_{S}} = -\frac{2}{3}(\xi_y)_{i+\frac{1}{2}}(\eta_z)_{i+\frac{1}{2},j\pm\frac{1}{2}} + (\xi_z)_{i+\frac{1}{2}}(\eta_y)_{i+\frac{1}{2},j\pm\frac{1}{2}} \quad , \tag{A.18}$$

$$\beta^{\xi 3}_{4\,{}^{T}_{B}} = -\frac{2}{3}(\xi_y)_{i+\frac{1}{2}}(\zeta_z)_{i+\frac{1}{2},k\pm\frac{1}{2}} + (\xi_z)_{i+\frac{1}{2}}(\zeta_y)_{i+\frac{1}{2},k\pm\frac{1}{2}} \quad , \tag{A.19}$$

$$\alpha^{\xi 3}_{2\,{}^{E}_{W}} = (\xi_x)_{i+\frac{1}{2}}(\xi_y)_{i+^{1}_{0}} - \frac{2}{3}(\xi_y)_{i+\frac{1}{2}}(\xi_x)_{i+^{1}_{0}} \quad , \tag{A.20}$$

$$\alpha^{\xi 3}_{3\,{}^{E}_{W}} = (\xi_x)_{i+\frac{1}{2}}(\xi_x)_{i+^{1}_{0}} + \frac{4}{3}(\xi_y)_{i+\frac{1}{2}}(\xi_y)_{i+^{1}_{0}} + (\xi_z)_{i+\frac{1}{2}}(\xi_z)_{i+^{1}_{0}} \quad , \tag{A.21}$$

$$\alpha^{\xi 3}_{4\,{}^{E}_{W}} = -\frac{2}{3}(\xi_y)_{i+\frac{1}{2}}(\xi_z)_{i+^{1}_{0}} + (\xi_z)_{i+\frac{1}{2}}(\xi_y)_{i+^{1}_{0}} \quad . \tag{A.22}$$

A.2.3. Momentum in the z-direction

The metric coefficients are

$$\beta^{\xi 4}_{2\,{}^{N}_{S}} = (\xi_x)_{i+\frac{1}{2}}(\eta_z)_{i+\frac{1}{2},j\pm\frac{1}{2}} - \frac{2}{3}(\xi_z)_{i+\frac{1}{2}}(\eta_x)_{i+\frac{1}{2},j\pm\frac{1}{2}} \quad , \tag{A.23}$$

$$\beta^{\xi 4}_{2\,{}^{T}_{B}} = (\xi_x)_{i+\frac{1}{2}}(\zeta_z)_{i+\frac{1}{2},k\pm\frac{1}{2}} - \frac{2}{3}(\xi_z)_{i+\frac{1}{2}}(\zeta_x)_{i+\frac{1}{2},k\pm\frac{1}{2}} \quad , \tag{A.24}$$

$$\beta^{\xi 4}_{4\,{}^{N}_{S}} = (\xi_y)_{i+\frac{1}{2}}(\eta_z)_{i+\frac{1}{2},j\pm\frac{1}{2}} - \frac{2}{3}(\xi_z)_{i+\frac{1}{2}}(\eta_y)_{i+\frac{1}{2},j\pm\frac{1}{2}} \quad , \tag{A.25}$$

$$\beta^{\xi 4}_{4\,{}^{T}_{B}} = (\xi_y)_{i+\frac{1}{2}}(\zeta_z)_{i+\frac{1}{2},k\pm\frac{1}{2}} - \frac{2}{3}(\xi_z)_{i+\frac{1}{2}}(\zeta_y)_{i+\frac{1}{2},k\pm\frac{1}{2}} \quad , \tag{A.26}$$

$$\beta^{\xi 4}_{3\,{}^{N}_{S}} = (\xi_x)_{i+\frac{1}{2}}(\eta_x)_{i+\frac{1}{2},j\pm\frac{1}{2}} + (\xi_y)_{i+\frac{1}{2}}(\eta_y)_{i+\frac{1}{2},j\pm\frac{1}{2}} + \frac{4}{3}(\xi_z)_{i+\frac{1}{2}}(\eta_z)_{i+\frac{1}{2},j\pm\frac{1}{2}} \quad , \tag{A.27}$$

$$\beta^{\xi 4}_{3\,{}^{T}_{B}} = (\xi_x)_{i+\frac{1}{2}}(\zeta_x)_{i+\frac{1}{2},k\pm\frac{1}{2}} + (\xi_y)_{i+\frac{1}{2}}(\zeta_y)_{i+\frac{1}{2},k\pm\frac{1}{2}} + \frac{4}{3}(\xi_z)_{i+\frac{1}{2}}(\zeta_z)_{i+\frac{1}{2},k\pm\frac{1}{2}} \quad , \tag{A.28}$$

$$\alpha^{\xi 4}_{2\,{}^{E}_{W}} = (\xi_x)_{i+\frac{1}{2}}(\xi_z)_{i+^{1}_{0}} - \frac{2}{3}(\xi_z)_{i+\frac{1}{2}}(\xi_x)_{i+^{1}_{0}} \quad , \tag{A.29}$$

$$\alpha^{\xi 4}_{4\,{}^{E}_{W}} = (\xi_y)_{i+\frac{1}{2}}(\xi_z)_{i+^{1}_{0}} - \frac{2}{3}(\xi_z)_{i+\frac{1}{2}}(\xi_y)_{i+^{1}_{0}} \quad , \tag{A.30}$$

$$\alpha^{\xi 4}_{3\,{}^{E}_{W}} = (\xi_x)_{i+\frac{1}{2}}(\xi_x)_{i+^{1}_{0}} + (\xi_y)_{i+\frac{1}{2}}(\xi_y)_{i+^{1}_{0}} + \frac{4}{3}(\xi_z)_{i+\frac{1}{2}}(\xi_z)_{i+^{1}_{0}} \quad . \tag{A.31}$$

A.2.4. Energy Equation

The metric coefficients are

$$\beta^{\xi 5}_{2N} = u_{i+\frac{1}{2}}\beta^{\xi 2}_{2N} + v_{i+\frac{1}{2}}\beta^{\xi 3}_{2N} + w_{i+\frac{1}{2}}\beta^{\xi 4}_{2N} \quad , \tag{A.32}$$

$$\beta^{\xi 5}_{2S} = u_{i+\frac{1}{2}}\beta^{\xi 2}_{2S} + v_{i+\frac{1}{2}}\beta^{\xi 3}_{2S} + w_{i+\frac{1}{2}}\beta^{\xi 4}_{2S} \quad , \tag{A.33}$$

$$\beta^{\xi 5}_{2T} = u_{i+\frac{1}{2}}\beta^{\xi 2}_{2t} + v_{i+\frac{1}{2}}\beta^{\xi 3}_{2T} + w_{i+\frac{1}{2}}\beta^{\xi 4}_{2T} \quad , \tag{A.34}$$

$$\beta^{\xi 5}_{2B} = u_{i+\frac{1}{2}}\beta^{\xi 2}_{2B} + v_{i+\frac{1}{2}}\beta^{\xi 3}_{2B} + w_{i+\frac{1}{2}}\beta^{\xi 4}_{2b} \quad , \tag{A.35}$$

$$\beta^{\xi 5}_{5\,{}^{N}_{S}} = (\xi_x)_{i+\frac{1}{2}}(\eta_x)_{i+\frac{1}{2},j\pm\frac{1}{2}} + (\xi_y)_{i+\frac{1}{2}}(\eta_y)_{i+\frac{1}{2},j\pm\frac{1}{2}} + (\xi_z)_{i+\frac{1}{2}}(\eta_z)_{i+\frac{1}{2},j\pm\frac{1}{2}} \quad , \tag{A.36}$$

$$\beta^{\xi 5}_{5\,{}^{T}_{B}} = (\xi_x)_{i+\frac{1}{2}}(\zeta_x)_{i+\frac{1}{2},k\pm\frac{1}{2}} + (\xi_y)_{i+\frac{1}{2}}(\zeta_y)_{i+\frac{1}{2},k\pm\frac{1}{2}} + (\xi_z)_{i+\frac{1}{2}}(\zeta_z)_{i+\frac{1}{2},k\pm\frac{1}{2}} \quad , \tag{A.37}$$

$$\alpha^{\xi 5}_{2E} = u_{i+\frac{1}{2}}\alpha^{\xi 2}_{2E} + v_{i+\frac{1}{2}}\alpha^{\xi 3}_{2E} + w_{i+\frac{1}{2}}\alpha^{\xi 4}_{2E} \quad , \tag{A.38}$$

$$\alpha^{\xi 5}_{2W} = u_{i+\frac{1}{2}}\alpha^{\xi 2}_{2W} + v_{i+\frac{1}{2}}\alpha^{\xi 3}_{2W} + w_{i+\frac{1}{2}}\alpha^{\xi 4}_{2E} \quad , \tag{A.39}$$

$$\alpha^{\xi 5}_{5E} = (\xi_x)_{i+\frac{1}{2}}(\xi_x)_{i+1} + (\xi_y)_{i+\frac{1}{2}}(\xi_y)_{i+1} + (\xi_z)_{i+\frac{1}{2}}(\xi_z)_{i+1} \quad , \tag{A.40}$$

$$\alpha^{\xi 5}_{5W} = (\xi_x)_{i+\frac{1}{2}}(\xi_x)_{i} + (\xi_y)_{i+\frac{1}{2}}(\xi_y)_{i} + (\xi_z)_{i+\frac{1}{2}}(\xi_z)_{i} \quad . \tag{A.41}$$

A.2.5. Turbulence Transport Equations

Finally the metric coefficients are

$$\beta^{\xi 7}_{7\,{}^{N}_{S}} = \beta^{\xi 6}_{6\,{}^{N}_{S}} = \beta^{\xi 5}_{5\,{}^{N}_{S}} \quad , \tag{A.42}$$

$$\beta^{\xi 7}_{7\,{}^{T}_{B}} = \beta^{\xi 6}_{6\,{}^{T}_{B}} = \beta^{\xi 5}_{5\,{}^{T}_{B}} \quad , \tag{A.43}$$

$$\alpha^{\xi 7}_{7E} = \alpha^{\xi 6}_{6E} = \alpha^{\xi 5}_{5E} \quad , \tag{A.44}$$

$$\alpha^{\xi 7}_{7W} = \alpha^{\xi 6}_{6W} = \alpha^{\xi 5}_{5W} \quad . \tag{A.45}$$